PETROGRAPHIC & GEOCHRONOLOGICAL INVESTIGATION OF S-TYPE GRANITES FROM A LOW-PRESSURE HIGH-TEMPERATURE REGIONAL AUREOLE: MT STAFFORD, CENTRAL AUSTRALIA.

| Field Location: **Mt Stafford** Anmatjira Range NT | Date: **7-12 July 2010** |
| Base Camp: **028185N 7558920E** (53 WGS84) |

Katherine Farrow, BSc
(Student 30516579)

Presented to the Department of Earth and Planetary Sciences,
Division of Environmental and Life Sciences,
in Partial Fulfillment of the Requirements for the Degree of:

Honours, BSc
Macquarie University, Sydney
June 2012

ARC National Key Centre for Geochemical Evolution & Metallogeny of Continents (GEMOC),
Department of Earth and Planetary Sciences, Macquarie University

STATEMENT OF ORIGINALITY

All the work submitted in this thesis is the original work of the author except where otherwise acknowledged. No part of this thesis has previously been submitted to any other university or institution.

Signed – Katherine Farrow Student 30516579	***Dated***

ACKNOWLEDGEMENTS

Thank you to all the GEMOC, GAU and associated Science staff at Macquarie University, who have provided a suite of machinery, equipment and laboratory testing facilities without which my research would not be possible.

A special thanks to my co-supervisors Nathan Daczko (Macquarie University) and Geoffrey Clarke (University of Sydney), who have given me the opportunity to study an amazing suite of metamorphic rocks, and spent time and energy hiking across the Australian Outback to collect samples. Norman Pearson for your advice and assistance regarding geochemical analyses. Dick Flood for your valuable input into my thesis and for introducing me to geology. Mark Lackie, thanks for your understanding regarding my re-location to regional NSW for the first half of my honours degree.

Rima and Inkeri Clarke also deserve special mention for their company and culinary skills during my fieldwork, without which malnutrition and insanity would have added to the list of adverse field conditions. Thank you Eileen Dunkley for the hard work during your PhD co-research and your company and support during our fieldwork. Thanks to Max Lines for allowing us to camp and conduct our fieldwork on Coniston Station and traverse the 4WD dirt tracks, even following the heavy rain. The fresh T-bone steaks were welcomed too.

Thanks to all the laboratory staff, including Manal Bebbington, Steve Craven, Kevin Grant and Will Powell, who offered me their assistance and advice in preparing samples and carrying out mineral analysis necessary to gain crucial data for my thesis. Thanks for showing me where to get the best coffee Steve! I would also like to thank the Australian Institute of Geoscientists organisation (AIG) for granting me the 2010 AIG Honours Bursary. This provided valuable financial support during my studies.

A big thank you to my mother and father (Ros and Tony Farrow) who's expert proof-reading and literary skills enabled me to produce my final thesis, and who gave me courage and the personal strength to undertake my honours research (part-time) while working full-time in regional NSW. I am eternally gratefully for your support and encouragement to pursue my passion for geology.

ABSTRACT

Two S-type granite intrusions form part of a high-temperature low-pressure regional aureole at Mt Stafford, in the Central Australian outback of the Northern Territory. They are intimately related to a package of metasedimentary migmatites and associated mafic sills or lavas of the Mt Stafford Member, locally metamorphosed from greenschist to granulite facies.

Petrographic, geochemical and Hf-isotopic analyses indicate the eastern and northern granites are mineralogically and chemically similar, resulting from the same larger thermal event responsible for the metamorphism at Mt Stafford. Hf-isotope compositions suggest a significant contribution of recycled crustal material in local granite production, also reflected by the abundance of inherited zircon, particularly in the northern granite samples.

The application of zircon geochronology suggests the granites were emplaced ca. 1786 ±15Ma, based on magmatic rims of grains with cores interpreted as inherited. Older cores in the eastern granite indicate they are sourced from material ca. 1824 ±14Ma. This indicates that the inherited source from the eastern granite is younger than the surrounding metasedimentary rocks, which are dated at 1866 ±3Ma. A tectonic model is presented involving thrusting of ca. 1866 ±3M metasedimentary crust over 1824 ±14Ma metsedimentary crust. Granite is produced from the partial melting of the deeper, younger crust and emplaced into the older crust.

TABLE OF CONTENTS

LIST OF FIGURES

LIST OF TABLES

LIST OF ACRONYMS

ACRONYM	DESCRIPTION
GEMOC	Geochemical Evolution and Metallogeny of Continents
GAU	Geochemical Analysis Unit
XRF	X-Ray Fluorescence
EMP	Electron Microprobe
BSE	Back-Scattered Electron
SEM	Scanning Electron Microscope
CL	Cathodoluminescence
LAM-ICP-MS	Laser Ablation Microprobe Inductively Coupled Plasma Mass Spectrometry
LAM-MC-ICP-MS	Laser Ablation Microprobe Multi-Collector Inductively Coupled Plasma Mass Spectrometry

MINERAL ABBREVIATIONS

Ser	Sericite
Pin	Pinite
	other mineral abbreviations per Whitney & Evans, 2010

APPENDICES

1. INTRODUCTION

Two S-type granite intrusions form part of a high-temperature low-pressure regional aureole at Mt Stafford, in the Central Australian outback of the Northern Territory. They are intimately related to a package of metasedimentary migmatites and associated mafic sills or lavas of the Mt Stafford Member, locally metamorphosed from greenschist to granulite facies. While the heat source for the metamorphism is not known with certainty, it has been inferred that the Mt Stafford granites form part of a larger thermal event, intruding at depth in the crust.

Application of zircon dating techniques and trace element analyses may provide further geochronological constraint on magmatic and metamorphic events at Mt Stafford. Hf-isotopic studies are applied to investigate relative contributions of juvenile and recycled crustal material to local granite production, and processes leading to their formation.

1.1 STUDY AREA

Mt Stafford is located ~200km northwest of Alice Springs, in the central Arunta Region of the Northern Territory. The Mt Stafford area comprises a regional metamorphic aureole in the northwest Anmatjira-Reynolds Ranges (Figure 1.1).

The Proterozoic to early Palaeozoic Arunta Region is a 200,000km^2 area recording an overprinting of geological events from ca. 1800Ma to the Palaeozoic (~542Ma) (Collins & Shaw, 1995, Shaw *et al*., 1984). Division of the Arunta Region into provinces is based on the characteristic and distinctive tectono-stratigraphic evolution of discrete geological terranes (Scrimgeour, 2003, cited Claoué-Long & Edgoose, 2008). The Aileron Province preserves continuity with provinces of the Tennant and Tanami regions to the north, with widespread clastic metasedimentary units collectively known as the Lander Package occupying <60% of the exposed geology (Pietsch, 2001, cited Claoué-Long & Edgoose, 2008, Claoué-Long *et al*., 2008).

The northwest trending Anmatjira and Reynolds Ranges (Figure 1.1) preserve a regional transition from high-grade gneisses in the south, to low-grade gneisses and schists in the north, with several rock units continuous between the two ranges (Clarke *et al*., 1990).

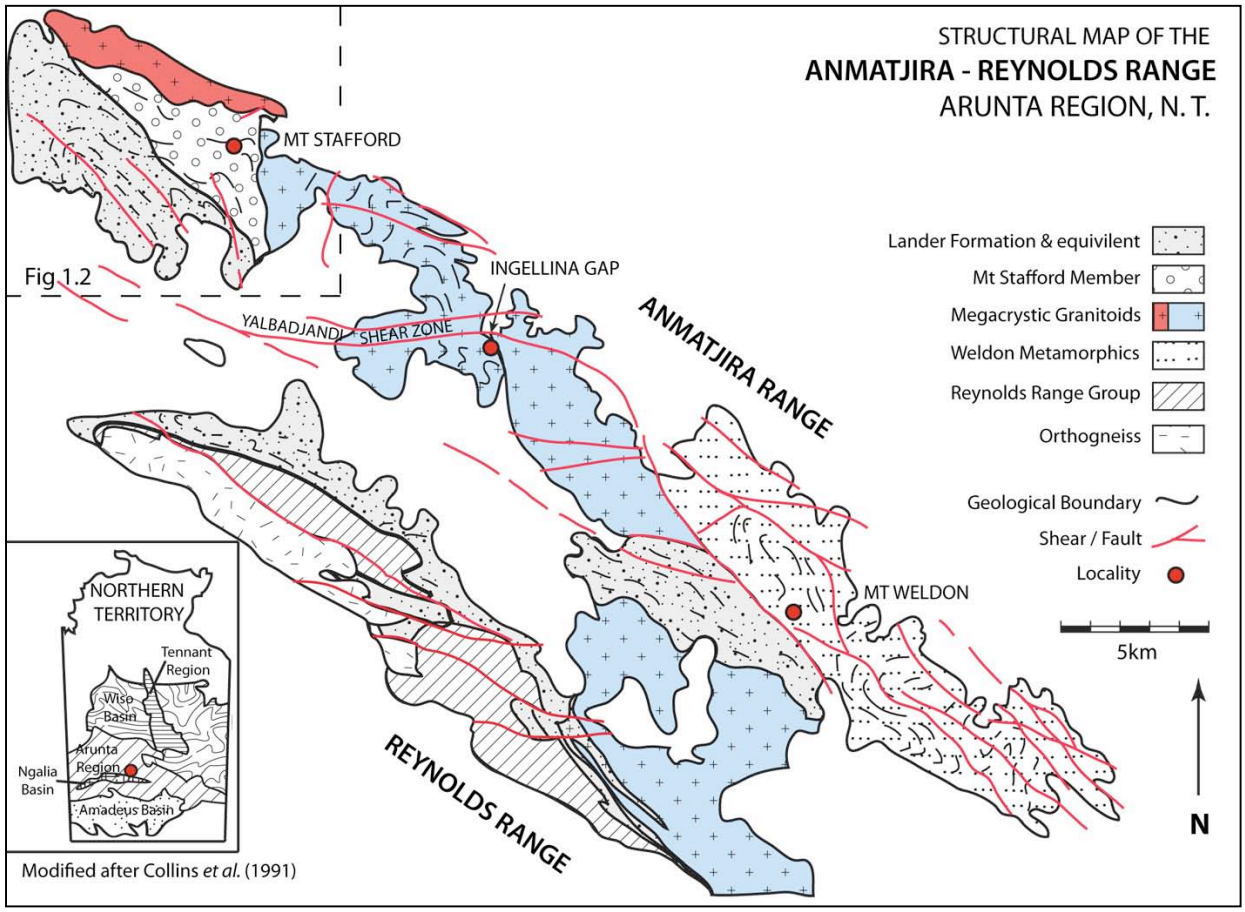

Figure 1.1 Structural Map of the Anmatjira – Reynolds Range
(Modified after Collins *et al*., 1991)
The Lander Package is continuous across the Anmatjira and Reynolds Ranges.
Areas of no outcrop are not shown (blank)

The study location covered 140km^2 across the Mt Stafford area, with 21 sampling sites and over 250kg of samples recovered. A schematic geological map with sample locations relevant to this study is presented in Figure 1.2. The Lander River marks the southern extent of the field site, which includes an area 10km north and 14km east, to the northern and eastern granitoid plutons respectively. Fieldwork and sampling rationale are described in detail in Chapter 3.

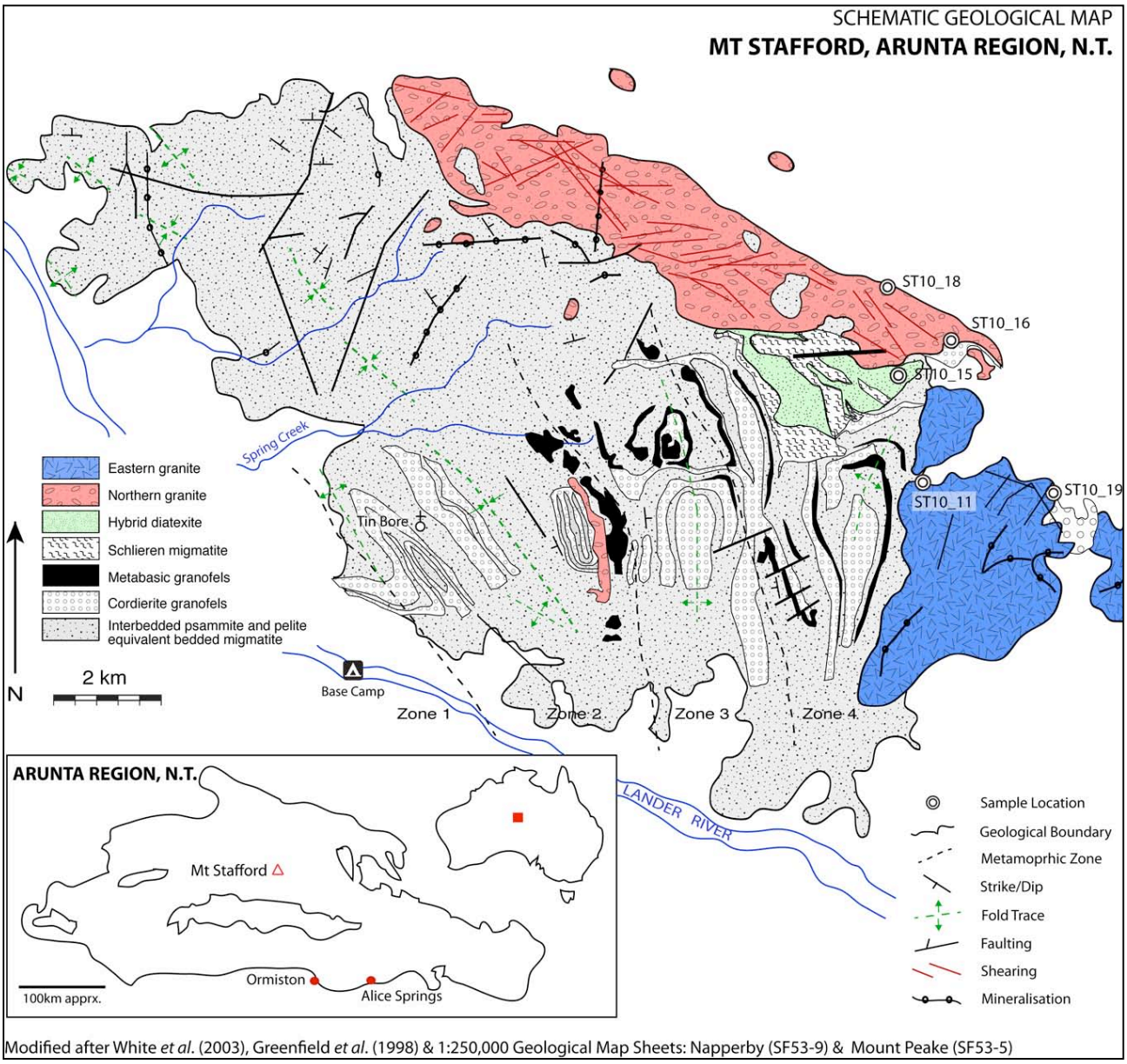

Figure 1.2 Schematic Geological Map of the Mt Stafford Area
(Modified after White *et al*. (2003), Greenfield *et al*. (1998) &
1:250,000 Geological Map Sheets: Napperby (SF53-9) & Mount Peake (SF53-5)).
Sample locations relevant to this study are shown,
along with division of metamorphic zones in the metasedimentary Mt Stafford member.

1.2 RESEARCH AIMS & OBJECTIVES

This honours research is supervised by Nathan Daczko (Macquarie University), and co-supervised by Norman Pearson (Macquarie University) and Geoffrey Clarke (University of Sydney).

The research aims to build upon previous metamorphic and dating studies at Mt Stafford, further defining and constraining age relationships between the intrusive granitoids and their age relationship with metasedimentary rocks of the Mt Stafford Member. This study will focus mainly on three sample groups: the granite plutons (eastern and northern), the proposed quartz-diorite – granite mingling zone and the hybrid diatexite zone. Petrographic, geochemical, geochronological and Hf-isotopic techniques used are detailed in Chapter 4.

OBJECTIVES

To achieve the aims of this study, several key objectives have been identified:

- Compare/contrast geochemistry of the two granite intrusions, the hybrid diatexite and the quartz-diorite – granite mingling zone, using petrographic analysis and XRF bulk chemistry data.
- Determine age relationships between the eastern and northern granites through U-Pb dating of selected zircon grains.
- Investigate the timing of magmatic and metamorphic events, using U-Pb dating and trace element analysis, with a view to further constraining the age of metamorphism at Mt Stafford.
- Develop criteria for distinguishing inherited from magmatic zircon of a similar age.
- Explore the characteristics of inherited zircon grains within the granitoid bodies, using U-Pb age, trace element and Hf-isotope analyses.
- Determine relative contributions of juvenile and recycled crust or reworked material in local granite production, through Hf-isotope values.
- Examine the structural, microstructural and geochemical relationships between the granite intrusions and quartz-diorite dyke/sill in the proposed mingling zone.

1.3 REVIEW: METAMORPHISM & DATING STUDIES

Zircon is a ubiquitous accessory mineral found in almost all rocks. It is widely used in geochronological studies because of its physical and chemical durability, resistance to high temperature diffusive re-equilibration, and incorporation of trace elements including radio-nuclides (Belousova *et al*., 2002, 2006a, Hoskin & Schaltegger, 2003). By integrating the study of morphology, trace elements, U-Pb age and Hf-isotope composition, the constraint of models for granite petrogenesis becomes possible (Belousova *et al*., 2006a).

Zircon morphology preserves a record of magmatic history, with different forms related to temperature and magmatic composition (Hoskin & Schaltegger, 2003, Belousova *et al*., 2006a). Mixing of magmas with components of different origins may generate variation in the Hf-isotope composition of crystallising zircon (Belousova *et al*., 2006a). Using this approach, it may be possible to investigate relationships at the proposed quartz-diorite mingling zone with the eastern granite.

Previous studies at Mt Stafford have concentrated on the metasedimentary Lander Package (previously known as the Lander Rock Formation or Lander Rock Beds) and correlation of stratigraphy across the Aileron Province. Regional geology has been well-constrained by the previous studies of Clarke *et al*. (1990), Collins *et al*. (1991), Vernon *et al*. (1993), Greenfield *et al*. (1996, 1998) and White *et al*. (2003), which are reviewed in Chapter 2.

Claoué-Long *et al.* (2008) describe the Lander Package as the earliest known sequence within the Aileron Province. The metasedimentary package contains detritus from magmatic and metamorphic rocks ca. 1880-1840Ma, intruded by ca. 1820-1800Ma magmatism (Clarke *et al*, 1990, Claoué-Long *et al*., 2008). The bi-modal ca. 1790-1810Ma Mt Stafford magmatic event intruded and metamorphosed the pre-existing Lander Package, resulting in an interlayering of metabasic sills or lavas and the intrusion of several granitoid plutons (Claoué-Long *et al*., 2008, Claoué-Long & Edgoose, 2008).

Deposition of the Lander Package is suggested by a detrital peak at ca. 1866 ±3Ma, with a subordinate older Proterozoic group and rare material older than ca. 2700Ma (Claoué-Long *et al*., 2008). This correlates the Lander Package with the Killi Killi Formation (Tanami Region) and the Ooradidgee Group (Tennant Region) to the north and east (Claoué-Long *et al*., 2008).

There are limited published ages for the Mt Stafford granites. The age of emplacement of the eastern granite is reported at 1805 ±3Ma for zircon and 1802 ±3Ma for monozite, using $^{207}Pb/^{206}Pb$ SHRIMP data (Rubatto *et al*., 2006). Two dates for the northern granite are suggested at 1818 ±15Ma and 1857 ±19Ma for two samples, based on $^{207}Pb/^{206}Pb$ SHRIMP data (Colins & Page, unpublished cited G.A 2007, Collins & Williams, 1995). Interestingly, reported ages for these northern granite samples do not overlap.

1.4 REVIEW: THE TERRANECHRON® METHODOLOGY

The TerraneChron® methodology, developed by the ARC National Key Centre for Geochemical Evolution and Metallogeny of Continents (GEMOC) at Macquarie University, is based on the integrated *in-situ* analysis of zircons for U-Pb age, Hf-isotopic ratio and trace element composition using laser-ablation microprobe (LAM) and electron-microprobe (EMP) technologies (Belousova *et al*., 2006c). The TerraneChron® approach provides an age distribution of magmatic rocks and an indication of the source (juvenile or reworked) of magmatic material (Griffin *et al*., 2002, 2004).

A statistically meaningful sample should comprise 60-80 randomly selected zircon grains judged to be representative of key morphological populations (Andersen, 2005 and Griffin *et al*., 2007). An age population consists of zircons whose U-Pb age lies between arbitrarily defined upper and low age limits, and are based on ages from published literature and those inferred through field relationships (Andersen, 2005).

2. REGIONAL GEOLOGY & GEOLOGICAL SETTING

2.1 INTRODUCTION

This section draws upon previous studies in the Aileron province to provide a broad overview of local geology, deformation and sub-division of the Mt Stafford member by metamorphic grade. The regional geology has been well-constrained by Clarke *et al*. (1990), Collins *et al*. (1991), Vernon *et al*. (1993), Greenfield *et al*. (1996, 1998) and White *et al*. (2003), and this chapter is essentially a literature review of their work.

2.2 REGIONAL GEOLOGY:

Proterozoic volcanic, plutonic and metasedimentary rocks of the Arunta Region comprise an extensively deformed and metamorphosed suite (Clarke *et al*., 1990, Claoué-Long *et al*., 2008). Three broad stratigraphic divisions subdivide the Arunta Region. Division 1 comprises interlayered mafic and felsic granofelses, conformably overlain by minor metapsammo-pelites and calc silicates (Collins *et al*., 1991). Division 2 rocks are dominated by metasedimentary turbidite sequences, locally interlayered with metabasic sills or lavas and intruded by extensive granitoids (Clarke *et al*., 1990, Collins *et al*., 1991, Claoué-Long *et al*., 2008). Division 3 is characterised by shallow marine/platform quartzite-metashale-calcsilicate sequences that unconformably overly divisions 1 and 2 (Collins *et al*., 1995).

Divisions within the Arunta Region represent a three-stage evolution from bi-modal volcanism to deep-water flysch-style sedimentation, followed by deposition of mature marine platform sediments (Stewart *et al*., 1984, Clarke *et al.,* 1990). During metamorphism, all divisions were intruded by granitoids, before high-grade rocks were exhumed to the surface prior to deposition of unconformable late-Proterozoic sediments of the Reynolds Range Group (Warren, 1983, Claoué-Long & Edgoose, 2008).

2.3 LANDER PACKAGE

Division 2 rocks represent the metasedimentary Lander Package, ubiquitous throughout the Anmatjira Range, and locally metamorphosed from greenschist to granulite facies at Mt Stafford (Collins *et al*., 1991, Greenfield *et al*., 1998, White *et al*., 2003, Claoué-Long *et al*., 2008, Figure 1.1). Sedimentary structures (ripple cross-laminations and graded bedding) indicate the sequence is right-way up, younging to the north (Collins *et al*., 1991, this study).

Metabasic sills or lavas are interlayered with the metasedimentary sequences and variably metamorphosed with them (Greenfield *et al*., 1996, White *et al*., 2003, Claoué-Long *et al*., 2008). Recrystallised mafic intrusions are interpreted as a stacked sequence of subvolcanic sills and dykes, 10m to 120m thick and outcropping for distances of <3km along strike (Meixner & Hoatson, 2004).

2.4 Mt Stafford Member of the Lander Package

The Mt Stafford Member (of the Lander Package) comprises interbedded aluminous metapelite, metapsammite and cordierite granofels, deformed and syn-metamorphosed with the intrusion of flat-lying megacrystic granitoid sheets to the north and east (Clarke *et al*., 1990, Greenfield *et al*., 1996, White *et al*., 2003, G.A., 2005, 2006). The cordierite granofels is derived from a cordierite-rich Al-poor siltstone protolith lacking sedimentary structures common in metapsammitic layers (Greenfield *et al*., 1996, White *et al*., 2003).

Migmatites that preserves bedding (termed 'bedded migmatite') comprises an interbedded metapelite and metapsammite unit dominating the outcrop at Mt Stafford (Greenfield *et al.*, 1996, White *et al*., 2003). The moderate strain experienced by the Mt Stafford migmatites means that processes involved in their generation may be studied without the complexity caused by strong deformation (Greenfield *et al*., 1996, 1998).

2.5 Metamorphic Zones

Metasedimentary gneisses of the Mt Stafford member show a steep geothermal gradient forming a 10km wide, low-pressure high-temperature (LPHT) regional aureole surrounding granite intrusions to the north and east (Greenfield *et al*., 1998, White *et al*., 2003). Isograd boundaries are gradational over distances of several hundred metres in the near flat-lying strata (Clarke *et al*., 1990, this study).

The Mt Stafford member is divided into five metamorphic zones ranging from greenschist to granulite facies. Migmatites occur in all but the lowest metamorphic zone (Greenfield *et al*., 1996). The isograd boundaries are defined by M_1 mineral assemblages (Clarke *et al*., 1990, Greenfield *et al*., 1996, White *et al*., 2003, summarised in Table 2.1). Mineral abbreviations used throughout this study follow those of Whitney & Evans (2010).

Table 2.1 Summary of M_1 Mineral Assemblages
(after Greenfield et al., 1996, White et al., 2003)
Protolith to cordierite granofels shown in zone 1, after Greenfield *et al*., 1996

Summary of M1 Mineral Assemblages defining Metamorphic Zones, Mt Stafford				
Rock Type	**Zone 1**: Bt+Qz	**Zone 2**: Crd+Kfs+Bt	**Zone 3**: Crd+Kfs	**Zone 4**: Crd+Kfs
Aluminous Metapelite	± Ms+And ± Ms+Chl	± Qz+And/Sil	± Qz+Sil ± Spl+Bt+Sil	± Qz+Sil ± Spl+Sil
Subaluminous Metapelite	± Ms ± Ms+And	± Qz+And/Sil	± Bt+Qz ± Bt+Qz+Grt ± Spl+Bt+Sil ± Spl+Bt	± Bt+Qz ± Qz ± Spl ± Bt+Spl ± Qz+Grt
Metapsammite	± Ms	± Qz+And/Sil	± Bt+Qz ± Bt+Qz+Grt	± Qz+Grt+Opx ± Qz+Grt ± Qz+Opx
Massive Metasiltstone (cordierite granofels protolith) Cordierite Granofels	± Ms+Crd+And ± Crd+Kfs ± Crd+Kfs+And			
		± Qz ± And/Sil ± Qz+And/Sil	± Bt+Qz ± Bt+Sil ± Bt+Sil+Spl ± Bt+Qz+Sil	± Qz ± Qz+Grt ± Qz+Sil ± Qz+Bt+Sil

ZONE 1: MS-CHL-QZ-BT SCHIST:

Interbedded metapelite and metapsammite schists comprise the poorly outcropping zone 1 rocks. Metapelite layers of muscovite-biotite-quartz-chlorite mineralogy, have an S_1 foliation defined by fine-grained muscovite (Greenfield *et al*., 1996, White *et al*., 2003). Graded bedding and ripple laminations of relict 10-50cm thick bouma sequences preserve younging to the north (Greenfield *et al*., 1996). Metapsammitic layers are quartz rich, with minor biotite-muscovite (Greenfield *et al*., 1996). Auto-metamorphic basic sills of hornblende-plagioclase-biotite-illmenite ±metamorphic amphibole generated contact aureoles 20-50m wide, producing cordierite spots 2-3cm enclosing metapelite layers (Greenfield *et al*., 1996).

ZONE 2A: AND-CRD-KFS-QZ GRANOFELS:

Zone 2a, at the lower limit of zone 2, is defined by the appearance of K-feldspar by subsolidus breakdown of muscovite to andalusite-K-feldspar assemblages, and the appearance of pseudomorphous biotite-andalusite-quartz symplectites (Greenfield *et al*., 1996, White *et al*., 2003). Insipient stages of partial melting are observed as leucocratic segregations of quartz-biotite-K-feldspar (Greenfield *et al*., 1996).

ZONE 2B: AND-CRD-KFS-BT-QZ MIGMATITE:

First leucosome and metatexite formation defines the lower limit of zone 2b. Metapelite layers within the metatexite contain K-feldspar-cordierite-andalusite-biotite assemblages with interconnected leucocratic segregations (Greenfield *et al*., 1996, White *et al*., 2003). Fine-grained metapsammite layers have quartz-biotite-cordierite-muscovite mineralogy (Greenfield *et al*., 1996).

Cordierite granofels appears in zone 2b as banded layers of coarse-grained cordierite (>60%) with minor andalusite-biotite-quartz (Greenfield *et al*., 1996, White *et al*., 2003). The upper limits of zone 2b are defined by two-pyroxene mafic granofels, interlayered with sillimanite-bearing migmatite (Greenfield *et al*., 1996).

ZONE 2C: AND-SIL-SPL-CRD-KFS-BT-QZ±GRT MIGMATITE:

Zone 2c is defined by sillimanite coaxially replacing andalusite, with pseudomorphs retaining the prismatic andalusite morphology, as shown in Figure 2.1 (Vernon, 1987, cited Greenfield *et al*., 1996, White *et al*., 2003, this study). Cordierite-spinel symplectites partially pseudomorph aluminosilicate in the cordierite granofels and bedded migmatite (Greenfield *et al*., 1996). Metapelite layers have abundant K-feldspar, whilst metapsammitic layers are rich in cordierite (Greenfield *et al*., 1996).

In zone 2c, bedded migmatite is more common than metatexite, and metapelite layers within it show abundant leucosome centred on aluminosilicate and filling extensional boudin neck structure, shown in Figure 2.2 (Greenfield *et al*., 1996, White *et al*., 2003).

ZONE 3: SIL-SPL-CRD-KFS±BT±QZ±GRT MIGMATITE:

Zone 3 is characterised by a marked decrease in biotite and an increase in topographic relief up to ~400m (Greenfield *et al*., 1996, White *et al*., 2003). Bedded migmatite metapelite layers contain K-feldspar-cordierite-biotite-quartz-sillimanite±garnet assemblages, with subordinate metapsammite layers (Greenfield *et al*., 1996). Prismatic sillimanite, after andalusite, is surrounded by reaction coronas of symplectitic cordierite-spinel (White *et al*., 2003).

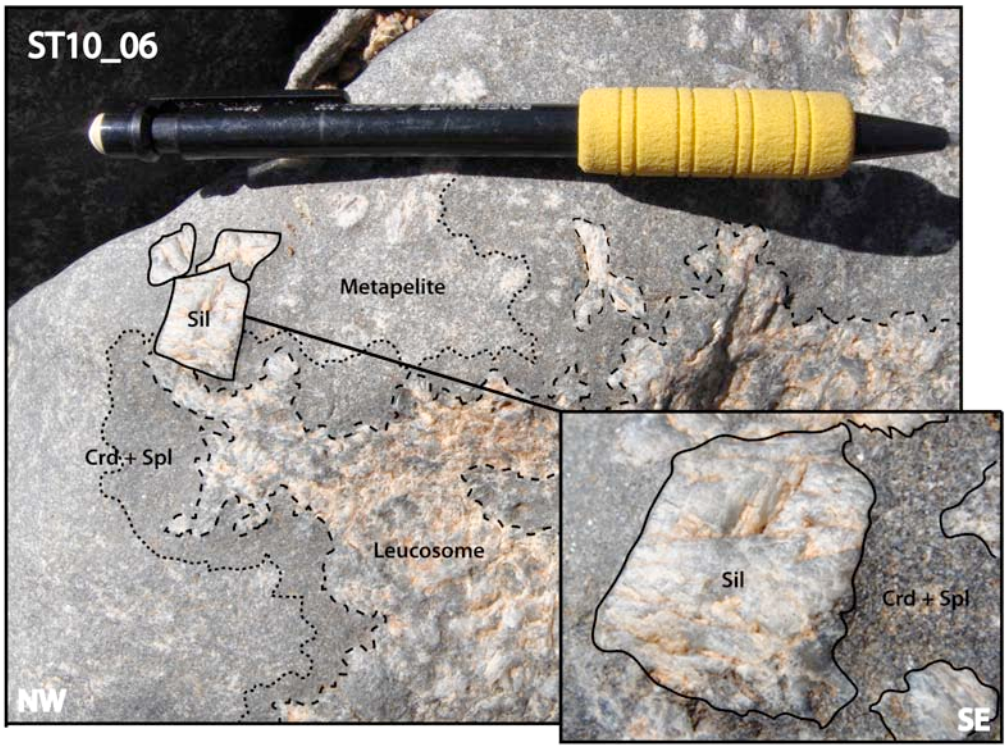

Figure 2.1 Zone 2C Sillimanite Pseudomorphing Andalusite
Sillimanite pseudomorph retains prismatic andalusite morphology.
Patches of leucosome are surrounded by cordierite and spinel coronas.
(Pencil used for scale is 135mm in total length. See **Appendix A**)

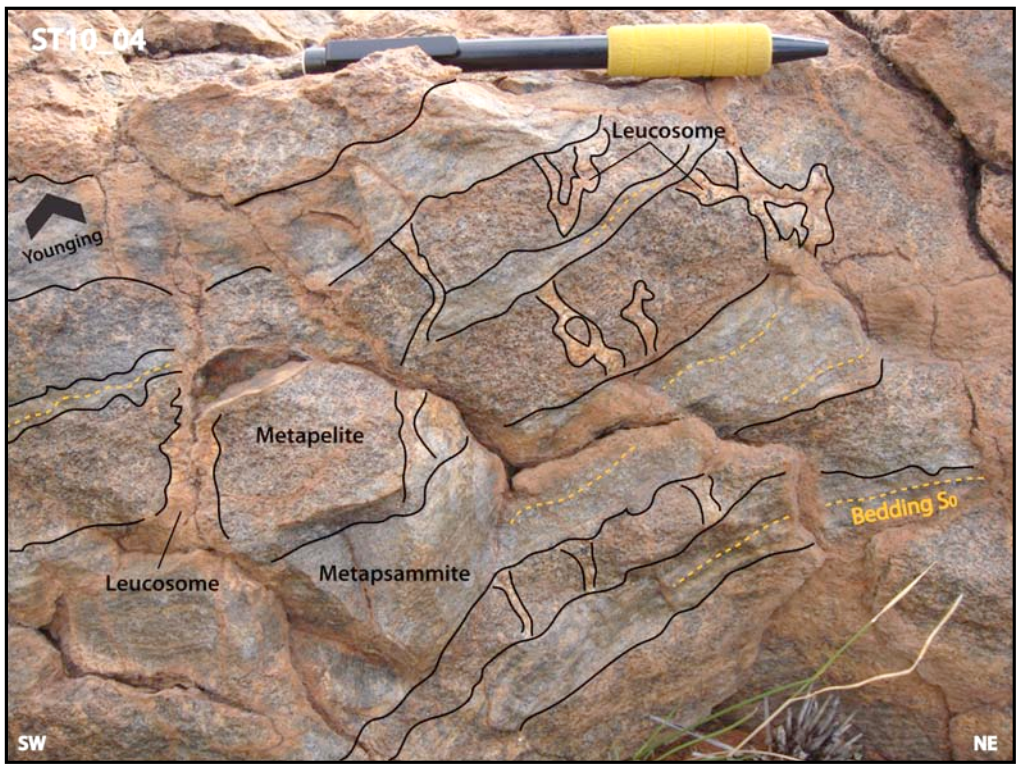

Figure 2.2 Zone 2 First Stage Metapelite Leucosome
Bedded metapsammite separates boudinaged cordierite-rich metapelite,
as a pre-cursor to schlieren migmatite formation. Graded bedding indicates younging north.

Zone 3 contains the first schlieren migmatite and well-developed melanosome (Greenfield *et al.,* 1996). Metapsammite layers retain compositional layering, while metapelite layers are increasingly mobilised and disrupted (Greenfield *et al*., 1996). Melanosomes feature fine-grained, dark brown selvages with sharp boundaries and commonly enclose isolated garnet porphyroblasts up to 25mm (Greenfield *et al*., 1996, this study).

Mafic dykes or sills consist of two-pyroxene granofels, with poikiloblastic orthopyroxene and clinopyroxene enclosing plagioclase-hornblende-ilmenite-biotite assemblages (Greenfield *et al*., 1996). Elongate clusters of pyroxene define an L_{1a} mineral stretching lineation (Greenfield *et al*., 1996, this study).

ZONE 4: GRT-OPX-CRD-KFS MIGMATITE:

Zone 4 is typified by orthopyroxene-garnet bearing metapsammite layers, indicating metamorphic temperatures in excess of ~810ºC and pressures of 2.5 ±0.6kbar (Greenfield *et al*., 1996, White *et al*., 2003). Bedding is highly contorted in the schlieren migmatite, with melanosome separating mobilised leucosome (metapelite) (Greenfield *et al*., 1996, Figure 2.3).

Strongly-peraluminous cordierite granofels were extensively melted and mobilised such that relict bedding was destroyed and diatexite formed (Greenfield *et al*., 1996). Distinct leucosomes isolate blocks of cordierite granofels, and retains peritectic cordierite-spinel symplectites pseudomorphing sillimanite (Greenfield *et al*., 1996). Partially melted metabasic dykes or sills produced coarse-grained orthopyroxene-plagioclase segregations (Greenfield *et al*., 1996).

ZONE 5: CRD-KFS-BT-QZ±GRT±OPX DIATEXITE:

Zone 5 biotite-cordierite-plagioclase hybrid diatexite represents a gradational contact between the zone 4 migmatites and megacrystic granitoid intrusions (Greenfield *et al*., 1996). The hybrid diatexite is characterised by complete loss of bedding structure and represents a mixture of in-situ and injected melt (Greenfield *et al*., 1996, 1998). Layering is progressively disrupted and the abundance of K-feldspar megacrysts increases as one approaches contact with the northern granite (Greenfield *et al*., 1996). Discontinuous screens of metapsammite and schlieren migmatite preserve a steeply dipping layering (Greenfield *et al*., 1996, this study).

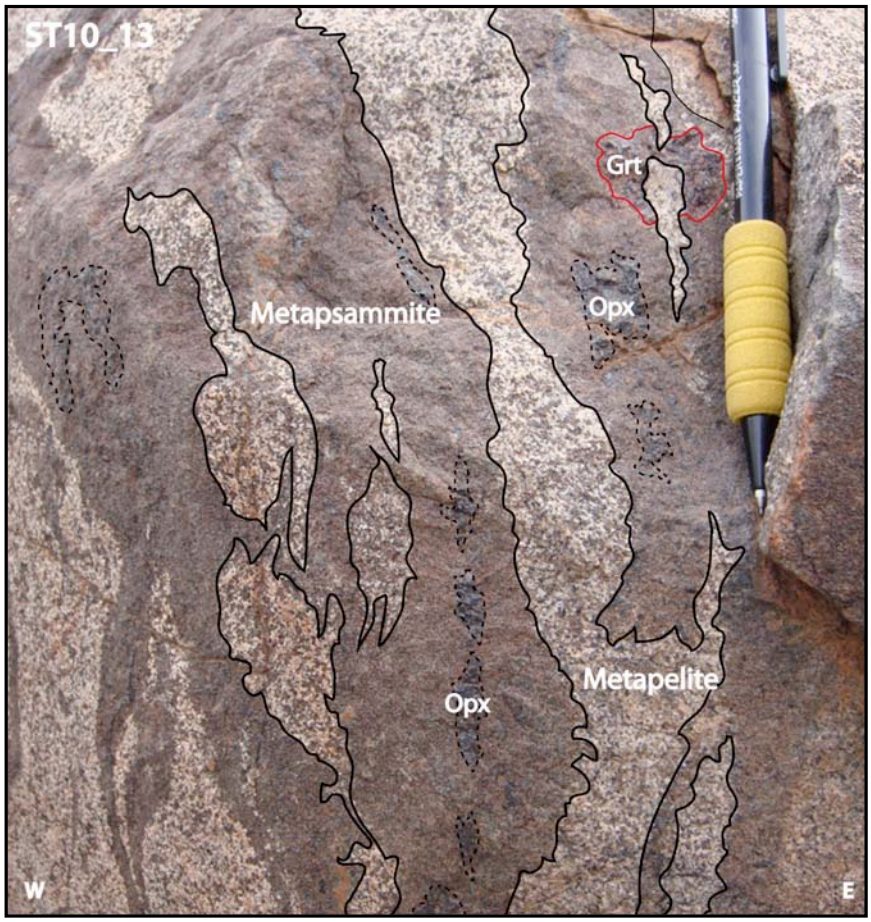

Figure 2.3 Zone 4 Schlieren Migmatite Formation
Metaspammite melanosome separate mobilised metapelite leucosome.
Orthopyroxene-garnet assemblages have melt reaction rims.

GRANITE INTRUSIONS:

Megacrystic syntectonic granites of the Mt Stafford Domain were intruded as relatively flat-lying sheets dipping 10-20º north, overlying the metasedimentary units (Collins & Vernon, 1991). The eastern granite has aligned elongate tabular K-feldspar megacrysts up to 15mm defining a weak to moderate foliation striking 355° and dipping 70° west. Biotite-rich mafic enclaves are dispersed throughout, showing general alignment to the foliation (this study, Figure 2.4). These have been interpreted as entrained xenoliths of Mt Stafford metasedimentary rocks (Vernon *et al.*, 1993)

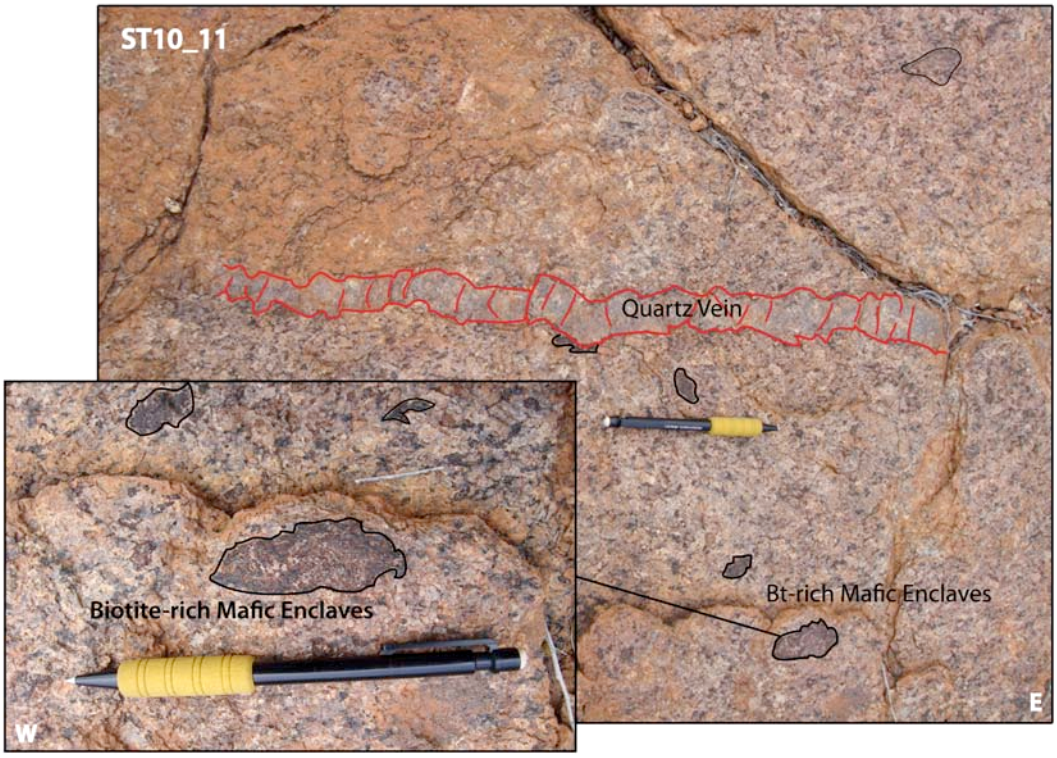

Figure 2.4 Eastern Granite Biotite-rich Mafic Enclaves (ST10_11)
Coarse-grained eastern granite with tabular K-feldspar aligned to a moderate foliation. Foliation is indicated by the pencil, running approximately horizontal across the image(s) Biotite-rich mafic enclaves are generally aligned in this foliation represent xenoliths of country rock. Quartz veins up to ~30mm across trend toward 010º, shown in red.

A quartz-diorite sill or dyke up to 30m wide trending toward 330° is located near the eastern boundary of the eastern granite. Field relationships suggest magma assimilation and/or arrested dyking as shown in Figure 2.5. It is proposed this site represents a quartz-diorite – granite mingling zone (this study). First stage mixing appears to begin with rapakivi K-feldspar "floating" in quartz-diorite, followed by second stage entrainment of granitoid xenoliths (shown in Figure 2.5).

The northern granite cuts across the metamorphic isograds, intruding late in the M_1-D_1 event (Greenfield *et al*., 1996). At the northern boundary, this unit features rapakivi K-feldspar up to 30mm in length, many with euhedral plagioclase cores and fine recrystallised mantles (this study) as shown in Figure 2.6. The rapakivi K-feldspar define a steep mineral lineation plunging 85º toward the east (090°) (this study). Networks of biotite define a foliation striking 120° and dipping 72º to the north (this study).

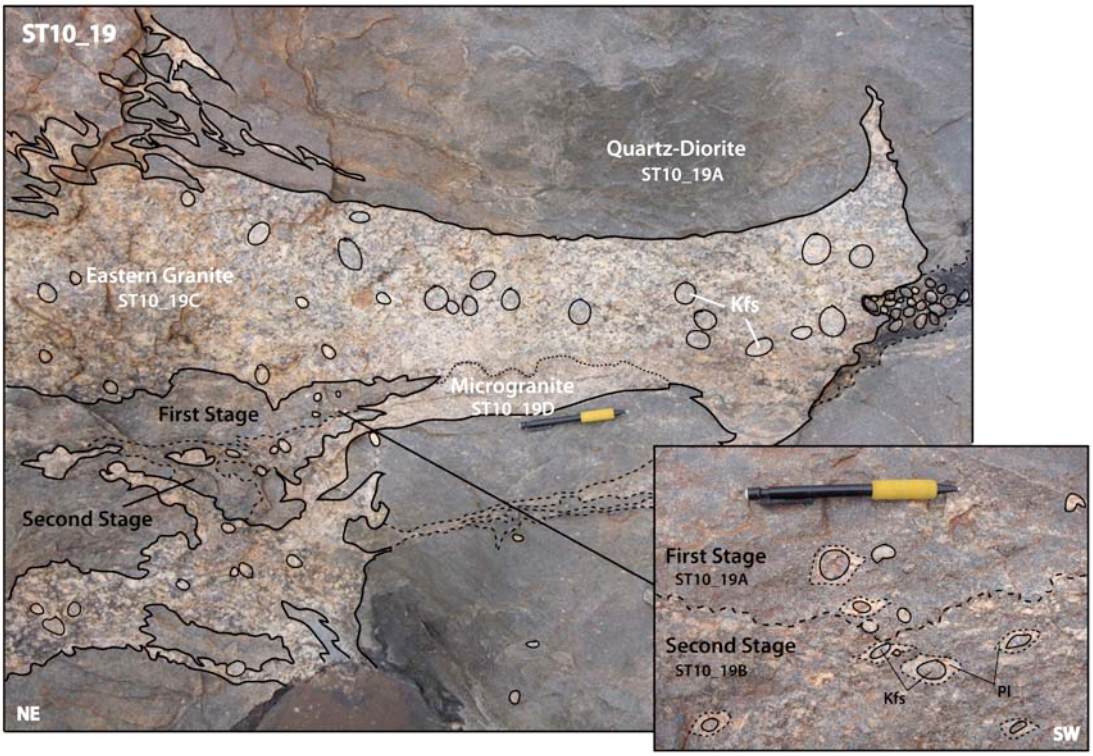

Figure 2.5 Eastern Granite Quartz-Diorite – Granite Mingling Zone
First stage mixing with rapakivi K-feldspar "floating" in quartz-diorite.
Second stage mixing occurs with entrainment of granitoid xenoliths.

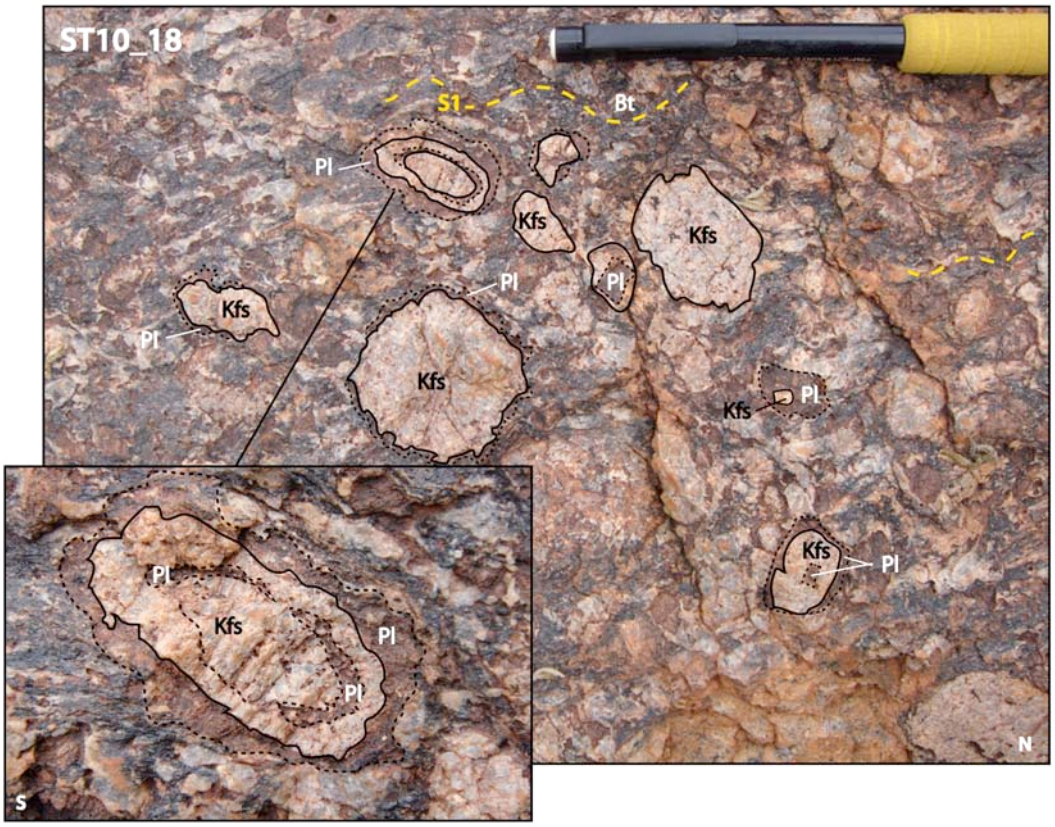

Figure 2.6 Northern Granite Rapakivi Feldspar
Ovoid rapakivi K-feldspar megacrysts up to ~30mm feature recrystallised plagioclase mantles, with some euhedral plagioclase cores. Feldspar are separated by biotite, defining a moderate foliation.

2.6 DEFORMATION HISTORY

Proterozoic metasedimentary and granitic rocks of the Anmatjira and Reynolds Ranges were affected by a minimum of three temporally distinct metamorphic events (M_{1a}, M_{1b}, M_{1c}) and deformation events (D_{1a}, D_{1b}, D_{1c}) ca. 1820-1590 Ma (Clarke *et al*., 1990). The Mt Stafford rocks demonstrate effects of the pre-1820Ma D_1-M_1 event, showing limited effects of the ca. 1780-1770Ma D_2-M_2 event responsible for extensive recrystallisation of the Weldon Metamorphics approximately 25km east (Clarke *et al*., 1990, Greenfield *et al*., 1996, White *et al*., 2003). Nomenclature of deformation (D_{1a}, D_2 etc) and metamorphic (M_{1a}, M_{1b}, etc) events are those developed by Greenfield *et al*., 1996.

D_1 DEFORMATION:

Three phases of deformation are attributed to tectonic cycle D_1-M_1, resulting in a low-pressure high-temperature (LPHT) regional aureole below a syn-deformational granite sheet (Greenfield *et al*., 1996). Peak metamorphism and partial melting occurred simultaneously with localised D_{1a} extension in the migmatites, evident in migration of leucosome to boudin necks and development of conjugate extensional shear zones (White *et al*., 2003). The intimate and gradational relationship between zone 5 and the northern granite indicates intrusion coeval with or post D_{1a}-M_{1a} (Greenfield *et al*., 1996). F_{1a} folds occur in high-grade rocks and show consistent west-verging symmetry on a regional scale (Collins *et al*., 1991). High-grade metapelitic migmatites define S_{1a} axial planar foliation (Greenfield *et al*., 1996, this study).

Kilometre-scale, open to tight, north-trending upright F_{1b} folds deform the D_{1a} extensional structures, migmatites, high-grade S_{1a} mineral foliation and intra-folial F_{1a} folds (Greenfield *et al*., 1996, 1998, White *et al*., 2003). F_{1b} folds are absent from lower-grades (Clarke *et al*., 1990, Collins *et al*., 1991). Cross-cutting the S_{1b} foliation, the eastern granite, although of similar composition, intruded later than the northern granite (White *et al.,* 2003).

F_{1c} folds control the outcrop pattern at Mt Stafford, changing progressively from sub-horizontal open NW-trending folds in the west, to isoclinal steeply plunging N-trending folds in higher-grade regions to the east (Collins *et al*., 1991). In low-grade areas, S_{1c} delineates a slaty cleavage, developing to a cordierite-biotite defined schistosity and cm-scale migmatitic leucosomes at higher-grades (Collins *et al*., 1991). Leucosome align parallel to the axial plane of upright to reclined, northeast-verging $F1_c$ folds (Clarke *et al*., 1990). At the highest grades, S_{1c} is poorly developed and F_{1c} folds rotate earlier fabrics (Collins *et al*., 1991).

Peak metamorphic conditions occurred during F_{1b-1c} in low-grade assemblages, diachronous to recumbent layer-parallel S_{1b} foliation (Vernon *et al*., 1990, cited Clarke *et al*., 1990). The thermal peak migrated outwards from the granitoid sheets, following an anticlockwise P-T-t path (Collins & Vernon, 1995). The post-peak replacement of cordierite, spinel, orthopyroxene and ilmenite by symplectitic biotite-sillimanite-garnet-magnetite indicate increasing pressure during cooling (Collins & Vernon, 1995). Peak conditions during earlier F_{1a-1b} in high-grade regions suggest conditions of ≥ 750ºC and 2.5 ±0.6kbar increased to 3.7 ±0.5kbar during S_{1b-1c} (Clarke *et al*., 1990).

D_2 DEFORMATION:

D_2 deformation resulted in the re-orientation of F_{1c} folds to N-S attitudes at the eastern periphery of Mt Stafford. This produced a progressive eastward tightening, tilting and overturning of F_{1c} fold limbs, telescoping M_1 isograds so they are more narrowly spaced in the south-east (Collins *et al*., 1991). An axial planar S_2 foliation developed in the eastern granitoid, culminating in formation of an S-C fabric as a result of D_2 thrusting (Collins *et al*., 1991).

RETROGRADE SHEAR ZONES:

Conjugate quartz-muscovite-dominated retrograde shear zones cut all earlier fabrics, inferred to be last active during the Late Devonian to Early Carboniferous Alice Springs Orogeny (Collins & Teyssier, 1989, Clarke *et al*., 1990, Greenfield *et al*., 1996). The dominant set is east-trending with sinistral movement, while the subordinate set trends north-east with a dextral shear movement (Greenfield *et al*., 1996, White *et al*., 2003, this study).

3. FIELDWORK

3.1 OVERVIEW

Fieldwork was conducted over five days between July 7 and July 11 2010, in conjunction with Eileen Dunkley, and supervised by Nathan Daczko and Geoffrey Clarke. Mt Stafford is located on Coniston Station, a cattle station owned and managed by Max Lines. The field site is accessible via the Pine Hill Road (4WD only), directly from the Stuart Highway, 19km north of Aileron Station, 151km north of Alice Springs.

3.2 SAMPLING METHODOLOGY

Field traverses were made on foot, generally along dry creek beds, allowing access to the exposed geology and avoiding the spinifex covered hillsides surrounding them. Traverses were made across the metamorphic isograds to reveal changes in mineralogy and metamorphic grade (day 2). A traverse along IGCP Creek (International Geological Correlation Program) revealed locations of significant interest discussed in previous studies (day 5). The eastern and northern granites represent the farthest extent of the field site (days 3 and 4). Sample locations relevant to this study are presented in Figure 1.2.

Metamorphosed turbiditic mudstone (metapelite) and sandstone (metapsammite) pairs were collected from metamorphic zones 1-5. Samples were also gathered from the granitoid intrusions to the north and east, and associated mafic sills or lavas.

4. LABORATORY TECHNIQUES & ANALYTICAL METHODS

4.1 INTRODUCTION & SAMPLE PREPARATION

Samples were prepared at the ARC National Key Centre for Geochemical Evolution and Metallogeny of Continents (GEMOC), in the Department of Earth and Planetary Sciences at Macquarie University. Sample preparation, imaging and laboratory geochemical analyses were conducted within the Geochemical Analysis Unit (GAU) at GEMOC, and are described below.

For zircon separation, rock samples were fragmented using a Selfrag, discharging 120kV at 3.0Hz, with the portion passing a 350μm sieve retained for further separation. Heavy mineral portions were liberated by panning the sample using a lotoc pan then further concentrated by panning with a 100mm watch-glass. Approximately 120 zircon grains from each sample were hand picked under a microscope and prepared as mineral separates, mounted in epoxy and polished to show grain centres.

4.2 PETROGRAPHY

Polished thin sections for petrographic analysis were prepared and analysed for the granitoid samples and associated hybrid diatexite and quartz-diorite – granite mingling zone specimens. Petrographic analysis aims to typify the mineralogy within each group, investigate the nature of any remnant igneous or metamorphic textures, and note the modal abundance of mineral assemblages. Analysis focused on mineral assemblages, growth habit, grain size, modal abundance, igneous and/or metamorphic textures, grain boundary relationships and structures. All major and accessory mineral modes were estimated by visual inspection under the microscope.

Samples were cut into blocks using a diamond blade circular rock saw, removing external weathered surfaces and selecting the freshest part representing significant or distinguishing features and textures. Oversize samples were split with a hydraulic press prior to cutting with the circular saw. The surface was polished using a grinding wheel. Nine polished thin sections of ~30μm thickness were prepared and mounted on glass slides. Analyses were conducted using monocular and binocular transmitted-light petrographic microscopes. Photomicrographs were taken of distinguishing or characteristic features using a digital SLR camera and remote capture software.

4.3 BACKSCATTERED ELECTRON (BSE) IMAGING & ELECTRON MICROPROBE (EMP) MINERAL CHEMISTRY

Back-scattered electron (BSE) images were taken of two thin sections. Five sites for imaging and chemical analysis were selected based on mineral and textural relationships identified during petrographic analysis. BSE images were obtained with a Cameca SX100 EMP using an acceleration voltage of 15keV, beam current of 20nA with a ~500μm field of view (FOV). A transparent carbon coating was applied to the thin sections using an Edwards Auto306 Carbon Coater, providing a low background signal and greater electrical conductivity (E.M.S., 2011).

Electron microprobe (EMP) analysis of thin sections provides quantitative trace and major element composition, allowing determination of mineral chemistry. Major element oxides assessed include SiO_2, TiO_2, Al_2O_3, Cr_2O_3, FeO, MnO, MgO, CaO, Na_2O and K_2O. Appropriate sites of interest were selected using a transmitted light microscope and marked on the thin section to aid navigation.

EMP analyses were conducted with a Cameca SX100 EMP using an acceleration voltage of 15keV, a beam current of 20nA, and a spot size of 30μm. Coordinates for each spot analysis were manually loaded into the controller and left to run overnight. Lower limits of detection (LLD) for the SX100 EMP are listed in Table 4.1.

Table 4.1 Lower Limit of Detection of Major & Trace Element by EMP Analysis

Major & Trace Element Lower Limit of Detection by EMP		
Major Element	**Wt % Oxide**	**Relative Standard Deviation** (%)
SiO_2	0.03	0.19
TiO_2	0.02	0.19
Al_2O_3	0.01	0.18
FeO	0.03	0.34
MnO	0.03	0.55
MgO	0.03	0.22
CaO	0.03	0.27
Na_2O	0.02	0.56
K_2O	0.01	0.49
HfO_2	0.03	0.19
ZrO_2	0.03	0.30
Y_2O_3	0.03	0.34
P_2O_5	0.01	0.65

4.4 X-RAY FLUORESCENCE (XRF) WHOLE ROCK CHEMISTRY

X-ray fluorescence (XRF) allows determination of whole-rock chemistry, providing a complete geochemical and compositional analysis. This enables different samples to be assessed and compared in a qualitative manner. After being crushed with a hydraulic press, samples were reduced to a fine homogenous powder using a TEMA tungsten-carbide mill. The material selected is representative of the bulk sample, and care was taken to ensure no weathered surfaces were included in the powder. Between each sample, the TEMA mill was thoroughly cleaned with water and ethanol to avoid cross-contamination. Reference standards are shown in Table 4.2

Table 4.2 Measured & Reported Reference Standards for XRF Analysis

Measured & Reported References Standard used for XRF Analysis						
	BHVO-1	Mean (n=8)	StDev	**BHVO-2**	Mean (n = 9)	StDev
SiO_2	49.94	49.8	0.11	47.77	47.53	0.70
TiO_2	2.71	2.78	0.02	0.96	0.97	0.01
Al_2O_3	13.80	13.8	0.12	15.35	15.43	0.10
Fe_2O	12.23	12.23	0.06	11.26	11.55	0.05
MnO	0.17	0.17	0.00	0.17	0.17	0.00
MgO	7.23	7.23	0.06	9.68	9.73	0.08
CaO	11.4	11.4	0.04	13.24	13.47	0.06
Na_2O	2.26	2.26	0.12	1.75	1.79	0.07
K_2O	0.52	0.52	0.01	0.03	-	-
P_2O_5	0.27	0.27	0.01	0.05	0.02	0.00
H_2O+	0.16			0.10		
H_2O-	0.05			0.07		
CO_2	0.04			0.02		
Total	100.79			100.45		

Fused glass discs were prepared for major element analysis, by heating the powder to 1100ºC, using 1.50g borate glass, 0.2g sodium nitrate and 0.28g of sample material to give a sample/flux ratio of 1:5.42 (lithium borate flux). Samples were analysed for major oxides: SiO_2, TiO_2, Al_2O_3, Fe_2O_3, MnO, MgO, CaO, Na_2O, K_2O and P_2O_3. Wax pressed-powder discs (10% w/w) with a boric acid backing were prepared for trace element analysis. Samples were analysed for trace elements as shown in Table 4.3 and reported in parts per million (ppm).

XRF analyses were conducted using a Spectro XLAB2000 Energy-Dispersive X-ray Spectrometer. Table 4.3 lists the elements assessed and lower limits of detection for all XRF analyses. Trace elements were normalised to chondrite prior to assessment, using values listed in Table 4.4 (Taylor & McLennan, 1985).

Table 4.3 Lower Limit of Detection of Major & Trace Element by XRF Analysis

Major & Trace Element Lower Limit of Detection by XRF Analysis					
Major Element	**Wt % Oxide**	**Trace Element**	**ppm**	**Trace Element**	**ppm**
SiO_2	0.01	V	1.0	Cd	0.2
TiO_2	0.01	Cr	0.3	In	0.3
Al_2O_3	0.03	Co	0.4	Sn	0.4
Fe_2O_3	0.01	Ni	0.3	Sb	0.5
MnO	0.01	Cu	0.3	Te	1.0
MgO	0.02	Zn	0.3	I	1.0
CaO	0.01	Ga	0.3	Cs	1.5
Na_2O	0.04	Ge	0.2	Ba	1.5
K_2O	0.01	As	0.3	La	2.0
P_2O_5	0.01	Se	0.2	Ce	3.0
		Br	0.3	Nd	5.0
		Rb	0.3	Hf	2.0
		Sr	0.2	T1	0.7
		Y	0.2	Pb	0.2
		Zr	0.2	Bi	0.5
		Nb	0.2	Th	0.5
		Mo	0.2	U	0.5

Table 4.4 Chondrite Values used to Normalise Trace Element Data
(Taylor & McLennan, 1985)

Chondrite Values used to Normalise XRF Trace Element Data							
Element	**ppm**	**Element**	**ppm**	**Element**	**ppm**	**Element**	**ppm**
P	2300	Ni	16500	Sn	2.52	Tm	0.0381
Li	2.4	Cu	168	In	0.117	Yb	0.248
Be	0.04	Zn	462	Sb	0.233	Lu	0.0381
B	1.9	Ga	15.2	Te	3.42	Hf	0.179
Na	7245	Ge	48.3	Ba	3.41	Ta	0.026
Mg	143000	As	2.87	Cs	0.279	W	0.089
Al	12900	Se	27.3	La	0.367	Re	0.055
Si	160000	Rb	3.45	Ce	0.957	Os	1.049
K	854	Si	11.9	Pr	0.137	Ir	0.71
Ca	13500	Y	2.25	Nd	0.711	Pt	1.43
Sc	8.64	Zr	5.54	Sm	0.231	Au	0.218
Ti	654	Nb	0.375	Eu	0.087	Hg	0.585
V	85	Mo	1.38	Gd	0.306	Tl	0.215
Cr	3975	Rh	0.201	Tb	0.058	Pb	3.65
Fe	278000	Pd	0.836	Dy	0.381	Bi	0.167
Mn	2940	Ag	0.33	Ho	0.0851	Th	0.0425
Co	764	Cd	1.010	Er	0.249	U	0.0122

4.5 CATHODOLUMINESCENCE (CL) IMAGING

Scanning Electron Microprobe Cathodoluminescence (SEM-CL) imaging allows analysis of zircon grain structure. This includes characterisation of the appearance (crystal shape, zoning pattern, texture, inclusion assemblages) and may assist in the interpretation of igneous and/or metamorphic processes leading to its formation (Rubatto *et al*., 2006). The grain mount was carbon coated prior to imaging and analysis.

CL investigation of zircon grains from samples ST10_11 and ST10_16B was conducted using a Zeiss EVO MA15 Scanning Electron Microprobe (SEM) working at 15kV, with a beam current of 60μA and ~12.5mm working distance. 60 grains from each sample were imaged; adjusting focus, zoom, brightness and contrast settings for each grain. A scanning speed of 9-10 was used for most images, with 5-6 grains imaged at 12-13 to obtain higher resolution images for reporting and publishing. CL investigation of 60 zircon grains from each of samples ST10_18 and ST10_19C was conducted using a Cameca SX100 EMP with CL and BSE detectors, whilst the SEM was under repair.

EMP examination of 50-60 individual zircon grains provided reference HfO_2 data for use during trace element analysis. Cores and rims of several zircon grains were probed to allow comparison of data. CL images were utilised to select appropriate sites for analysis. EMP analyses were conducted with a Cameca SX100 electron microprobe as outlined in Section 4.3. LLD for the analyses are presented in Table 4.5.

Table 4.5 Lower Limits of Detection for EMP Zircon Analyses

Major & Trace Element Lower Limit of Detection (LLD) by EMP			
Element	**ppm**	**Oxide**	**wt%**
Hf	1700	HfO_2	0.002
Si	150	SiO_2	0.03
Zr	1200	ZrO_2	0.16
Y	1550	Y_2O_3	0.39
P	550	P_2O_5	0.25
Sm	1000	SmO	0.11
Dy	1200	Dy_2O_3	0.28
Th	1100	ThO_2	0.13
U	1400	U_2O_3	0.31
Pb	20000	PbO	2.15

4.6 U-Pb Zircon Geochronology & Trace Element Analysis by Laser-Ablation-Microprobe Inductively-Coupled Plasma Mass Spectrometry (LAM-ICP-MS)

U-Pb Zircon Geochronology

U-Pb dating of individual zircon grains is obtained by laser ablation microprobe-inductively coupled plasma mass spectrometry (LAM-ICP-MS), to characterise the geochronology of magmatic and metamorphic events (Jackson *et al*., 2004, Andersen, 2005, Belousova *et al*., 2006b, Rubatto *et al*., 2006). U-Pb zircon ages in high grade rocks date peak metamorphic P-T conditions (Rubatto *et al*., 2006).

U-Pb dating of zircons was carried out using the Agilent 7500s series LAM-ICP-MS connected to a New Wave UP-213nm Nd:YAG laser. Operating conditions are summarised in Table 4.6. Analyses were conducted in runs of ten spots. Runs 1 to 3 were ablated with a spot size of 30μm, which was increased to 40μm at run 4 improving signal levels and reducing uncertainty. 50 to 60 grains of varying morphology and size were analysed from each sample, analysing rims and cores where possible. CL/BSE images were used to select appropriate analysis sites.

Table 4.6 Operating Conditions of Agilent 7500s LAM-ICP-MS for U-Pb Zircon Geochronology

Operating Conditions of Agilent 7500s LA-ICP-MS	
Condition	**Property**
ICP-MS Type	Quadrapole
Brand / Model	Agilent 7500s
Laser	Nd:YAG UP-213
Wavelength	213 nm
Beam Diameter (Spot Size)	30-40 μm
Laser Intensity	8.9 J/cm^2
Laser Pulse Rate	5 Hz
Carrier Gas	He (0.8 L/min)
Make Up Gas	Ar (0.7 L/min)
Ar Gas Pressure	625 kPa
Water Temperature	19ºC
External Calibration Standard	GJ Red Zircon (U-Pb) NIST-610 Glass (trace elements)
Reference Standard	91500 Zircon (U-Pb) BCR-2 (trace elements)
Background Signal Time	60 seconds
Acquisition Signal Time	100-120 seconds
Isotope Dwell Times	10ms nominal ^{206}Pb = 15ms, ^{207}Pb = 30ms, ^{238}U = 15ms
Data Reduction Software	Glitter v4.41, rev 3

Runs were bracketed by multiple analyses of external zircon and trace element calibration standards GJ red zircon (Jackson *at al*., 2004) and NIST-610 glass (Pearce *et al*; 1996), along with reference standards 91500 zircon (Wiedenback *et al*., 1995) and BCR-2 (Norman *et al*., 1998). Standards were run at the beginning and end of each day to monitor accuracy of analyses and instrument drift. Table 4.7 summarises the values of standards used. Data reduction/processing was performed using the GEMOC Laser ICP-MS Total Trace Element Reduction interactive online software package (GLITTER©) v4.41 (Griffin *et al*., 2007).

Table 4.7 External Calibration Standards & Reference Materials for LA-ICP-MS - Zircon U-Pb Geochronology & Trace Element Analysis

External Calibration Standards & Reference Materials for LA-ICP-MS					
	Standards	**Reported Values** (Ma) (n = 100)		**Values in this Study** (Ma) (n = 69)	
		Mean Age	**Mean** 1σ	**Mean Age**	**Mean** 1σ
Zircon U-Pb	**GJ Red Zircon** ($^{206}Pb/^{238}U$) (Jackson *et al*., 2004)	600.39	0.65	600.00	11.02
	91500 ($^{207}Pb/^{206}Pb$) (Weidenback *et al*., 1995)	1065.40	1.01	1062.46	31.69
Trace Elements	**BCR-2** (Norman *et al*., 1998)	-		-	
	NIST-610 Glass (Pearce *et al*., 1996)	-		-	

LAM-ICP-MS U-Pb ages were corrected for the effects of common lead contamination and lead loss using excel data worksheets developed for Terranechron® analysis, based on algorithms of Andersen (2002). The common-Pb worksheets round to the nearest 1Ma during the first step of processing, so raw GLITTER© values (to one decimal place) were used for analyses that were not corrected for common-Pb. Concordia, Cumulative Probability diagrams, and Weighted Average Age calculations were produced using the Isoplot excel plug-in developed by Ludwig (2003). As the samples are older than 1000Ma, $^{207}Pb/^{206}Pb$ ages are used. Several dismissal criteria were developed and tested, and are discussed in Chapter 8.

TRACE ELEMENT ANALYSIS

Trace element analysis of Hf, Y, U, Th, Yb and Lu gained by LAM- ICP-MS provides information about the composition of magmatic systems responsible for zircon crystallisation (Griffin *et al*., 2004, 2007, Belousova *et al*., 2006b). Data may be used for zircon thermometry and assessing equilibrium with major rock-forming metamorphic minerals, showing chemical variation with age and response to metamorphic events (Rubatto *et al*., 2006).

Trace or rare earth element (REE) analyses were collected during U-Pb geochronology, using the Agilent 7500S series LAM-ICP-MS and New Wave UP-213nm Nd:YAG laser, with operating conditions in Table 4.5. Data was processed using GLITTER©, entering HfO_2 data obtained during EMP analysis and known values of reference standards, as shown in Table 4.8. The minimum detection limits obtained during analyses are provided in Table 4.9, showing the highest values of minimum detection. Prior to interpretation, data was normalised to chondrite values of Taylor & McLennan (1985) listed in Table 4.4.

Table 4.8 External Reference Values for GLITTER© Trace Element Processing

External Reference Values for GLITTER © Trace Element Analysis		
Standards	**Zr** (ppm)	**Hf** (ppm)
GJ Red Zircon	-	7800.00
91500 Zircon	-	5511.86
BCR-2 (Norman *et al*., 1998)	191.70	-
Nist-610 Glass (Pearce *et al*., 1996)	Values of Pearce *et al*., 1996	

Table 4.9 Internal Minimum Detection Limits : LAM-ICP-MS Trace Element Analysis
Highest minimum detection limited (MDL) values obtained during analysis is reported (normalised to values of Taylor & McLennan, 1985)

Internal Minimum Detection Limits: LAM-ICP-MS Zircon Trace Element					
Isotope	**MDL/Chondrite**	**Isotope**	**MDL/Chondrite**	**Isotope**	**MDL/Chondrite**
P31	0.019	Nd146	1.391	Tm169	0.223
Ti49	0.006	Sm147	1.225	Yb173	2.641
Y89	0.295	Eu151	0.839	Lu175	3.596
Zr92	2.504	Gd157	1.220	Hf178	10.670
Nb93	0.320	Tb159	0.969	Ta181	2.497
La139	0.790	Dy163	1.336	Th232	7.929
Ce140	0.484	Ho165	1.457	U238	30.738
Pr141	1.591	Er166	1.040		

4.7 HF-ISOTOPE COMPOSITION BY LASER-ABLATION-MICROPROBE MULTI-COLLECTOR INDUCTIVELY-COUPLED PLASMA MASS SPECTROMETRY (LAM-MC-ICP-MS)

Hf-isotope composition of zircon grains separated from the granite samples was gained by Laser-Ablation-Microprobe Multi-Collector Inductively-Coupled Plasma Mass Spectrometry (LAM-MC-ICP-MS). Hf-isotopic ratios represent the decay of $^{176}Lu \rightarrow {}^{176}Hf$, while ^{177}Hf is a stable isotope (Griffin *et al*., 2007). During mantle melting processes, Hf is partitioned more strongly into the melt than Lu, and over time $^{176}Hf/^{177}Hf$ ratios evolve to higher values in the mantle than in crustal rocks (Griffin *et al*., 2007). Therefore, high values of $^{176}Hf/^{177}Hf$ ($\varepsilon_{Hf} >> 0$) in magmatic rocks indicate juvenile mantle input (re-melting of mantle-derived younger crust or directly by mantle-derived mafic melts). Low $^{176}Hf/^{177}Hf$ values ($\varepsilon_{Hf} < 0$) provide evidence of older reworked crustal material (Griffin *et al*., 2007). Mixing of mantle- and crustal-derived magmas produces heterogeneity in Hf-isotope composition.

Grains deemed most suitable during initial U-Pb geochronology were selected for Hf-isotope analysis; ≤ ±2% common-Pb, ≤ ±10% or ≤±15% central discordance and ≤ 2150Ma. Hf isotopic ratios were collected using the Nu Plasma 005 Multi-Collector ICP-MS with New Wave UP-213nm laser. Operating conditions are summarised in Table 4.10.

Table 4.10 Operating Conditions of New Plasma 005 Multi Collector LAM-ICP-MS for Hf-Isotope Analysis

Operating Conditions of New Plasma 005 Multi Collector LAM-ICP-MS	
Condition	**Property**
ICP-MS Type	Multi-Collector
Brand / Model	Nu Plasma 005
Laser	Nd:YAG New Wave UP-213
Wavelength	213 nm
Beam Diameter (Spot Size)	40 μm
Laser Power	3.65 J/cm^2
Laser Pulse Rate	5 Hz
Carrier Gas	He (~0.9 L/min)
Make Up Gas	Ar (~0.7 L/min)
Reference Standard	Temora Zircon Mud Tank (MT) Zircon
Background Signal Time	~30 seconds
Acquisition Signal Time	~200 seconds
Data Reduction Software	Nu Plasma Time Resolved Software

Hf-isotope analyses were conducted in runs of ten grains, using a 40μm spot size, on the same spot or within the same domain (core or rim) as U-Pb dating and trace element analyses. Runs were bracketed by analyses of two reference standards; Mud Tank (MT) Zircon **(**Griffin *et al*., 2007) and Temora Zircon (Black *et al*., 2003). MT zircon values obtained during this study are within published range, as summarised in Table 4.11. Correction of initial $^{177}Hf/^{176}Hf$ (Hf_i) follows ^{178}Lu decay constant ($1.93x10^{-11}$) (Blichert-Toft *et al*., 1997), and εHf using 176Lu decay constant of $1.865x10^{-11}$ (Scherer *et al*., 2001), as provided in the TerranChron® Isoplot data template. Depleted mantle (DM) and chondrite uniform reservoir (CHUR) values provided in the template are those of Blichert-Toft *et al*. (1997).

Table 4.11 External Calibration Standards & Reference Materials for LAM-MC-ICP-MS Zircon Hf Isotope Analysis ($^{176}Hf/^{177}Hf$)

$^{176}Hf/^{177}Hf$ External Calibration Standards & Reference Materials for LAM-MC-ICP-MS						
Standards	**Reported Values**			**Values in this Study**		
	Mean Ratio	**Mean 2σ**	***n***	**Mean Ratio**	**Mean 2σ**	***n***
Mud Tank Zircon (Griffin *et al*., 2007)	0.282522	± 4.20E-05	83	0.282519	± 1.1E-05	14
Temora Zircon (Black *et al*., 2003)	0.282686	± 1.09E-03	31	0.282664	± 1.4E-05	3

Combined trace element data may be used to estimate source rock composition using the GEMOC Classification and Regression Tree (CART) diagram (Belousova *et al*., 2002). The CART diagram estimates the composition of the host rock, recognising a grain from a granitic rock with a probability of correct prediction ≥ 80% (Belousova *et al*., 2002). Only suitable U-Pb grains will be classified using the CART diagram.

5. PETROGRAPHY

5.1 INTRODUCTION

For petrology, samples from Mt Stafford have been divided into groups based on their occurrence and field associations: 1) eastern granite, 2) northern granite, 3) hybrid diatexite and 4) quartz-diorite – granite mingling zone (after Greenfield *et al*., 1996, this study). This chapter provides a summary of field and hand-specimen observations along with petrographic analysis. Mineral modal abundance (%) was estimated during petrography. Detailed petrographic descriptions are contained in Appendix B-1.

5.2 PETROGRAPHIC ANALYSIS

5.2.1 EASTERN GRANITE

The eastern granite sample ST10_11 is a coarse-grained granitoid, from the western edge of the pluton (refer Figure 1.2), that has tabular K-feldspar megacrysts <12mm surrounded by mantles of fine-grained quartz and K-feldspar. The tabular grains define a moderate foliation aligned 355° and dipping 70º west. Well-preserved crystal terminations indicate this is an igneous foliation. Abundant fine-grained biotite-rich enclaves are generally also aligned in this foliation. They represent xenoliths of the surrounding Mt Stafford metasedimentary rocks.

Sample ST10_19C represents the eastern granite associated with the proposed mingling zone (refer Figure 1.2). In outcrop, the megacrystic rapakivi texture has foliated biotite wrapping around ovoid K-feldspar megacrysts <20mm. Elongate mafic enclaves are dispersed throughout the megacrystic granitoid groundmass.

The eastern granite mineralogy is dominated by microcline (20-25%), cordierite (15-20%) and quartz (15-20%), with plagioclase (10-15%) and biotite (~15%) (summarised in Table 5.1). Secondary minerals include epidote (<5%), chlorite (<5%), spinel (<5%), fibrolite (<5%), white mica (sericite, <5%), pinite (<5%) and ilmenite (<2%). Trace amounts of apatite, zircon and sulphide grains (opaque) are present.

Table 5.1 Summary of Mineral Modal Abundance: Eastern Granite
Modal abundances were estimated visually during petrographic analysis

Summary of Mineral Modal Abundance: Eastern Granite						
Sample	**Major** Minerals		**Secondary** Minerals		Trace Minerals	
ST10_11 Eastern Granite	Microcline	~20-25%	Epidote	~ 5%	Apatite	< 1%
	Plagioclase	~ 10%	Spinel	5%	Zircon	< 1%
	Quartz	15-20%	Fibrolite	< 5%	Opaques	< 1%
	Biotite	15%	Sericite	10%		
	Cordierite	15-20%	Pinite	< 5%		
	Aluminosilicate	5%	Chlorite	< 5%		
			Ilmenite	< 2%		
ST10_19C Eastern Granite (Mingling Zone)	Microcline	15-20%	Spinel	5%	Tourmaline	< 1%
	Plagioclase	15%	Epidote	~ 5%	Apatite	< 1%
	Quartz	~ 10%	Sericite	10%	Zircon	< 1%
	Biotite	10-15%	Pinite	< 5%	Opaques	< 1%
	Cordierite	10-15%	Chlorite	~ 5%		
			Titanite	< 2%		

Irregular microcline and cordierite grains with embayed and commonly sutured boundaries are separated by fine-grained secondary pinite (comprising recrystallised muscovite and clay-minerals). Several microcline grains preserve simple-twinned cores (shown in Figure 5.1, centre), and perthitic lamellae of albite are common. Cordierite grains have a yellow weathering rind (Figure 5.1, upper left) and lamellar twinning. Cordierite is commonly partially replaced by spinel and pinite symplectites centred along grain boundaries and fractures. Myrmekites of vermicular quartz and plagioclase replacing microcline occur along some grain boundaries.

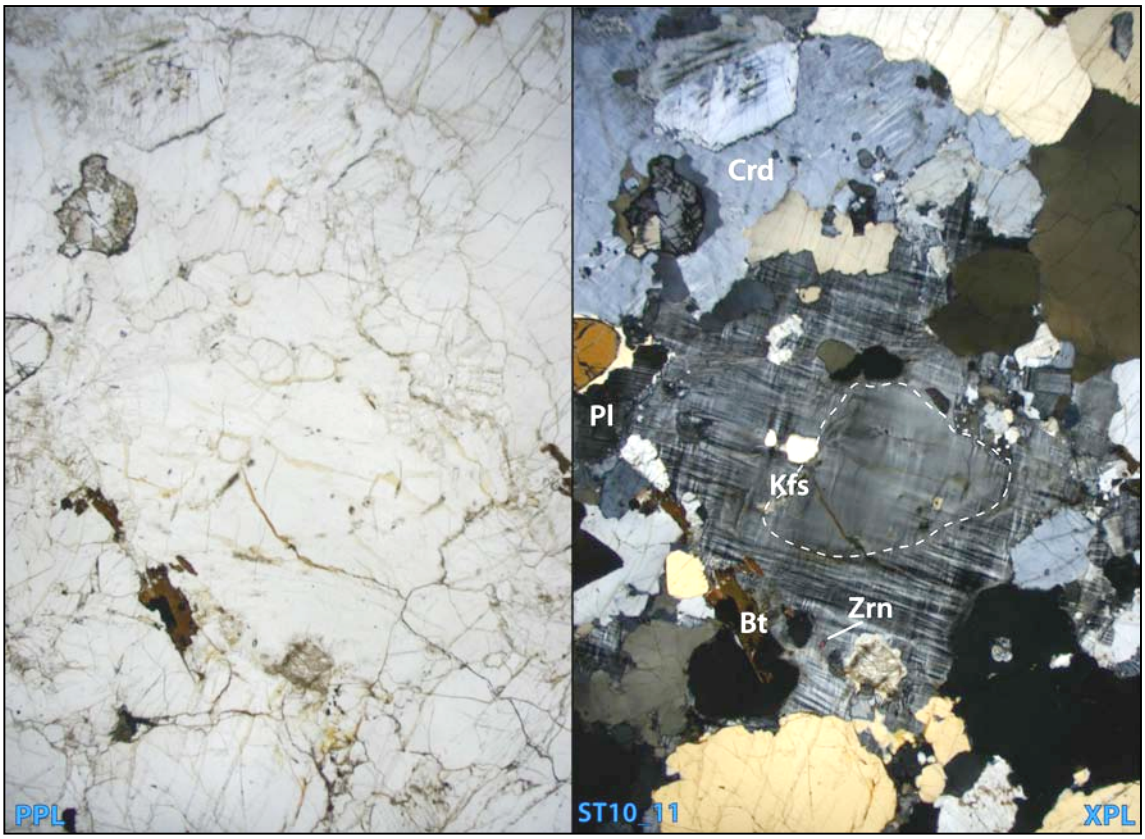

Figure 5.1 Eastern Granite ST10_11: Microcline with simple-twinned core

Large irregular microcline grain (centre) preserves near simple-twinned core. Microcline (centre) and cordierite (left upper) have embayed boundaries. Cordierite (upper left) with yellow weathering rind shows lamellar twinning. Biotite (left of centre) found in interstices between cordierite and microcline grains. Field of View (FOV) = 7×10.5mm

Biotite is breaking down to white mica (sericite) and fibrolite (shown in Figure 5.2, centre right). Biotite-quartz symplectites occur between biotite and quartz grains (Figure 5.2 upper centre). At grain boundaries with cordierite, biotite is being replaced by epidote, chlorite and granular spinel (Figure 5.2, centre). Apatite is present as inclusions in biotite and chlorite. Prismatic sillmanite (not pictured) is partially replaced by biotite and spinel ±ilmenite.

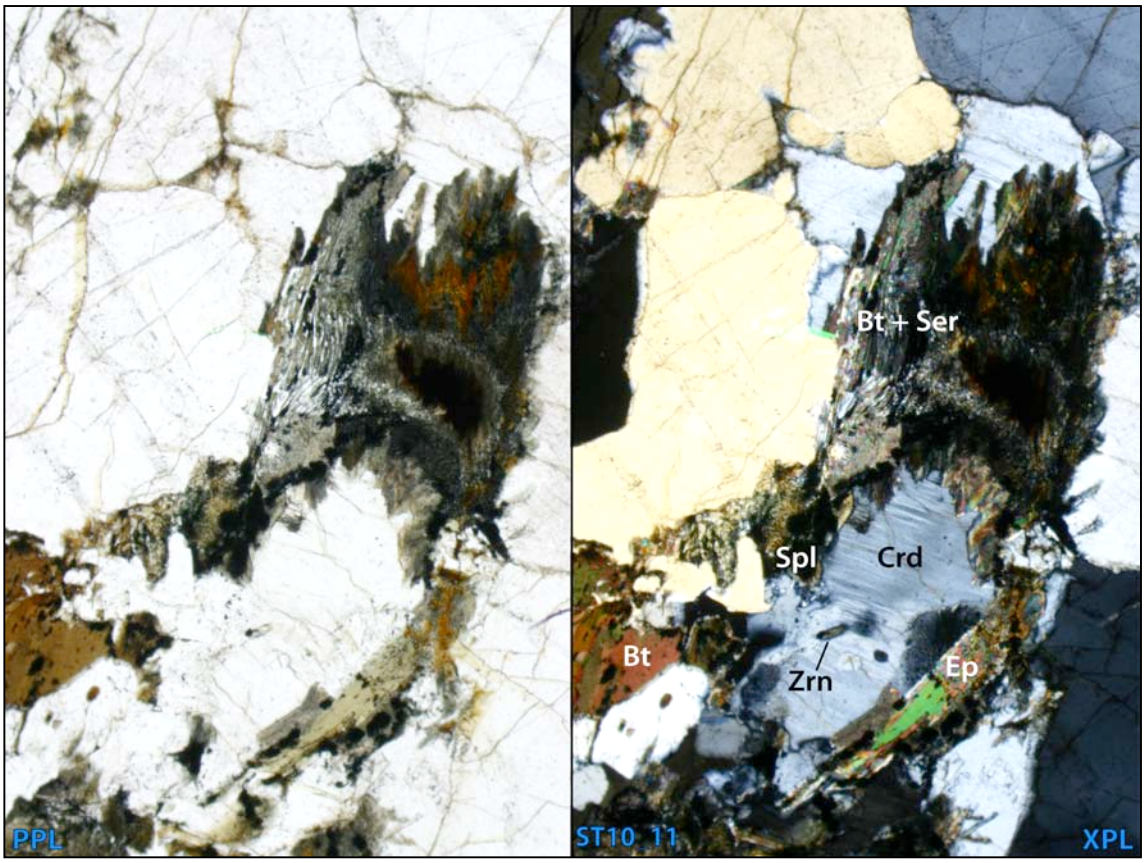

Figure 5.2 Eastern Granite (ST10_11): Biotite partially replaced by epidote, sericite & spinel

Irregular biotite (right centre) partially replaced by sericite, spinel ± fibrolite. Large biotite shows near-complete recrystallisation. Cordierite (lower centre) with lamellar twinning is surrounded by epidote and spinel ±chlorite partially replacing biotite. Biotite-quartz symplectites (centre) occur between quartz and biotite grains. The upper left area is dominated by fractured quartz. FOV = 1.7×2.5 mm

The granite associated with the mingling zone (ST10_19C) has a moderate foliation defined by elongate tan-brown biotite and epidote, intergrown with granular titanite. The foliation wraps around microcline and quartz grains (Figure 5.3, centre). Titanite was not expected in this S-type granite sample. Pale-blue tourmaline is found as inclusions in quartz and microcline and in interstices between grains (Figure 5.3, centre left).

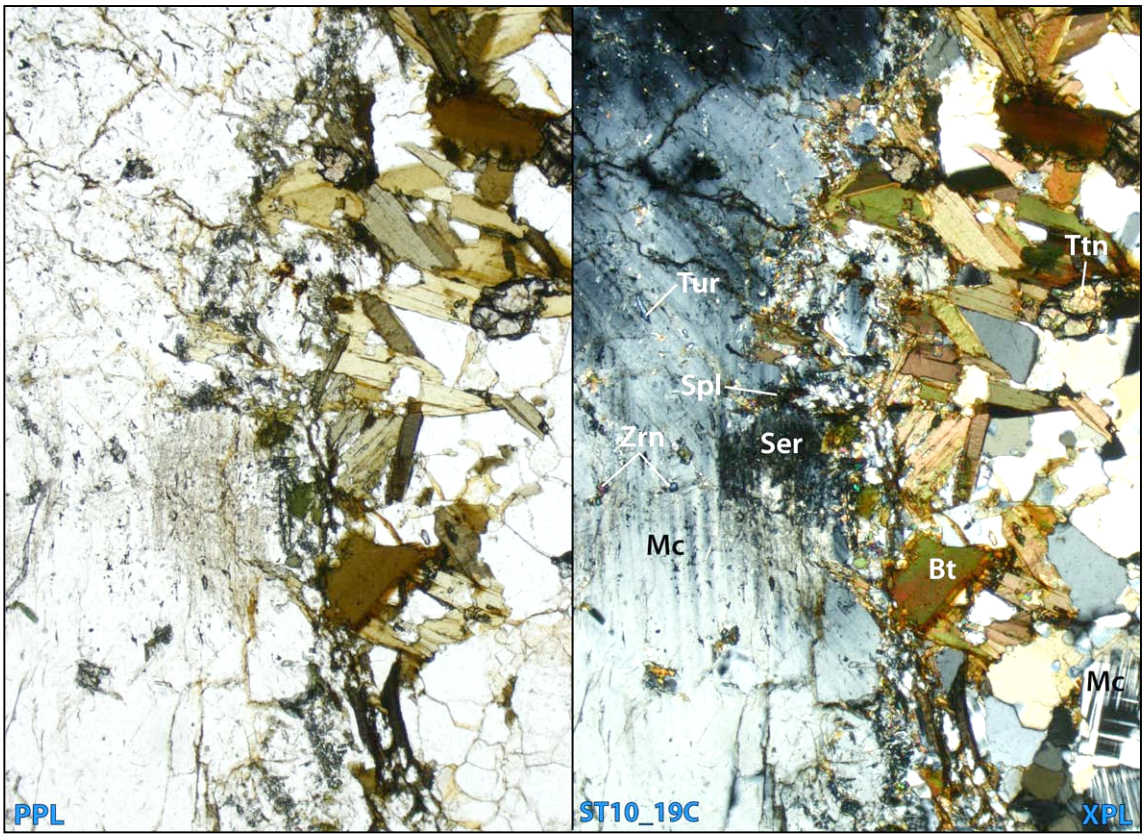

Figure 5.3 Eastern Granite (ST10_19C): Microcline rimmed by biotite & titanite

Microcline (left) is partially replaced by sericite and spinel (centre) along grain boundaries. Microcline shows imperfect cross-hatch twinning. Biotite, epidote and titanite are intergrown in networks (right) wrapping around microcline. Pale-blue tourmaline (centre left) occurs as inclusions in microcline. FOV = 1.7×2.5 mm

5.2.2 Northern Granite

The northern granite is a coarse-grained to megacrystic (up to 30mm) granitoid. At the southern edge, near contact with the hybrid diatexite (Figure 1.2), the sample is non-foliated, with patches of biotite <12mm separating granular quartz and plagioclase. Weathered surfaces are heavily pitted following corrosion of biotite and cordierite. Biotite and cordierite commonly have feldspathic mantles.

Sample ST10_18 is a sheared granite, collected at the northern boundary of the northern granite, an area cut by numerous shear zones (refer Figure 1.2). This sample is characterised by rapakivi ovoid K-feldspar megacrysts <30mm surrounded by foliated biotite networks <25mm. The rapakivi K-feldspar define a steep mineral lineation, plunging 85º towards east (090°), and have plagioclase mantles (some showing euhedral plagioclase cores).

In thin section, the northern granites are dominated by quartz (20-25%), microcline (~20%), biotite (~15%), plagioclase (10-15%) and cordierite (10-15%). Sericite mica is present as a secondary mineral up to 10%, along with pinite (<5%), epidote (<5%), chlorite (<5%), spinel (<5%). Trace amounts of apatite, zircon and sulphides are present. Approximate mineral modes are presented in Table 5.2.

Table 5.2 Summary of Mineral Modal Abundance: Northern Granite
Modal abundances were estimated visually during petrographic analysis

Summary of Mineral Modal Abundance: Northern Granite						
Sample	**Major** Minerals		**Secondary** Minerals		Trace Minerals	
ST10_16B Northern Granite (contact w/ Hybrid Diatexite)	Microcline	~20%	Sericite	~ 10%	Apatite	< 1%
	Plagioclase	~ 10%	Pinite	~ 5%	Zircon	< 1%
	Quartz	20-25%	Epidote	~ 5%	Opaques	< 1%
	Biotite	10-15%	Spinel	< 5%		
	Cordierite	10-15%	Chlorite	~ 5%		
ST10_18 Northern Granite (shear zone)	Microcline	20-25%	Sericite	~10%	Opaques	< 2%
	Plagioclase	10-15%	Pinite	~ 5%	Apatite	< 1%
	Quartz	20%	Spinel	< 5%	Zircon	< 1%
	Biotite	15-20%	Epidote	< 5%		
	Cordierite	~15%	Chlorite	< 5%		

Quartz grains <2.5mm exhibit undulose extinction, forming irregular sub-grain domains. Myrmekites occur between larger quartz and plagioclase crystals. Microcline <2.5mm with embayed boundaries commonly have perthitic albite lamellae parallel to the 001 face. Microcline and cordierite grains are being replaced by fine-grained biotite and sericite along grain boundaries (shown in Figure 5.4, centre left). Rounded apatite inclusions occur in microcline and biotite.

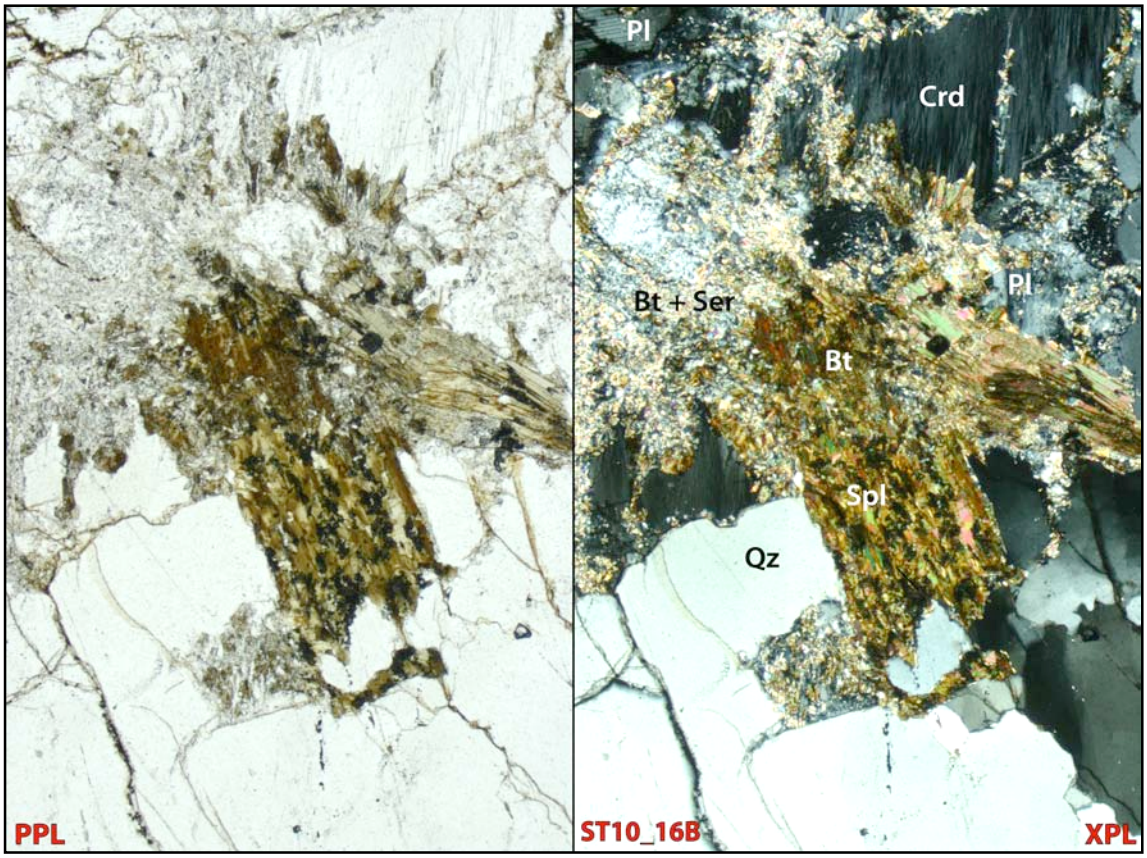

Figure 5.4 Northern Granite (ST10_16B): Sericite & biotite partially replacing cordierite & microcline
Intergrown biotite and sericite (left centre) overgrow microcline, plagioclase and cordierite.
Biotite (centre right) shows minor alteration to chlorite.
Quartz grains (lower left) have embayed boundaries and undulose extinction.
FOV = 7×10.5 mm

Cordierite shows lamellar twinning (Figure 5.5, centre left). Tan-brown biotite is partially replaced by sericite, epidote (clinozoisite?) and granular spinel (shown in Figure 5.5, centre). Cordierite is being replaced by biotite and sericite (Figure 5.5, centre top). Grain boundaries are irregular and commonly embayed.

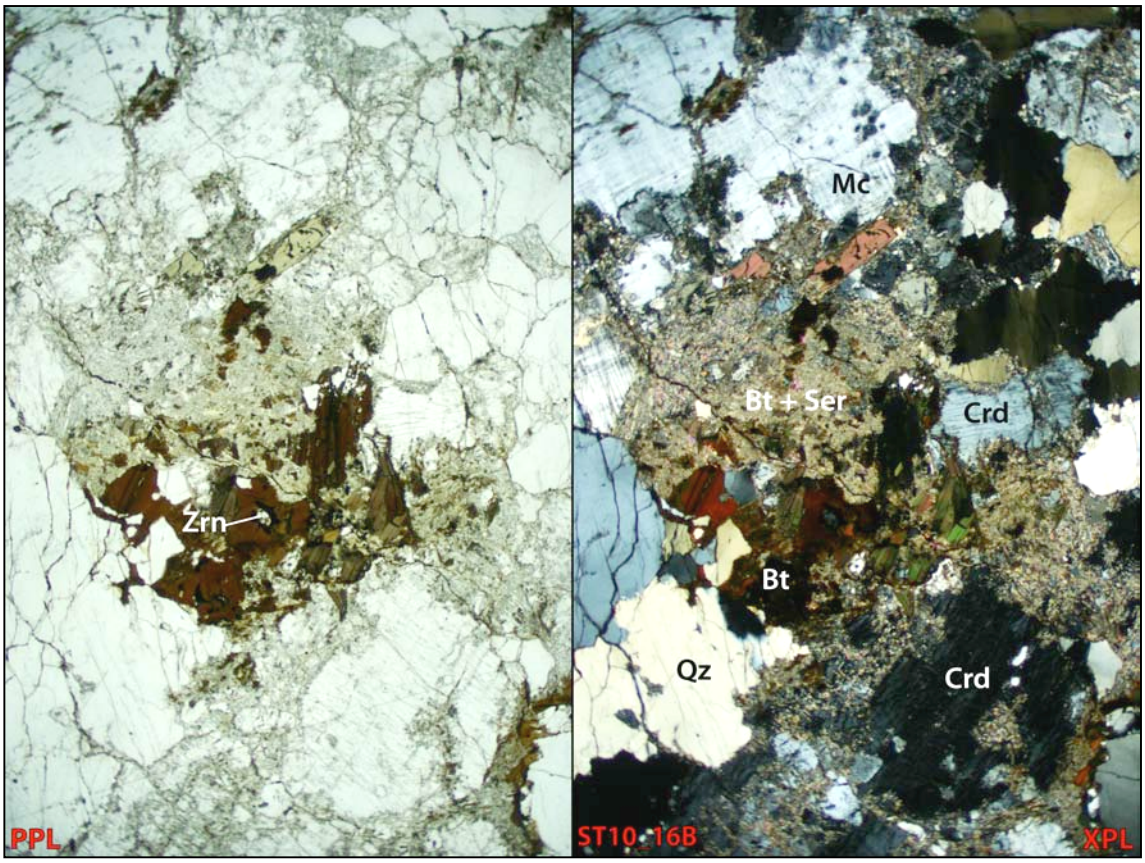

Figure 5.5 Northern Granite (ST10_16B): Biotite partly replaced by sericite, epidote, chlorite & spinel
Biotite (centre) is partially replaced by sericite, epidote, chlorite and granular spinel. Plagioclase and cordierite (top left and right) are partially replaced by fine-grained biotite and sericite. Quartz (lower right) exhibits undulose extinction, and the formation of sub-grain domains. FOV = 1.7×2.5 mm

The sheared granite (ST10_18) shows a higher degree of recrystallisation. Mantles of granular plagioclase surround quartz and microcline, defining the foliation (shown in Figure 5.6). Elongate biotite and muscovite are intergrown, and are also aligned in this foliation (Figure 5.6, centre right). Quartz grains (bottom right) have sutured boundaries and form irregular sub-grains.

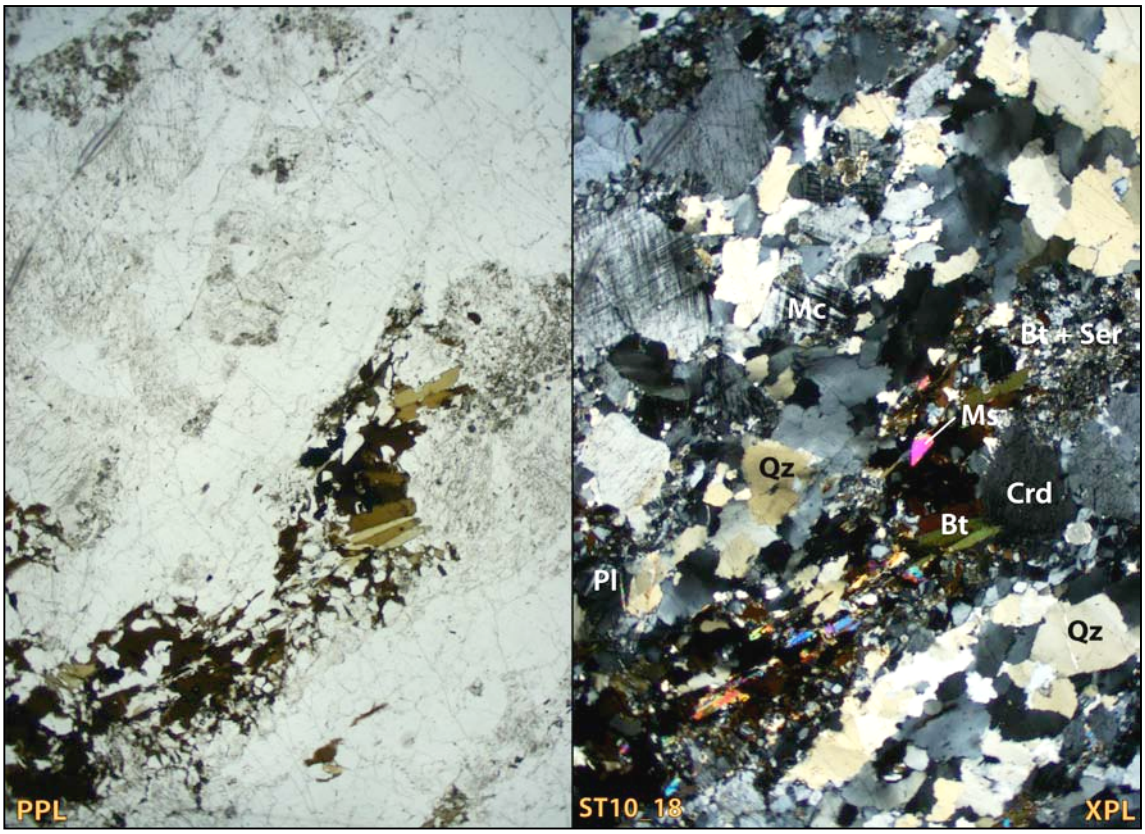

Figure 5.6 Northern Granite (ST10_18): Biotite & muscovite foliation with quartz & microcline
Pale areas (upper left and lower right) comprise quartz, microcline and cordierite partially replaced by biotite, sericite and spinel. Some microcline grains (top right) have recystallised mantles. Muscovite (centre) has partially replaced biotite. Quartz grains (lower right) exhibit undulose extinction and have embayed sub-grain boundaries. FOV = 7×10.5 mm

5.2.3 Hybrid Diatexite Microgranitoid (ST10_15D)

Sample ST10_15D, a microgranitoid from the hybrid diatexite zone (after Greenfield *et al.,* 1996, Figure 1.2), has a granoblastic texture. In outcrop, granular K-feldspar up to 2mm with a green tinge and random elongate biotite grains < 4mm define no distinct foliation. Dark cordierite grains <3mm form clots, giving a spotted appearance.

The thin section shows a dominance of quartz (20-25%), with cordierite (15-20%), microcline (15-20%), plagioclase (~15%) and biotite (10-15%), as summarised in Table 5.3. Secondary minerals include sericite, pinite, epidote and tourmaline up to 20%, and trace amounts of zircon, monazite, apatite and sulphide grains. Quartz <2mm and cordierite grains <0.6mm form a granoblastic texture (Figure 5.7). Quartz grains have irregular, embayed boundaries and exhibit undulose extinction. Simple-twinned cordierite is breaking down to pinite, forming networks through and around grains.

Table 5.3 Summary of Mineral Modal Abundance: Hybrid Diatexite

Modal abundances were estimated visually during petrographic analysis

Summary of Mineral Modal Abundance: Hybrid Diatexite						
Sample	**Major** Minerals		**Secondary** Minerals		Trace Minerals	
ST10_15D Microgranite, (Hybrid Diatexite Zone)	Microcline	15-20%	Sericite	~ 5%	Zircon	< 1%
	Plagioclase	10-15%	Pinite	< 5%	Monazite	< 1%
	Quartz	20-25%	Epidote	~ 5%	Apatite	< 1%
	Biotite	10-15%	Tourmaline	< 5%	Opaques	< 1%
	Cordierite	15-20%				

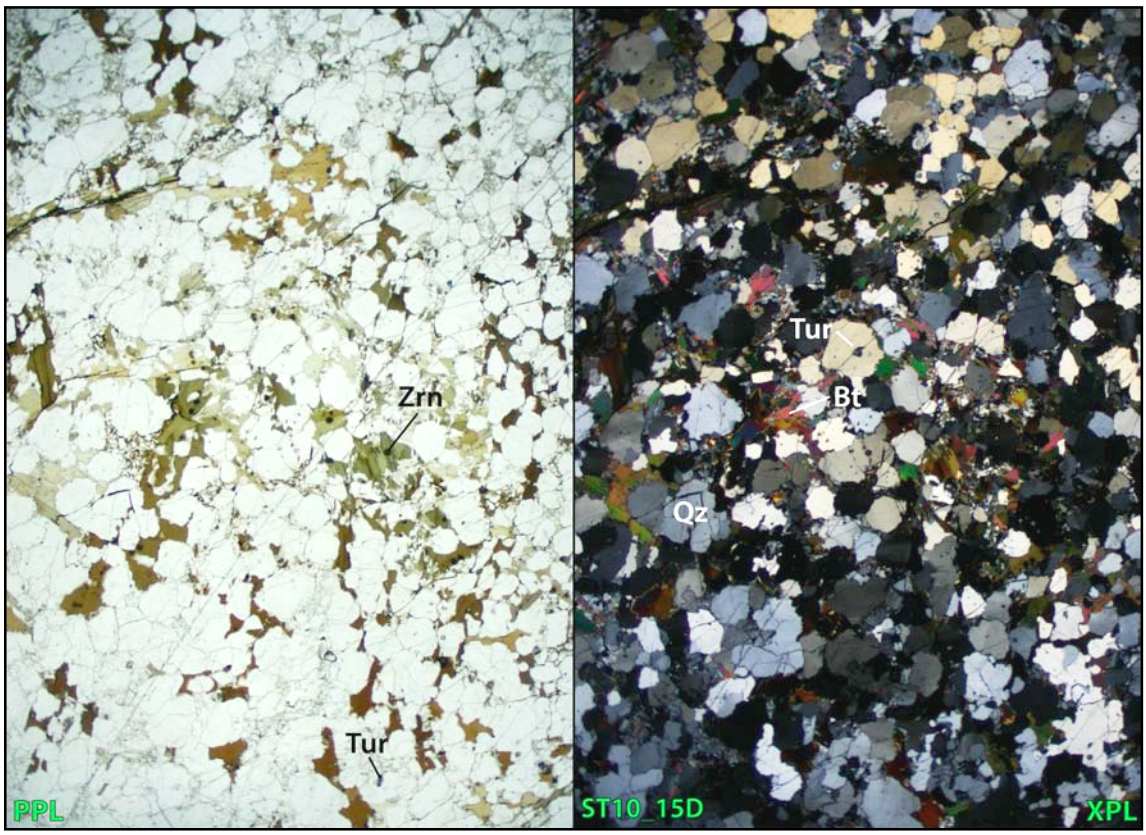

Figure 5.7 Hybrid Diatexite (ST10_15D): Brown & green biotite surround quartz grains

Pale areas are predominantly quartz, with plagioclase, microcline & cordierite. Quartz grains have irregular, embayed boundaries. Both green biotite (centre) and tan-brown biotite (top centre) can be seen. FOV = 7×10.5 mm (per image)

Irregular plagioclase <0.6mm and microcline <0.7mm are breaking down to sericite, centred along irregular, embayed grain boundaries (Figure 5.7). Several plagioclase grains show zoned extinction and/or sub-grain domains. Biotite present in two types: olive green with an anhedral elongate habit, and tan to dark brown with a fine acicular habit (Figure 5.7). Fine-grained pale-blue tourmaline is associated with sericite. The linear fractures are a result of the sampling method (sledgehammer).

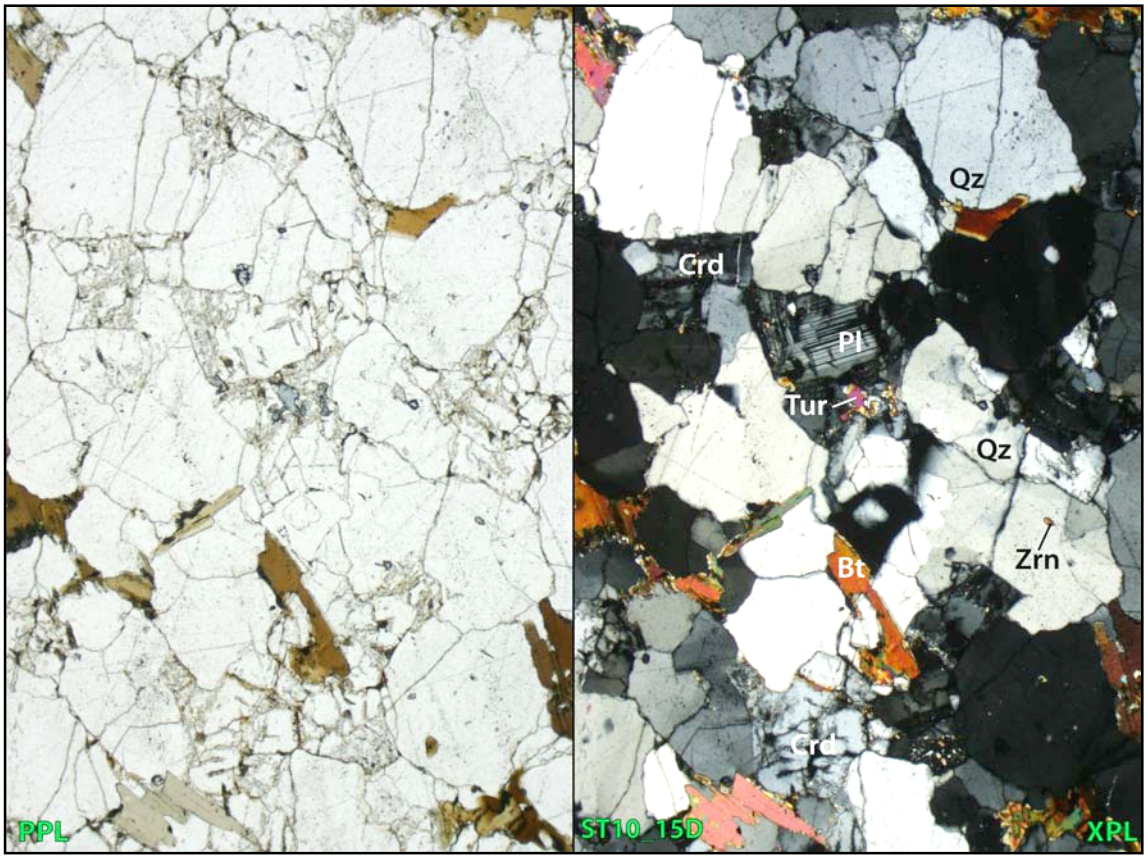

Figure 5.8 Hybrid Diatexite (ST10_15D): Sericite partially replaces plagioclase & cordierite

Plagioclase (centre) is being partially replaced by sericite, centred along grain boundaries. Cordierite (lower centre) is partially replaced by pinite. Several quartz grains show undulose extinction (lower left). Pale-blue tourmaline (centre) is found as inclusions within or in interstices between quartz grains. FOV = 1.6×2.5 mm

5.2.4 Quartz-Diorite - Granite Mingling Zone (ST10_19A, B & D)

Quartz-diorite samples were collected from the proposed quartz-diorite – granite mingling zone within the eastern granite (Figure 1.2). Field observations identified random rapakivi K-feldspar megacrysts <40mm "floating" within a quartz-diorite groundmass. Biotite clots <2.5mm isolate tabular plagioclase phenocrysts <3mm. This mafic unit is approximately 30m wide, trending toward 150°/330°. Mafic xenoliths of varying scale (mm to 10's cm) form biotite-rich rims where they contact the granitoid material in which they are entrained.

In thin section, the quartz-diorite samples are dominated by plagioclase (~25%), with biotite (~20%), epidote (15-20%), green amphibole (~15%), microcline (~15%) and minor quartz (5-10%). Titanite is also present up to 5%, along with trace amount of apatite and zircon. Modal percentages observed during petrography are presented in Table 5.4

Table 5.4 Summary of Mineral Modal Abundance: Mafic Mingling Zone
Modal abundances were estimated visually during petrographic analysis

Summary of Mineral Modal Abundance: Quartz-Diorite Mingling Zone						
Sample	**Major** Minerals		**Secondary** Minerals		Trace Minerals	
ST10_19A Quartz-Diorite (Mingling Zone)	Microcline	15-20%	Titanite	< 5%	Apatite	< 1%
	Plagioclase	20-25%			Zircon	< 1%
	Quartz	5-10%				
	Biotite	15-20%				
	Epidote	~20%				
	Amphibole	15-20%				
ST10_19B Quartz-Diorite (Mingling Zone)	Microcline	~20%	Titanite	< 5%	Tourmaline	< 1%
	Plagioclase	~25%			Apatite	< 1%
	Quartz	5-10%			Zircon	< 1%
	Biotite	15-20%				
	Epidote	~15%				
	Amphibole	15%				
ST10_19D Microgranite (Mingling Zone)	Microcline	~20%	Epidote	~ 5%	Apatite	< 1%
	Plagioclase	20-25%	Sericite	< 5%	Zircon	< 1%
	Quartz	10-15%	Pinite	< 5%	Opaques	< 1%
	Biotite	10-15%	Spinel	< 5%		
	Cordierite	15-20%	Titanite	< 5%		
	Aluminosilicate	< 5%	Ilmenite	< 2%		

Cumulate mafic material comprising elongate biotite, epidote and green amphibole, define a moderately intense foliation (shown in Figure 5.9). The foliation wraps around non-foliated green patches or clots of plagioclase intergrown with epidote, amphibole and titanite (Figure 5.9, centre).

Plagioclase <2mm show undulose extinction, irregular twinning and the formation of irregular sub-grains (shown in Figure 5.10). Several larger grains have inclusions of epidote, elongate biotite and apatite, while some are partially replaced by biotite and epidote. Granular titanite <0.5mm is intergrown with amphibole and epidote (Figure 5.10, centre left).

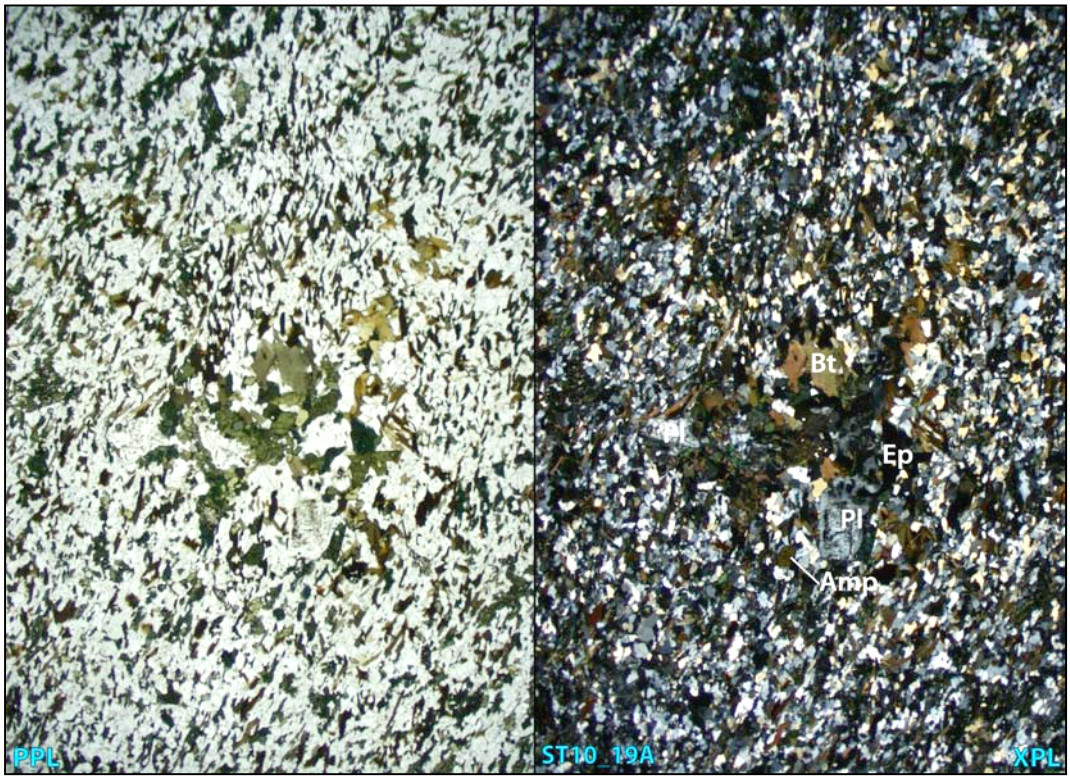

Figure 5.9 Mingling Zone (ST10_19A): Plagioclase porphyroblast in amphibole & epidote foliation

Pale grains are dominated by irregular plagioclase and microcline. Elongate biotite flakes are integrown with amphibole and epidote, defining a foliation that wraps around porphyroblasts. FOV = 7×10.5mm

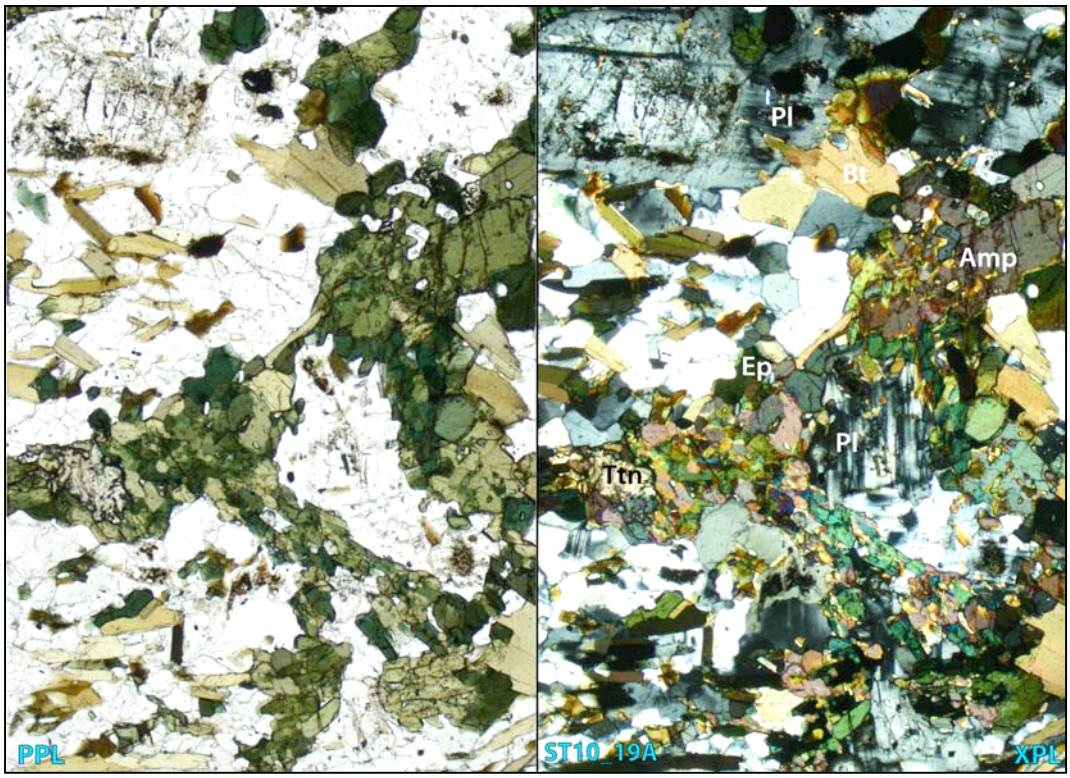

Figure 5.10 Mingling Zone (ST10_19A): Intergrown amphibole, epidote & titanite

Irregular amphibole (right centre) and epidote (centre left) is intergrown with titanite (left centre). Plagioclase with imperfect twinning (top left) is partially altered to sericite and epidote. The alignment of biotite flakes defines the foliation (across the photo). FOV = 1.7×2.5 mm

Plagioclase poikiloblasts <20mm contain biotite, epidote and amphibole inclusions (shown in Figure 5.11, bottom right). Microcline grains have irregular embayed boundaries, and commonly display imperfect twinning. Many crosshatched microcline grains <1.7mm appear to be zoned, and several preserve simple twinned (albitic) cores. Minor quartz grains have sutured boundaries and tourmaline inclusions.

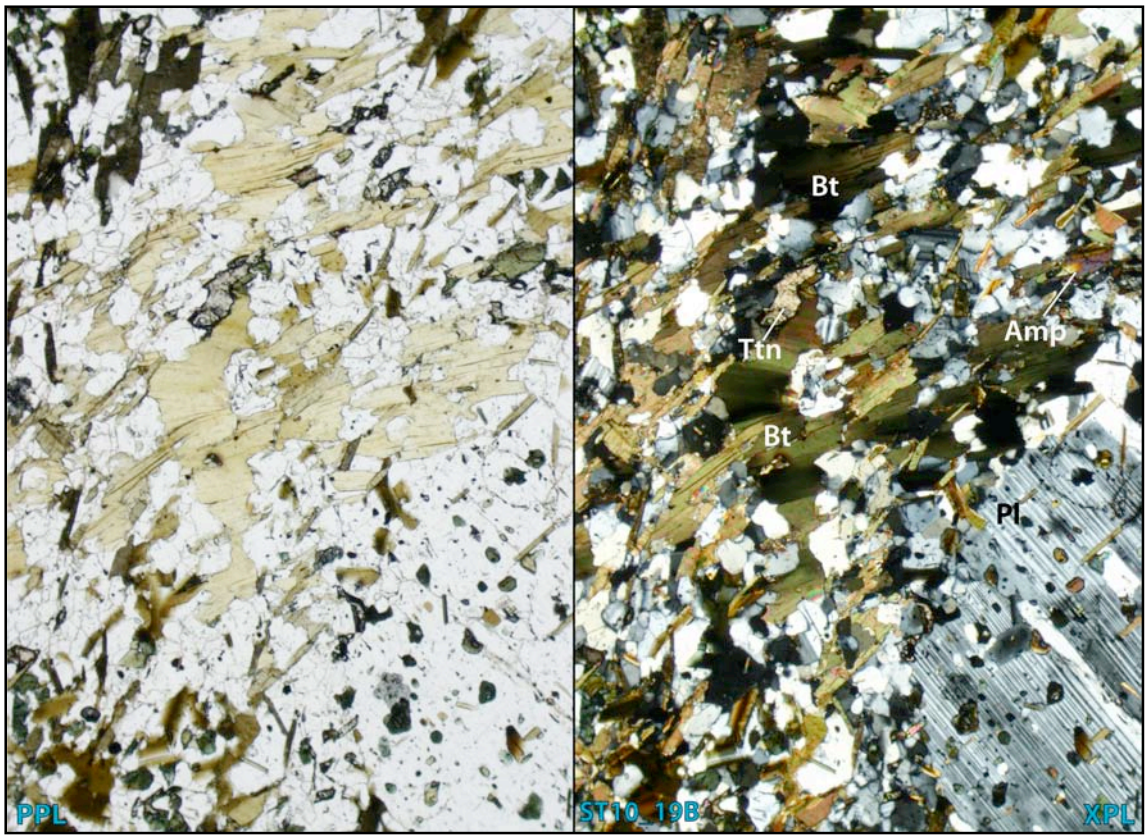

Figure 5.11 Mingling Zone (ST10_19B): Poikiloblastic plagioclase with biotite & epidote inclusions

Poikiloblastic plagioclase (lower right) with rounded to elongate biotite and rounded epidote inclusions. Pale areas in the surrounding groundmass (left) comprise plagioclase and K-feldspar (minor quartz). Foliation defined by biotite, titanite, epidote and amphibole running lower left to top right in this image. FOV = 1.7×2.5 mm

The fine-grained granitoid material from the mingling zone (represented by sample ST10_19D) is dominated by plagioclase (20-25%), microcline (~20%), cordierite (15-20%), biotite (10-15%), and quartz (10-15%). Altered aluminosilicate comprise approximately 5% of the sample. Secondary minerals include epidote (~5%) with sericite and pinite (10%), spinel (<5%), titanite (<5%) and ilmenite (<2%) and trace amounts (<1%) of apatite, zircon and sulphide grains.

Prismatic aluminosilicate (sillimanite) grains are near completely replaced by granular spinel and sericite ± ilmenite (shown in Figure 5.12). Tan-brown biotite <0.5mm is commonly elongate, defining a weak foliation (Figure 5.12, centre upper and lower). Cordierite <1.5mm are being replaced by pinite and spinel giving a spotted or striped appearance to the grains (Figure 5.12, lower centre). Epidote and biotite appear to overgrow quartz and plagioclase phenocrysts. Titanite is associated with biotite and epidote. Sericite and epidote are replacing plagioclase along fractures and grain boundaries.

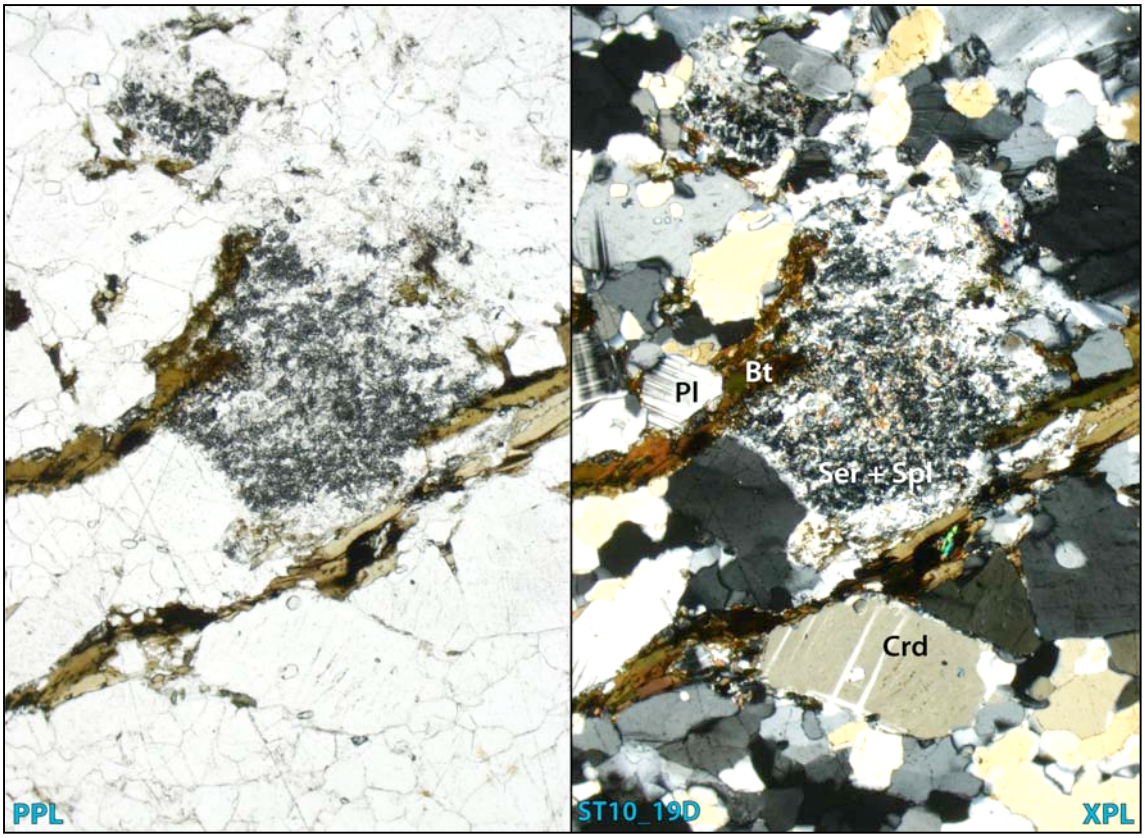

Figure 5.12 Mingling Zone (ST10_19D): Sericite & spinel partially replace sillimanite

Aluminosilicate is suggested to be sillimanite, per Greenfield *et al*., 1996.

Sillimanite (centre) near-completely replaced by fine-grained sericite and granular spinel. Irregular, rounded plagioclase (centre, left) shows multiple twinning. Cordierite (bottom centre) has lamellar twinning and is being replaced by sericite. Partial replacement of cordierite by sericite given a striped appearance (PPL). Elongate biotite (centre) defines a weak foliation. FOV = 1.7×2.5 mm

5.3 PETROGRAPHIC INTERPRETATION

Petrographic analysis shows the granite samples have a similar mineral assemblage, with a dominance of K-feldspar, cordierite and quartz, with plagioclase and biotite in varying amounts. Quartz-diorites from the mingling zone are more readily identifiable, containing amphibole, epidote and titanite, and higher proportions of plagioclase and biotite. Modal abundances observed are summarised in Table 5.5.

Table 5.5 Summary of Mineral Modal Abundance Observed during Petrography.

Summary of Mineral Modal Abundance observed during Petrography								
	Eastern Granite		Northern Granite		Diatexite	Granite – Quartz-Diorite Mingling Zone		
	ST10_11	ST10_19C	ST10_16B	ST10_18	ST10_15D	ST10_19A	ST10_19B	ST10_19D
Microcline	20-25%	~20%	~20%	15-20%	20-25%	10-15%	~20%	~20%
Plagioclase	~ 10%	10-15%	~ 10%	10-15%	10-15%	20-25%	~25%	20-25%
Quartz	15-20%	15-20%	20-25%	10-15%	20-25%	5-10%	5-10%	10-15%
Biotite	~ 15%	10-15%	10-15%	15-20%	10-15%	15-20%	15-20%	10-15%
Cordierite	15-20%	~20%	~ 10-15%	~ 10%	15-20%			15-20%
Sericite	10%	10%	~ 10%	~ 5%	~ 5%			< 5%
Pinite	< 5%	~ 5%	~ 5%	~ 5%	< 5%			< 5%
Spinel	5%	5%	< 5%	< 5%				< 5%
Aluminosilicate	5%							~ 5%
Fibrolite	< 5%							
Epidote	~ 5%	~ 5%	~ 5%	< 5%	~ 5%	~20%	~15%	~ 5%
Chlorite	~ 5%	~ 5%	~ 5%	< 5%				
Amphibole						15-20%	~ 15%	
Titanite		< 2%				< 5%	< 5%	< 5%
Ilmenite	< 2%							< 2%
Tourmaline		< 1%			< 5%		< 1%	
Apatite	< 1%	< 1%	< 1%	< 1%	< 1	< 1%	< 1%	< 1%
Zircon	< 2%	< 1%	< 1%	< 1%	< 1%	< 1%	< 1%	< 1%
Monazite					< 1%			
Opaques	< 1%	< 1%	< 1%	< 2%	< 1%			< 1%

Modal abundances were estimated during petrographic examination.

Cordierite is present in all granitic samples, excluding the quartz-diorites from the mingling zone (ST10_19A and ST10_19B). The high proportion of cordierite in the granites was expected for S-type granites (Chappell & White, 2001), reflecting a metasedimentary source.

Tourmaline was only identified in the hybrid diatexite (ST10_15D) and granitic mingling zone samples (ST10_19C and D), not in the eastern or northern granites or quartz-diorite samples. Titanite was only identified in the quartz-diorite and granite mingling zone samples (ST10_19A, B, D and C), and is associated with epidote and amphibole. Titanite found in the eastern granite samples at this location (ST10_19C and D) reflects the influence of quartz-dioritic material on local granite composition.

Petrographic analysis has shown the granite samples from Mt Stafford have experienced strain and/or deformation and recrystallisation to varying degrees. This is indicated by the prevalence of undulose extinction in quartz and feldspar, formation of sub-grain domains and improperly twinned feldspar and cordierite. Rectangular feldspar are generally absent from thin section view.

Hydrothermal alteration has affected all granitoid samples to some degree, evident in the alteration of biotite, cordierite and feldspar (plagioclase and microcline). Myrmekite textures in several samples are characteristic of high-temperature metamorphism (Vernon, 2004). In general, samples retain their igneous textures, despite the evident alteration.

ST10_18 from the northern granite indicates a high degree of shearing, with a higher degree of recrystallisation and a significant proportion of minerals exhibiting undulose extinction. These textures likely reflect the quartz-muscovite shear zones documented in the literature (Greenfield *et al*., 1996, White *et al*., 2003).

Although granitoid samples show some variation in microstructure, they have a broadly similar mineralogy. The hybrid diatexite and mingling zone samples are more readily identified, due to their more silicic or mafic mineralogy (respectively). Petrography does suggest some differences between eastern granite samples. The sample associated with the mingling zone (ST10_19C) contains minor titanite, reflecting a compositional influence from the quartz-diorites it is related to in the field.

6. BSE IMAGING & EMP MINERAL CHEMISTRY

6.1 INTRODUCTION

Electron microprobe (EMP) spot analyses for major element oxides were conducted to characterise mineral chemistry, allowing confirmation of petrographic identification and comparison of the eastern with the northern granite. Four sites were selected from the eastern granite (ST10_11), and one site from the northern granite (ST10_16B). Back-scattered electron (BSE) images were used to target the main mineral assemblages within each sample, as summarised in Table 6.1. Complete EMP results are contained in Appendix C-1.

Table 6.1 Minerals in Thin Section Targeted for Analysis by EMP
(× indicates mineral targeted)

Minerals Targeted for EMP Analysis					
Sample	**ST10_11**				**ST10_16B**
Analysis	TS11-001	TS11-002	TS11-003	TS11-004	TS16B-001
	Symplectite	Residual & Replacement Texture	Residual & Replacement Texture	Residual & Replacement Texture	Replacement Texture
K-Feldspar		×		×	×
Plagioclase		×			×
Quartz	×				
Biotite	×		×	×	×
Muscovite					×
Pinite					×
Epidote			×		
Cordierite		×	×		
Sillimanite				×	
Spinel		×	×	×	
Opaques			×		×

6.3 BSE THIN SECTION IMAGES

Figure 6.1 (eastern granite ST10_11) shows intergrown quartz and biotite with a vermicular myrmekite texture (centre). K-feldspar (left) is being partially replaced by biotite and sericite along grain boundaries. Figure 6.2 (eastern granite ST10_11) shows spinel and biotite near-completely replacing aluminosilicate (sillimanite, centre). This texture is also shown Figure 6.3. The spinel is intergrown with sericite and biotite.

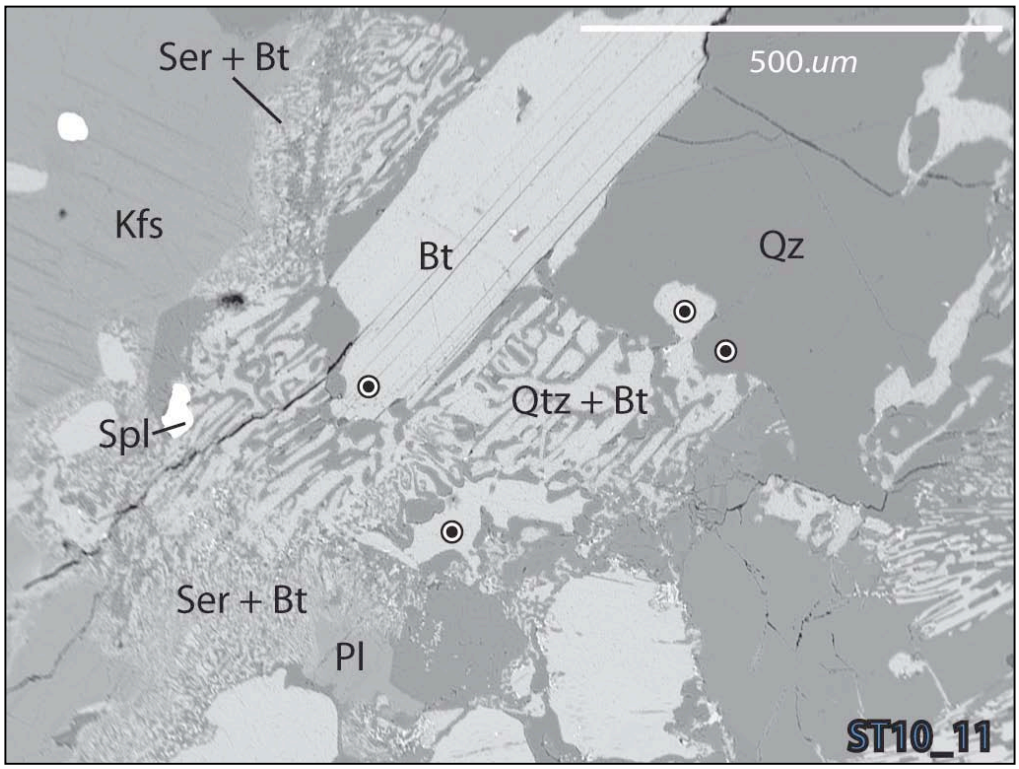

Figure 6.1 Eastern Granite (ST10_11): Intergrown Quartz-Biotite Myrmekite BSE Image

Intergrown biotite and quartz form vermicular myrmekite texture. Cleavage can be seen in biotite (centre upper). Sericite and biotite are replacing feldspar (microcline and plagioclase)
◎ indicates location probed for analysis

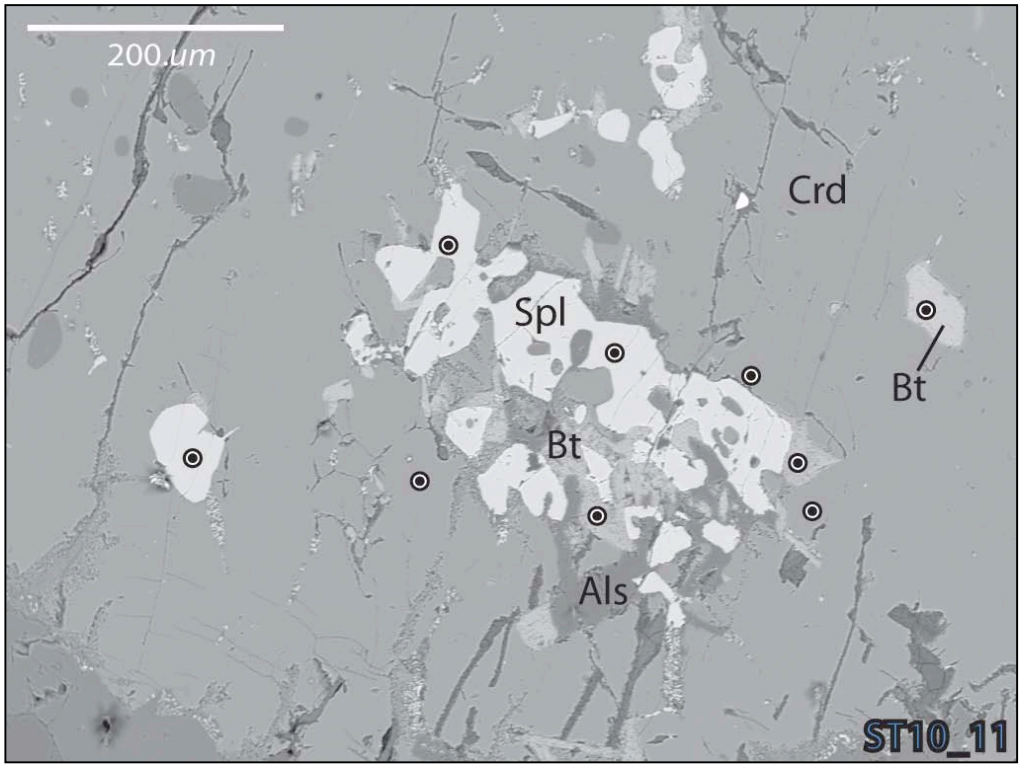

Figure 6.2 Eastern Granite (ST10_11): Biotite & Spinel Replacing Aluminosilicate (Sillimanite)

Biotite and spinel have near completely replaced the aluminosilicate grain (centre), surrounded by cordierite. ◎ indicates location probed for analysis

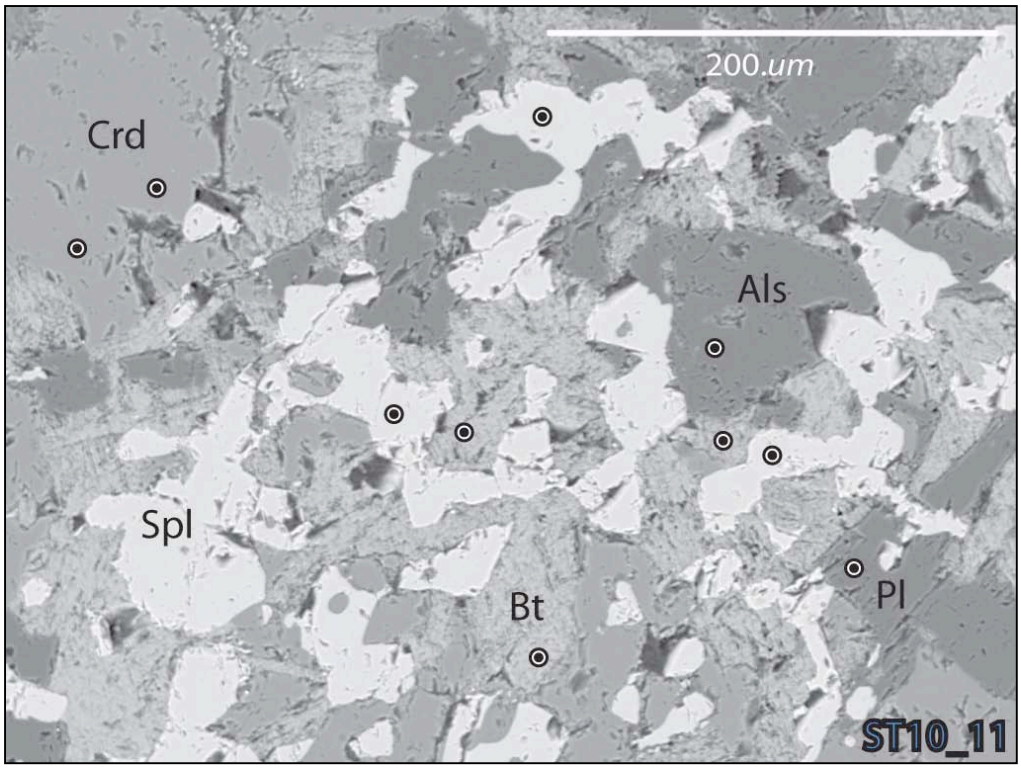

Figure 6.3 Eastern Granite (ST10_11): Biotite & Spinel Replacing Aluminosilicate (Sillimanite) Biotite and spinel replace aluminosilicate (sillimanite, after Greenfield *et al*., 1996). Cordierite is fractured and showing replacement by sericite and biotite.◎ indicates location probed for analysis

BSE image from the northern granite ST10_16B (Figure 6.4) shows K-feldspar being replaced by sericite and biotite along fractures and grain boundaries (centre right). Biotite has irregular embayed grain boundaries. Sulphide minerals (centre left) are associated with biotite. Quartz (left) shows zircon inclusions.

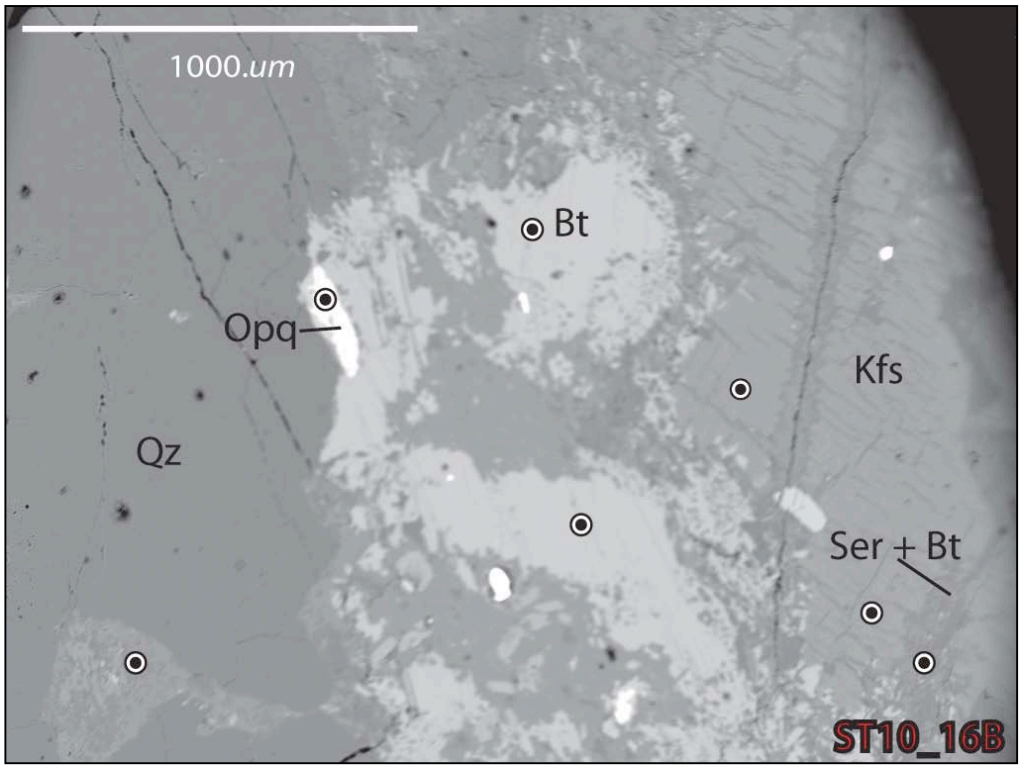

Figure 6.4 Northern Granite (ST10_16B): Biotite & Sericite have Partially Replaced K-Feldspar
Biotite and sericite are replacing K-feldspar along fractures and grain boundaries (right). Sulphide minerals (centre left) are associated with biotite. ◎ indicates location probed for analysis

6.3 EMP Mineral Chemistry

Of the 41 points targeted, nine did not analyse the intended grain and/or analysed several grains together, so are rejected. Quartz was analysed in the quartz-biotite symplectite in the eastern granite and inadvertently analysed in the northern granite instead of feldspar. Aluminosilicate probed in the eastern granite is proposed to be sillimanite (Greenfield *et al.*, 1996). These minerals will not be discussed in detail. EMP results are summarised in Table 6.2. EMP analysis of zircon are discussed in Chapter 8.4.

Table 6.2 Summary of EMP Mineral Chemistry Data

Thin Section EMP Mineral Chemistry Summary (ST10_11 & ST10_16B)					
Feldspar	**XAn**	**XAb**	**XOr**		**No. Oxygen**
ST10_11	25.39 – 27.54	71.82 – 73.61	0.64 – 1.00		8
ST10_16B	0.34	30.54	69.12		
Biotite	**XFe**	**XMg**	**K_2 Site**	**Ti Value**	
ST10_11	59.15 – 70.34	29.66 – 40.85	1.51 - 1.94	0.14 - 0.48	22
ST10_16B	64.87 – 68.47	31.53 – 35.13	1.90 - 1.97	0.14 - 0.22	
Muscovite	**XFe**	**XMg**	**K_2 Site**	**XNa**	
ST10_11	56.41	34.31	1.97	3.15	22
ST10_16B	49.70 – 56.41	43.59 – 50.30	1.97 - 2.01	3.15 – 3.17	
Cordierite	**XMg**	**XFe**	**XMn**		
ST10_11	40.48 – 42.71	56.86 – 58.90	1.00 – 1.52		18
Spinel	**XHe + XGx**	**XSp**	**XGh**		
ST10_11	91.07 – 91.48	5.19 – 6.05	2.88 – 3.39		4
Quartz	**SiO_2** (wt%)				
ST10_11	99.2				2
ST10_16B	99.7				
Aluminosilicate	**$Al+Fe^{3+}$**				
ST10_11	1.90 - 1.92				5

6.3.1 FELDSPAR

Feldspar was analysed in both the eastern granite (ST10_11) and the northern granite (ST10_16B). Feldspar has three end members:

$$\text{Albite (XAb)} = NaAlSi_3O_8$$

$$\text{Anorthite (XAn)} = CaAl_2Si_2O_8$$

$$\text{Orthoclase K-Feldspar (XOr)} = KAlSi_3O_8$$

Plagioclase feldspar compositions have complete solid solution between $Na[AlSi_3O_8]$, $Ca[Al_2Si_2O_8]$ and $K[AlSi_3O_8]$. This causes a variation between end-members albite, anorthite and orthoclase respectively, generally associated with composition of the host rock and/or grade in metamorphic systems (Deer *et al*., 1992).

Feldspar end-members are calculated for classification on a ternary diagram (Figure 6.5):

$$XAb = [Na/(Na+Ca+K)] *100$$

$$XOr = [K/(Na+Ca+K)] *100$$

$$XAn = [Ca/(Na+Ca+K)] *100$$

Oligoclase plagioclase in the eastern granite shows compositions of $XAb_{72\text{-}74}$, $XAn_{25\text{-}28}$ and $XOr_{0.6\text{-}1.0}$. K-feldspar sanidine from the northern granite has a composition XOr_{69}, XAb_{31} and XAn_0. Results are summarised in Table 6.2.

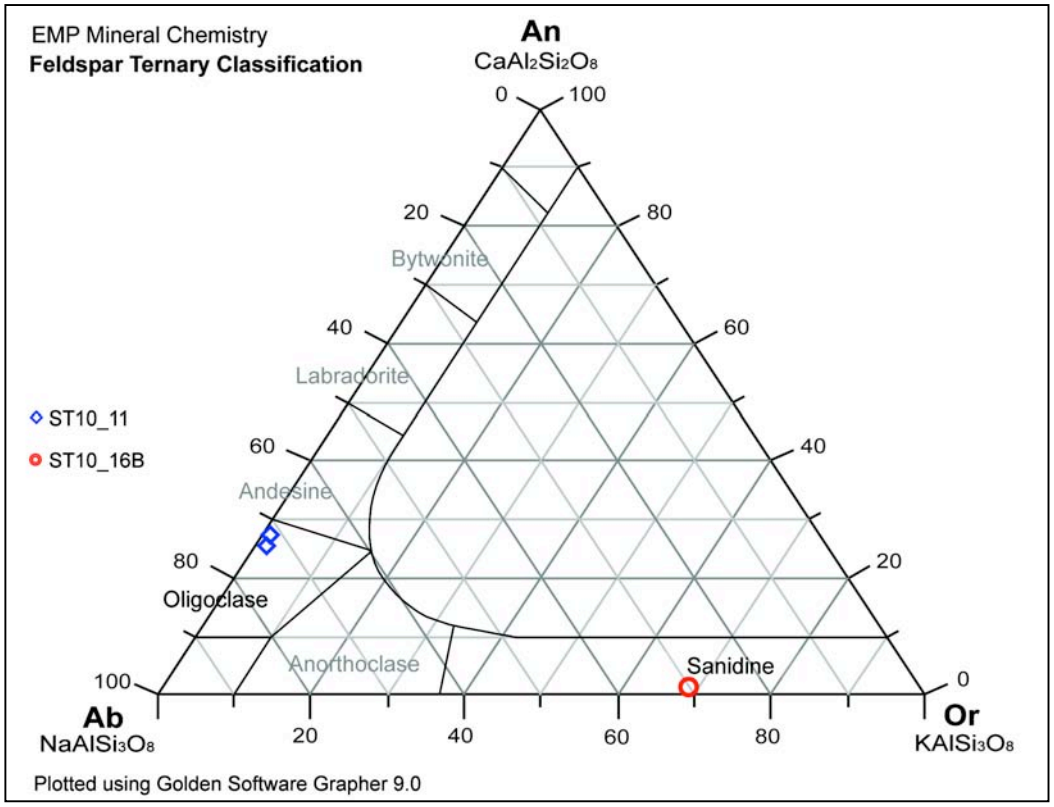

Figure 6.5 EMP Feldspar Ternary Classification Diagram (Ab, An & Or) Plotted using Golden Software *Grapher* 9.0

6.3.2 BIOTITE

Biotite was analysed from both samples, as shown in Table 6.1. Biotite has the formula:

$$K_2(Mg,Fe^{2+})_{6-4}(Fe^{3+},Al,Ti)_{0-2}[Si_{6-5}Al_{2-3}O_{20}](OH,F)_4$$

For mineral classification, cations were calculated to 22 oxygen anions per formula unit, with The Fe: Mg ratio, Ti values and the K_2 site examined (Table 6.2).

Fe^{2+} and Mg commonly substitute in biotite (Deer *et al.*, 1992). The Fe:Mg ratio was calculated using Fe^{2+} and Mg cations per formula unit:

$$XFe = [Fe^{2+}/(Mg+Fe^{2+})] *100$$

$$XMg = [Mg/(Mg+Fe^{2+})] *100$$

XFe values show the grains analysed are typically iron-rich (XFe ≥ 50), with XFe ranging between 59.15 and 68.32 for the eastern granite and 64.87 to 68.47 for the northern granite. XMg values are 29.66 to 40.85 for the eastern granite and 31.53 to 35.13 for the northern granite. The results indicate biotite from the eastern granite (ST10_11) are Fe end-members annite and siderophyllite, while ST10_16B analyses fall in the siderophyllite field (Figure 6.6a).

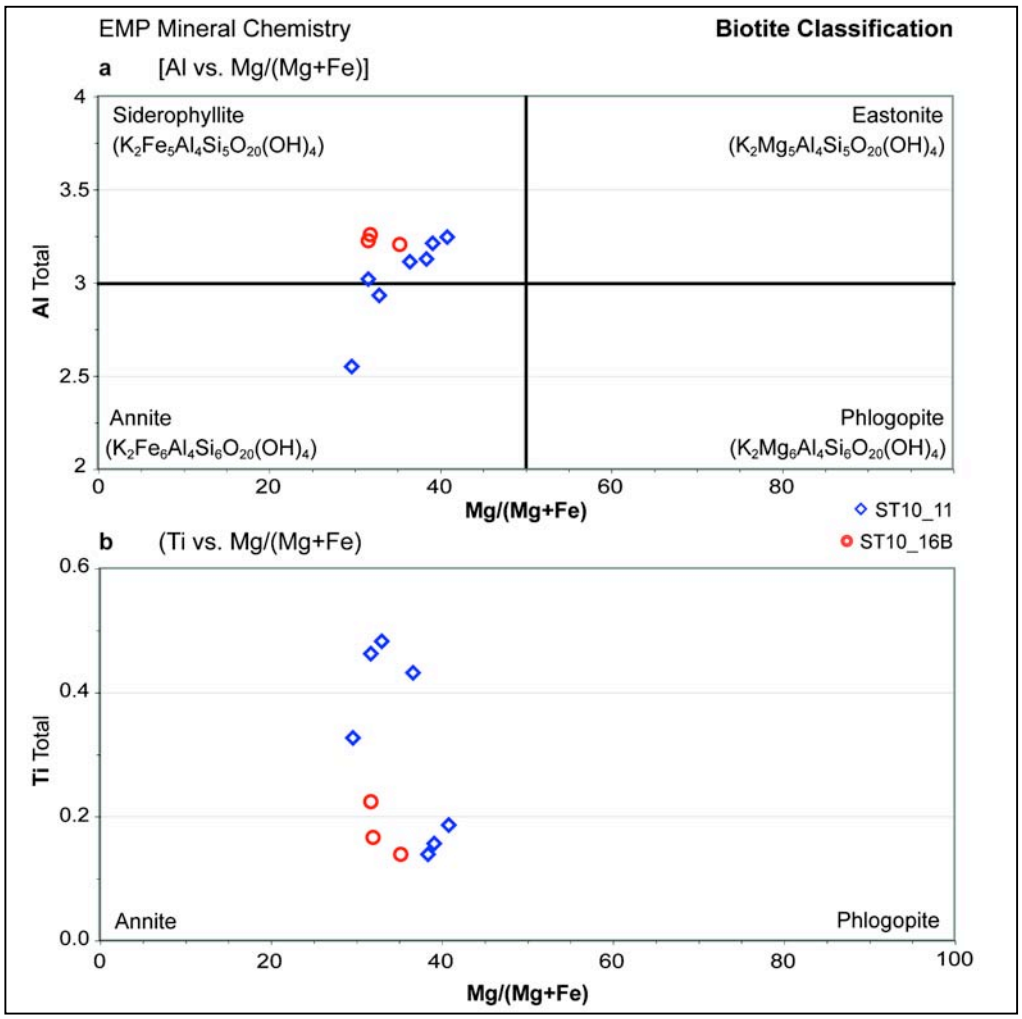

Figure 6.6 EMP Biotite Classification Al & Ti vs. Mg/(Mg+Fe)
a. Al vs. Mg/(Mg+Fe), b. Ti vs. Mg/(Mg+Fe)

Ti cations are typically low (<0.5), ranging from 0.14 to 0.48 in the eastern granite, and 0.14 to 0.22 for the northern granite (Figure 6.6b). Values are generally lower for sample ST10_16B and indicate a preservation of Ti when Al is lower, comparing Figures 6.6a and b.

The K_2 site values were calculated using the formula:

$$K_2 \text{ Site} = Na + K + Ca$$

Values range from 1.82 to 1.94 for the eastern granite, and 1.90 to 1.97 for the northern granite. The results suggest no distinct variation between samples, calculating a standard deviation of 0.04 across all analyses. Low K_2 site values are characteristic of altered biotite (Deer *et al*., 1992).

6.3.4 MUSCOVITE

Muscovite is generally related to intrusive and metamorphic events, occurring at a range of metamorphic grades. (Winter, 2001). The formula for muscovite is:

$$K_2Al_4[Si_6Al_2O_{20}](OH,F)_4.$$

For mineral classification, cations were calculated to 22 oxygen anions per formula unit, with Fe: Mg ratio, the K_2 site and paragonite component examined (Table 6.2). The muscovite Fe: Mg ratio was calculated using Fe^{2+} and Mg cations per formula unit:

$$XFe = [Fe^{2+}/(Mg+Fe^{2+})] *100$$

The grains analysed have XFe values of 49.70 to 56.41.

The K_2 site values were calculated using the formula:

$$K_2 \text{ Site} = Na + K + Ca$$

Values are 1.97 and 2.01 for the northern granite, with fine sericite mica included in these analyses. While it does not have appreciably different chemistry, sericite commonly has higher MgO and lower K_2O (Deer *et al*., 1992).

Muscovite may contain 10-20% solid solution paragonite (XNa), which is calculated by:

$$\text{Paragonite component (XNa)} = [Na/(Na+K)] *100$$

The paragonite component is 3.15 to 3.68 for all analyses (Table 6.2).

Phengite occurs when Si:Al ratios are greater than 3:1, and where high Si values are accompanied by Mg and Fe^{2+} substitution for octahedral Al (Deer *et al*., 1992). Low values of 1.09 to 1.28 indicate minimal phengite (refer Appendix C-1). The Mg: Fe ratio of any phengite component (XMg) is calculated as:

$$\text{XMg of Phengite component} = [Mg/(Mg+Fe^{2+}] *100$$

XMg of the phengite component ranges from 34.31 to 50.30 (Figure 6.7).

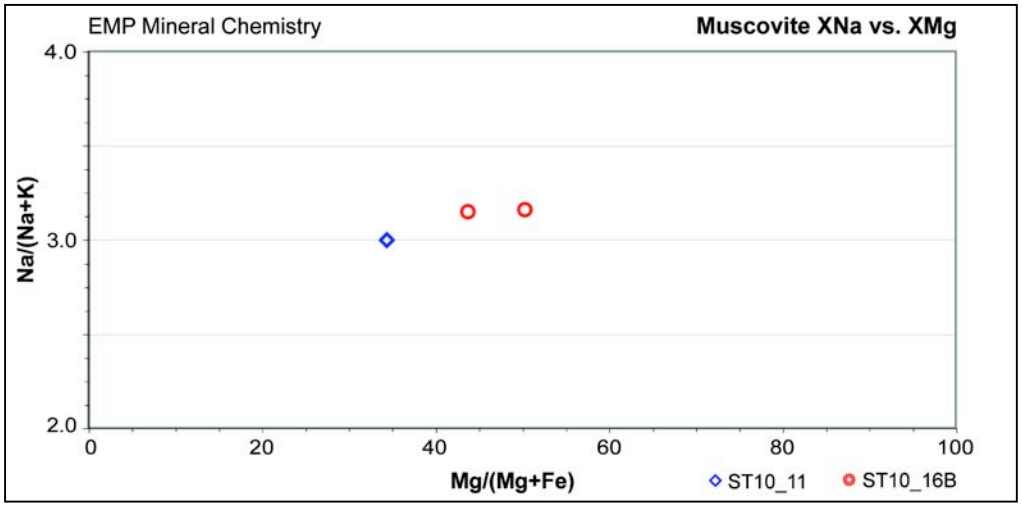

Figure 6.7 EMP Muscovite XNa vs. XMg

6.3.5 CORDIERITE

Cordierite grains were probed from the eastern granite (ST10_11). Cordierite may show solid solution between Cordierite (XMg) and Sekaninaite (XFe). Cordierite has the formula:

$$(Mg,Fe)_2[Si_5Al_4O_{18}].n\ H_2O$$

Cations were calculated to 18 oxygen anions per formula unit (Table 6.2 and Appendix C-1).

Discrimination of composition was made by:

$$XMg = [Mg/(Mg+Mn+Fe^{2+})] *100$$

$$XFe= [Fe^{2+}/(Mg+Mn+Fe^{2+})] *100$$

$$XMn = [Mn/(Mg+Mn+Fe^{2+})] *100$$

Cordierite assemblages analysed are generally enriched in Mg and Fe, containing only minor Mn (Figure 6.8). The sekaninanite (Fe-cordierite) end-member composition ranges between $Fe_{57\text{-}58}$, $Mg_{40\text{-}43}$ and $Mn_{1\text{-}2}$,

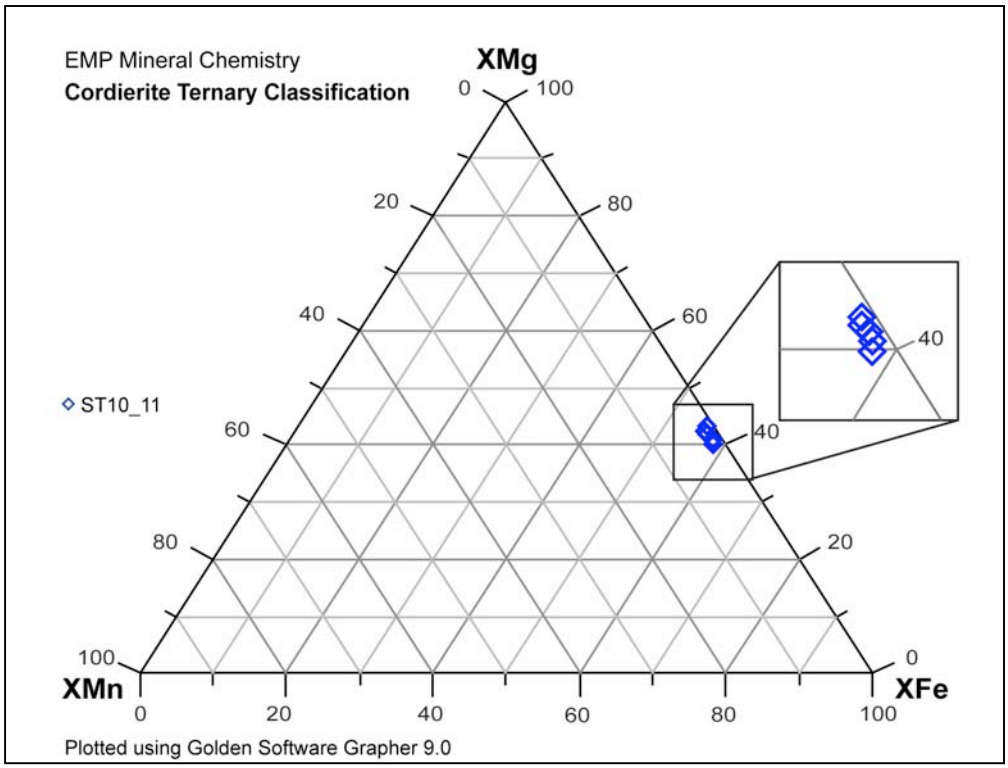

Figure 6.8 EMP Cordierite Ternary Diagram (XMg, XFe^{2+} & XMn)
Plotted using Golden Software *Grapher* 9.0

6.3.6 SPINEL

Spinel was probed from the eastern granite (ST10_11). In the spinel series within the spinel group, the trivalent ion is Al. End-member types are:

$$\text{Spinel (XSp)} = MgAl_2O_4$$

$$\text{Hercynite (XHe)} = Fe^{2+}Al_2O_4$$

$$\text{Gahnite (XGh)} = ZnAl_2O_4$$

$$\text{Galaxite (XGx)} = MnAl_2O_4$$

There is a continuous series from spinel (Mg) to hercynite (Fe). Cations for mineral classification were calculated using 4 oxygen anions per formula unit (Appendix C-1).

Compositions of spinel end-member types XHe, XSp, XGh and XGx are calculated by:

$$XHe = [Fe^{2+}/(Fe^{2+}+Mn+Mg+Zn)] *100$$

$$XSp = [Mg/(Fe^{2+}+Mn+Mg+Zn)] *100$$

$$XGh = [Zn/(Fe^{2+}+Mn+Mg+Zn)] *100$$

$$XGx = [Mn/(Fe^{2+}+Mn+Mg+Zn)] *100$$

The grains analysed represent the Fe end-member hercynite, with compositions of XHe_{92}, $XSp_{5\text{-}6}$ and XGh_3 (Figure 6.9). XHe and XGx are combined for plotting.

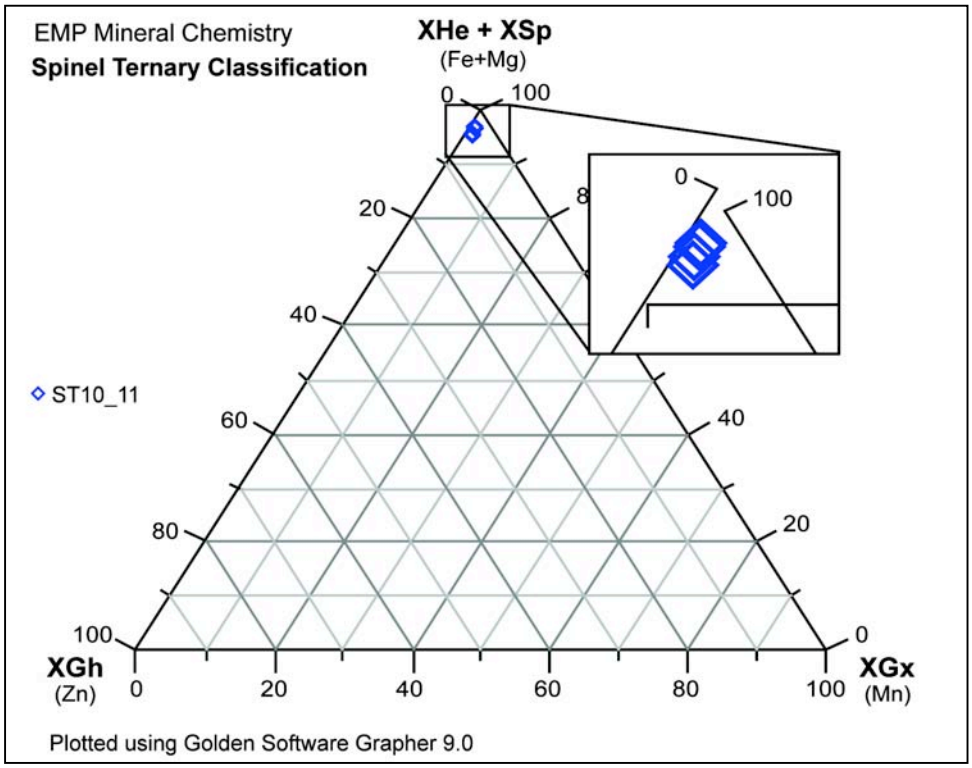

Figure 6.9 EMP Spinel Ternary Classification Diagram (XHe+XGx, XSp, XGh) Plotted using Golden Software *Grapher* 9.0

6.3 Discussion of EMP Mineral Chemistry

Minerals analysed during EMP and mineral chemistry results are summarised in Table 6.3. Alteration of biotite and muscovite is evident in both samples, indicated by low K_2 site values in the biotite and muscovite grains analysed (Deer *et al*., 1992). Further mineral comparisons could not be drawn, due to the limited number and several inconclusive analyses (shown as rejected in Appendix C-1). EMP mineral chemistry confirmed the petrographic identification of several minerals (namely aluminosilicate and cordierite).

Table 6.3 Summary of EMP Thin Section Mineral Chemistry

EMP Thin Section Mineral Chemistry Summary		
Sample	**ST10_11** Residual & Replacement Texture	**ST10_16B** Replacement Texture
K-Feldspar	-	Sanidine (XAb_{31}, XAn_{0}, XOr_{69})
Plagioclase	Oligoclase (XAb_{72-74}, XAn_{25-28}, XOr_{1})	-
Quartz	quartz	quartz
Biotite	Annite / Siderophyllite (XFe_{59-68})	Siderophyllite (XFe_{65})
Muscovite	Muscovite (XMg_{34}, XNa_{3})	Muscovite (XMg_{44-50}, XNa_{3})
Cordierite	Cordierite (Fe_{57-58}, Mg_{40-43}, Mn_{1-2})	--
Aluminosilicate	sillimanite (?)	--
Spinel	Hercynite (XHe_{92}, XSp_{5-6}, XGh_{3})	--

(- indicates mineral not probed, but present. -- indicates mineral not present at analysis location)

7. XRF WHOLE ROCK CHEMISTRY

7.1 INTRODUCTION

This chapter aims to characterise the whole-rock major- and minor- element chemistry across the Mt Stafford granite samples with a view to: 1) comparing bulk chemistry between the granite samples, 2) comparing bulk chemistry of the granite samples to high- and low-grade metasedimentary samples and 3) identifying any distinctive trends in elemental concentrations within and between samples analysed. XRF major element oxide and trace element data are presented in Appendix D-1 and D-2.

Bivariate (namely Harker) plots and classification diagrams for major element oxides reflect possible trends produced by accumulation and/or the fractionation of elements (Winter, 2001) and identify outliers in the dataset. Trace element data was normalised to chondrite values of Taylor & McLennan (1985) prior to assessment, and plotted in order of increasing compatibility. Comparison of Mt Stafford granites with the Lander Package metasedimentary samples is made possible using XRF major and trace element data provided by the PhD analyses conducted by Eileen Dunkley (unpublished).

7.2 XRF MAJOR ELEMENT OXIDE ANSLYSIS

From assessment of wt % oxides (SiO_2, TiO_2, Al_2O_3, MnO, MgO, CaO, K_2O, Na_2O and P_2O_5), SiO_2 displays a significant range of values from 63.85 to 83.65wt %. As expected following petrography, the data shows ST10_19A and ST10_19B are the most mafic of the samples tested, with 63.85% and 68.07wt% SiO_2 respectively. The highest value of 83.65wt% is reported for the hybrid diatexite (sample ST10_15D). Major element oxide (wt%) Harker variation diagrams are presented in Figure 7.1.

Al_2O_3 values indicate a trend with increasing silica concentration until SiO_2 reaches 71.79wt%, and values trend downward (Figure 7.1b). K_2O shows a similar pattern, although the trend is less distinct and values show some variation between 2.75 to 6.60wt% (sample ST10_15D and ST10_19D respectively).

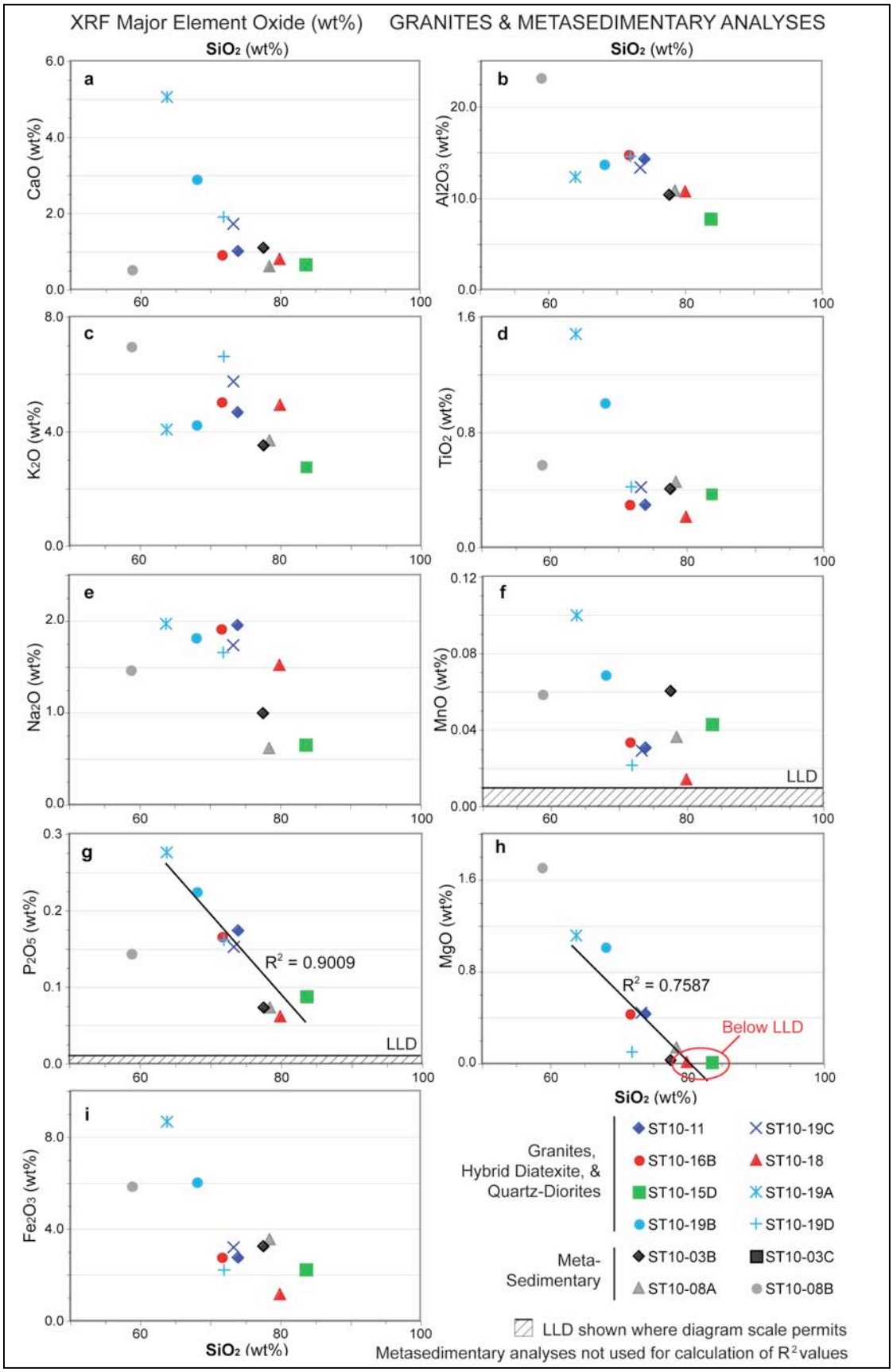

Figure 7.1 XRF Major Element Oxide Bi-Variate (Harker) Plots

Line of best fit & R^2 values do not include metasedimentary rock analyses

Lower Limit of Detection (LLD) shown where diagram scale permits

CaO values are higher (1.71 to 5.05wt%) for the mingling zone samples (ST10_19A, B & D) than for the remainder of samples (0.8 to 1.01wt%). A similar trend is observed in TiO_2, with a range 1.00 to 1.48wt% for ST10_19A & B and a range 0.29 to 0.42wt% for the other samples (Figure 7.1a & d).

A negative correlation trend shows preservation of P_2O_5 with decreasing SiO_2, with R^2 values of 0.90. MgO also indicates a negative trend, with R^2 values of 0.76, likely reflecting enrichment of this element in mafic minerals in the mingling zone samples (Figure 7.1g & h). However, two MgO values are below LLD.

The total alkalis ($K_2O + Na_2O$) versus silica (SiO_2) diagram (TAS), developed by Cox *et al*. (1979) for use on volcanic rock, was adapted for classification of plutonic rocks by Wilson (1989). Similar diagrams have been developed by Middlemost (1985 and 1994), and are shown in Figure 7.2 for comparison.

Using classification diagrams of Middlemost (1985 & 1994) (Figure 7.2a & b), samples from both the eastern and northern granites and the hybrid diatexite fall within the granite field. Mafic mingling zone samples (ST10_19A & B) are classified as quartz-diorite (granodiorite). Several samples (ST10_11, ST10_18 and ST10_15D plot below the classification diagram by Cox *et al.* (1979) (Figure 7.2c). ST10_11 has lower alkalis ($Na_2O + K_2O$) than the granite field accepts, whilst ST10_18 and ST10_15D have higher silica than the classification permits, terminating at 75.0 wt%.

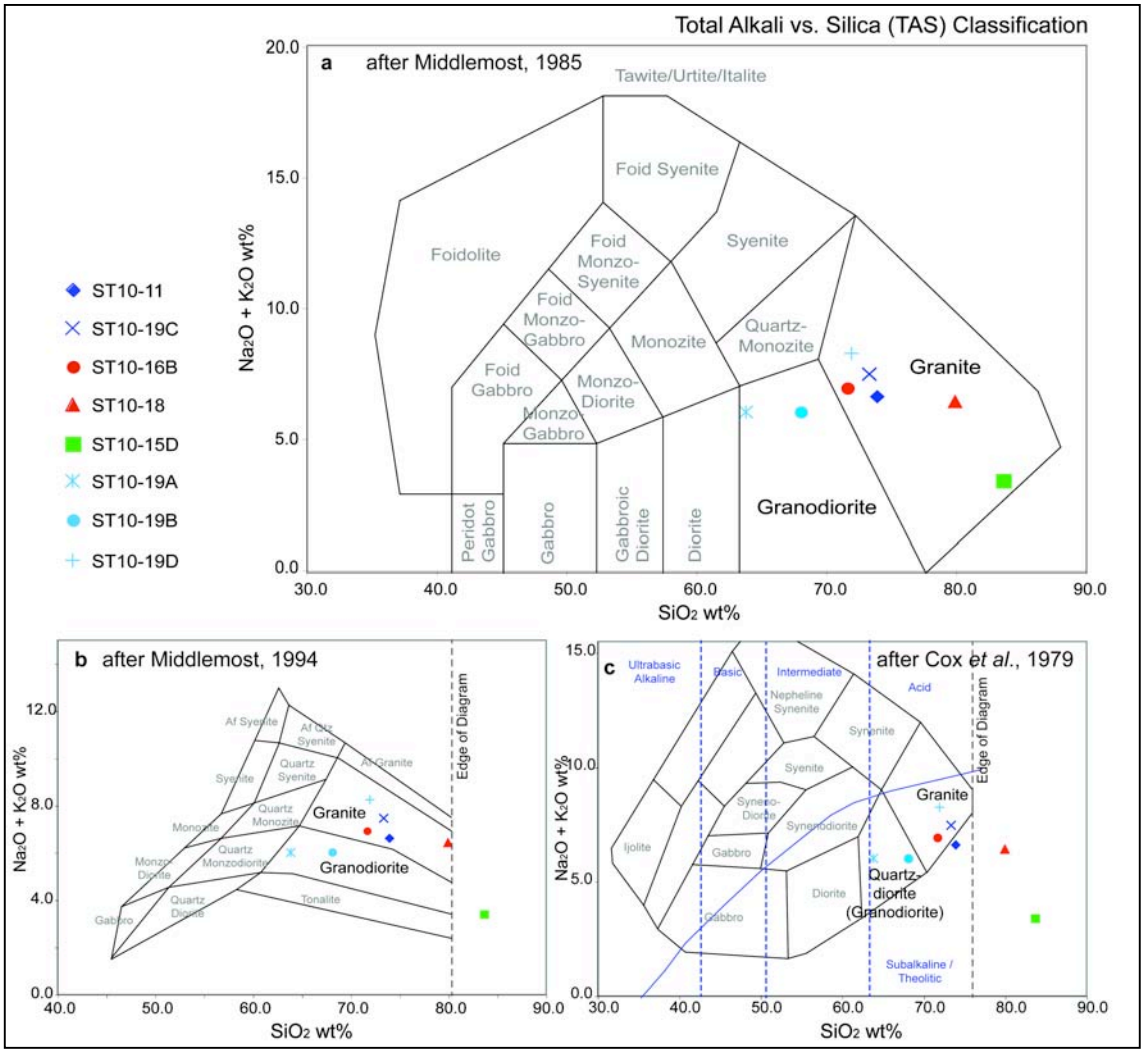

Figure 7.2 XRF Total Alkalis-Silica (TAS) Classification Diagrams after a. Middlemost, 1985. b. Middlemost, 1994. c. Cox *et al*., 1979

The AFM (F= FeO + Fe_2O_3, M= MgO and A= alkalis (Na_2O + K_2O)) diagram presented in Figure 7.3 (after Irvine & Baragar, 1971) indicates the mafic mingling zone samples (ST10_19A & B) are theolitic, while the remainder of the samples fall within the calcalkaline field.

Using the K_2O versus silica classification diagram of Peccerillo & Taylor (1976) for the sub division of sub-alkalic rocks most samples plot outside the diagram, with the mafic mingling zone samples (< 70% SiO_2) within the high-K calcalkaline field (Figure 7.4). Extrapolating the diagram to higher SiO_2 shows the granite mingling zone samples (ST10_19C & D) plot in the shoshonite field, while the majority of samples plot in the high-K calcalkaline field.

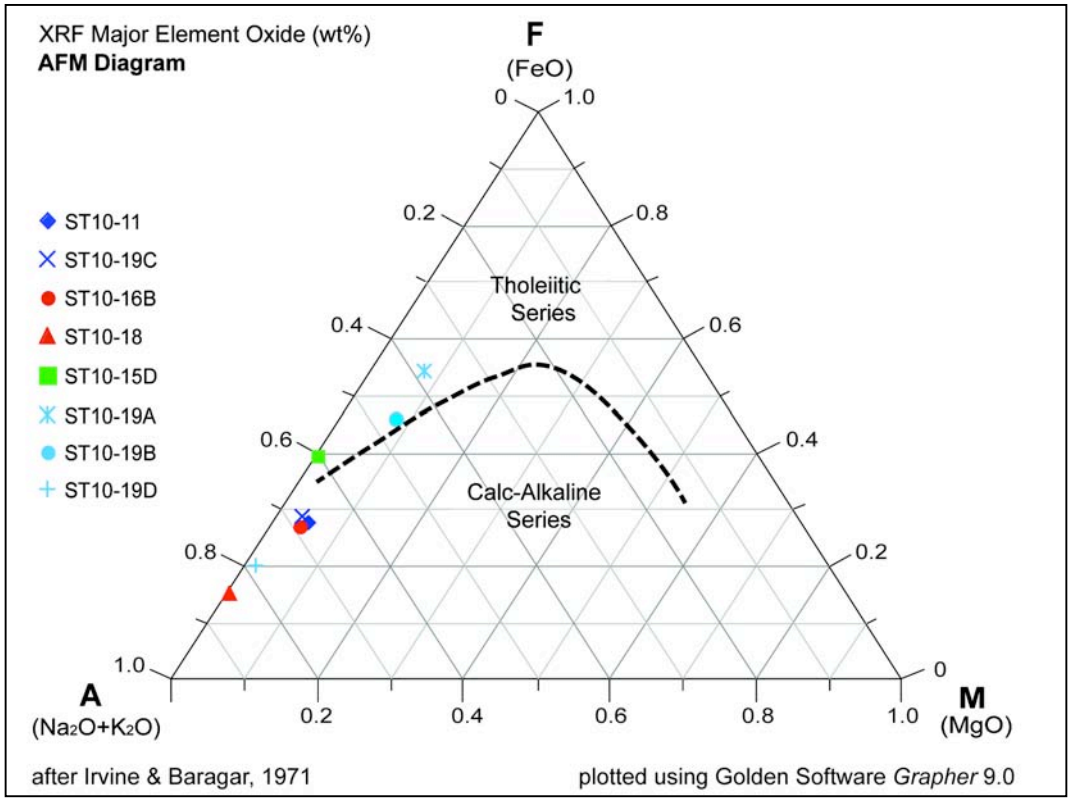

Figure 7.3 AFM Classification Diagram (A = Na_2O + K_2O, F = FeO & M = MgO) after Irvine & Baragar, 1971. Plotted using Golden Software Grapher 9.0

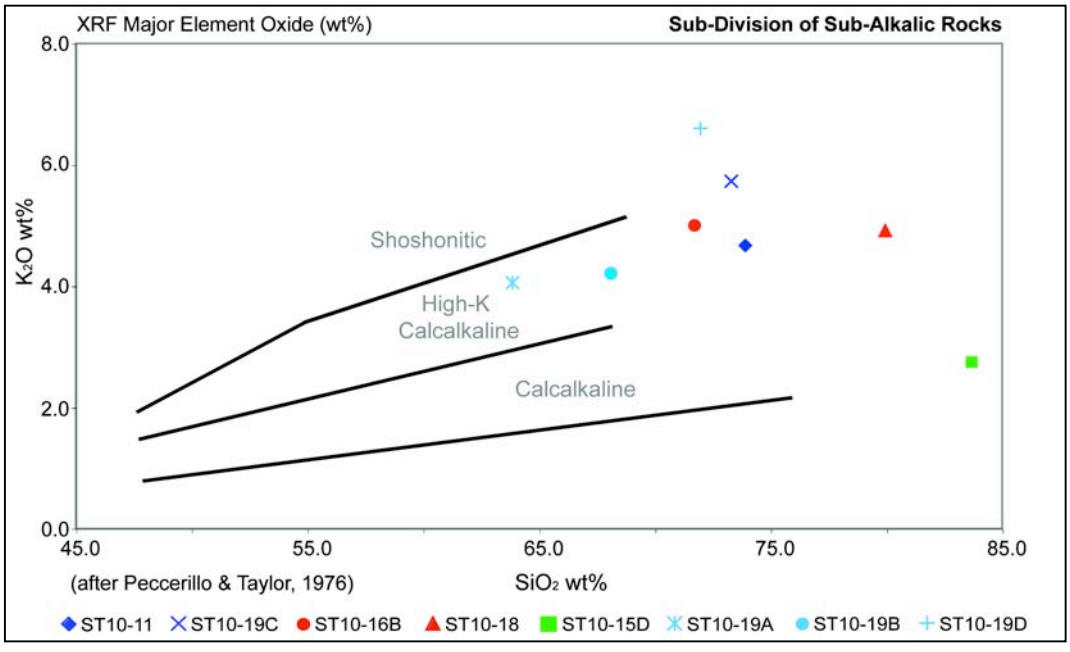

Figure 7.4 Sub-Division of Sub-Alkalic Rocks (SiO_2 vs. K_2O) after Peccerillo & Taylor, 1976

XRF major element oxides were also analysed in China by University of Sydney PhD student Wei Wang. Harker Variation diagrams (Figure 7.5) show close similarity between the two datasets. Na_2O values show minor variation; the dataset from China indicating higher concentrations. SiO_2 values remain constant between the datasets.

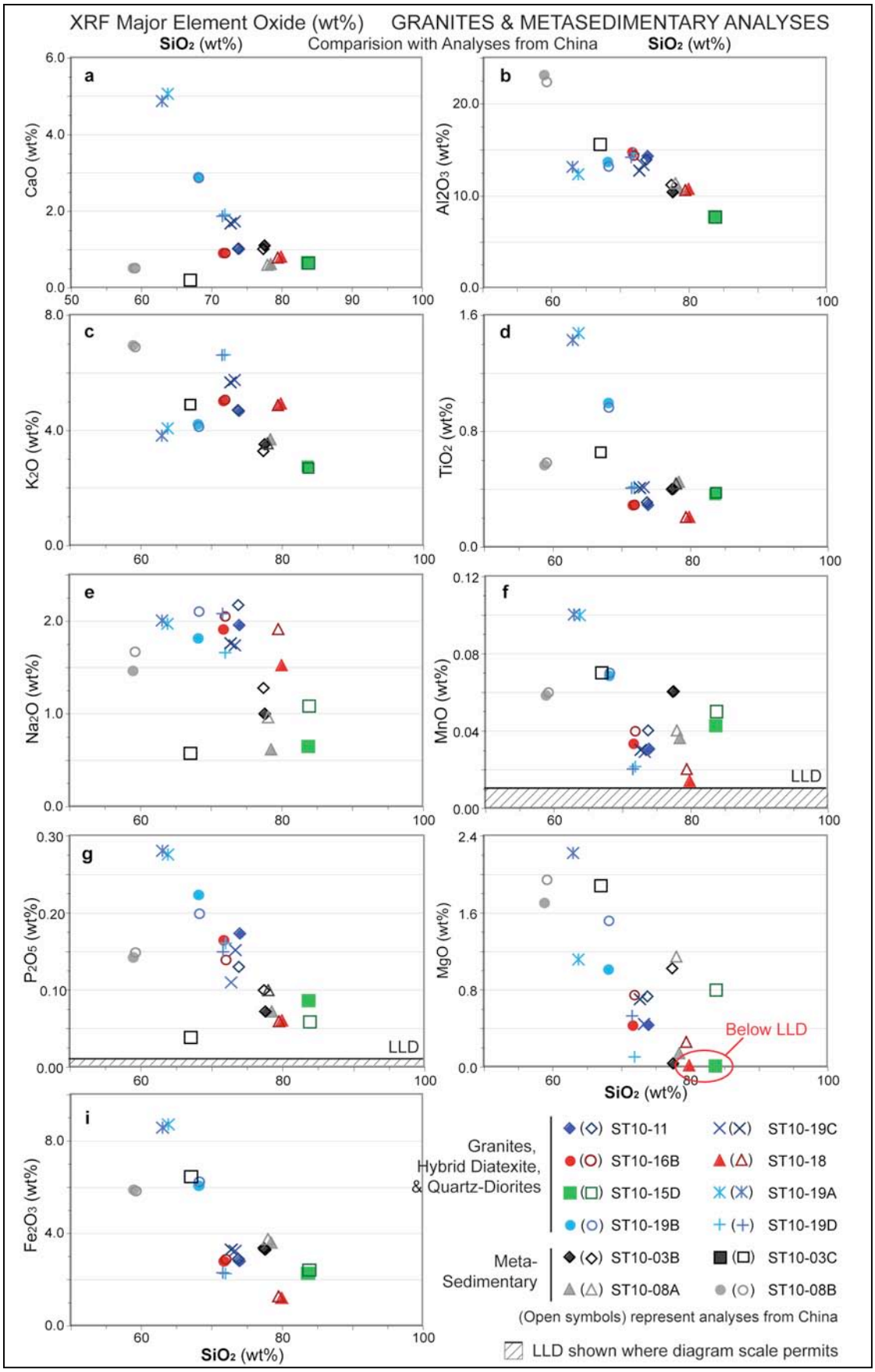

Figure 7.5 XRF Major Element Oxide Bi-Variate (Harker) Plots:

Comparison with Analyses from China

LLD shown where diagram scale permits

7.3 XRF Trace Element Analysis

Trace Elements comparison of the eastern granite and northern granite show minor variation between the four samples. Variation is apparent in chondrite-normalised (c.n) Th, U and Hf abundance (Figure 7.6). Samples with the lowest Hf are those to be used for zircon examination (ST10_11, ST10_19C, ST10_16B and, ST10_18). The highest standard deviation (1s.d) occurs in Th and U data, with values of 225.6 and 127.3 c.n (respectively), while 1s.d for Hf is 13.69. Hf is below LLD (<11 c.n) in ST10_11 and ST10_19A.

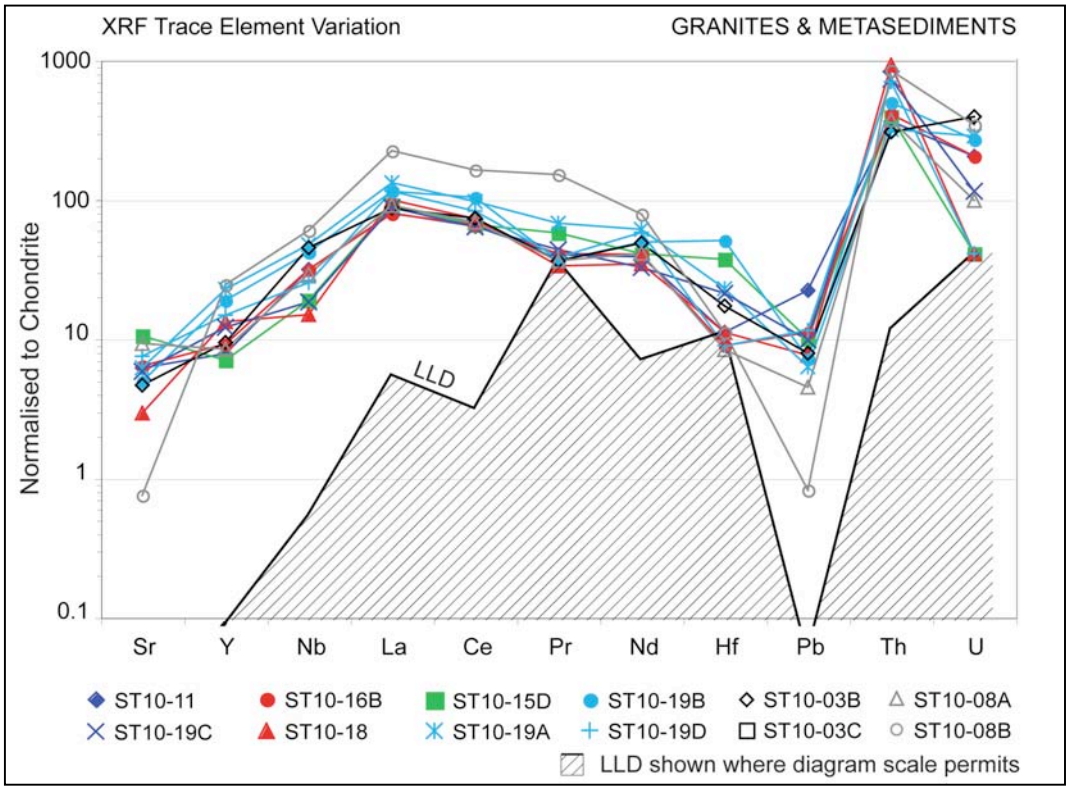

Figure 7.6 XRF Trace Element Variation (ppm) Diagram: Granite vs. Metasedimentary Samples
LLD shown where diagram scale permits
Metasedimentary samples from Zone 2 (ST10_03) and Zone 4 (ST10_08) (refer Chapter 2).

U values in the eastern granite (ST10_11 & ST10_19C) are 204.9 and 114.8 c.n respectively and the northern granite (ST10_16B & ST10_18) are 204.9 and 40.98 c.n respectively. U concentrations are below LLD (< 40.98 c.n) for samples ST10_15D, ST10_18 and ST10_19C. Contrasting these granites with the mingling zone shows the mingling zone samples have lower concentrations of Sr, Pb and Th, and generally higher values of other trace elements analysed.

Samples show a similar REE pattern, but the hybrid diatexite show some variation from the trend with low U and high Hf. The hybrid diatexite demonstrates values similar to the northern granite ST10_18, but higher Hf and Pr, and lower Th and Y. These samples along with the microgranite from the proposed mingling zone (ST10_19D) show comparatively low U values. Strontium shows some variation, with values ranging from 2.9 (ST10_18) to 10.5 c.n (ST10_15D). The remainder of the samples have values between 4.9 to 7.5 c.n.

Trace element data from metasedimentary units is compared in Figure 7.6. While displaying similar La, Ce, Nd, Y and Nb concentrations, significant variation is shown for other elements, creating a distinctly different curve. Specifically, Th, U and Hf values are considerably lower than the granite samples. No trends can be identified between the low-grade metasedimentary sample from zone 2 and high-grade metasedimentary unit sample but is likely artefact of the limited sample analyses.

7.4 Summary & Interpretation of XRF Whole Rock Chemistry

As demonstrated, the assessment of wt % oxides (SiO_2, TiO_2, Al_2O_3, MnO, MgO, CaO, K_2O, Na_2O and P_2O_5) shows minor grouping of results according to sample field occurrence. Samples ST10_11 and ST10_19C (eastern granite), ST10_16B (northern granite), and ST10_19D (mingling zone microgranite) have generally similar bulk composition.

Quartz-diorite samples from the mingle zone (ST10_19A & B) have similar outlying values in the majority of bivariate plots. In general, they have appreciably higher MnO, MgO, Fe_2O_3 reflecting their composition including mafic minerals. Higher P_2O_5 is likely a result of the high modal abundance of apatite noted during petrography. These results provide evidence in favour of a bi-modal mingling zone associated with the eastern granite, and may provide further research objectives regarding its formation.

The hybrid diatexite (ST10_15D) shows distinctive high SiO_2 (84 wt%) with generally lower alkalis (Na and K) and elements found in mafic minerals (Ca, Al, Mg and Fe). The bulk composition reflects the felsic nature of this sample and contamination and/or assimilation of country rock.

Northern granite sample ST10_18 can be distinguished by high SiO_2 and low MnO, MgO, Fe_2O_3. Bulk composition of this sample is most similar to the hybrid diatexite (ST10_15D) than other samples. However, strontium displays some variation. The hybrid diatexite and northern granite represent the highest and lowest strontium values (respectively) bracketing a main sample population.

Analysis of bulk rock composition resulted in no significant distinction between the northern and eastern granites at Mt Stafford. Geochemically and petrologically these samples are very similar. Although this may be a result of the limited size of the sample population, the two granites cannot be clearly distinguished based on their major or trace element compositions alone.

8. LAM-ICP-MS U-Pb ZIRCON GEOCHRONOLOGY & TRACE ELEMENT ANALYSIS

8.1 INTRODUCTION

U-Pb ages of zircon typically date igneous or peak metamorphic conditions at the time of their formation, therefore offering a means to determine age relationships, magmatic and metamorphic episodes and investigate inheritance. Trace elements may be used to further distinguish zircon populations. 240 individual zircon grains from four samples were imaged, and analysed by electron microprobe (EMP) for reference HfO_2 values used in the quantification of trace element data.

A range of rejection criteria were developed and tested to derive an accepted U-Pb age for each sample. Steps for assessing rejection criteria are divided into three broad categories:

1. Rejection based on individual grain characteristics,
2. Rejection based on trace element patterns and groups, and
3. Rejection based on detrital inheritance.

Individual grain characteristics include; the amount of common-Pb, discordance (%), $^{207}Pb/^{206}Pb$ age and core/rim location. This chapter will investigate the U-Pb age characteristics of the granite samples, with a view to assessing the extent of zircon inheritance and its influence on age calculations.

8.2 ZIRCON MORPHOLOGY

Zircon grains were imaged by cathodoluminescence (CL) techniques. The colour of each grain was noted as they were picked and mounted, with the morphology of grain shapes assessed during imaging. The dark colour of the individual zircon grains resulted in a generally low/dark CL response. The CL images show varied morphological types, a broad range of internal textures and overgrowths of different thicknesses.

8.2.1 EASTERN GRANITE

Zircon selected from sample ST10_11 are predominantly clear pink-brown, euhedral grains displaying double terminations (60-70%). In general, the grains range in size from ~90μm to ~370μm long, averaging 200μm (summarised in Table 8.1). It is noted that a 355μm sieve was used to concentrate the grains, therefore biasing the grain size population. The presence of zircon grains larger than 355μm cannot be stated with certainty.

Table 8.1 Zircon Grain Size (μm) Summary from CL Imaging

Grain sizes are rounded to the nearest 5μm. Error shown is estimated measurement error.

Summary of Zircon Grain Size (μm)				
Number of Grains (n = 60)	**ST10_11**	**ST10_16B**	**ST10_18**	**ST10_19C**
Average (Length)	200 ±5μm	225 ±5μm	175 ±5μm	215 ±5μm
Smallest (Length)	90 ±5μm	115 ±5μm	95 ±5μm	135 ±5μm
Largest (Length)	370 ±5μm	355 ±5μm	285 ±5μm	315 ±5μm

Grains are elongate and/or tabular in morphology. They generally have CL-bright zones surrounding a darker core, while some grains have CL-bright cores with CL-dark outer rims. Some grains show undulating wavy grain edges and several grains picked are fragments. Figure 8.1 shows several representative grains used in this study. Complete grain size data are presented in Appendix E-2.

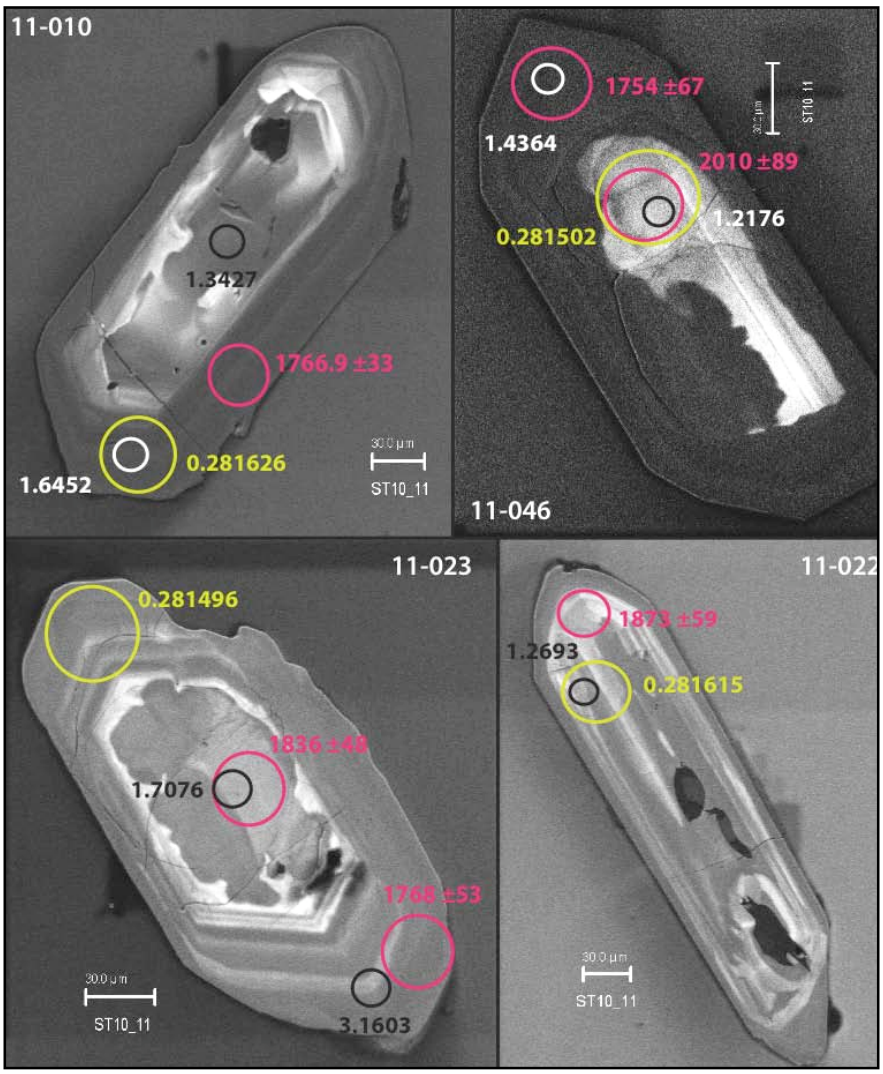

Figure 8.1 CL Zircon Images: Eastern Granite (ST10_11)

Scale bars are 30 μm. Spot analyses circled: HfO_2 wt% (EMP) in black/white, $^{207}Pb/^{206}Pb$ Age Ma (LAM-ICP-MS) in pink $^{176}Hf/^{177}Hf$ (MC-LAM-ICP-MS) in yellow

Sample ST10_19C is dominated by clear honey-brown, euhedral, elongate to prismatic grains. Minor subpopulations noted include a clear pink-brown, euhedral to rounded-stubby group (~10%), a clear orange-brown, prismatic, elongate population (~10%) and several clear, rounded, elongate grains. Grains picked range in size from ~135μm to ~315μm, with an average of 215μm (Table 8.1). Many grains have thick, dark unzoned overgrowths around bright cores, which may indicate alteration (metamictisation). Others grains have bright oscillatory zones. Representative CL images are presented in Figure 8.2.

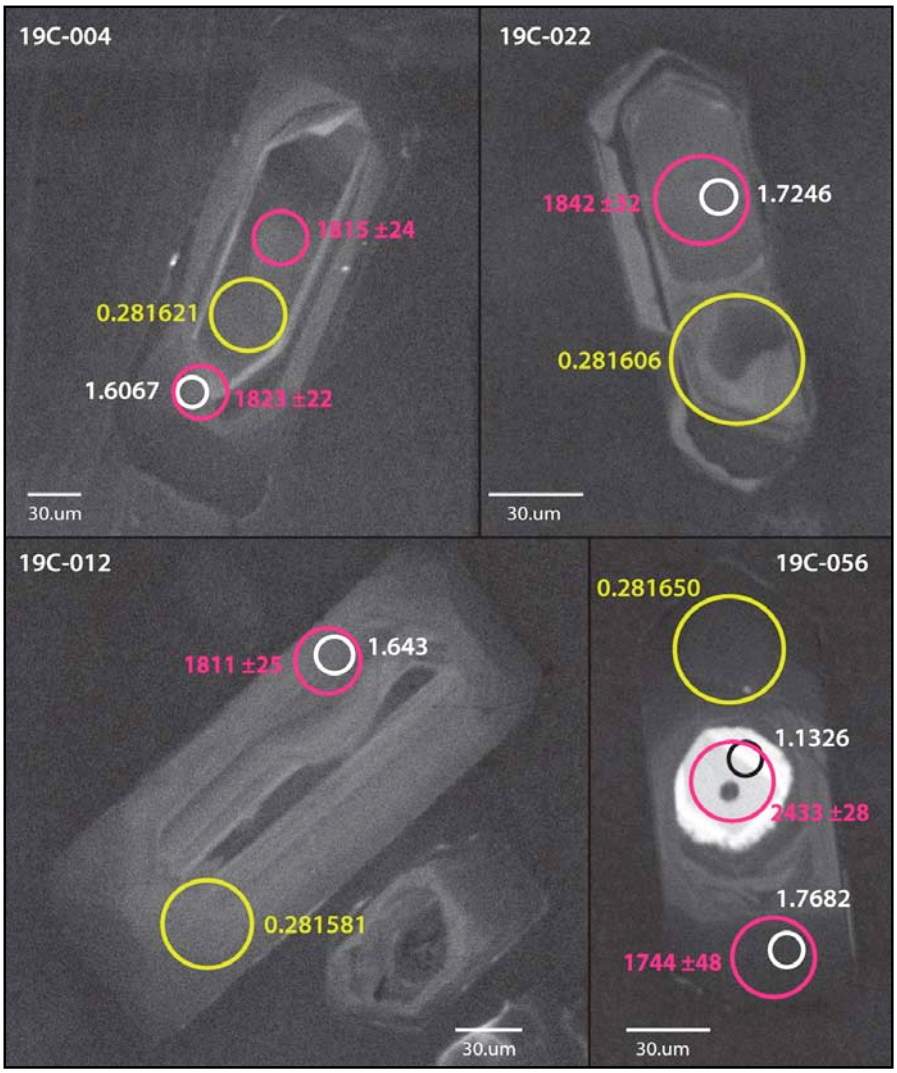

Figure 8.2 CL Zircon Images: Eastern Granite (ST10_19C)

Scale bars are 30 μm. Image obtained by EMP with CL-probe. Spot analyses circled: HfO_2 wt% (EMP) in black/white, $^{207}Pb/^{206}Pb$ Age Ma (LAM-ICP-MS) in pink $^{176}Hf/^{177}Hf$ (MC-LAM-ICP-MS) in yellow

8.2.2 NORTHERN GRANITE

In sample ST10_16B, the main population (~70-80%) is represented by clear honey-brown, anhedral to euhedral prismatic grains. A subpopulation of opaque pink-red stubby, euhedral grains is also present (~20%). Several clear/white grains picked were monazite. Overall, grains average 225μm in length, ranging from ~115μm to ~355μm (Table 8.1). A number of grains picked are anhedral to subhedral, with fine pervasive fractures radiating about bright cores, and are likely metamict grains (Hanchar & Miller, 1993). Most grains show concentric oscillatory zoning around generally euhedral cores. Figure 8.3 shows representative grains picked for analysis.

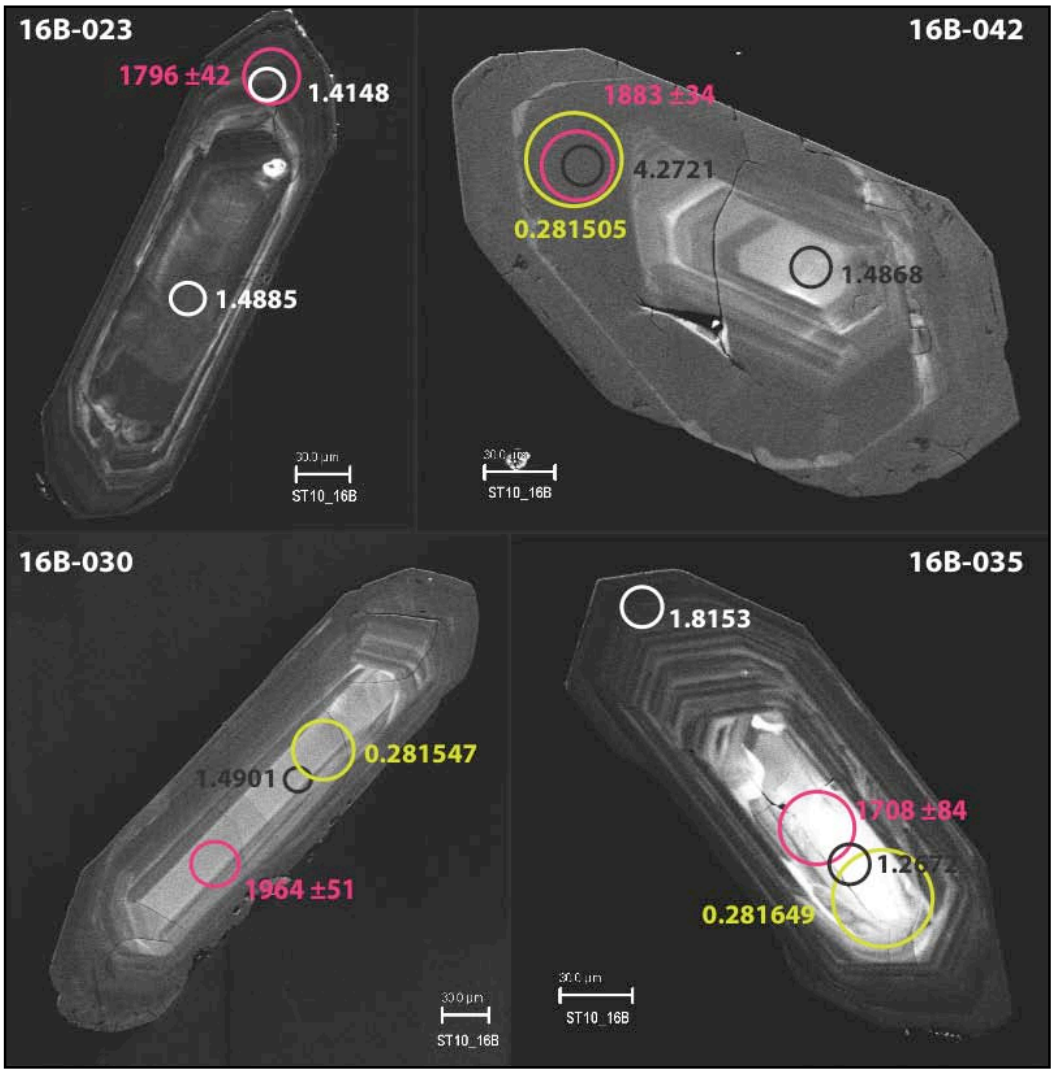

Figure 8.3 CL Zircon Images: Northern Granite (ST10_16B)

Scale bars are 30 μm. Spot analyses circled: HfO_2 wt% (EMP) in black/white, $^{207}Pb/^{206}Pb$ Age Ma (LAM-ICP-MS) in pink $^{176}Hf/^{177}Hf$ (MC-LAM-ICP-MS) in yellow

Sample ST10_18 has a main population of clear honey-brown, irregular, anhedral crystals with embayed boundaries (~75-80%). This population varies in morphology from stubby or equant to elongate, and anhedral to eudedral. A large number of grains are pervasively fractured and feature large inclusions with both bright and dark CL responses. Overall, grains show irregular to oscillatory-zoned cores surrounded by CL-dark, unzoned or poorly-zoned overgrowths, reflecting the alteration of many grains. Grain sizes range from ~95μm to ~285μm and average of 175μm across the population. Representative grain images are shown in Figure 8.4.

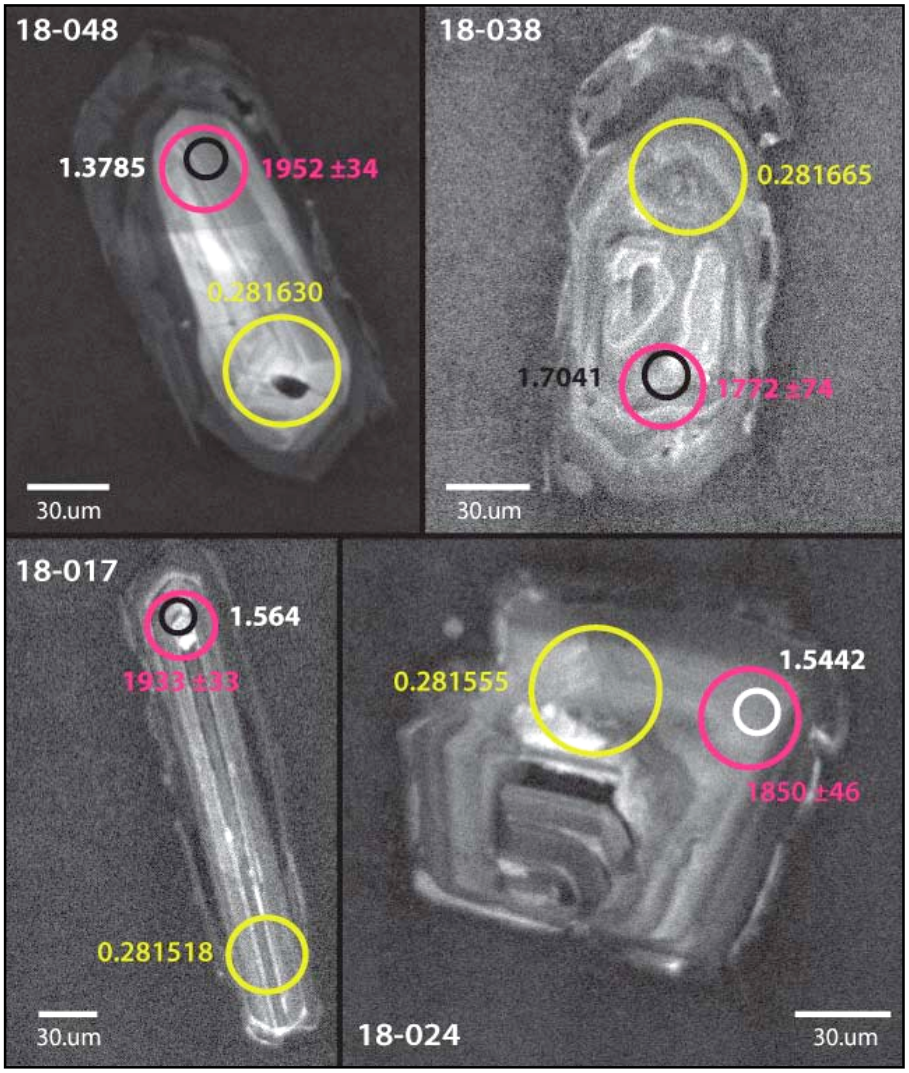

Figure 8.4 CL Zircon Images: Northern Granite (ST10_18)
Scale bars are 30 μm. Image obtained by EMP with CL-probe. Spot analyses circled: HfO_2 wt% (EMP) in black/white, $^{207}Pb/^{206}Pb$ Age Ma (LAM-ICP-MS) in pink $^{176}Hf/^{177}Hf$ (MC-LAM-ICP-MS) in yellow

8.3 SUMMARY OF ZIRCON MORPHOLOGY

CL features of the four samples show a range of internal zoning patterns and core-rim relationships that appear consistent across all samples. The main populations of clear honey-brown, orange-brown and pink-brown grains had a generally CL-dark response. The majority of grains show brighter zones and/or cores within a generally CL-dark grain. No correlation was identified between grain size, morphology or oscillatory zoning pattern with sample location.

All samples include fractured and fragmented grains. Grains from ST10_18 have a greater proportion of open fractures than other samples. Fractured grains may reflect deformation and/or alteration experienced by this sample following crystallisation. This interpretation also draws upon observations made in the field and from petrography (Chapter 5).

Some grains do not contain inherited cores, whereas other grains have large, sometimes idiomorphic or euhedral cores. Three samples generally showed a greater number of grains with unzoned cores overgrown by oscillatory zoned rims. Sample ST10_18 showed a larger proportion of oscillatory-zoned cores with poorly-zoned, CL-dark overgrowths.

A large proportion of grains display oscillatory zoning. If zircon crystallises over a period of time, compositional zoning of individual grains record changes in the chemical environment during growth (Belousova *et al*., 2006a). In many grains, cores are overgrown by euhedral oscillatory zones and rims, interpreted as magmatic. Granitoid magmas commonly contain older inherited zircon, exhibiting rounded cores overgrown by zoned euhedral magmatic zircon (Belousova *et al*., 2006a). Brighter zones may be enriched in U, Th and REE (Fowler *et al*., 2002 cited Belousova *et al*., 2006a), and this relationship will be further investigated during trace element analysis.

8.4 ZIRCON EMP GEOCHEMISTRY

EMP major element oxide data was collected from zircon to provide reference HfO_2 data for quantification of LAM-ICP-MS trace element analysis and to provide comparison between the eastern and northern granites. During initial analysis (ST10_11 and ST10_16B), zircon trace element data was collected and will be briefly discussed. Data are presented in Appendix E-3.

Variation diagrams for oxides of Hf and Y were constructed for all four granite samples, with two samples analysed for Y_2O_3, SmO, Dy_2O_3, ThO_2, U_2O_3 and PbO (Figure 8.5). Values for trace oxides of SmO, Dy_2O_3, ThO_2 and PbO are generally below lower limit of detection (LLD) and will not be discussed.

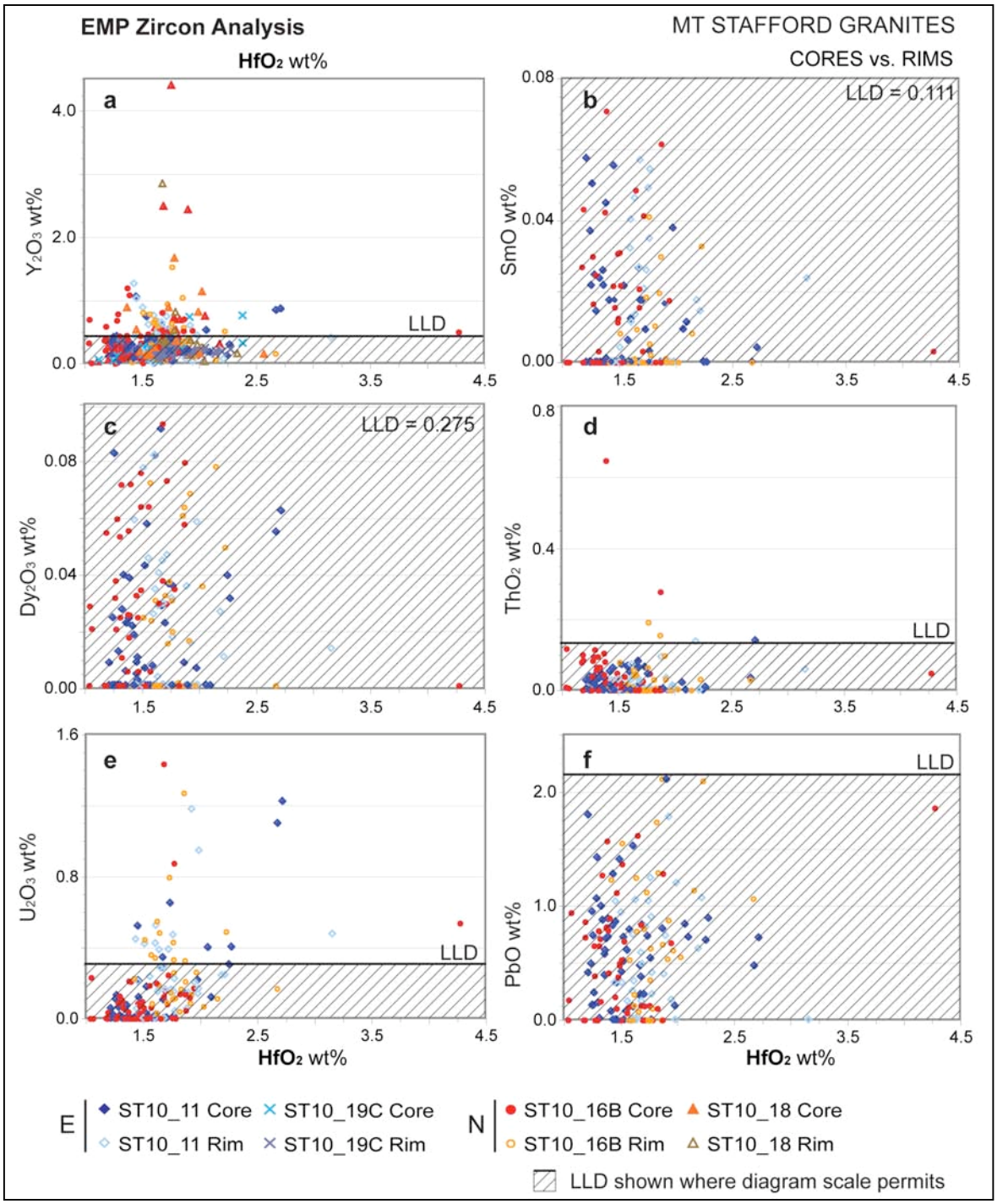

Figure 8.5 EMP Zircon Trace Element Bivariate Diagrams: Cores vs. Rims

HfO2 vs. **a**) Y_2O_3, **b**) SmO, **c**) Dy_2O_3, **d**) ThO_2, **e**) U_2O_3 & **f**) PbO. Outer core & core analyses are combined. LLD shown where diagram scale permits

HfO_2 values for the eastern granite range from 1.1wt% (ST10_19C) to 3.2wt% (ST10_11), averaging 1.7wt% across both samples (Figure 8.5). HfO_2 values for the northern granite range from 1.0wt% (ST10_16B) to 4.3wt% (ST10_16B), averaging 1.7wt% for both ST10_16B and ST10_18. All HfO_2 values are well above LLD (> 0.002wt%). Values of Y_2O_3 range from below LLD (< 0.4wt%) to 1.5wt%, with U_2O_3 values similar between samples, from below LLD (< 0.3wt%) to 1.4wt%.

From comparison of HfO_2, Y_2O_3 and U_2O_3 there are no discernable trends between core and rims analyses as shown (Figure 8.5). Grains display a similar range of values between samples. The higher values of Y_2O_3 and U_2O_3 may reflect alteration, but a lack of correlation between the oxide total and Y_2O_3 argues against this.

8.5 Discussion of EMP Zircon Geochemistry

EMP zircon analyses presented indicate HfO_2 shows a similar range of values in all samples. The locations probed indicate grains are of similar composition, and no distinct sub-populations between samples, or magmatic and inherited grains are apparent. Higher Y_2O_3 may reflect alteration of the grains noted during CL imaging. Zircon REE will be further investigated.

8.6 ZIRCON U-Pb GEOCHRONOLOGY

Individual $^{207}Pb/^{206}Pb$ zircon ages obtained using the LAM-ICP-MS. Initial zircon ages were examined to correct for the addition of common-Pb, $^{207}Pb/^{206}Pb$ ages, discordance and relative uncertainties were examined to isolate potential outliers due to inheritance, and provide criteria for rejection of individual grains relevant to determining igneous crystallisation age. Rejection of analyses was based on a number of grain characteristics to generate specific criteria as follows (in order of exclusion):

1. Analyses containing $\geq \pm 2\%$ common-Pb,
2. Analyses with $\geq \pm 32\%$ Discordance,
3. Analyses with $^{207}Pb/^{206}Pb$ age $\geq$ 2150Ma (interpreted as older inherited material),
4. Analyses with $\geq \pm 15\%$ Discordance,
5. Analyses with $\geq \pm 10\%$ Discordance, and
6. Analyses with $\geq \pm 5\%$ Discordance.

Concordia diagrams were constructed to assess discordant age results. Cumulative probability charts define age population peaks and the number of grains within each age range. $^{207}Pb/^{206}Pb$ ages were used to define weighted average ages. Grains were progressively excluded using the above criteria to obtain a low mean square weighted deviation (MSWD) approaching 1.0 and a high probability $\geq$ 0.05 (reflecting an age estimate at 95% confidence).

The first two rejection steps are specified by the Terranechron® spreadsheets used during age calculations. Comparison between calculated $^{207}Pb/^{206}Pb$ age after rejection of $\geq \pm 15\%$ discordance and rejection of $\geq \pm 5\%$ discordance showed an increase in MSWD, average uncertainty and probability of fit, as the number of grains analysed (*n*) decreases. Following rejection of grains based on discordance, grains were assessed for statistical weighting on the age calculation (weighted residual). Grains with the highest weighted residual were excluded, and will be described in detail below. This step was reversed prior to further rejections based on discordance. Based on assessment of the age data, those grains used for $^{207}Pb/^{206}Pb$ age calculation shall be here-in collectively referred to as U-Pb grains, and will be discussed below.

8.6.1 Eastern Granite Geochronology

Analysis of zircon grains from sample ST10_11 shows individual $^{207}Pb/^{206}Pb$ ages ranging between 1716 ±77Ma to 2547 ±77Ma (Table 8.2). The Cumulative Probability diagram shows a main population peak at ca. 1815 ±19Ma, with an older sub-population creating a tail on the main peak (Figure 8.6a). An older population peak is also evident ca. 2491 ±53.

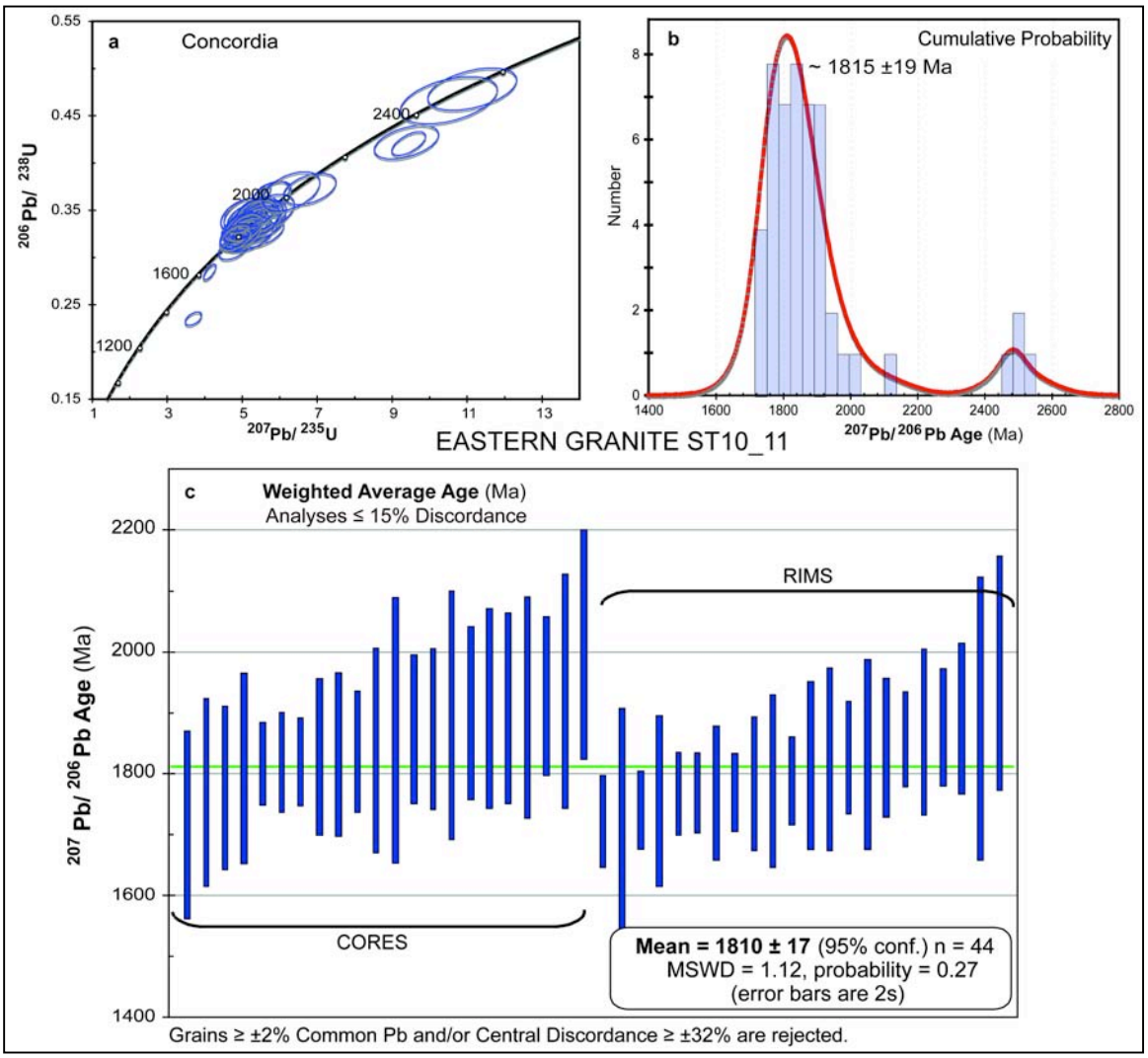

Figure 8.6 Eastern Granite (ST10_11) $^{207}Pb/^{206}Pb$ Age, Concordia & Probability
a) Concordia, **b**) Probability Histogram, **c**) Weighted Average Age (Ma)
Plotted from TerraneChron® spreadsheets using *Isoplot EX3.0* Excel Plugin (Ludwig, 2003)

Grains have a high level of concordance (Figure 8.6b) and low incidence of common-Pb. Of the 50 grains analysed, none were rejected with common-Pb ≥ ±2% or discordance ≥ ±32%. Four grains older than 2150Ma were excluded as inherited. As criteria were tightened, two grains were excluded with ≥ ±15% discordance, leaving $n = 44$ grains suitable for age calculation. Further reducing discordance criteria to ≥ ±10% and ≥ ±5% resulted in increased uncertainty (1s.d) and MSWD. The pooled age of cores and rims shown in Figure 8.6c is 1810 ±17Ma.

Assessment of core and outer core $^{207}Pb/^{206}Pb$ ages show similar results across the domains (1850 ±48Ma and 1846 ±43Ma respectively), so analyses were combined for calculation of core ages (Figure 8.7a). Weighted average age of the cores analysed is 1841 ±26Ma, with an MSWD of 0.73 and probability of 0.80 (Table 8.3).

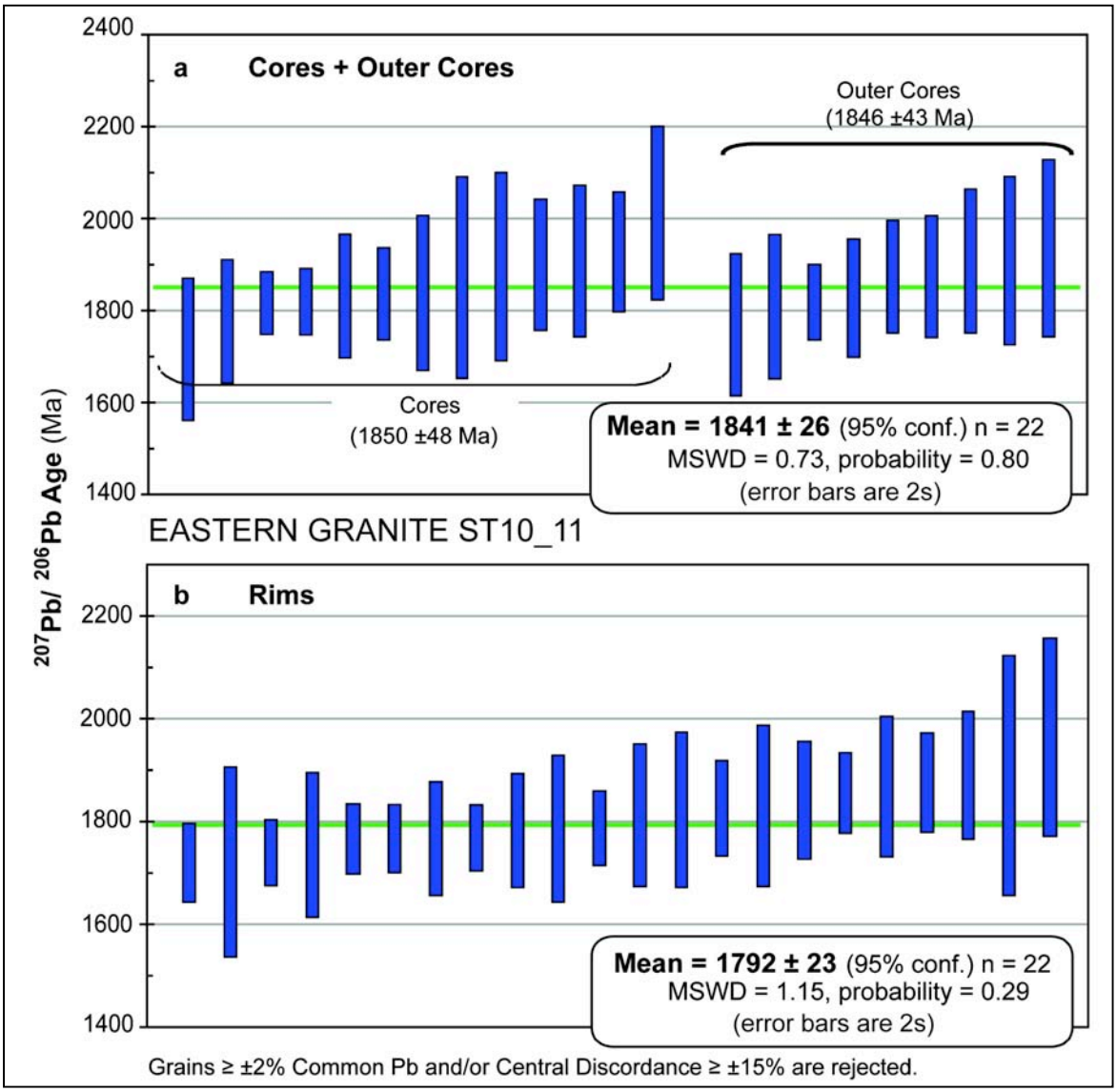

Figure 8.7 Eastern Granite (ST10_11) $^{207}Pb/^{206}Pb$ Age: Core & Rim Analysis
a) core + outer core analyses. **b**) rim analyses
Plotted from TerraneChron® spreadsheets using *Isoplot EX3.0* Excel Plugin (Ludwig, 2003)

Analyses of rims provide an age of 1792 ±23Ma, with an MSWD of 1.15 and probability of 0.29 (Figure 8.7b). While uncertainties are generally high (±23 to ±26), results of core analyses appear to indicate rims 10Ma to 98Ma younger than cores. The results of core and rim analyses are summarised in Table 8.3.

Table 8.3 Eastern Granite ST10_11 $^{207}Pb/^{206}Pb$ Weighted Average Age (Ma): Core & Rim Analyses

U-Pb Zircon Weighted Average Age (Ma) of Cores & Rims								
Rejection Criteria	***n***	**Weighted Average Age** ($^{207}Pb/^{206}Pb$) Ma	**MSWD** %	**Prob. of Fit**	***n***	**Weighted Average Age** ($^{207}Pb/^{206}Pb$) Ma	**MSWD** %	**Prob. of Fit**
	CORES				**RIMS**			
ST10_11 Eastern Granite								
All Grains ≤ 2150Ma	24	1850 ±29	1.20	0.20	22	1792 23	1.15	0.29
Common Pb ≥ ±2.0%								
Discordance ≥ ±32%								
Discordance ≥ ±15%	22	1841 ±26	0.73	0.80	22	1792 ±23	1.15	0.29
Discordance ≥ ±10%	21	1845 ±26	0.63	0.89	19	1796 ±27	1.30	0.20
Discordance ≥ ±5%	17	1859 ±33	0.67	0.83	11	1815 ±31	0.66	0.76

Weighted Residual calculation (to identify statistical outliers) reversed prior to further rejections. Shown where positively impacted.

n Number of grains used during age calculation

'Blanks' indicate no grains meeting that criteria were excluded

Data in red indicate ages to be used in this study

Quoted uncertainties are ±1 standard deviation (1σ)

Several core-rim grain pairs were analysed to investigate core-rim relationships within individual grains. Results complement the weighted averages, indicating older cores are surrounded by younger rims. However, the individual ages do show some overlap or are within error of each other (Table 8.4).

Table 8.4 Eastern Granite ST10_11 $^{207}Pb/^{206}Pb$ Age (Ma): Core-Rim Grain Pairs

$^{207}Pb/^{206}Pb$ Age: Core-Rim Grain Pairs				
Grain No.	**Weighted Average Age** ($^{207}Pb/^{206}Pb$) Ma	**Discordance**	**Weighted Average Age** ($^{207}Pb/^{206}Pb$) Ma	**Discordance**
	CORES		**RIMS**	
ST10_11 Eastern Granite (≤ ±15% Discordance)				
11-020	2129.9 ±75	-4.8	1964.0 ±91	-8.1
11-021	1895.2 ±96	-2.8	1890.3 ±108	-1.3
11-023	1836.1 ±47	1.7	1768.1 ±53	8.0
11-045	1775.5 ±64	1.7	1813.0 ±66	2.5
11-046	2010.5 ±89	0.9	1754.6 ±67	9.1

SAMPLE ST10_19C

ST10_19C shows a spread of $^{207}Pb/^{206}Pb$ ages ranging from 1664 ±70Ma to 2433 ±28Ma (Table 8.5). There is a dominant peak at 1830 ±22Ma (Figure 8.8b). An older sub-population peaks at 1900 ±60Ma and with an influence of younger grains 1700 ±60Ma. An older inherited population peaks at 2352 ±53Ma. The majority of analyses lie on the Concordia (Figure 8.8a) and there is a tight clustering of results. Error bars are smaller overall than for other samples.

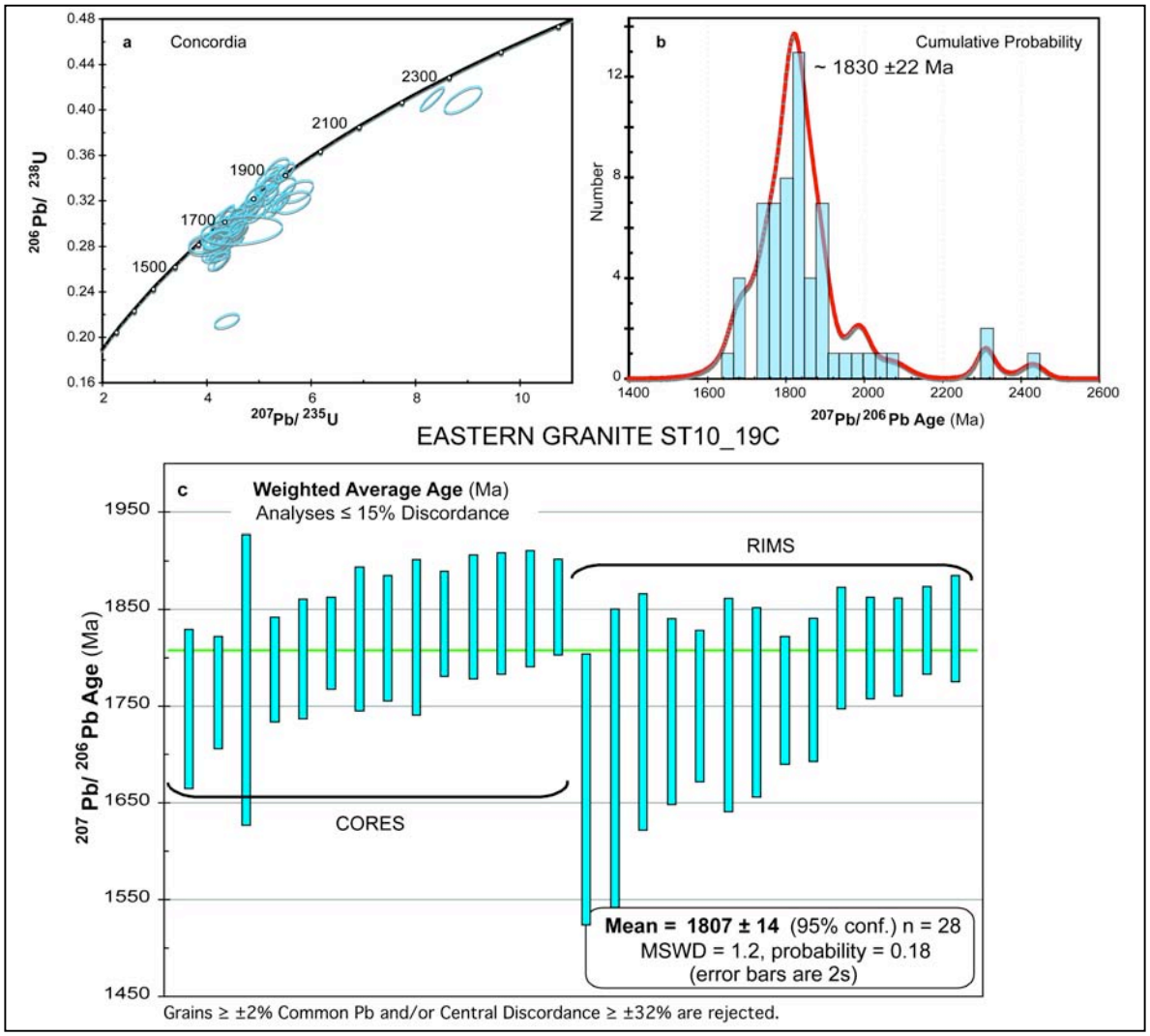

Figure 8.8 Eastern Granite (ST10_19C) ^{207}Pb/^{206}Pb Age, Concordia & Probability
a) Concordia, **b**) Probability Histogram, **c**) Weighted Average Age (Ma)
Plotted from TerraneChron® spreadsheets using *Isoplot EX3.0* Excel Plugin (Ludwig, 2003)

Of a total 60 grains analysed, six grains were rejected with common-Pb ≥ ±2%, and a further two grains ≥ 2150Ma rejected as inherited. Twenty four grains were excluded based on discordance ≥ ±10% and weighted residual ≥ 2.3, leaving $n = 28$ grains used to calculate ^{207}Pb/^{206}Pb age (Table 8.5). Grains excluded with weighted residual ≥ 2.3 are the oldest and youngest grains in the population, so that removing them effectively reduced the spread of ages in the population (refer Table 8.5). The pooled age of all analyses is shown in Figure 8.8c at ca.1807 ±14Ma.

The weighted average age of cores and outer cores were combined (1819 ±17Ma and 1808 ±510Ma respectively) (Figure 8.9a). Uncertainty in the outer cores is extremely high due to the limited number of analyses ($n = 2$). Combining the core and outer core analyses produced an age of 1834 ±16Ma, with MSWD of 0.94 and probability of 0.51 (Table 8.6).

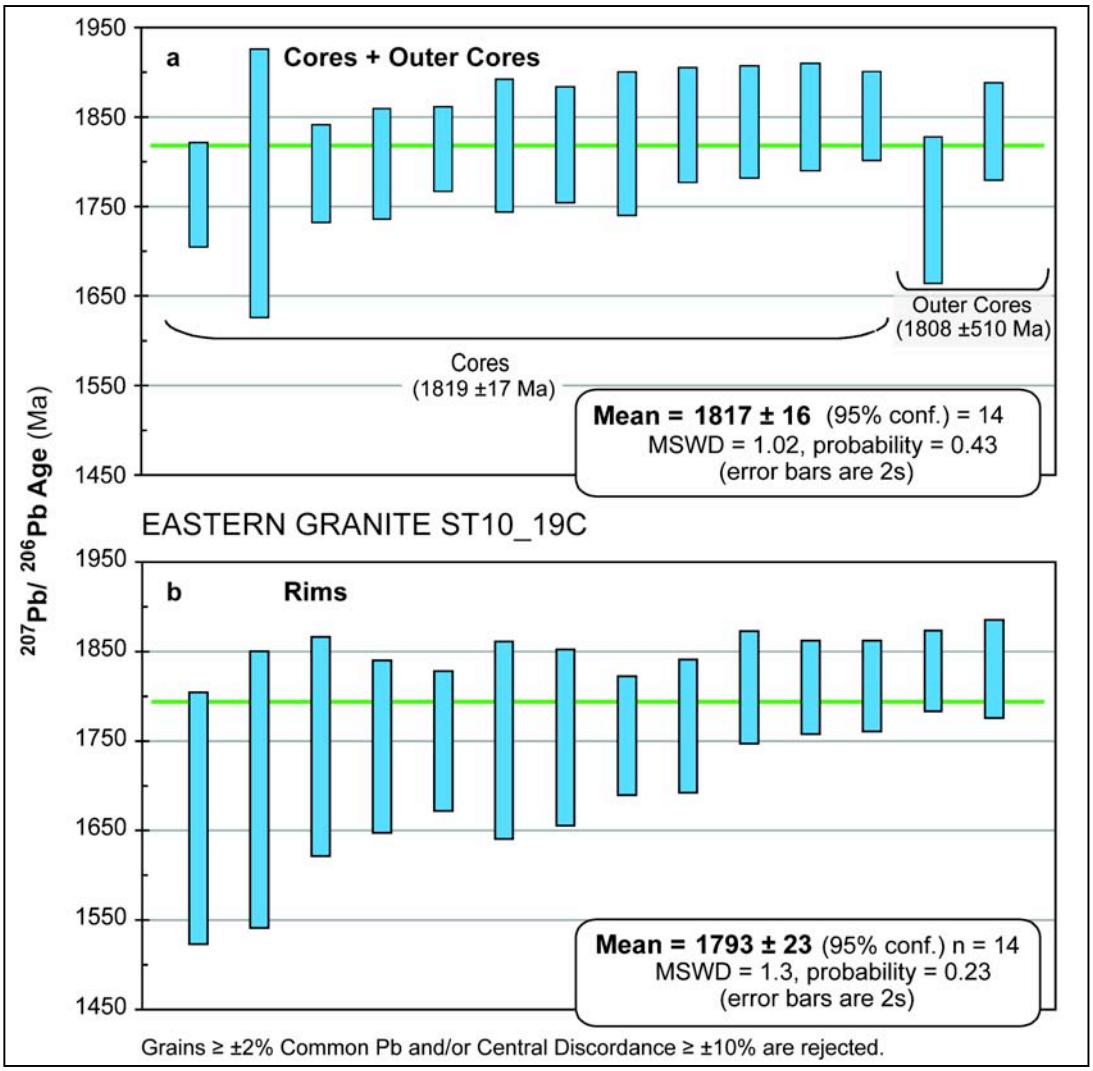

Figure 8.9 Eastern Granite (ST10_19C) $^{207}Pb/^{206}Pb$ Age: Core & Rim Analysis
a) core + outer core analyses. **b**) rim analyses
Plotted from TerraneChron® spreadsheets using *Isoplot EX3.0* Excel Plugin (Ludwig, 2003)

Rim analyses from this sample returned a weighted average age of 1793 ±23Ma, with 1.30 MSWD and 0.23 probability (Figure 8.9b). As for the previous sample, analyses indicate rims 12Ma to 80Ma younger than the cores (Table 8.6). This age is essentially identical to rims analysed in the previous eastern granite sample (refer Table 8.3).

Table 8.6 Eastern Granite ST10_19C $^{207}Pb/^{206}Pb$ Weighted Average Age (Ma): Core & Rim Analyses

U-Pb Zircon Weighted Average Age (Ma) of Cores & Rims								
Rejection Criteria	***n***	**Weighted Average Age** ($^{207}Pb/^{206}Pb$) Ma	**MSWD** %	**Prob. of Fit**	***n***	**Weighted Average Age** ($^{207}Pb/^{206}Pb$) Ma	**MSWD** %	**Prob. of Fit**
	CORES				**RIMS**			
ST10_19C Eastern Granite								
All Grains ≤ 2150Ma	34	1856 ±27	6.40	0.000	23	1801 ±29	4.70	0.000
Common Pb ≥ ±2.0%	31	1856 ±29	6.80	0.000	21	1790 ±29	4.10	0.000
Discordance ≥ ±32%								
Discordance ≥ ±15%	26	1856 ±32	7.00	0.000	21	1790 ±29	4.10	0.000
Discordance ≥ ±10%	19	1832 ±24	2.60	0.000	17	1775 ±35	4.30	0.000
weighted residual ≥2.3	14	1834 ±16	0.94	0.510	14	1793 ±23	1.30	0.230
Discordance ≥ ±5%	12	1847 ±22	1.40	0.140	8	1759 ±57	5.70	0.000

Weighted Residual calculation (to identify statistical outliers) reversed prior to further rejections. Shown where positively impacted.

n Number of grains used during age calculation ‘Blanks’ indicate no grains meeting that criteria were excluded

Data in red indicate ages to be used in this study Quoted uncertainties are ±1 standard deviation (1σ)

Of the six individual core-rim grain pairs analysed, two pairs passed through the rejection criteria. As for the previous sample, ages are generally within error or excluded due to inheritance or discordance, but do indicate younger rim ages (Table 8.7).

Table 8.7 Eastern Granite ST10_19C $^{207}Pb/^{206}Pb$ Age (Ma): Core-Rim Grain Pairs

Weighted Average Age (Ma): Core-Rim Grain Pairs				
Grain No.	**Weighted Average Age** ($^{207}Pb/^{206}Pb$) Ma	**Central Discordance**	**Weighted Average Age** ($^{207}Pb/^{206}Pb$) Ma	**Central Discordance**
	CORES		**RIMS**	
ST10_19C Eastern Granite (Mingling Zone) (≤ ±10% Discordance & ≤ 2.3 Weighted Residual)				
~~19C-004~~	1815.1 ±24	-7.0	1823.2 ±22	-12.2
19C-006	1764.2 ±29	-8.1	1767.0 ±37	-7.2
19C-014	1850.8 ±30	2.7	1810 ±26	-2.2
~~19C-009~~	1967.9 ±30	-10.5	1750 ±39	-7.2
~~19C-041~~	2000.6 ±23	-12.2	1820.1 ±24	-12.1
~~19C-056~~	2433.6 ±28	-10.8	1744 ±48	-8.0

~~Strikethrough~~ indicates grain excluded from age calculation (≥ 2% Com-Pb, ≥ 2150Ma or Discordance). Refer Table 8.6 for details.

U-Pb analyses from both eastern granite samples (ST10_11 and ST10_19C) were pooled to generate a combined age. Following the initial age calculation, individual analyses were examined for statistical weighting, calculating a weighted residual. Analyses were rejected consecutively with weighted residual ≥ 2.3, ≥ 2.0 and ≥ 1.5. The results are presented in Table 8.8. Exclusion of further grains based on this criteria had minimal effect on calculated age.

The $^{207}Pb/^{206}Pb$ age of the eastern granite is therefore represented by rims at 1792 ±15Ma based on a population of n = 36 grains, with an MSWD of 1.16 and probability of 0.24 (Figure 8.10b). Older cores, interpreted as inherited, are dated at 1828 ±14Ma, with an MSWD of 0.77 and probability of 0.82, using a population of n = 35 grains (Figure 8.10a).

Table 8.8 Eastern Granite Combined $^{207}Pb/^{206}Pb$ Weighted Average Age (Ma)

U-Pb Zircon Weighted Average Age (Ma) of Cores & Rims: Eastern Granite								
Rejection Criteria	***n***	**Weighted Average Age** ($^{207}Pb/^{206}Pb$) Ma	**MSWD** %	**Prob. of Fit**	***n***	**Weighted Average Age** ($^{207}Pb/^{206}Pb$) Ma	**MSWD** %	**Prob. of Fit**
	CORES				**RIMS**			
Eastern Granite (ST10_11 + ST10_19C)								
All U-Pb Grains	36	1824 ±14	0.88	0.670	36	1792 ±15	1.16	0.240
≥ 2.0 weighted residual	35	1828 ±14	0.77	0.820				
≥ 1.5 weighted residual	32	1828 ±15	0.53	0.990	28	1788 ±16	0.62	0.940

Ages are calculated using only those previously identified U-Pb grains with ≤ ±2% com-Pb & ≤ 10-15% discordance.

n Number of grains used during age calculation

'Blanks' indicate no grains meeting that criteria were excluded

Data in red indicate ages to be used in this study

Quoted uncertainties are ±1 standard deviation (1σ)

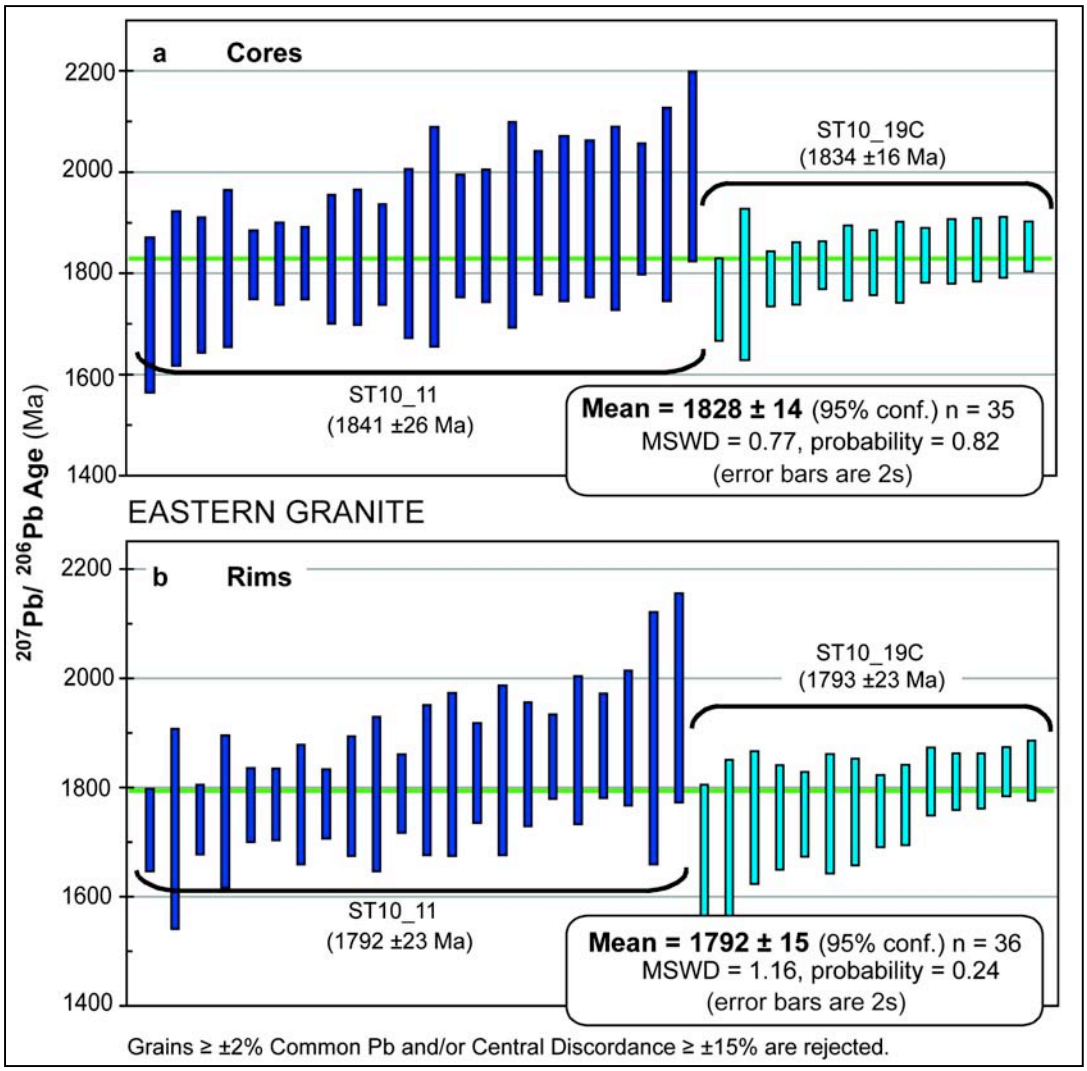

Figure 8.10 Eastern Granite Combined $^{207}Pb/^{206}Pb$ Age: Core & Rim

a) core + outer core analyses. **b**) rim analyses

Plotted from TerraneChron® spreadsheets using *Isoplot EX3.0* Excel Plugin (Ludwig, 2003)

U-Pb grains only (≤ ±2% common-Pb, ≤ 2150Ma and ≤ ±15% (ST10_11) and ≤ ±10% (ST10_19C) discordance). Error bars are 2σ.

8.6.2 Northern Granite Geochronology

Sample ST10_16B

Sample ST10_16B contained a large number of irregular grains with fine pervasive fractures. Areas with open fractures were generally avoided during analysis. This sample has a spread of $^{207}Pb/^{206}Pb$ ages ranging from 1656 ±114Ma to 2842 ±32Ma. Individual grain ages are presented in Table 8.9. One grain returned an age of 338 ±813Ma and was instantly rejected. The Cumulative Probability diagram (Figure 8.11b) shows a population peak 1882 ±24Ma, with older populations indicated by several older grains. Overall, error bars for this sample are generally smaller than both eastern granite samples.

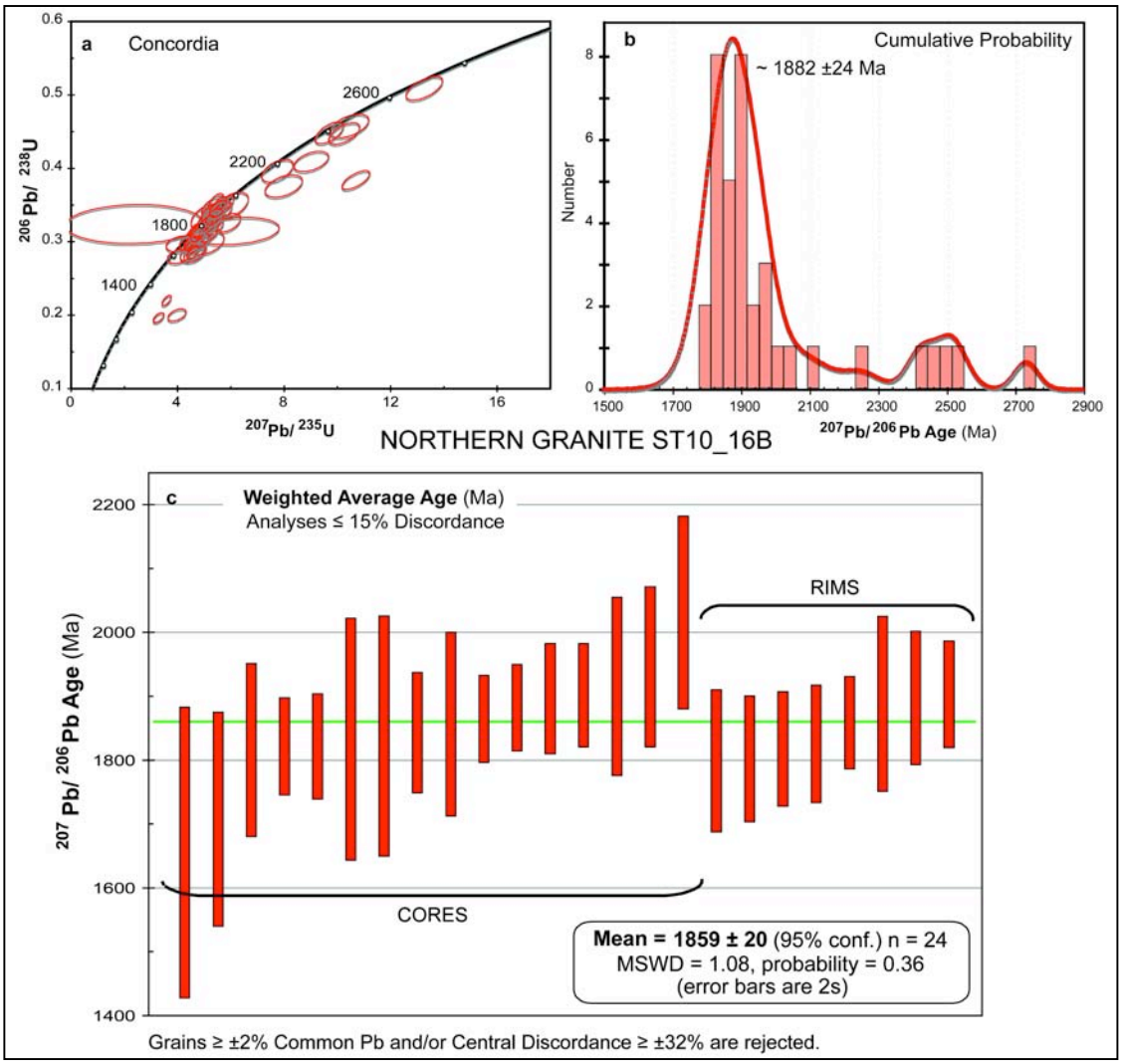

Figure 8.11 Northern Granite (ST10_16B) $^{207}Pb/^{206}Pb$ Age, Concordia & Probability
a) Concordia, **b**) Probability Histogram, **c**) Weighted Average Age (Ma)
Plotted from TerraneChron® spreadsheets using *Isoplot EX3.0* Excel Plugin (Ludwig, 2003)

Analyses produced a moderate to high level of discordance (Figure 8.11a). A total of 49 grains were analysed. 11 grains were rejected with common-Pb ≥ ±2% and discordance ≥ ±32%, with six inherited grains ≥ 2150Ma also excluded. A further eight grains were rejected with discordance ≥ ±10%, leaving a population of n = 24 suitable U-Pb grains (Table 8.9). The pooled age of core and rim analyses is presented in Figure 8.11c at ca. 1859 ±20Ma.

Core, outer-core and rim ages were assessed, using U-Pb grains with ≤ ±2% common-Pb and ≤ ±10% central discordance (Figure 8.12a). Combined core and outer core analyses produced a $^{207}Pb/^{206}Pb$ age of 1864 ±31Ma, calculating an MSWD of 1.30 and probability of 0.22, using n = 16 grains (Table 8.10). This included inner cores at 1857 ±45Ma (n = 11) and outer cores 1876 ±40Ma (n = 5).

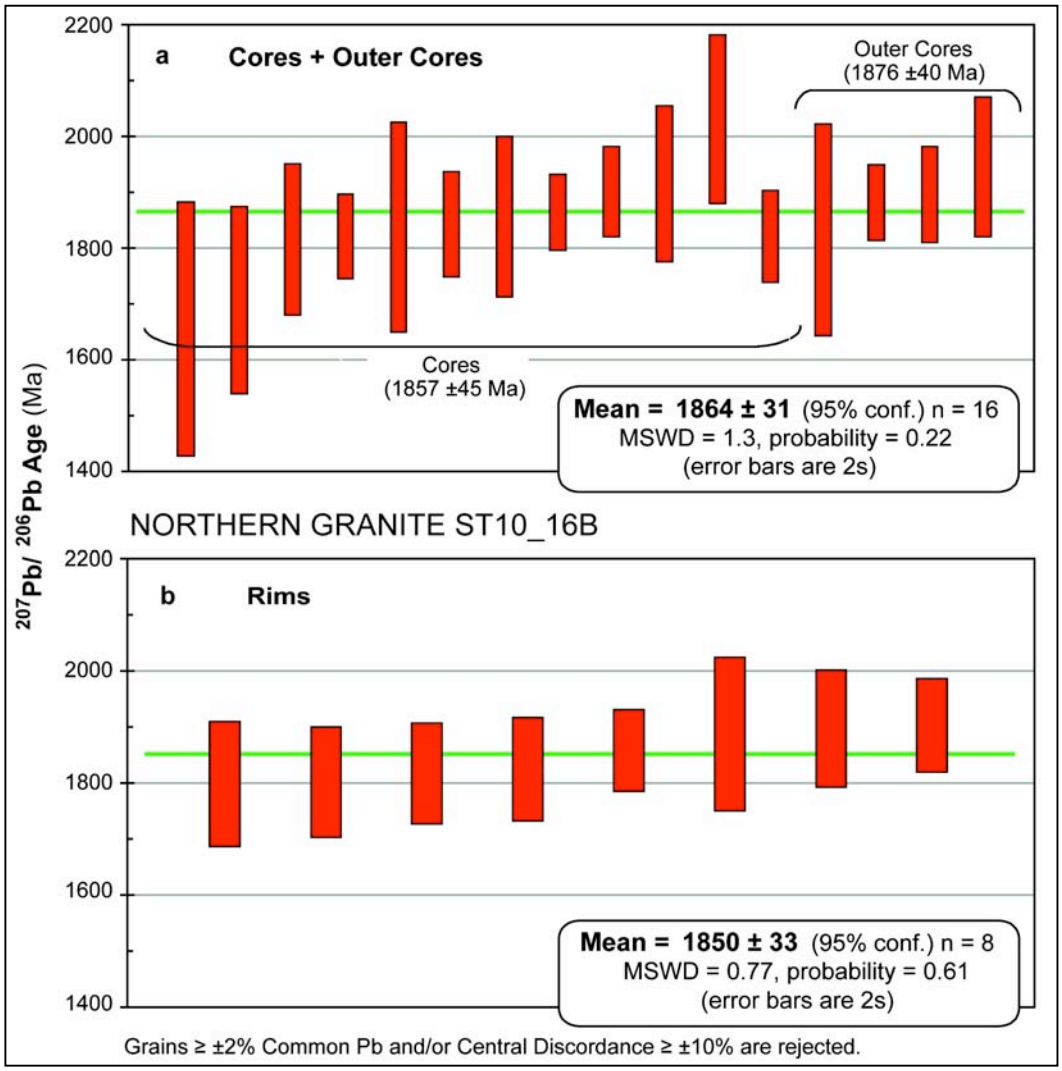

Figure 8.12 Northern Granite (ST10_16B) $^{207}Pb/^{206}Pb$ Age: Core & Rim Analysis
a) core + outer core analyses. **b**) rim analyses
Plotted from TerraneChron® spreadsheets using *Isoplot EX3.0* Excel Plugin (Ludwig, 2003)

Table 8.10 Northern Granite ST10_16B $^{207}Pb/^{206}Pb$ Age (Ma): Core & Rim Analyses

U-Pb Zircon Weighted Average Age (Ma) of Cores & Rims								
Rejection Criteria	***n***	**Weighted Average Age** ($^{207}Pb/^{206}Pb$) Ma	**MSWD** %	**Prob. of Fit**	***n***	**Weighted Average Age** ($^{207}Pb/^{206}Pb$) Ma	**MSWD** %	**Prob. of Fit**
	CORES				**RIMS**			
ST10_16B Northern Granite								
All Grains ≤ 2150Ma	27	1900 ±27	1.90	0.003	11	1848 ±29	0.96	0.480
Common Pb ≥ ±2.0%	24	1901 ±29	2.10	0.001	10	1855 ±31	0.88	0.540
Discordance ≥ ±32%	22	1894 ±31	2.1	0.002				
Discordance ≥ ±15%	19	1885 ±30	1.7	0.04	9	1851 ±32	0.68	0.71
Discordance ≥ ±10%	16	1864 ±31	1.30	0.220	8	1850 ±33	0.77	0.610
Discordance ≥ ±5%	10	1859 ±34	0.74	0.670	7	1845 ±34	0.75	0.610

Weighted Residual calculation (to identify statistical outliers) reversed prior to further rejections. Shown where positively impacted.
n Number of grains used during age calculation
'Blanks' indicate no grains meeting that criteria were excluded
Data in red indicate ages to be used in this study
Quoted uncertainties are ±1 standard deviation (1σ)

Analysis of rims produced an age of 1850 ±33Ma, with MSWD of 0.77 and probability of 0.61, based on the rims of $n = 8$ grains (Figure 8.12b). The ages returned for cores and rims are within uncertainty, however it is noted that ages are significantly higher than those for the eastern granite samples. Larger uncertainties are the result of a limited number of suitable analyses following rejection stages.

Four core-rim pairs were analysed, with only one pair passing rejection criteria. Other pairs are rejected due to inheritance (≥ 2150Ma) and/or ≥ ±32% discordance. In most cases, analyses show rims significantly older than cores, reflecting the complex nature of analyses from this sample (Table 8.11).

Table 8.11 Northern Granite ST10_16B $^{207}Pb/^{206}Pb$ Age (Ma): Core-Rim Grain Pairs

Weighted Average Age (Ma): Core-Rim Grain Pairs				
Grain No.	**Weighted Average Age** ($^{207}Pb/^{206}Pb$) Ma	**Central Discordance**	**Weighted Average Age** ($^{207}Pb/^{206}Pb$) Ma	**Central Discordance**
	CORES		**RIMS**	
ST10_16B Northern Granite (≤ ±10% Discordance & ≤ 2.3 Weighted Residual)				
16B-003	1816.5 ±68	-4.6	1799.8 ±56	-2.0
~~16B-012~~	1898.4 ±52	-5.7	2514.8 ±49	-4.1
~~16B-038~~	1822.3 ±38	-1.8	2423.3 ±38	8.5
~~16B-029~~	1826 ±46	3.3	2250 ±203	-24.6

~~Strikethrough~~ indicates grain excluded from age calculation (≥ 2% Com-Pb, ≥ 2150Ma or Discordance). Refer Table 8.10 for details.

SAMPLE ST10_18

Individual zircon ages from sample ST10_18 show a large range with variable uncertainty, from 1549 ±135Ma to 3899 ±22Ma (Table 8.12). Three grains were instantly rejected: one analysis that did not return a $^{207}Pb/^{206}Pb$ age, and two grains with ages 568 ±880Ma and 1131 ±857Ma. Analyses resulted in a high level of discordance (Figure 8.13a) and large error ellipses. The Cumulative Probability diagram (Figure 8.13b) shows the main population peaking at 1856 ±65Ma, with a complex curve showing many older grains generating subordinate populations peaks.

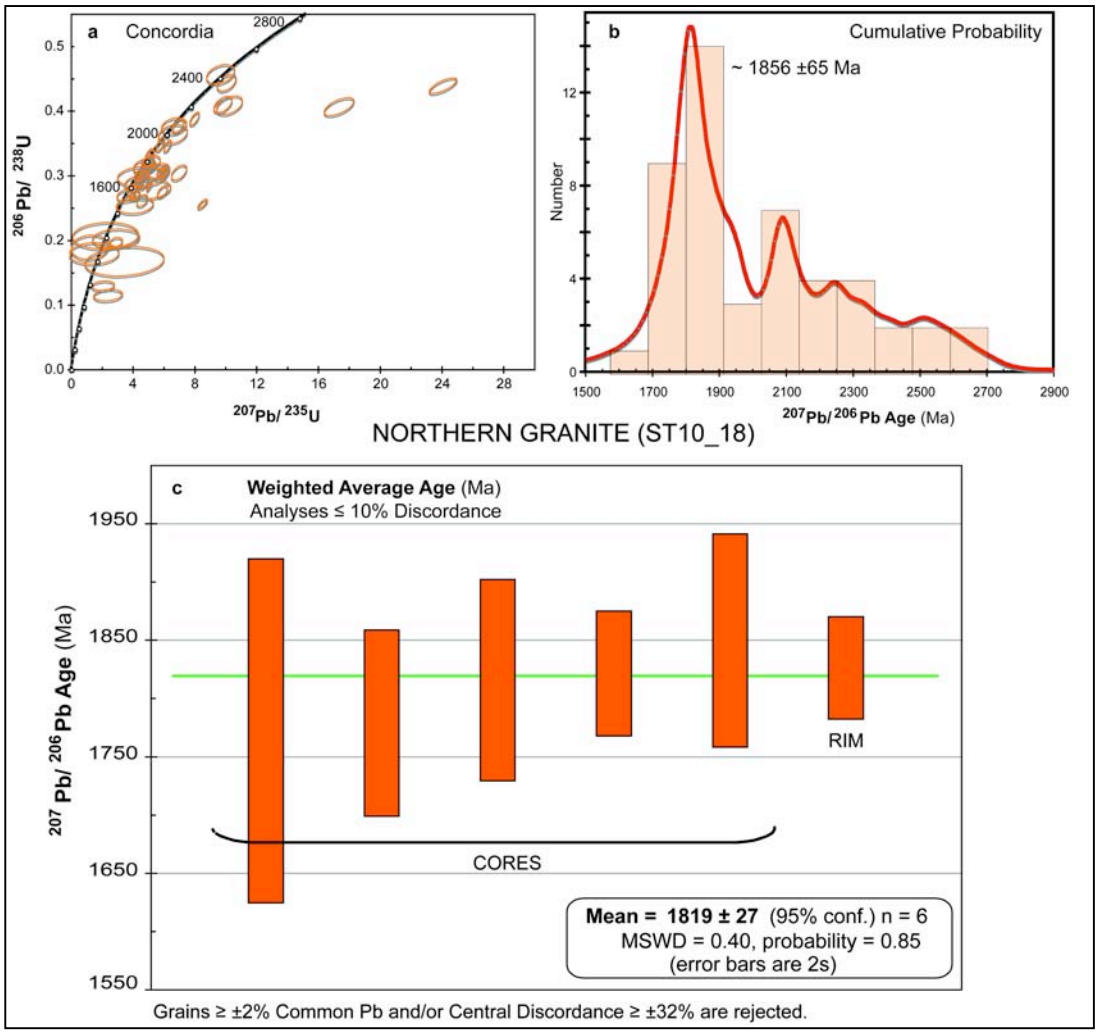

Figure 8.13 Northern Granite (ST10_18) $^{207}Pb/^{206}Pb$ Age, Concordia & Probability
a) Concordia, **b**) Probability Histogram, **c**) Weighted Average Age (Ma)
Plotted from TerraneChron® spreadsheets using *Isoplot EX3.0* Excel Plugin (Ludwig, 2003)

Of the 54 grains analysed, 35 were rejected containing ≥ ±2% common-Pb and ≥ 32% central discordance, with three grains ≥ 2150Ma (Table 8.12). A further 13 grains were rejected with central discordance ≥ ±10% and weighted residual of ≥ 2.3. The high level of discordance and common-Pb meant that 87% of grains were rejected, leaving only $n = 6$ grains for age calculation. The pooled ages of cores and rims indicate an age of 1819 ±27Ma (Figure 8.13c). Given the limited sample population, the age uncertainty is surprisingly low (±27Ma), but results will be treated with some caution.

Comparison of core, outer core and rim ages was problematical given the limited number of grains ($n = 6$) with ≤ ±2% common-Pb and ≤ ±10% central discordance. Two core and three outer core analyses were combined (as with previous samples) to provide a core age of 1808 ±27Ma (Figure 8.14). One rim analysis is dated at 1827 ±22Ma (Table 8.13).

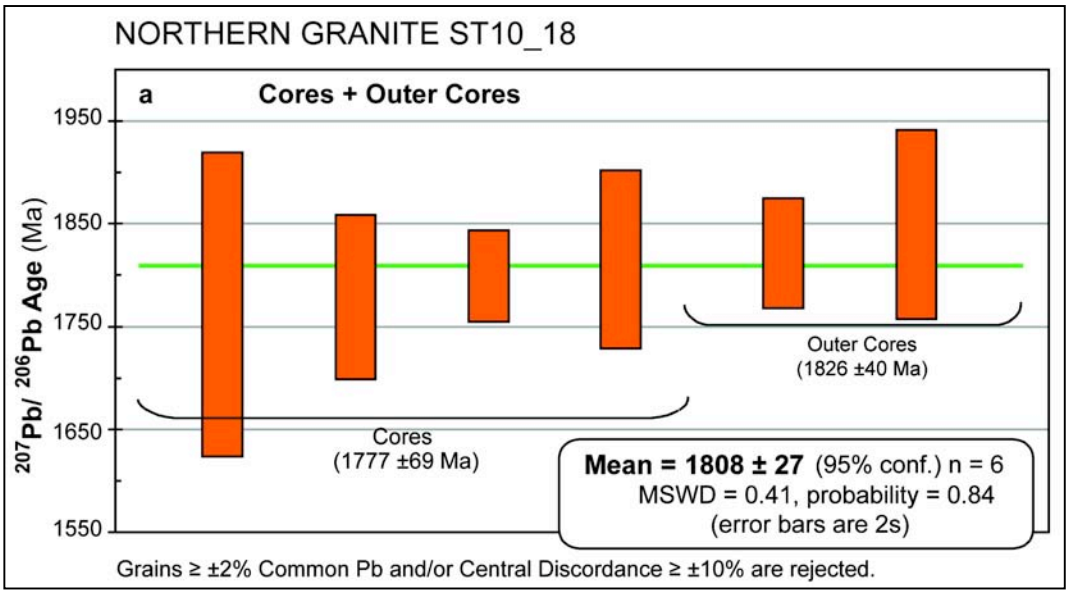

Figure 8.14 Northern Granite (ST10_18) ^{207}Pb/^{206}Pb Age: Core & Rim Analysis
Plotted from TerraneChron® spreadsheets using *Isoplot EX3.0* Excel Plugin (Ludwig, 2003)

Table 8.13 Northern Granite ST10_18 ^{207}Pb/^{206}Pb Age (Ma): Core & Rim Analyses

U-Pb Zircon Weighted Average Age (Ma) of Cores & Rims								
Rejection Criteria	***n***	**Weighted Average Age** (^{207}Pb/^{206}Pb) Ma	**MSWD** %	**Prob. of Fit**	***n***	**Weighted Average Age** (^{207}Pb/^{206}Pb) Ma	**MSWD** %	**Prob. of Fit**
	CORES				**RIMS**			
ST10_18 Northern Granite								
All Grains ≤ 2150Ma	28	1896 ±46	8.40	0.000	9	1866 ±90	7.70	0.000
Common Pb ≥ ±2.0%	12	1906 ±74	15.00	0.000	4	1876 ±230	20.00	0.000
Discordance ≥ ±32%								
Discordance ≥ ±15%	11	1880 ±67	10.00	0.000	2	1813 ±240	1.09	0.3
Discordance ≥ ±10%	8	1842 ±54	3.70	0.001				
weighted residual ≥2.3	6	1808 ±27	0.41	0.840	1	1827 ±22	Single Grain Age	
Discordance ≥ ±5%	5	1838 ±84	3.80	0.004				

Weighted Residual calculation (to identify statistical outliers) reversed prior to further rejections. Shown where positively impacted.
n Number of grains used during age calculation ‘Blanks’ indicate no grains meeting that criteria were excluded
Data in red indicate ages to be used in this study Quoted uncertainties are ±1 standard deviation (1σ)

Of the eight core-rim pairs analysed, none passed common-Pb, discordance or age dismissal. Results show erratic ages between cores and rims similar to the previous northern granite sample (Table 8.14).

Table 8.14 Northern Granite ST10_18 $^{207}Pb/^{206}Pb$ Age (Ma): Core-Rim Grain Pairs

Weighted Average Age (Ma): Core-Rim Grain Pairs				
Grain No.	**Weighted Average Age** ($^{207}Pb/^{206}Pb$) Ma	**Central Discordance**	**Weighted Average Age** ($^{207}Pb/^{206}Pb$) Ma	**Central Discordance**
	CORES		**RIMS**	
ST10_18 Northern Granite (≤ ±10% Discordance & ≤ 2.3 Weighted Residual)				
~~18-007~~	2247 ±30	-25.9	3121.4 ±23	-58.8
~~18-009~~	2341 ±296	-73.6	1912 ±225	-26.2
~~18-012~~	1886 ±273	-61.7	1736 ±113	-36.1
~~18-020~~	1823.7 ±30	-28.5	2286.2 ±34	-6.1
~~18-021~~	2501 ±47	-6.3	2667 ±61	-20.1
~~18-025~~	2384 ±71	2.2	2138 ±43	-4.0
~~18-026~~	1779 ±40	-7.4	1786 ±32	-10.2
~~18-035~~	1688 ±446	-32.1	1842 ±42	-17.9
~~18-041~~	1131 ±857	8.2	1809 ±64	-16.6

~~Strikethrough~~ indicates grain excluded from age calculation (≥ 2% Com-Pb, ≥ 2150Ma or Discordance). Refer Table 8.2 for details.

Age analyses from the northern granite samples (ST10_16B and ST10_18) were pooled using suitable U-Pb grains, shown in Figure 8.14. As for the eastern granite, individual ages were assessed for statistical weighting on the age calculation. Grains were progressively removed calculating ≥2.3, ≥2.0 and ≥1.5 weighted residual. The results presented in Table 8.15 show rims dated at 1842 ±26Ma based on $n = 9$ grains, with an MSWD of 0.77 and a probability of 0.63. Cores analysed produced a very similar age, at 1843 ±21Ma ($n = 20$) with an MSWD of 1.06 and probability of 0.4 (Figure 8.15).

Given the nature these similar ages, it seems plausible to combined all grains to produce an age of 1843 ±16Ma for zircon from the northern granite, using $n = 29$ grains, with an MSWD of 0.93 and 0.570 probability (Table 8.15).

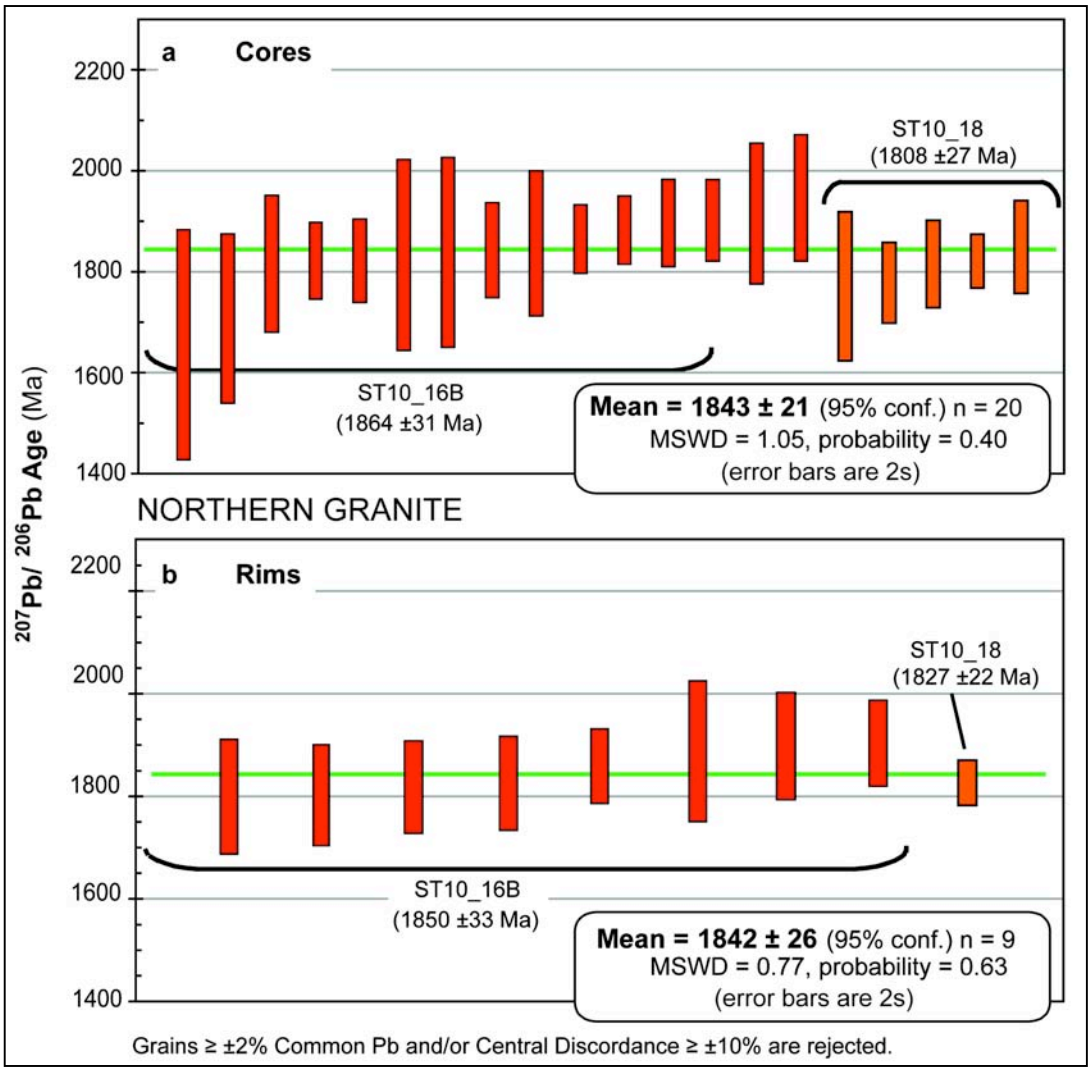

Figure 8.15 Northern Granite Combined $^{207}Pb/^{206}Pb$ Age: Core & Rim

a) core + outer core analyses. **b**) rim analyses

Plotted from TerraneChron® spreadsheets using *Isoplot EX3.0* Excel Plugin (Ludwig, 2003)

U-Pb grains only (≤ ±2% common-Pb, ≤ 2150Ma and ≤ ±10%) central discordance).

Table 8.15 Northern Granite Combined $^{207}Pb/^{206}Pb$ Weighted Average Age (Ma)

U-Pb Zircon Weighted Average Age (Ma) of Cores & Rims: Northern Granite								
Dismissal Criteria	***n***	**Weighted Average Age ($^{207}Pb/^{206}Pb$) Ma**	**MSWD %**	**Prob. of Fit**	***n***	**Weighted Average Age ($^{207}Pb/^{206}Pb$) Ma**	**MSWD %**	**Prob. of Fit**
	CORES				**RIMS**			
Northern Granite (ST10_16B + ST10_18)								
All U-Pb Grains	21	1847 ±25	1.30	0.160	9	1842 ±26	0.77	0.630
≥ 2.3 weighted residual	20	1843 ±21	1.05	0.400				
≥ 2.0 weighted residual	16	1849 ±22	0.60	0.870				
≥ 1.5 weighted residual								

Ages are calculated using only those previously identified U-Pb grains with ≤ ±2% com-Pb & ≤ 10-15% discordance.

n Number of grains used during age calculation

'Blanks' indicate no grains meeting that criteria were excluded

Data in red indicate ages to be used in this study

Quoted uncertainties are ±1 standard deviation (1σ)

8.7 DISCUSSION OF ZIRCON GEOCHRONOLOGY

More concordant ages were obtained from the eastern granite samples (ST10_11 and ST10_19C), with fewer grains containing common-Pb ≥ ±2% or central discordance ≥ ±15%. Zircon extracted from these samples were generally euhedral in morphology, with less fracturing apparent. The U-Pb analyses produced $^{207}Pb/^{206}Pb$ ages that indicate older inherited cores are overgrown by younger rims. Cores from the eastern granite show a weighted average age of 1824 ±14Ma (n = 36), while rims of grains are dated at 1792 ±15Ma. These grain rims, typically comprising oscillatory zoned overgrowths up to 50μm, are interpreted as magmatic, overgrowing older inherited cores. This is in agreement of published age of 1805 ±3Ma (Claoué-Long *et al*., 2008, Rubatto *et al*., 2006).

Samples from the northern granite (ST10_16B and ST10_18) had a high level of discordance and grains with common-Pb ≥ ±2%. Grains were pervasively fractured, with REE compositions reflecting increased alteration and lead loss experienced in this location. This was particularly evident in sample ST10_18, collected within the vicinity of previously identified shear zones (White *et al*., 2003, Collins *et al*., 1991). In the field, this sample was noted to have a mineral lineation and pervasive tectonic foliation (refer chapter 5). Only 10% of the grains picked from this sample (n = 6) were used for the age calculation.

Ages obtained from the northern granite show no variation between the cores and rims analysed. When pooled, analyses calculate rims at 1842 ±21Ma (n = 20) and cores at 1842 ±26Ma (n = 9). If combined, the analyses calculate an age of 1843 ±16Ma (n = 29) for the northern granite. This is significantly older than all analyses of the eastern granite. Since one eastern and one northern granite were analysed in each ICP-MS instrument session, the difference in age is not attributed to an artefact of instrument operation or calibration.

The difference in age between the northern granite and the eastern granite is distinct. At all stages, calculated age uncertainties are higher for the northern granite and ages indicate an older source for the zircon than that of cores from the eastern granite. While the age calculation for zircon from the granite samples has produced ages within uncertainty of those published, the question still remains to develop criteria for identifying inherited grains with ages close to the crystallisation age. Using trace element analyses and further examining age populations for potential rejection criteria, it may possible to distinguish inherited detrital grains from magmatic grains, and will be explored below.

8.8 ZIRCON TRACE ELEMENT ANALYSIS

The lanthanides, or rare earth elements (REE), are some of the least soluble trace elements, remaining relatively immobile during hydrothermal alteration and low-grade metamorphism. As such, characteristics obtained during magma genesis are generally retained (Winter, 2001). REE may however, be mobile in highly-metamorphosed rocks.

LAM-ICP-MS trace element concentrations were examined to expand the criteria for rejection of individual analyses from U-Pb dating, and to investigate differences between those grains interpreted as magmatic and older inherited grains. The features of the REE pattern will be compared and contrasted between samples. Prior to processing, data were normalised to chondrite using values from Taylor & McLennan (1985). Trace element analyses were collected simultaneously during LAM-ICP-MS U-Pb analysis and data are presented in Appendix E-4.

8.8.1 EASTERN GRANITE

SAMPLE ST10_11

Chondrite-normalised REE patterns for the eastern granite (ST10_11) indicate zircon grains are generally depleted in LREE and enriched in HREE (Figure 8.16). The negative Eu anomaly can be attributed the preferential incorporation of Eu into plagioclase during crystallisation, occurring prior to or coeval with the growth of zircon, resulting in a melt depleted in Eu (Bau, 1991). A strong positive Ce anomaly is a result of the inclusion of Ce^{4+} into zircon during growth (Thomas *et al.*, 2003).

Figure 8.16 shows two outlying data points: Grain 11-013 has an LREE pattern more characteristic of monazite. Grain 11-009 has a distinctly low Nd <LLD (<1.39ppm), and an overall lower enrichment in LREE.

Overall, there is a 10x range in REE abundances, reflecting a range of trace element compositions within the sample grains. There are no discernable trends in the dataset between discordance and concordant grains, or between older inherited grains ($\geq$ 2150Ma) and younger grains (Figure 8.16). Therefore, trace element data does not appear to identify inherited grains falling within the main age population.

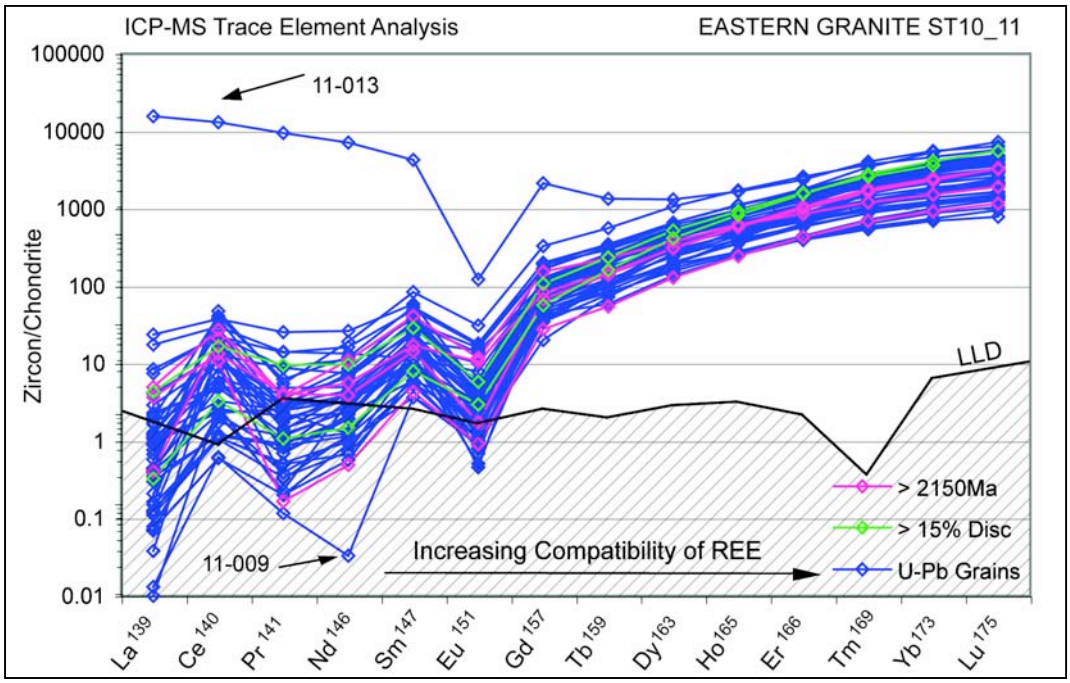

Figure 8.16 Eastern Granite (ST10_11) Zircon REE Patterns
LLD based on minimum detection limit obtained during individual analyses.

Comparison of REE between core and rim analyses (Figure 8.17) shows value cover a similar range for both cores and rims. Several core analyses show flatter patterns, with higher LREE, which may reflect the affect of alteration processes associated with metamictisation and incorporation of LREE.

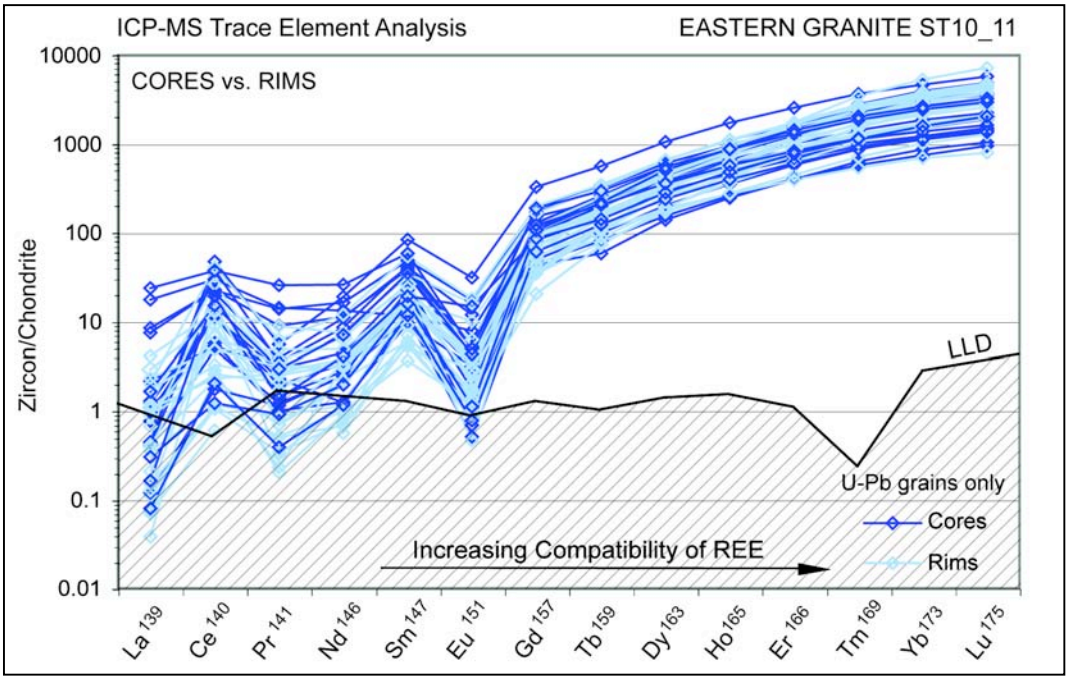

Figure 8.17 Eastern Granite (ST10_11) Zircon REE Pattern: Core vs. Rim
U-Pb grains only. REE outliers (as described) are excluded.
LLD based on minimum detection limit obtained during individual analyses.

SAMPLE ST10_19C

Chondrite-normalised REE pattern for sample ST10_19C is shown in Figure 8.18. There is a general enrichment in HREE, while LREE from this sample show higher values, reflected by a flatter pattern and less distinct Ce and Eu anomalies (compared with the previous sample). No trends are observed between discordant and concordant analyses, nor between inherited and younger grains analysed. All analyses are above LLD.

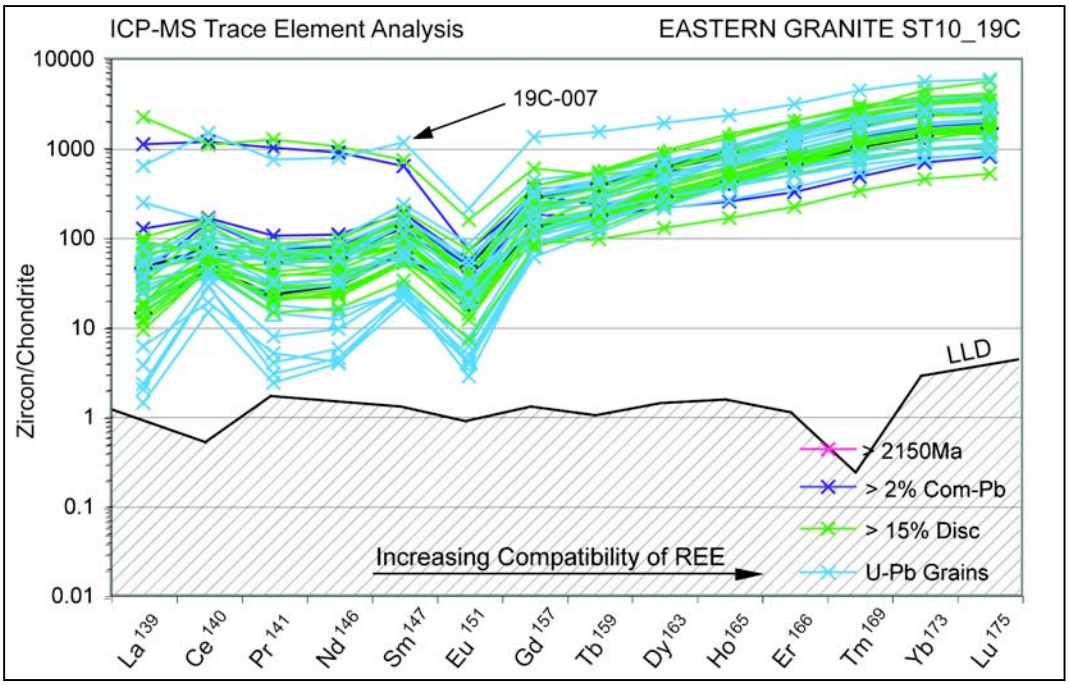

Figure 8.18 Eastern Granite (ST10_19C) Zircon REE Pattern
Normalised to Chondrite Values of Taylor & McLennan (1985).
LLD based on minimum detection limit obtained during individual analyses.

There are three grains with distinctly high LREE, plotting as outliers in the dataset. Similar to the previous sample, these analyses are likely a result of drilling through a grain inclusion (apatite). Analysis 19C-007 (used during initial U-Pb dating) will be excluded from further U-Pb analysis.

Examination of core and rim domains (Figure 8.19) shows consistent and overlapping results, which do not provide a means to readily identify the two groups. They show the same range of values, and cannot be distinguished based on REE composition.

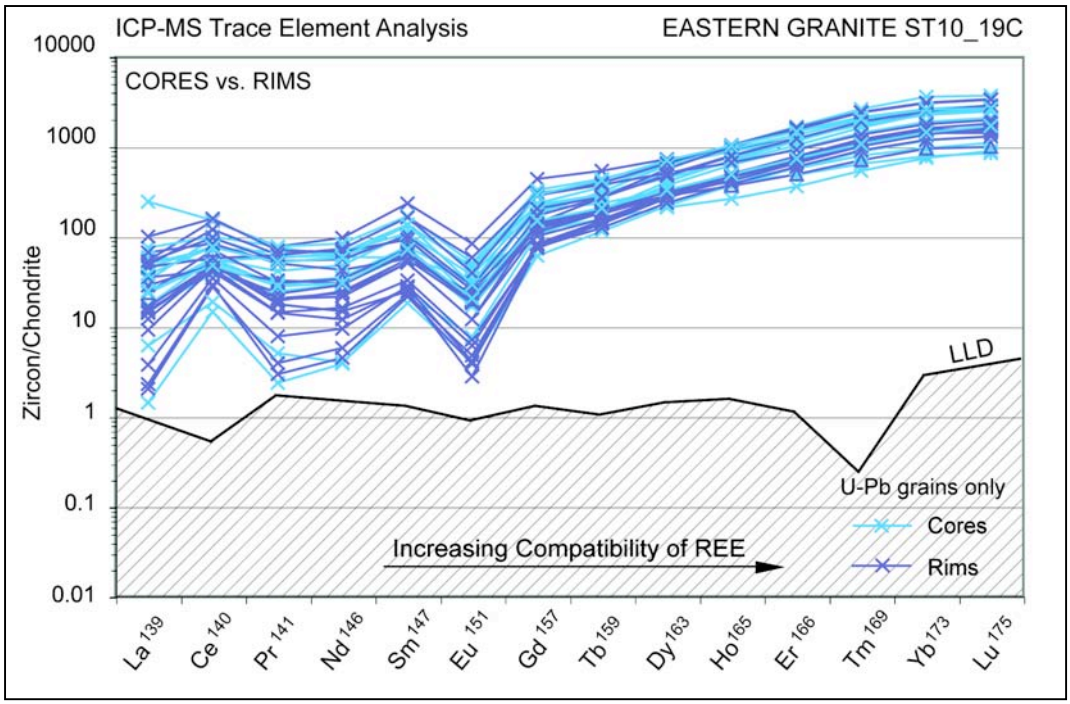

Figure 8.19 Eastern Granite (ST10_19C) Zircon REE Pattern: Core vs. Rim
U-Pb grains only. REE outliers (as described) are excluded.
Normalised to Chondrite Values of Taylor & McLennan (1985).
LLD based on minimum detection limit obtained during individual analyses.

A comparison of REE between the two eastern granite samples (ST10_11 and ST10_19C) is presented in Figure 8.20. The clear difference between the LREE compositions of these samples can be seen, while HREE between the two samples are consistent. The high values reflect the incorporation of LREE during alteration processes associated with metamictisation. However, U-Pb analyses show little evidence for lead loss in zircon from this sample, and analysis indicate ages are consistent between the two samples.

Th/U ratios obtained from U-Pb isotopic analysis display no significant trends (Figure 8.21). Values are generally between 0.01 to 1.32. A single grain from ST10_19C has a Th/U ratio of 2.99. No distinction can be made between values for rejected grains (inheritance ≥ 2150Ma or discordance) and those used for U-Pb age analysis.

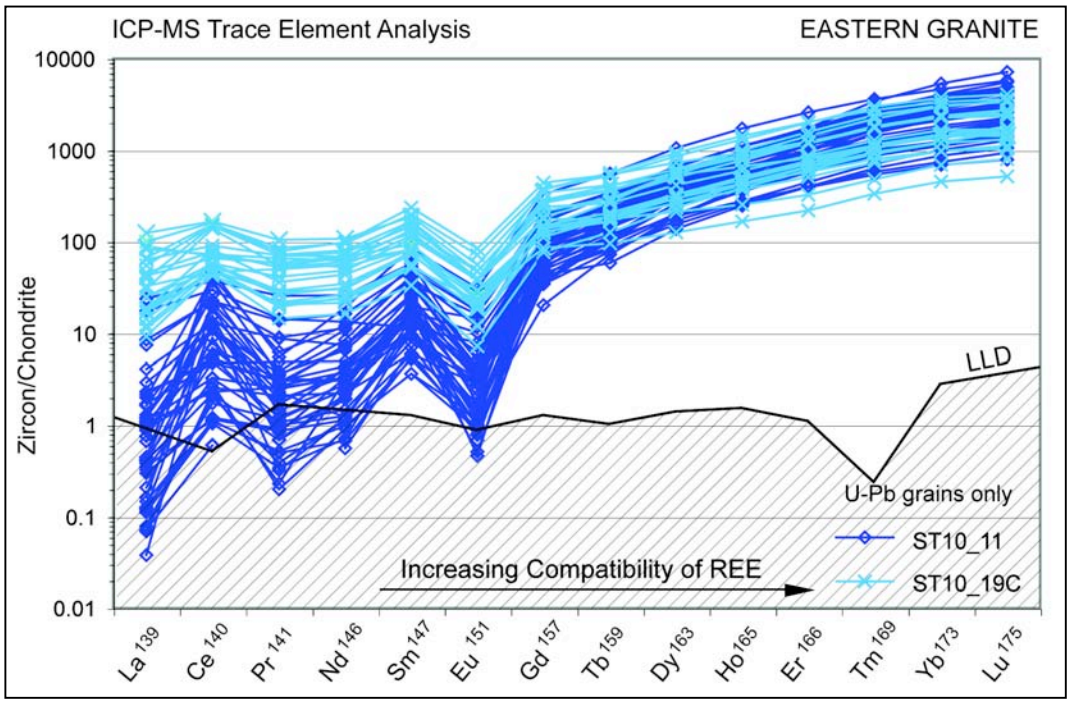

Figure 8.20 Eastern Granite Combined Zircon REE Pattern
U-Pb grains only. REE outliers (as described) are excluded.
Normalised to Chondrite Values of Taylor & McLennan (1985).
LLD based on minimum detection limit obtained during individual analyses.

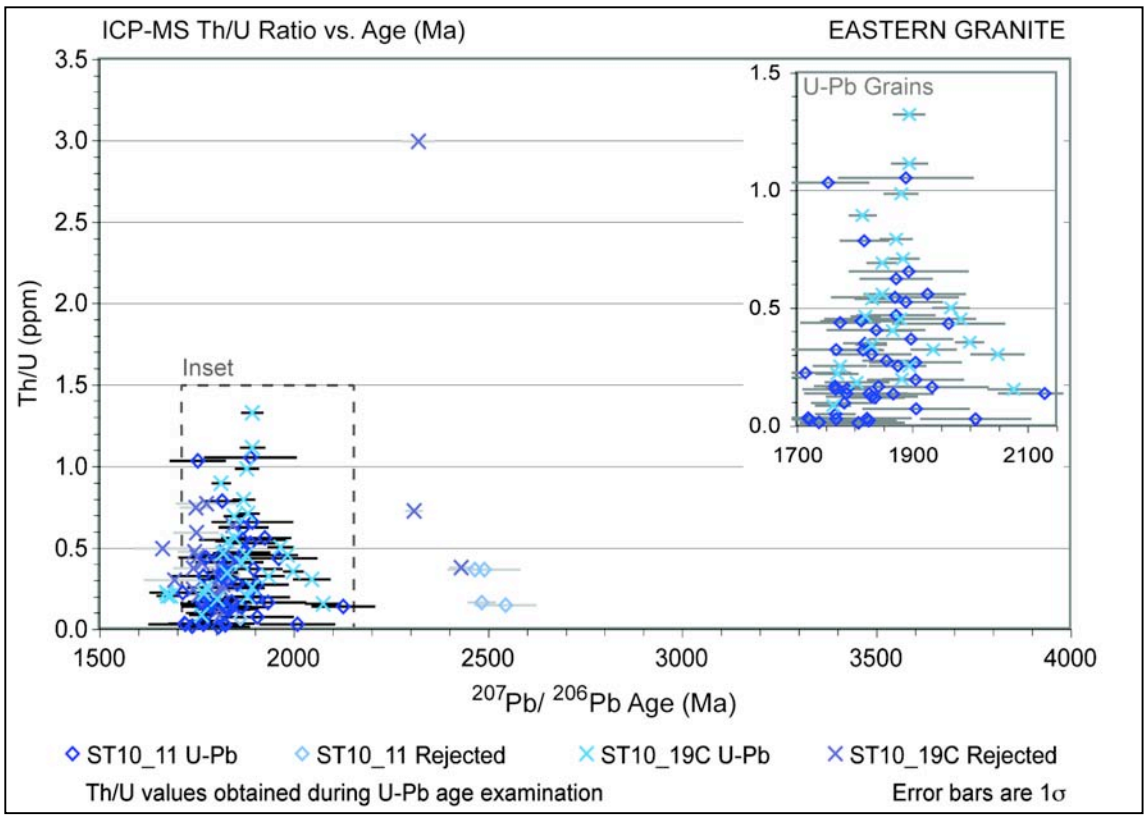

Figure 8.21 Eastern Granite Combined Th/U Ratio vs. Age (Ma)
Th/U ratio obtained during U-Pb analysis, and summarised in the Zircon Composition Summary (Appendix F-1). Age error bars are 1σ. Inset shows U-Pb grains only.
Axis scales match those of Figure 8.28 for ease of comparison.

Ce anomaly values (Ce*) of the eastern granite samples are shown in Figure 8.22a. ST10_11 displays a strong positive Ce* anomaly, with a positive trend from -0.99 to 41.53. Scattered values from ST10_19C range -34.6 to 1257.0, with 2 clusters of data either side of 100ppm Ce. This group does not appear to relate to age or Th/U, with both groups showing a similar range of values. The negative Eu anomaly (Eu*) is presented in Figure 8.22b. Sample ST10_11 shows a tight grouping of values with a negative trend. Sample ST10_19C also shows a negative trend, with a larger range of values from 0.01 to -801.3.

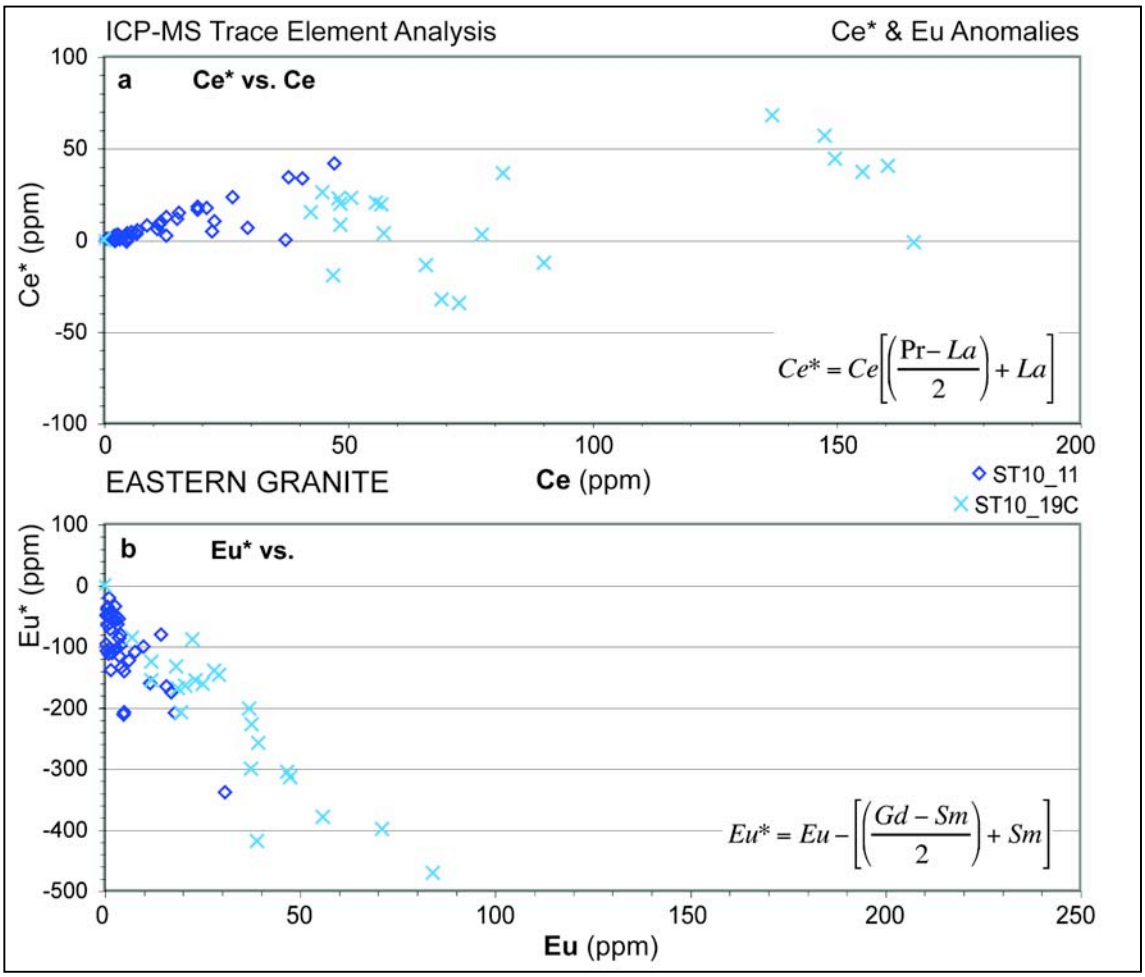

Figure 8.22 Eastern Granite Combined Ce* & Eu*
a) Ce* Anomaly (Ce* vs. Ce). **b**) Eu* Anomaly (Eu* vs. Eu) calculated as shown. Showing only U-Pb grains (≤ ±2% common-Pb, ≤ 2150Ma and/or ≤ ±15% (ST10_11) & ≤ ±15% (ST10_19C) discordance). Scale as per Figure 8.29 for ease of comparison.
Note: Two grains outlying grains (19C-003 & 19C-029) with Ce* values 1257.0 & 394.6 and Eu* of 801.3 and 537.0 are not shown to reduce diagram scale (see Figure 8.35).

8.8.2 NORTHERN GRANITE

SAMPLE ST10_16B

The chondrite-normalised REE patterns for zircon from sample ST10_16B are presented in Figure 8.23. The patterns show a large range of LREE values. There is some indication that discordant and inherited grains ≥2150Ma have higher LREE and flatter patterns. However, those grains used during U-Pb analysis also show a broad range of LREE values. HREE show a greater range in the sample than others analysed. The dataset indicates two outlying grains: 16B-022 with low Pr values <LLD (<1.59ppm) and 16B-048 with Nd values <LLD (<1.39ppm) (Figure 8.23).

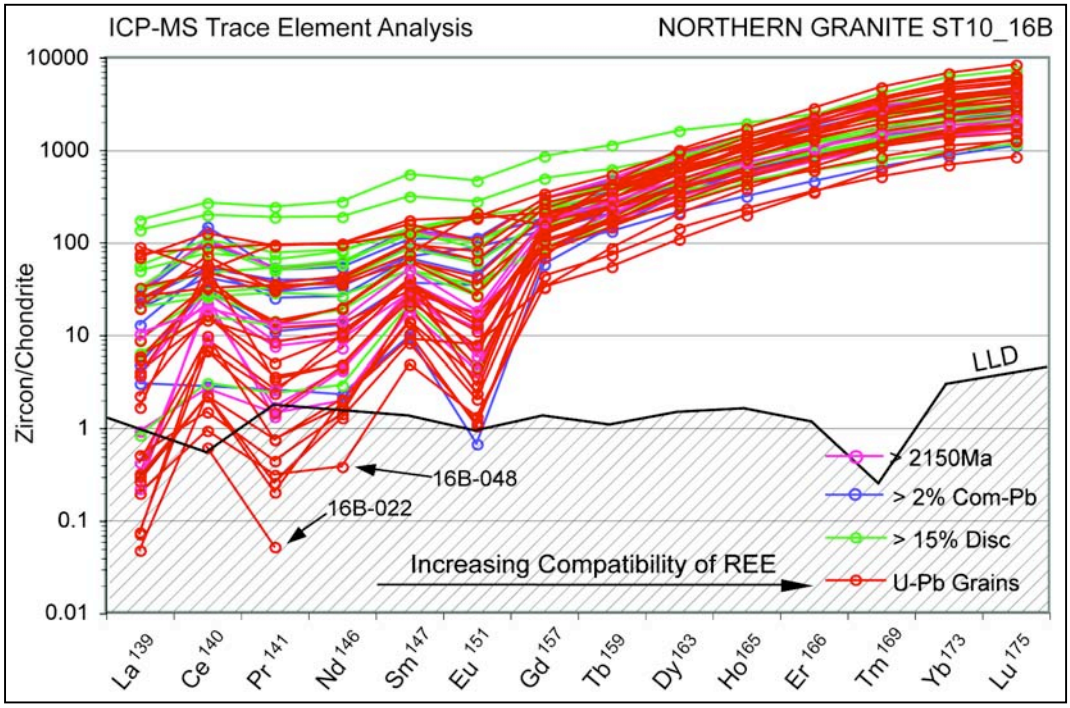

Figure 8.23 Northern Granite (ST10_16B) Zircon REE Pattern Normalised to Chondrite Values of Taylor & McLennan (1985). LLD based on minimum detection limit obtained during individual analyses.

Values for core and rim sites cover a similar range of LREE values, and no trends can be identified between these two groups (Figure 8.24).

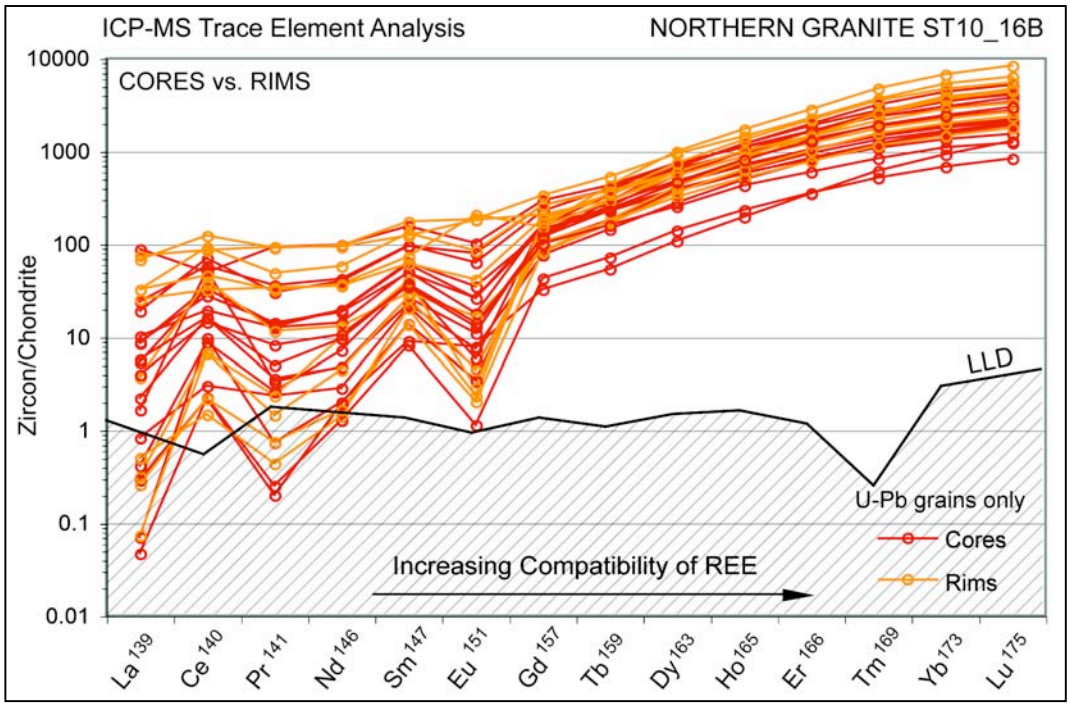

Figure 8.24 Northern Granite (ST10_16B) Zircon REE Pattern: Core vs. Rim
U-Pb grains only. REE outliers (as described) are excluded.
Normalised to Chondrite Values of Taylor & McLennan (1985).
LLD based on minimum detection limit obtained during individual analyses.

SAMPLE ST10_18

Chondrite-normalised REE data for sample ST10_18 (Figure 8.25) displays a large range of values. These variable results may in-part be due to the high proportion of grains with common-Pb and discordance, the result of alteration processes and incorporation of LREE during metamictisation.

A group with appreciably higher LREE were identified during initial U-Pb analysis as containing ≥ ±2% common-Pb, and are already excluded from age calculations (Figure 8.25). Many grains with ≥15% discordance also display flatter LREE curves. One grain with La <LLD (<0.79ppm) has ≥10% discordance, so was previously excluded from the age calculation.

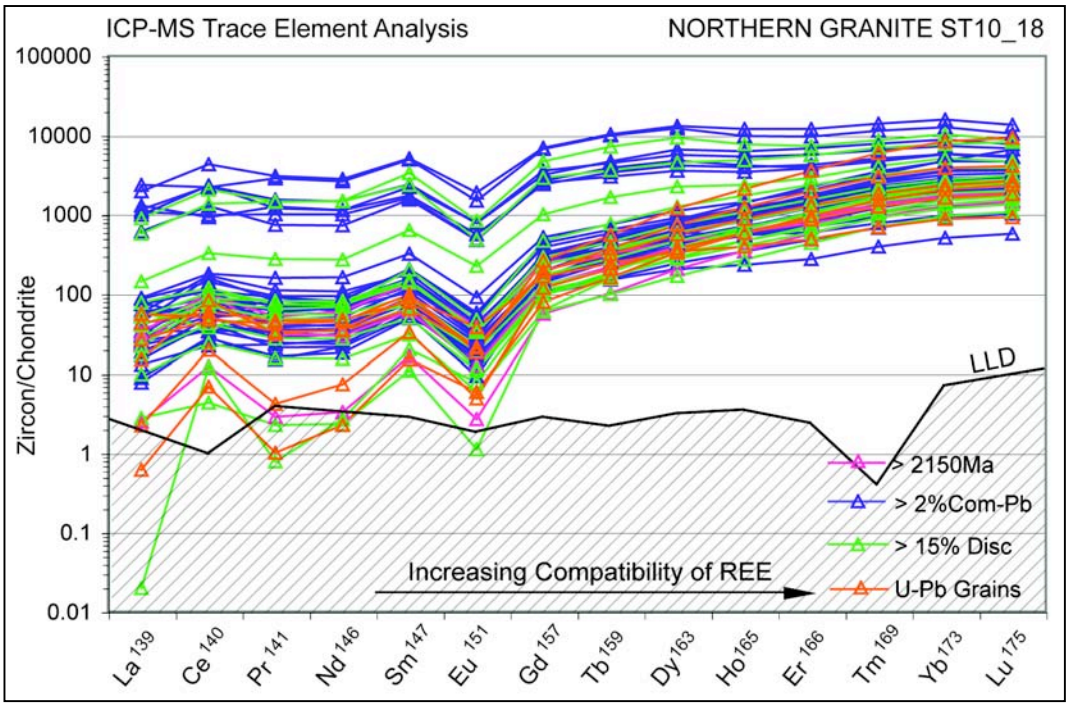

Figure 8.25 Northern Granite (ST10_18) Zircon REE Pattern
Normalised to Chondrite Values of Taylor & McLennan (1985).
LLD based on minimum detection limit obtained during individual analyses.

Due to the limited number of U-Pb analyses remaining after dismissals, analyses of core and rim relationships is inconclusive (Figure 8.26).

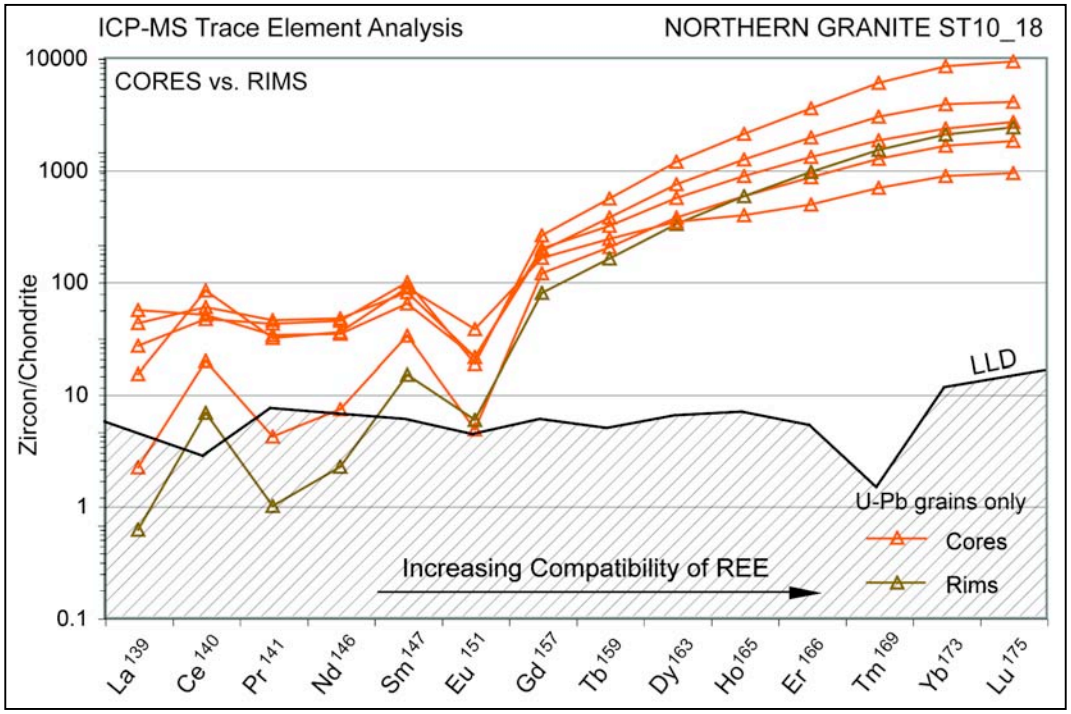

Figure 8.26 Northern Granite (ST10_18) Zircon REE Pattern: Core vs. Rim
U-Pb grains only. REE outliers (as described) are excluded.
Normalised to Chondrite Values of Taylor & McLennan (1985).
LLD based on minimum detection limit obtained during individual analyses.

Combined REE patterns for the northern granite samples (ST10_16B and ST10_18) show a large range of values (Figure 8.27). ST10_16B shows a greater range of values than U-Pb grains from sample ST10_18. However, this distinction between the two samples is likely an artefact of the limited number of analyses (n = 6) for ST10_18. REE patterns from the northern granite reflect a mixture of un-altered zircon grains with lower LREE and metamict grains with enriched LREE.

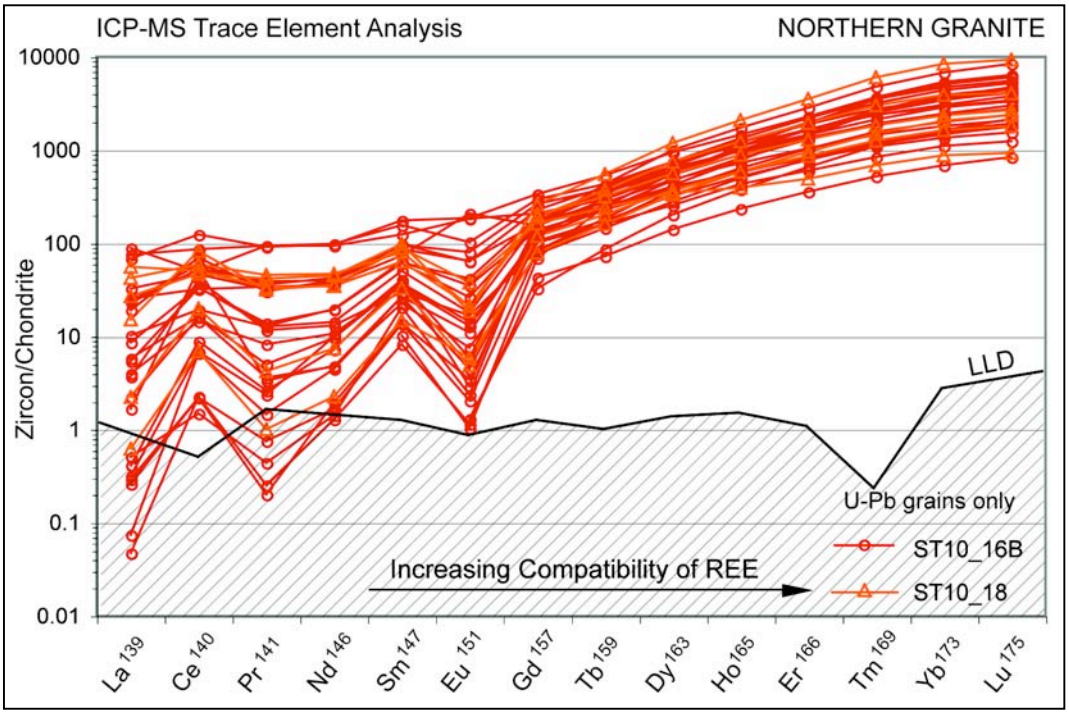

Figure 8.27 Northern Granite Combined Zircon REE Pattern
U-Pb grains only. REE outliers (as described) are excluded.
Normalised to Chondrite Values of Taylor & McLennan (1985).
LLD based on minimum detection limit obtained during individual analyses.

Th/U ratios exhibit no discernable trends or patterns (Figure 8.28). For the northern granite samples, values are typically between 0.02 to 1.53. One rejected grain from ST10_18 has a Th/U ratio of 2.22. Overall, zircon grains used during U-Pb analysis cover a similar range of values to those rejected with common-Pb, discordance or inherited grains ≤ 2150Ma.

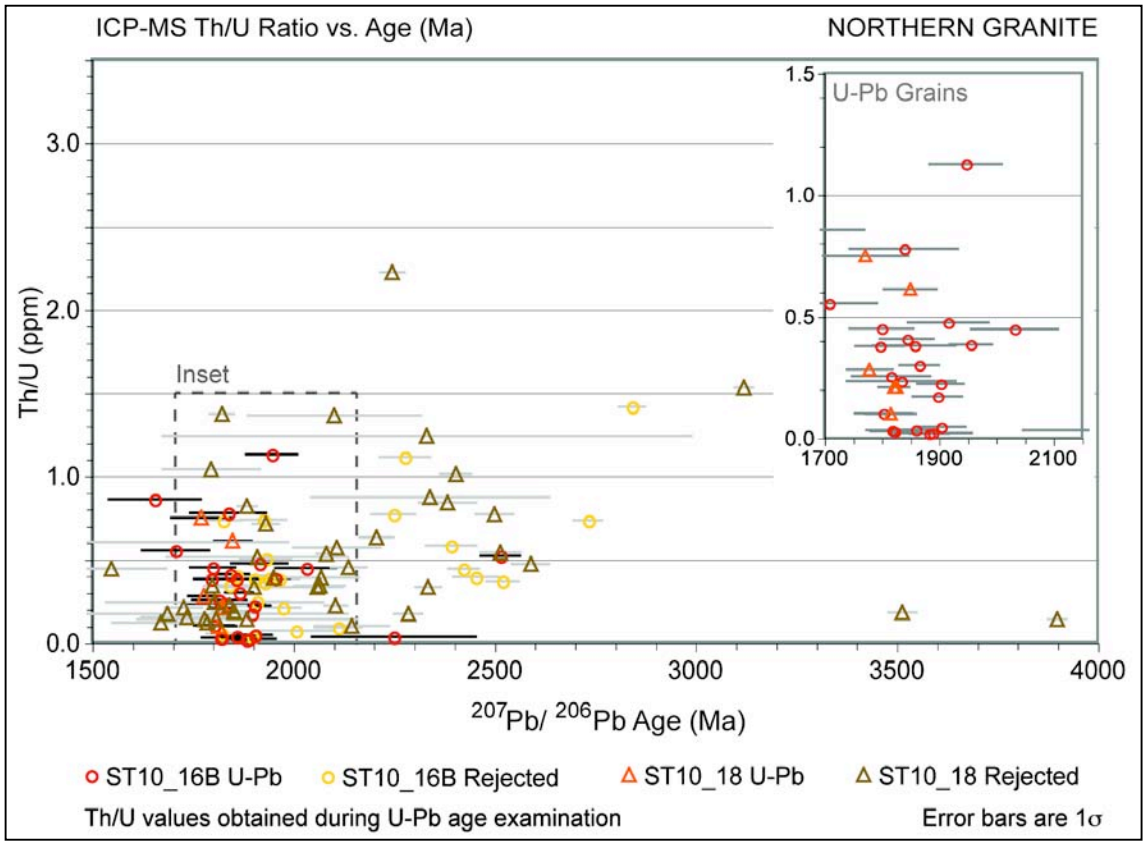

Figure 8.28 Northern Granite Combined Th / U Ratio vs. Age (Ma)
Th/U ratio obtained during U-Pb analysis, and summarised in the Zircon Composition Summary (Appendix F-1). Age error bars are 1σ. Inset shows U-Pb grains only.
Axis scales match those of Figure 8.21 for ease of comparison

Positive Ce* anomaly of the northern granites is shown in Figure 8.29a. ST10_16B displays an overall positive Ce* anomaly, however, scattered values cover a broad range from -89.7 to 48.3. The few analyses from ST10_18 are within the ranges of ST10_16B. The Eu* is broadly negative, but values from both samples cover a large range 18.6 to -290.8 (Figure 8.29b).

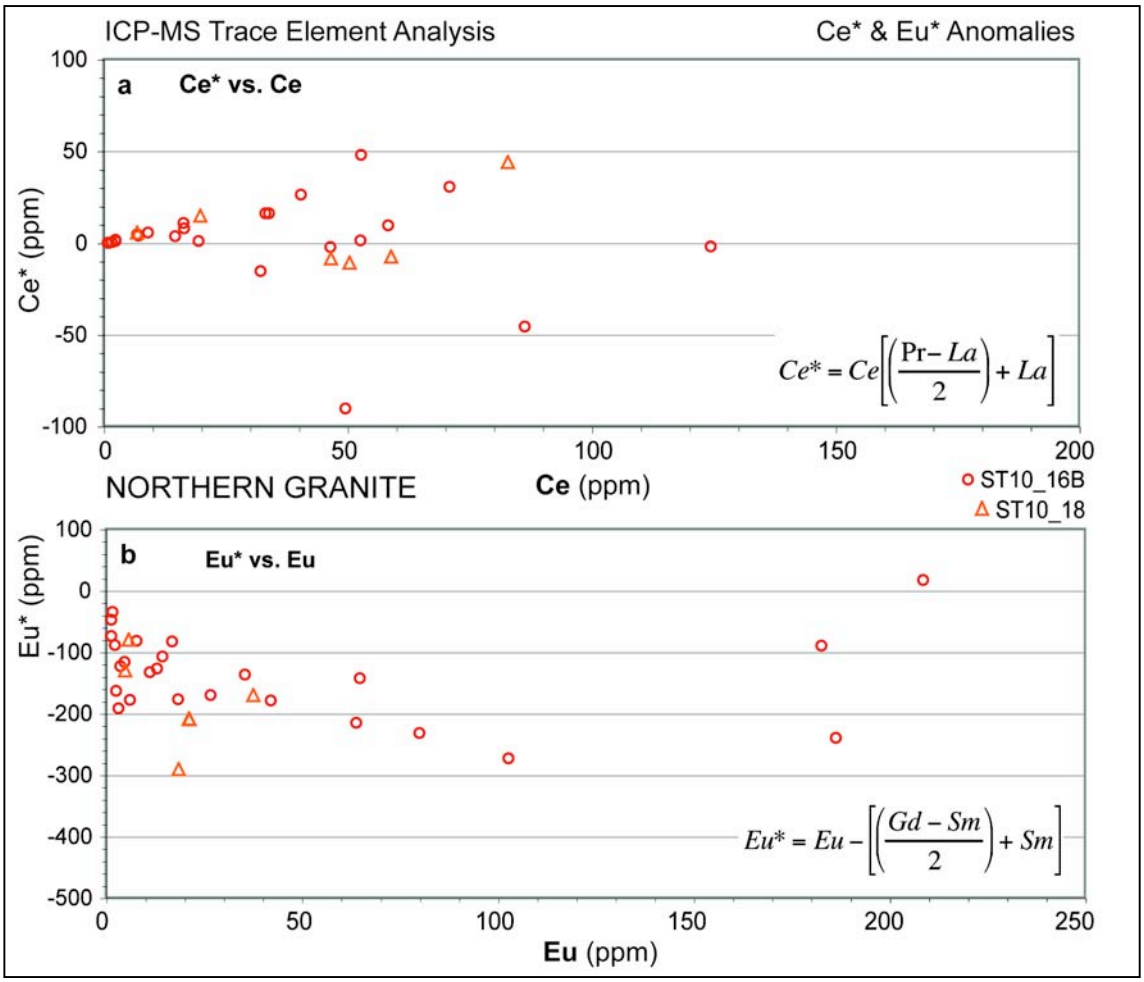

Figure 8.29 Northern Granite Combined Ce* & Eu* Anomalies
a) Ce* Anomaly (Ce* vs. Ce). **b**) Eu* Anomaly (Eu* vs. Eu) calculated as shown. Showing only U-Pb grains (≤ ±2% common-Pb, ≤ 2150Ma and/or ≤ ±15% (ST10_11) & ≤ ±15% (ST10_19C) Discordance). Scale as per Figure 8.22 for ease of comparison.

8.9 Discussion of Zircon Trace Element Analyses

Normalised REE patterns of the eastern and northern granites show a large range of values (Figure 8.30). LREE are higher for the northern sheared granite (ST10_18) and for the eastern granite associated with the mingling zone (ST10_19C). This pattern reflects the incorporation of LREE during alteration (metamictisation) and deformation experienced by these samples, identified during various stages of whole-rock and zircon analysis.

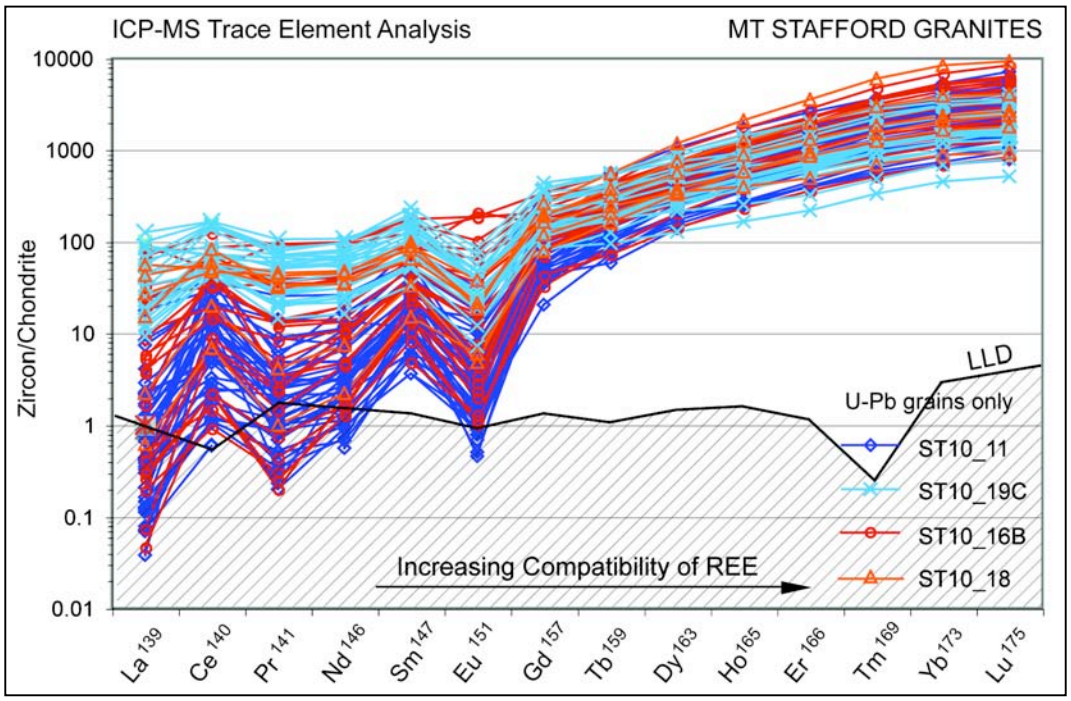

Figure 8.30 Combined Mt Stafford Granites Zircon REE Pattern
U-Pb grains only. REE outliers (as described) are excluded.
Normalised to Chondrite Values of Taylor & McLennan (1985).
LLD based on minimum detection limit obtained during individual analyses.

Despite the apparent alteration, there is no evidence for lead loss in zircon from the eastern granite associated with the mingling zone (ST10_19C). $^{207}Pb/^{206}Pb$ ages obtained for rim domains are remarkably and consistently similar for both eastern granite samples (1792 ±23Ma and 1793 ±23Ma for ST10_11 and ST10_19C respectively). As such, the ages calculated from the rims are interpreted to date the age of granite emplacement.

Zircon grains from the northern granite have been variably altered. This is reflected in the large range of LREE values, and incidence of grains experiencing lead-loss (≥ ±2% common-Pb) identified during initial U-Pb analysis. The majority of grains analysed from the northern granite sample were excluded from U-Pb age calculations.

Comparison of Th/U ratios for the four granite samples produce no discernable trends between cores, rims or discordant grains, with characteristic values between 0.01 and 1.53, averaging 0.39 across all samples (Figure 8.31). Two grains have the highest values of 2.22 (ST10_18) and 2.99 (ST10_19C), and are already excluded from age calculations.

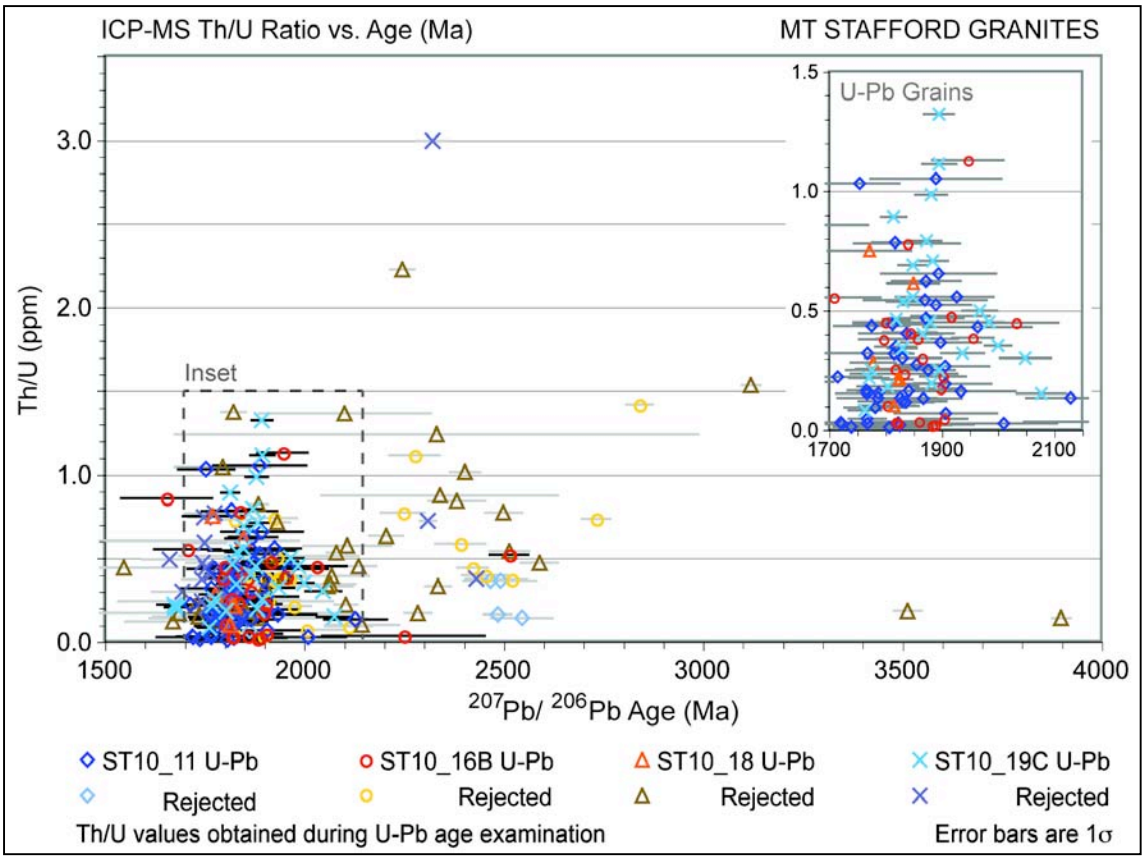

Figure 8.31 Combined Mt Stafford Granites Th/U Ratio vs. Age

Th/U ratio obtained during U-Pb analysis, and summarised in the Zircon Composition Summary (Appendix F-1). Age error bars are 1σ. Inset shows U-Pb grains only.

Grains from the eastern granite (ST10_11) show a more pronounced positive Ce* and negative Eu* than other samples analysed, visible as linear positive and negative trends in Figures 8.32a and b. The remainder of the samples show broadly positive Ce* and negative Eu* trends, but values are more scattered. Eu* shows no distinct trends as Th/U increases (shown in Figure 8.33), with ST10_19C showing the highest negative Eu* values.

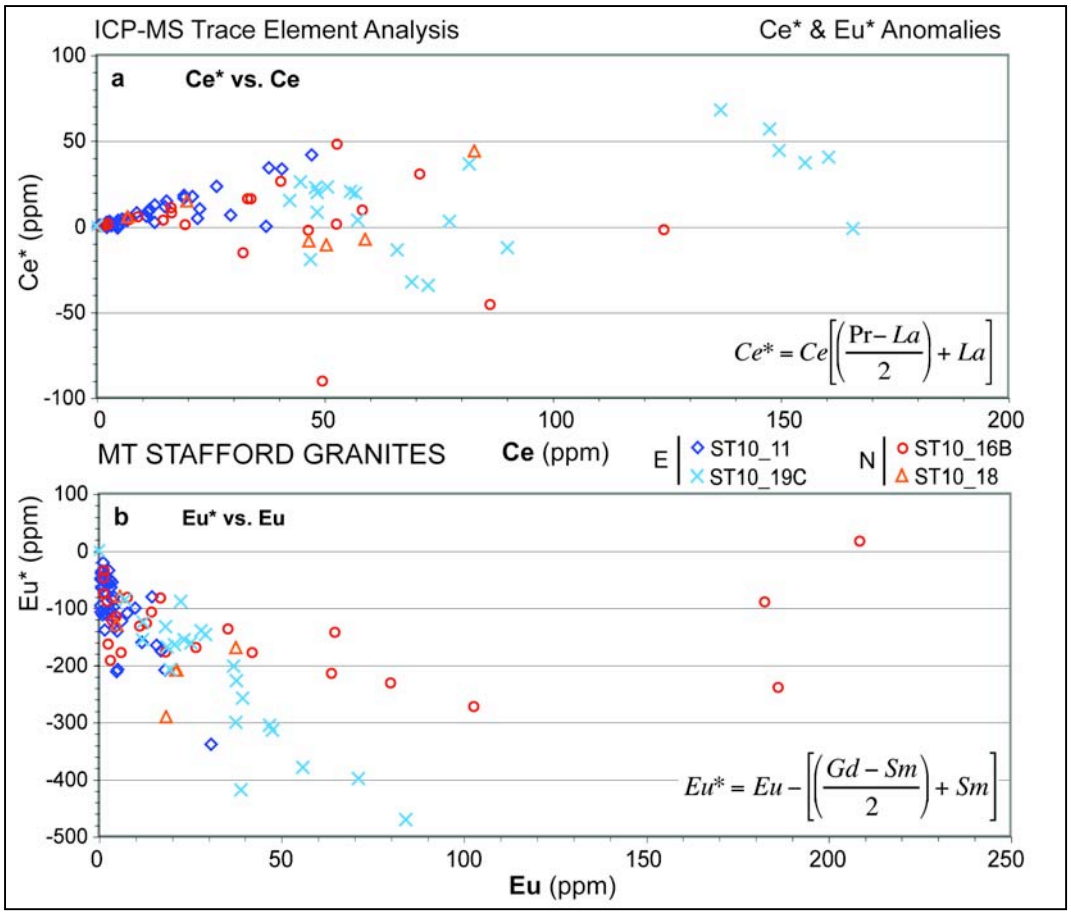

Figure 8.32 Mt Stafford Granites Combined Ce* & Eu* Anomalies
a) Positive Ce* Anomaly (Ce* vs. Ce). **b**) Negative Eu* Anomaly (Eu* vs. Eu)
Showing only U-Pb grains.

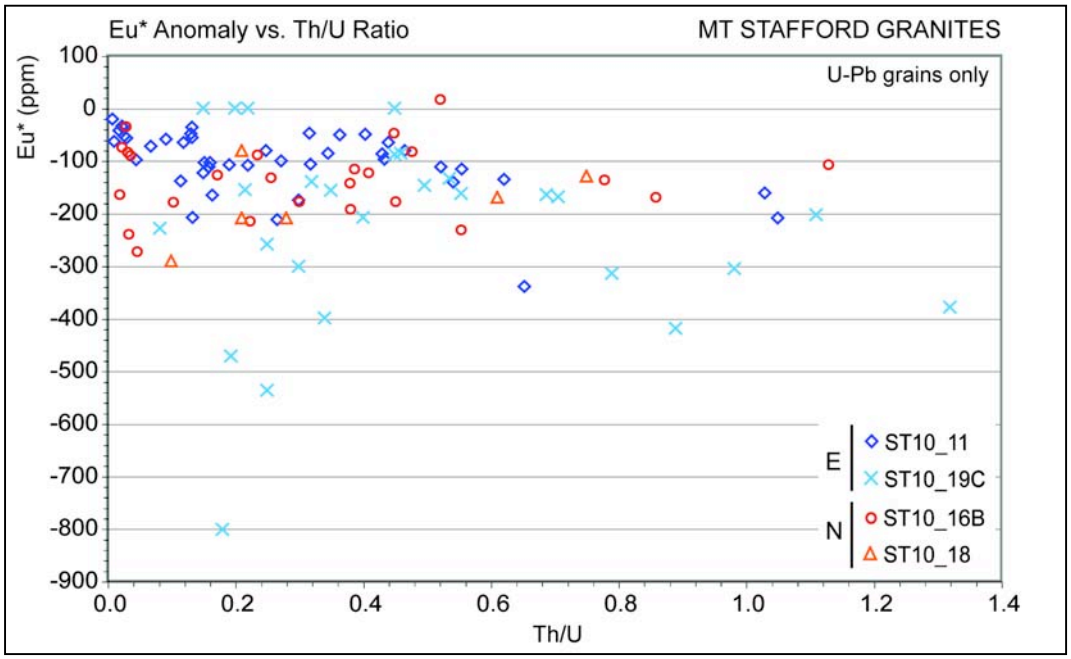

Figure 8.33 Mt Stafford Granites Combined Eu* Anomaly vs. Th/U
Th/U ratio obtained during U-Pb analysis, and summarised in the Zircon Composition Summary (Appendix F-1). Eu* calculated per Figures 8.32. Showing only U-Pb grains

While examination of REE was inconclusive in identifying trends between inherited and discordant groups and core / rim domains, it has provided quantitative compositional data on all grains used for U-Pb analysis. Outliers in the REE dataset are the result of drilling through apatite inclusions, and/or reflect monazite REE compositions. Any effect of removing these analyses from the U-Pb age calculation will be explored below.

8.10 Zircon U-Pb Geochronology: Trace Element Influence

Initial stages of U-Pb age analysis (Section 8.6) provided a range of rejection criteria used to remove outlying or statistically weighted grains from the age calculation, identifying suitable U-Pb grains. Following assessment of REE, several outlying grains were removed from the $^{207}Pb/^{206}Pb$ age calculation in the aim of reducing uncertainty on the calculated age.

8.10.1 Eastern Granite

Two U-Pb grains were identified from sample ST10_11 as REE outliers: 11-013 interpreted as monazite and ST10_009 with Nd <LLD. One outlier from sample ST10_19C is most likely apatite. Following dismissal of these three grains $^{207}Pb/^{206}Pb$ ages calculated for the eastern granite are 1827 ±14Ma for cores (n = 33), with rims at 1794 ±16Ma (n = 35) Table 8.16).

Table 8.16 Eastern Granites $^{207}Pb/^{206}Pb$ Weighted Average Age (Ma): Trace Element Outliers

U-Pb Zircon Weighted Average Age (Ma) Trace Element Outliers: Eastern Granite								
Dismissal Criteria	***n***	**Weighted Average Age** ($^{207}Pb/^{206}Pb$) Ma	**MSWD** %	**Prob. of Fit**	***n***	**Weighted Average Age** ($^{207}Pb/^{206}Pb$) Ma	**MSWD** %	**Prob. of Fit**
	CORES				**RIMS**			
Eastern Granite (ST10_11 + ST10_19C)								
All U-Pb Grains	35	1828 ±14	0.77	0.820	36	1792 ±15	1.16	0.240
REE Outliers	33	1827 ±14	0.85	0.710	35	1794 ±16	1.17	0.230

Ages are calculated using only those previously identified U-Pb grains with ≤ ±2% com-Pb & ≤ 10-15% discordance.

n Number of grains used during age calculation

'Blanks' indicate no grains meeting that criteria were excluded

Data in red indicate ages to be used in this study

Quoted uncertainties are ±1 standard deviation (1σ)

8.10.2 Northern Granite

Two grains from sample ST10_16B presented as REE outliers, with Pr and Nd values below LLD: ST10_16B-022 and ST10_16B-048. When these grains were removed, the recalculated $^{207}Pb/^{206}Pb$ age shows cores at 1845 ±21Ma (n = 19) and rims at 1840 ±27Ma (Table 8.17). Due to the limited number of suitable U-Pb grains from the sheared northern granite (ST10_18), REE outliers could not be identified.

Table 8.17 Northern Granites $^{207}Pb/^{206}Pb$ Weighted Average Age (Ma): Trace Element Outliers

U-Pb Zircon Weighted Average Age (Ma) Trace Element Outliers: Northern Granite								
Rejection Criteria	***n***	**Weighted Average Age** ($^{207}Pb/^{206}Pb$) Ma	**MSWD** %	**Prob. of Fit**	***n***	**Weighted Average Age** ($^{207}Pb/^{206}Pb$) Ma	**MSWD** %	**Prob. of Fit**
	CORES				**RIMS**			
Northern Granite (ST10_16B + ST10_18)								
U-Pb Grains	20	1843 ±21	1.05	0.400	9	1842 ±26	0.77	0.630
REE Outliers	19	1845 ±21	1.09	0.350	8	1840 ±27	0.81	0.580

Ages are calculated using only those previously identified U-Pb grains with ≤ ±2% com-Pb & ≤ 10-15% discordance.

n Number of grains used during age calculation

'Blanks' indicate no grains meeting that criteria were excluded

Data in red indicate ages to be used in this study

Quoted uncertainties are ±1 standard deviation (1σ)

8.11 Discussion of Trace Element Outliers affects on U-Pb Age

As presented, the removal of analyses identified as outliers during trace element analysis did not have a significant impact on the ages calculated. However, removal of these grains has provided a means of reducing uncertainty in the zircon analyses, identifying grains with compositions outside of the broader sample populations. These recalculated ages will be used for further U-Pb age investigation of inherited populations at or near crystallisation age.

8.12 Zircon U-Pb Geochronology: Igneous Inheritance

The $^{207}Pb/^{206}Pb$ ages of individual grains will be further examined and grouped according to age, in the aim of identifying the contribution of inherited zircon to the age calculation. U-Pb grains passing common-Pb and discordance rejection criteria will be used, along with older inherited grains ≥ 2150Ma. Grains were broadly grouped into populations identified using the cumulative probability diagrams (Figures 8.6b, 8.8b, 8.11b & 8.13b), published data and current work on the Mt Stafford Member metasedimentary rocks (Dunkley, unpublished). Given that inherited grains cannot be clearly isolated by other means (morphology, trace elements, Th/U ratios), grain populations will be examined based on their age.

U-Pb geochronology results obtained from three of the Mt Stafford metasedimentary rocks (Dunkley, unpublished), show a main population peak at ~1870Ma. Published work suggests provenance from ca. 1880-1840Ma crystalline rocks with a detrital population peak ca. 1866 ±3Ma (Blake & Page, 1988, cited Clarke *et al*., 1990, Claoué-Long *et al*., 2008, Claoué-Long & Edgoose, 2008).

The 1790-1810Ma Mt Stafford Event is responsible for widespread bi-modal magmatism across the region and termination of the basin phase of the Mt Stafford member deposition (Claoué-Long & Edgoose, 2008). Therefore, metasedimentary rocks must have been deposited in a narrow window ~1860Ma to ~1810Ma. Known age relationships will be used to further constrain reported granite ages in this study.

Older Inherited Grains ≥ 1870Ma

Assessment of $^{207}Pb/^{206}Pb$ ages of older inherited grains ≥ 1870Ma resulted in high uncertainty (1σ) due to the limited number of grains. High uncertainty, combined with high MSWD and low probability ≤ 0.05 yielded ages that are not statistically valid (summarised in Table 8.18). Older inherited grains ≥ 2150Ma with ≥ ±2% common-Pb or ≥ 32% discordance were excluded. The eastern granite (ST10_11 and ST10_19C) yielded ages of 2388 ±91Ma for cores older than 2150Ma (Figure 8.34a).

Table 8.18 Eastern Granite $^{207}Pb/^{206}Pb$ Age (Ma): Older Inherited Material ≥ 1870Ma

U-Pb Zircon Weighted Average Age (Ma): Older Inherited Material ≥1870Ma								
Rejection Criteria	***n***	**Weighted Average Age** ($^{207}Pb/^{206}Pb$) Ma	**MSWD** %	**Prob. of Fit**	***n***	**Weighted Average Age** ($^{207}Pb/^{206}Pb$) Ma	**MSWD** %	**Prob. of Fit**
	CORES				**RIMS**			
Eastern Granite (ST10_11 + ST10_19C)								
U-Pb Grains	36	1824 ±14	0.88	0.670	36	1792 ±15	1.16	0.240
Older Inherited Grains								
Grains ≥ 2150Ma	6	2388 ±91	6.60	0.000				
Grains ≥ 1870Ma	17	2267 ±120	22.0	0.000				
Grains 1870 – 2150Ma	11	1905 ±47	0.21	0.995	4	1892 ±66	0.22	0.880

Ages are calculated using only those previously identified U-Pb grains with ≤ ±2% com-Pb & ≤ 10-15% discordance.

n Number of grains used during age calculation ‘Blanks’ indicate no grains meeting that criteria were excluded

Data in red indicate ages to be used in this study Quoted uncertainties are ±1 standard deviation (1σ)

U-Pb grains with individual ages ≥ 1870 to 2150Ma were present only in sample ST10_11: cores yielded an age of 1905 ±47Ma (*n* = 11), shown in Figure 8.34b. The cores are within uncertainty of older rim analyses of 1892 ±66Ma (*n* = 4) (Table 8.18).

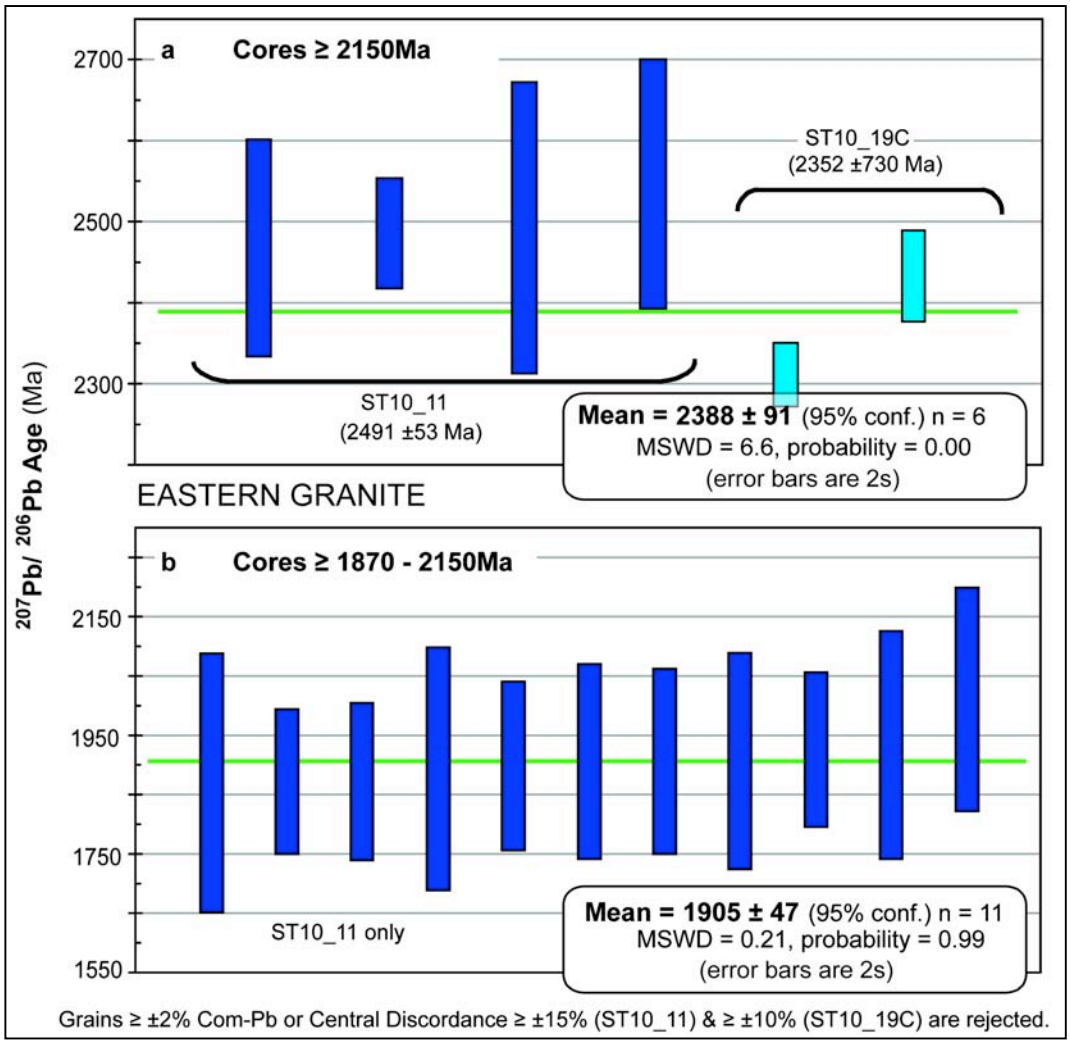

Figure 8.34 Eastern Granite $^{207}Pb/^{206}Pb$ Age (Ma): Older Inherited Zircon
Plotted from TerraneChron® spreadsheets using *Isoplot EX3.0* Excel Plugin (Ludwig, 2003)
a) core analyses ≥ 2150Ma. **b**) core analyses ≥ 1870 – 2150Ma

The northern granite (ST10_16B) contains older inherited material ≥ 2150Ma that produce weighted average ages of 2545 ±220Ma (n = 5) (Table 8.19). Another inherited population is evident in grains ≥ 1870 – 2150Ma (ST10_16B only), with cores yielding ages of 1900 ±39Ma (n = 5) and rims at 1902 ±64Ma (n = 2) (Figure 8.35). The ages of these inherited populations are within uncertainty of those identified in the eastern granite.

Table 8.19 Northern Granite $^{207}Pb/^{206}Pb$ Age (Ma): Older Inherited Material ≥ 1870Ma

U-Pb Zircon Weighted Average Age (Ma): Older Inherited Material ≥1870Ma								
Rejection Criteria	***n***	**Weighted Average Age** ($^{207}Pb/^{206}Pb$) Ma	**MSWD** %	**Prob. of Fit**	***n***	**Weighted Average Age** ($^{207}Pb/^{206}Pb$) Ma	**MSWD** %	**Prob. of Fit**
	CORES				**RIMS**			
Northern Granite (ST10_16B + ST10_18)								
U-Pb Grains	20	1843 ±21	1.05	0.400	9	1842 ±26	0.77	0.630
Older Inherited Grains								
Grains ≥ 2150Ma	5	2545 ±220	16.0	0.000				
Grains ≥ 1870Ma	10	2228 ±260	65.0	0.000				
Grains 1870 – 2150Ma	5	1900 ±39	0.22	0.930	2	1902 ±64	0.008	0.93

Ages are calculated using only those previously identified U-Pb grains with ≤ ±2% com-Pb & ≤ 10-15% discordance.

n Number of grains used during age calculation

'Blanks' indicate no grains meeting that criteria were excluded

Data in red indicate ages to be used in this study

Quoted uncertainties are ±1 standard deviation (1σ)

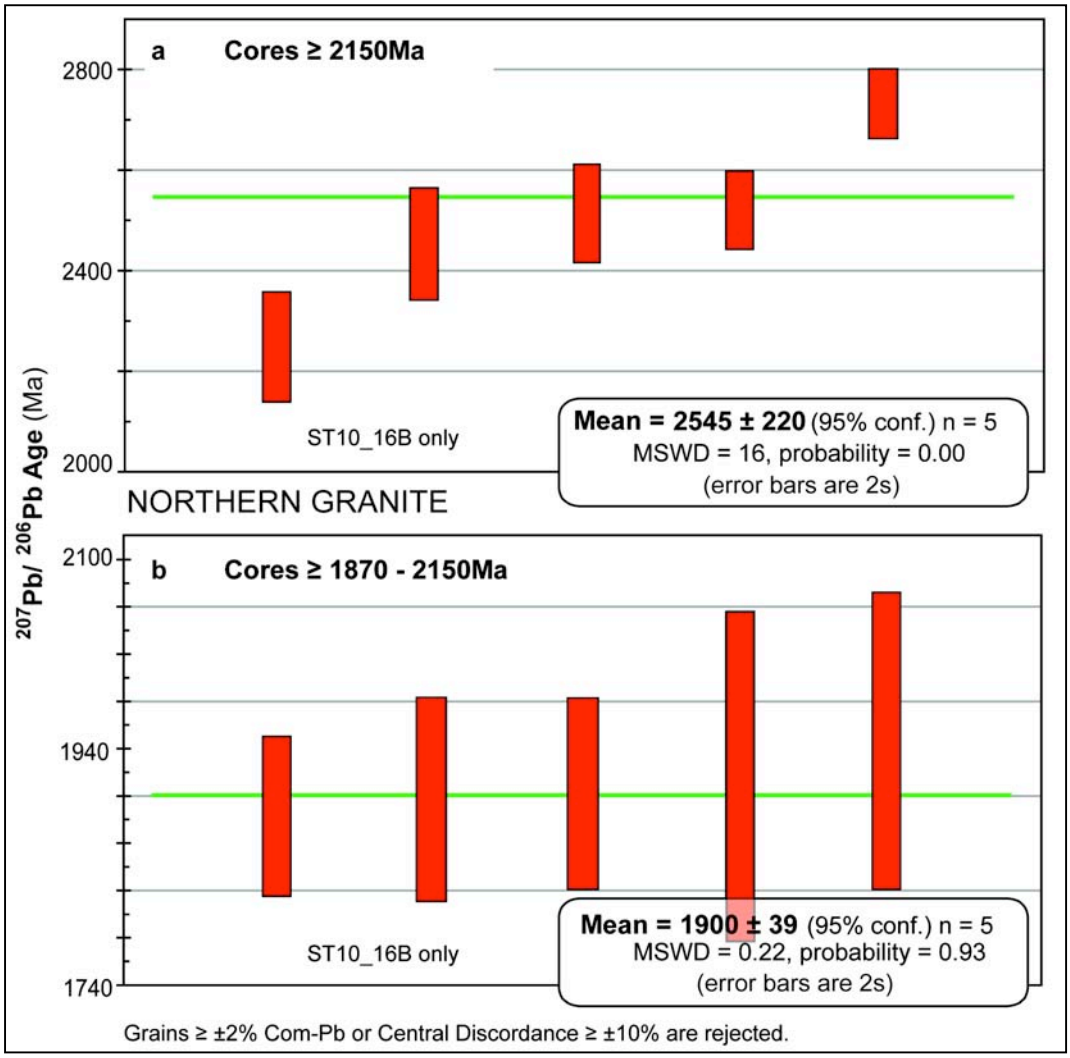

Figure 8.35 Northern Granite $^{207}Pb/^{206}Pb$ Age (Ma): Older Inherited Zircon

Plotted from TerraneChron® spreadsheets using *Isoplot EX3.0* Excel Plugin (Ludwig, 2003)

a) core analyses ≥ 2150Ma. **b**) core analyses ≥ 1870 – 2150Ma

Near-Crystallisation Age Inherited Grains ≤ 1870Ma

U-Pb grains ≤ 1870Ma were divided into age groups to characterise potentially inherited populations. Not surprisingly, as older grains were removed (≥ 1870Ma, ≥ 1850Ma and ≥ 1830Ma, ≥ 1815Ma) the average age was reduced (as shown in Table 8.20). As a consequence of reducing the number of grains (*n*), the MSWD generally increased while the probability decreased. Given the high proportion of inherited grains in the northern granite samples (ST10_16B and ST10_18), they were not included in further U-Pb rejections based on inheritance ages.

Removing grains ≥ 1870Ma from core analyses of the eastern granite resulted in a reduction in age and but an increase in uncertainty (Table 8.20). No grains ≥ 1870Ma were rejected from sample ST10_19C. Interesting, there were no rim analyses ≥ 1870Ma remaining after rejection stages.

Table 8.20 Eastern Granite $^{207}Pb/^{206}Pb$ Age (Ma): Detrital Inheritance Test

U-Pb Zircon Weighted Average Age (Ma): Metasedimentary Inheritance Test								
Rejection Criteria	***n***	**Weighted Average Age** ($^{207}Pb/^{206}Pb$) Ma	**MSWD** %	**Prob. of Fit**	***n***	**Weighted Average Age** ($^{207}Pb/^{206}Pb$) Ma	**MSWD** %	**Prob. of Fit**
	CORES				**RIMS**			
Eastern Granite (ST10_11 + ST10_19C)								
U-Pb Grains	36	1824 ±14	0.88	0.67	36	1792 ±15	1.16	0.24
Inherited Grains near Crystallisation Age								
Grains ≤ 1870Ma	22	1819 ±15	0.62	0.91				
Grains ≤ 1850Ma	20	1812 ±17	0.50	0.96	29	1786 ±15	0.92	0.58
Grains ≤ 1830Ma	14	1801 ±20	0.39	0.97	26	1781 ±15	0.86	0.67
Grains ≤ 1815Ma	10	1788 ±26	0.33	0.97	23	1772 ±17	0.66	0.88

n Number of grains used during age calculation
'Blanks' indicate no grains meeting that criteria were excluded
Data in red indicate ages to be used in this study
Quoted uncertainties are ±1 standard deviation (1σ)

As criteria were further tightened to grains ≤ 1850Ma, uncertainty further increased in the core analyses, but remained stable for the rims (Table 8.20). The eastern granite samples (ST10_11 and ST10_19C) produced ages of 1786 ±15Ma (*n* = 36) based on the rim analyses shown in Figure 8.36. Cores ≤ 1850Ma produced an age at 1812 ±17Ma. However, given that cores are interpreted as being inherited, calculation of ages based on cores ≤ 1850Ma is not reasonably valid given this rejection process actively excludes inherited grains.

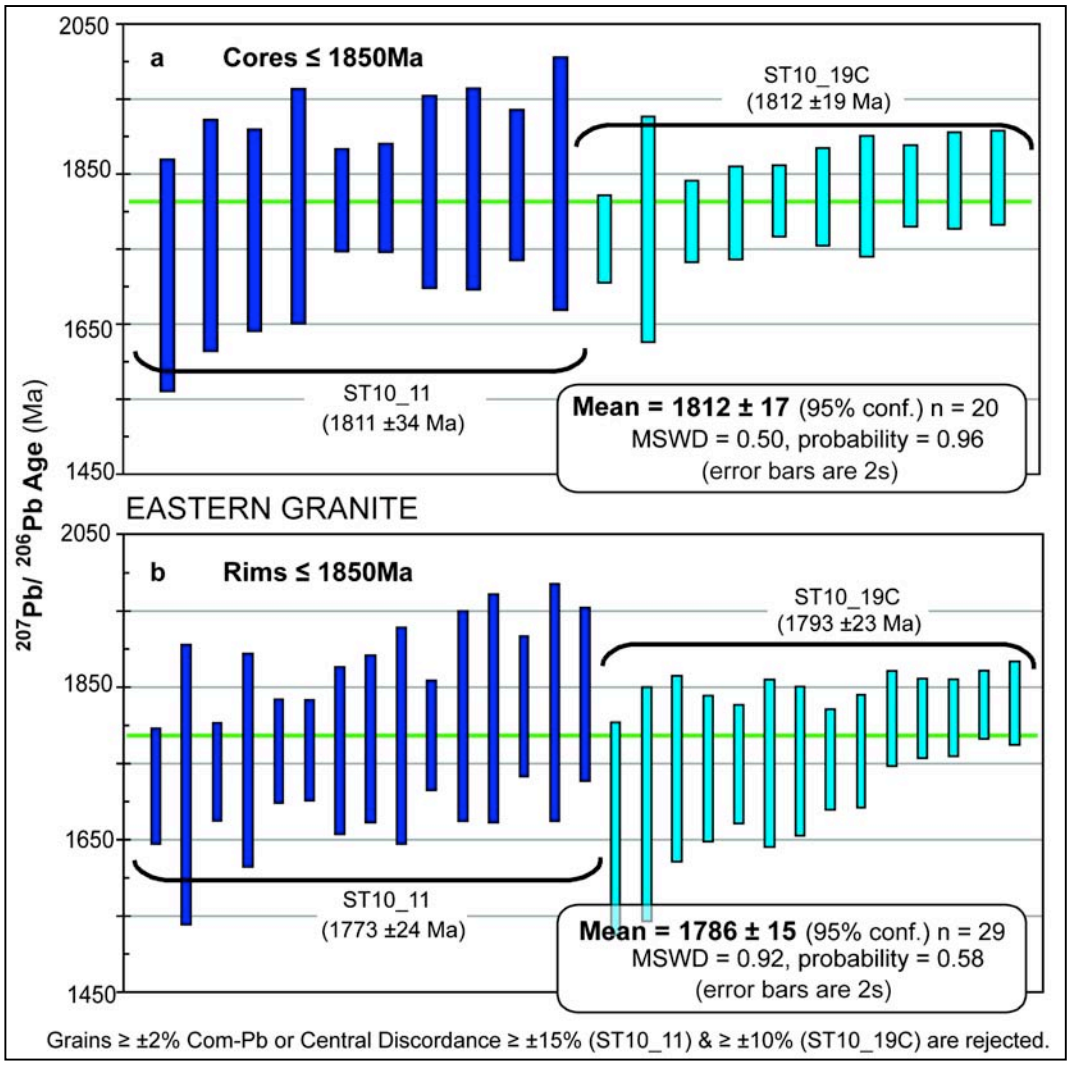

Figure 8.36 Eastern Granite $^{207}Pb/^{206}Pb$ Weighted Average Age (Ma): Grains ≤ 1850Ma
Plotted from TerraneChron® spreadsheets using *Isoplot EX3.0* Excel Plugin (Ludwig, 2003)
a) core + outer core analyses ≤ 1850Ma. **b**) rim analyses ≤ 1850Ma

Reducing the inherited rejection age to ≥ 1830Ma produced an increase in uncertainty by reducing the MSWD further from 1.0 (Table 8.20). Twenty-six rim analyses produce an age of 1781 ±15Ma, with an MSWD of 0.86 and probability of 0.67.

As a final step, grains ≥ 1815Ma were excluded in an attempt to confine the granite emplacement age. Not surprisingly, there is a significant reduction in age, with a minor decrease in MSWD and probability and increasing uncertainty (Table 8.20). Rim analyses from the eastern granite ≤ 1815Ma produce an age of 1772 ±17 (n = 23).

8.12 DISCUSSION OF IGNEOUS INHERITANCE

From the results presented above, it is clear that the zircon extracted from the Mt Stafford granites contain a large proportion of grains inherited from a variety of sources of different ages. Two older populations were identified in both the eastern and northern samples with peaks at ~1900 ±60Ma and ~2450 ±100Ma, based on the analysis of core ages ≥ 1870Ma and ≥ 2150Ma (respectively).

Using 1870Ma as the rejection age for detrital grains in the granite samples was inconclusive. The majority of U-Pb grains were ≤ 1870Ma, resulting in few dismissals and minimal effect on the calculation. Given the age and inheritance characteristics of the northern granite, those analyses were not included in calculations of the granite emplacement age.

Removing grains ≥ 1850Ma resulted in a decrease in calculated age, but generally increased the 1σ uncertainty compared with initial U-Pb results. This increasing uncertainty is a direct result of reducing the number of grains (*n*) in the sample population. Grains ≤ 1850Ma from the eastern granite samples indicate a rim age ca. 1786 ±15Ma, based on $n = 29$ rims interpreted as magmatic. This age is just outside of published data of Rubatto *et al*. (2006) of 1805 ±3Ma, also based on analysis of magmatic rims. The rims surround older cores at 1824 ±14Ma ($n = 36$) (based on U-Pb grains), interpreted as being inherited.

8.12 GEOCHRONOLOGICAL INTERPRETATION

Zircon grains from the Mt Stafford granite samples show a range of characteristics and ages. Typical grains are clear honey-brown, pink-brown and orange-brown with an overall dark CL response. Grains from the northern granite, ST10_18 in particular, were irregular with pervasive open fractures and a large proportion were rejected with ≥ ±2% common-Pb and discordance ≥ 32%. Analysis of zircon ages from the eastern granite were more concordant, with few grains containing common-Pb.

Assessment of REE patterns indicated no distinct compositional differences between older cores and younger rims. In both northern granite samples, analyses have a broad range of LREE. All grains analysed from the eastern granite associated with the mingling zone (ST10_19C) have high LREE, forming a tighter population of values than other samples.

These flatter, higher LREE patterns are typical of zircon having experienced alteration processes associated with metamictisation (Hoskin & Black, 2000). While this evident alteration has resulted in lead loss in the northern granite, there is no evidence for lead loss in the eastern granite samples.

Ages reported here are comparable with published ages. Of interesting note is the difference between the eastern and northern granites. Consistently, throughout U-Pb age analysis, calculated ages are noticeably higher for the northern granite. 1σ uncertainty is generally twice as large, there is a high incidence of grains with common-Pb (experienced lead loss) and many analyses are discordant. The higher proportion of lead loss reflects the contribution of inherited zircon in the northern granite samples.

A similar variation is reported in the limited published literature. Collins & Page (unpublished, cited G.A., 2007, Collins & Williams, 1995) suggest ages of 1818 ±15Ma and 1857 ±19Ma for the northern granite, using SHRIMP $^{207}Pb/^{206}Pb$ zircon data (two samples). Results reported here are within error, indicating an age of 1843 ±16Ma (n = 29) for zircon in the northern granite, based on pooled ages of cores and rims, both interpreted as inherited.

U-Pb geochronology results presented here indicate little difference in morphology and composition between inherited and magmatic grains analysed. The only significant difference between the populations is age. Rejecting rim analyses based on a maximum detrital inheritance age of ≥ 1850Ma has provided a reasonable estimate of emplacement age, at 95% confidence and with low 1σ uncertainty of ±0.8% relative.

Published results of Rubatto *et al*. (2006) report the eastern granite at 1805 ±3Ma, using SHRIMP $^{207}Pb/^{206}Pb$ data. While uncertainties of this magnitude cannot be reproduced in this study, the age reported for the eastern granite is 1786 ±15Ma (n = 29), based on rims ≤ 1850Ma interpreted as magmatic. These magmatic rims surround older cores at 1824 ±14Ma (n = 20), interpreted as inherited.

Of interest are the ages of inherited grains analysed. Inherited cores from the eastern granite produced ages of 1824 ±14Ma, while inherited grains from the northern granite produced ages within uncertainty, at 1843 ±16 (n = 20), using pooled analyses of cores and rims. These results indicate the inherited grains may be derived from a source younger than the Mt Stafford metasedimentary rocks.

Inherited grains, including cores from the eastern granite and all analyses from the northern granite, indicate an inherited source age of 1833 ±10Ma (n = 66), outside of uncertainty on the accepted age of 1866 ±3Ma for the Lander Package metasedimentary units (Claoué-Long *et al.*, 2008).

9. LA-MC-ICP-MS HF ISOTOPE ANALYSIS

9.1 INTRODUCTION

S-type granites, being generated by partial melting of crustal materials, typically contain abundant inherited zircon (Jeon *et al*; 2012). Inherited zircon provides information on the age and Hf-isotopic compositions of the source rock components and may be used to estimate relative contributions of juvenile and re-worked material in granite production (Griffin *et al*., 2007, Jeon *et al*; 2012). Hf-isotopic composition was obtained on U-Pb grains identified during initial U-Pb geochronology, and are presented Appendix F-2.

9.2 ZIRCON Hf-ISOTOPE ANALYSIS

9.2.1 EASTERN GRANITE

Thirty-eight Hf-isotope analyses were completed for ST10_11, on grains that yielded U-Pb compositions with ≤ ±2% common-Pb, ≤ ±15% discordance and ≤ 2150Ma. Initial $^{176}Hf/^{177}Hf$ ratios (Hf_i) show minor variation, ranging from 0.281420 to 0.281626 (Figure 9.1a). Values for inherited analyses (core and rim) older than 1850Ma cluster about the model CHUR evolution line, whereas those analyses (core and rim) younger than 1850Ma considered magmatic are below the CHUR line.

A similar trend is reflected by εHf values, displaying a range of -7.44 to +1.40 (Figure 9.1b). εHf is higher for inherited grains ≥ 1850Ma (-2.47 to 1.40), clustering about the CHUR model line. Magmatic rims ≤ 1850Ma have εHf values ranging from -7.44 to -1.32, and are well below the CHUR model line. There is no distinction in either εHf or Hf_i values between the cores and rims analysed.

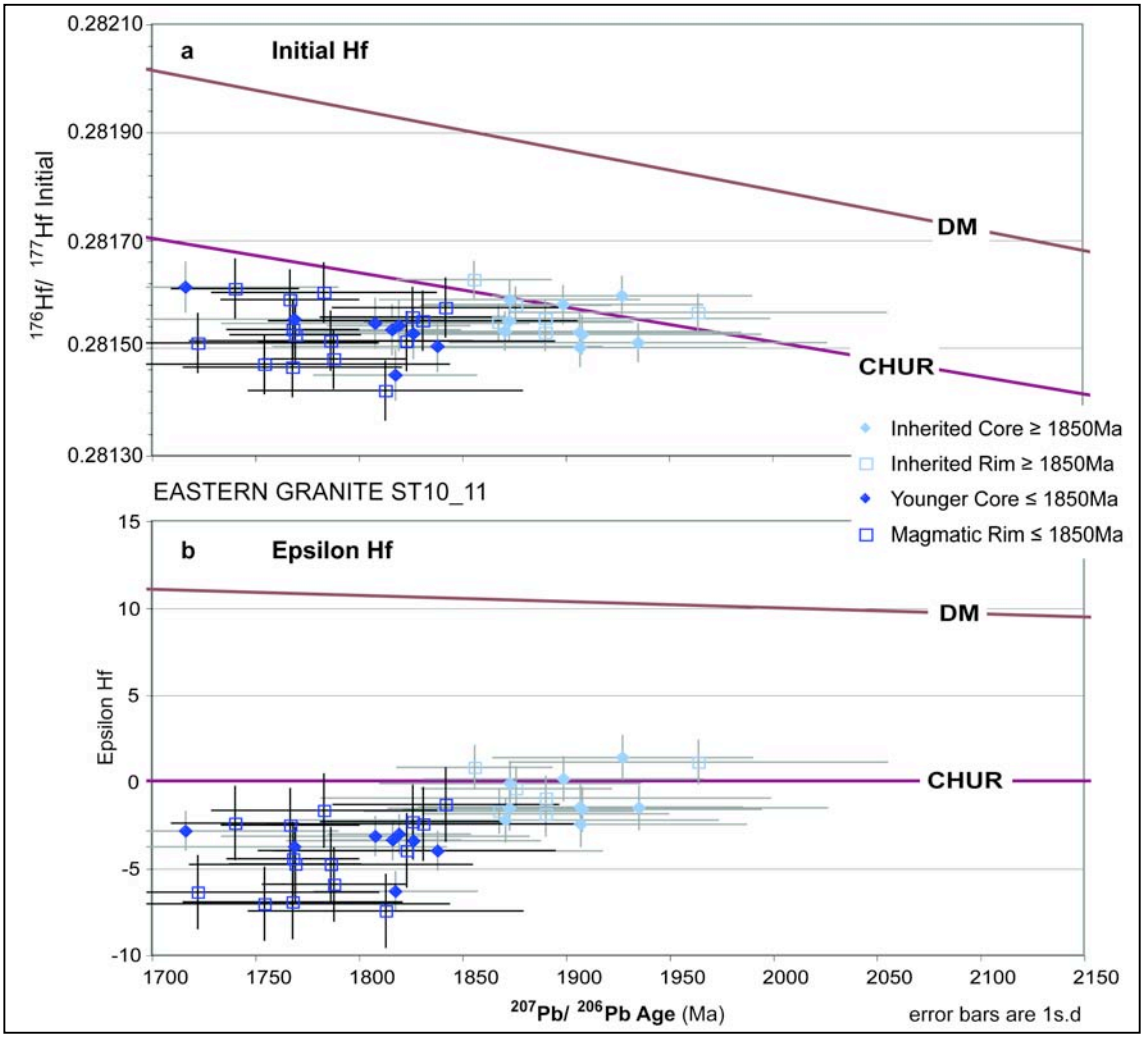

Figure 9.1 Eastern Granite ST10_11 Hf-Isotope Analysis (Hf_i & εHf)
Plotted from TerraneChron® spreadsheets using *Isoplot EX3.0* Excel Plugin (Ludwig, 2003)
a) Initial Hf (Hf_i) after Blichert-Toft *et al*., 1997. **b**) Epsilon Hf (εHf) after Scherer *et al*., 2001

Hf-isotope analyses of 32 grains from sample ST10_19C produce a similar range in Hf_i values, but are slightly higher than the previous sample: 0.281465 to 0.281707 (Figure 9.2a). Values for inherited cores ≥ 1850Ma cluster about the CHUR model, with magmatic grains on the CHUR model line.

εHf values range -5.93 to +3.57 (Figure 9.2b) and are again higher for inherited cores ≥ 1850Ma (-2.77 to +2.12) than for rims ≤ 1850Ma (-3.71 to +0.77). In general, this sample has higher Hf_i and εHf values that the other eastern granite, with the majority of results plotting near the CHUR line.

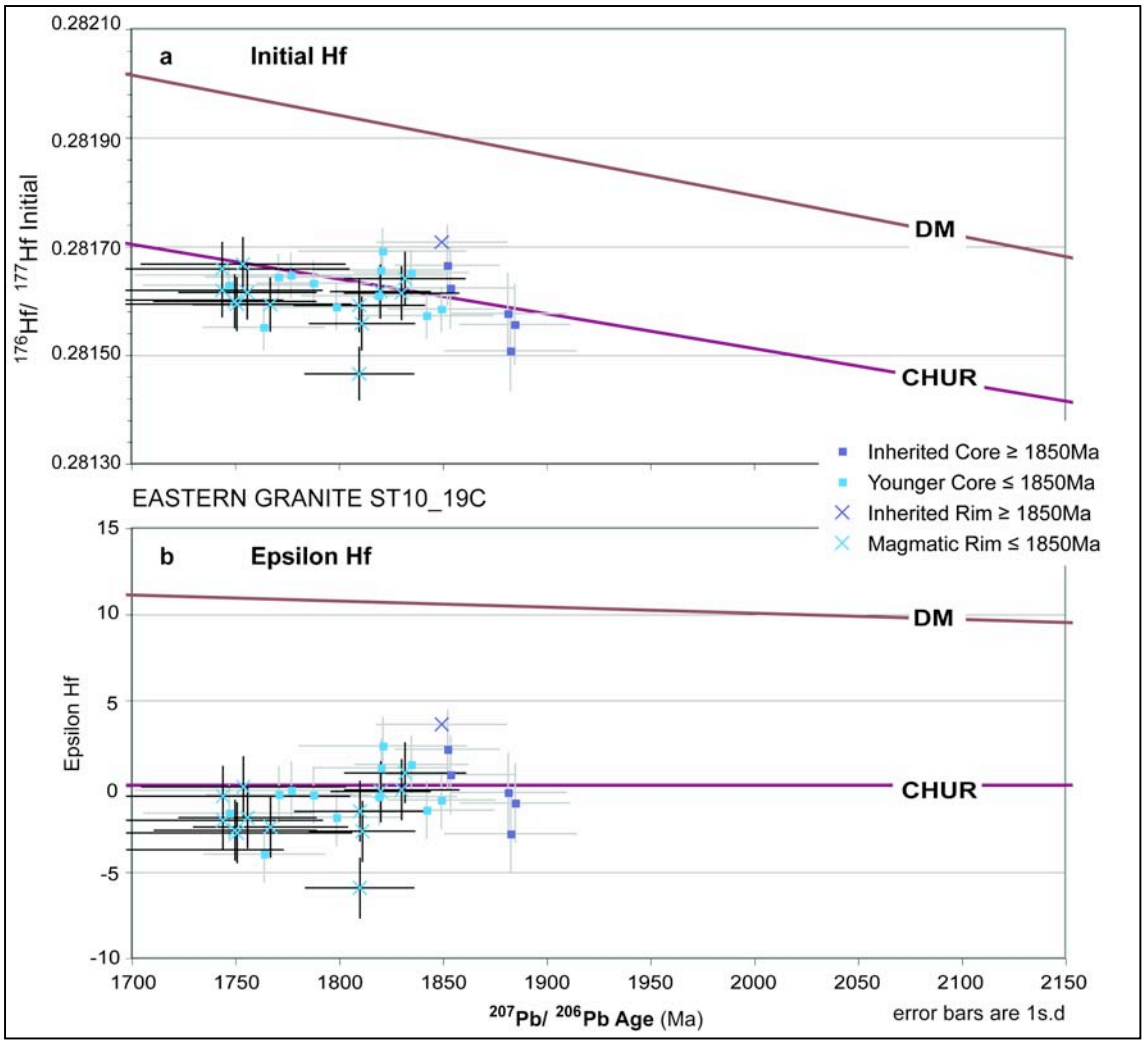

Figure 9.2 Eastern Granite ST10_19C Hf-Isotope Analysis (Hf_i & εHf)
Plotted from TerraneChron® spreadsheets using *Isoplot EX3.0* Excel Plugin (Ludwig, 2003)
a) Initial Hf (Hf_i) after Blichert-Toft *et al*., 1997. **b**) Epsilon Hf (εHf) after Scherer *et al*., 2001

9.2.2 Northern Granite

Forty-four Hf-isotope analyses for sample ST10_16B were completed. Hf_i values have a significantly larger variation than other samples, ranging from 0.280982 to 0.281623 (Figure 9.3a). Analyses (cores and rims) ≥ 1850Ma are clustered about the CHUR model, with analyses ≤ 1850Ma plotting below the CHUR line.

εHf values also reflect the large Hfi variation, ranging -15.90 to +4.02 (Figure 9.3b). Values are generally lower for younger rims ≤ 1850Ma (-8.72 to -1.72). Grains cores ≥ 1850Ma show a range of higher values (-1.07 to 2.94), with older rims ≥1850Ma the highest range of -5.49 to 5.72, increasing toward the CHUR line. Several outlying less-radiogenic grains reflect altered, inherited grains ≥ 1850Ma (Figure 9.3).

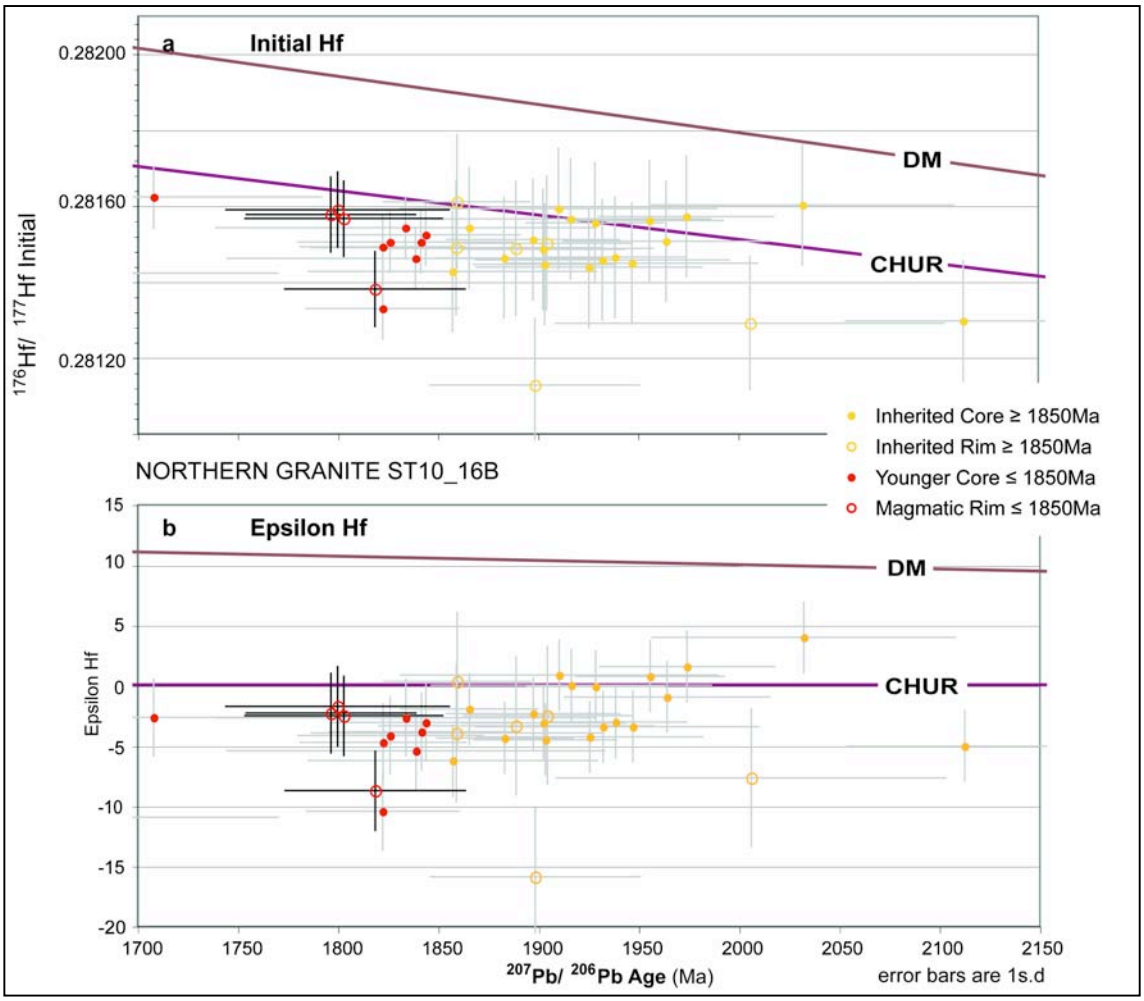

Figure 9.3 Northern Granite ST10_16B Hf-Isotope Analysis (Hf_i & εHf)
Plotted from TerraneChron® spreadsheets using *Isoplot EX3.0* Excel Plugin (Ludwig, 2003)
a) Initial Hf (Hf_i) after Blichert-Toft *et al*., 1997. **b**) Epsilon Hf (εHf) after Scherer *et al*., 2001

Only seven Hf analyses were completed on sample ST10_18 due the high number of discordant grains and those with common-Pb. Hf_i ranges from 0.281494 to 0.281677 (Figure 9.4a) with εHf from -3.01 to +3.31 (Figure 9.4b). An apparent low range of values is a result of limited number of analysis, however the range is not dissimilar to previous samples (ST10_11).

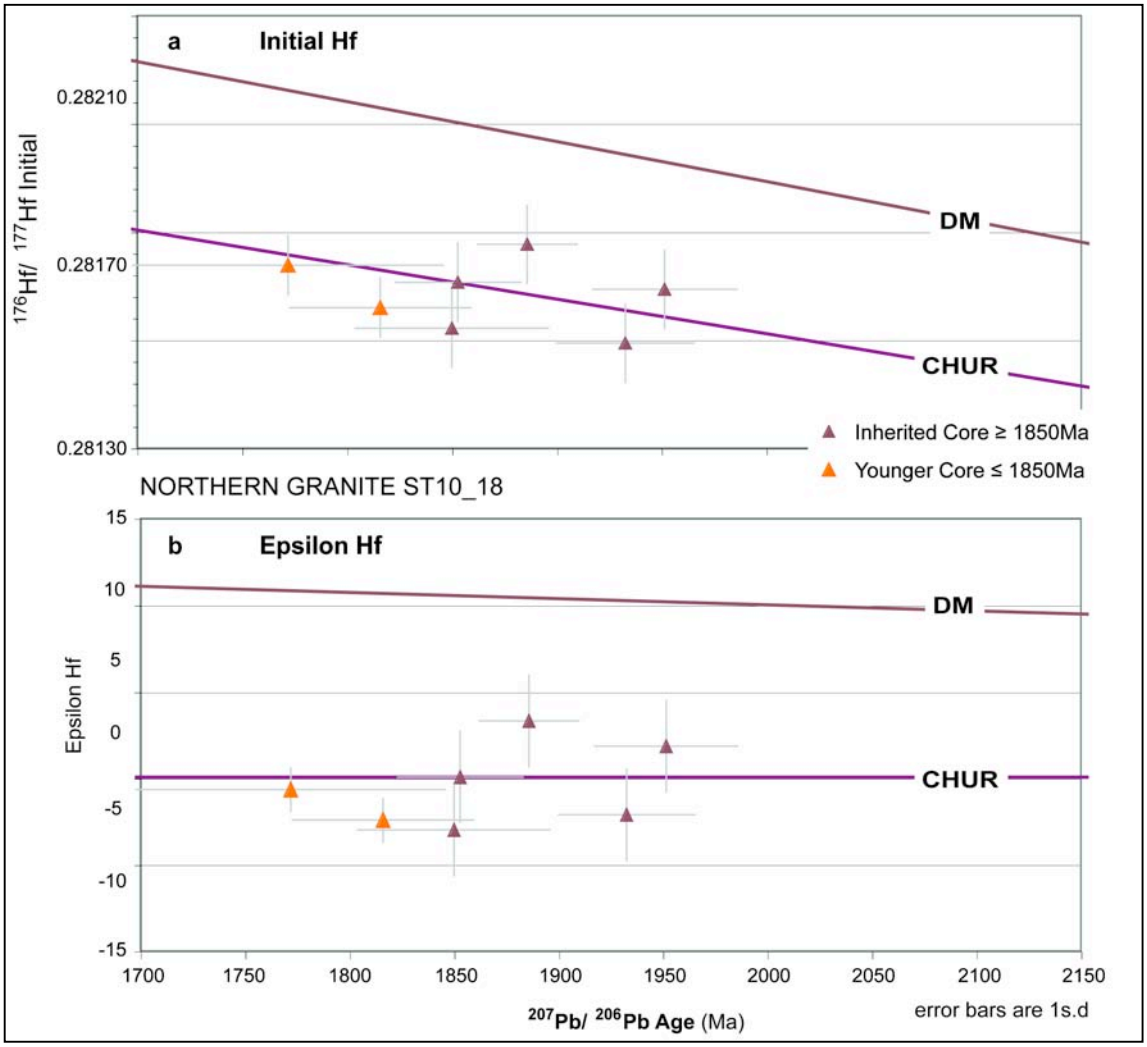

Figure 9.4 Northern Granite ST10_16B Hf-Isotope Analysis (Hf_i & εHf)
Plotted from TerraneChron® spreadsheets using *Isoplot EX3.0* Excel Plugin (Ludwig, 2003)
a) Initial Hf (Hf_i) after Blichert-Toft *et al*., 1997. **b**) Epsilon Hf (εHf) after Scherer *et al*., 2001

Overall, Hf_i demonstrates no discernable trends with age (Figure 9.5). This may represent the reworking of grains along Concordia, and therefore reflects the influence of reworked material in the granite production. The northern granite ST10_16B shows a greater variation in both Hf_i and εHf values. Hf_i and εHf in ST10_19C from the proposed mingling zone are marginally more radiogenic than other samples analysed.

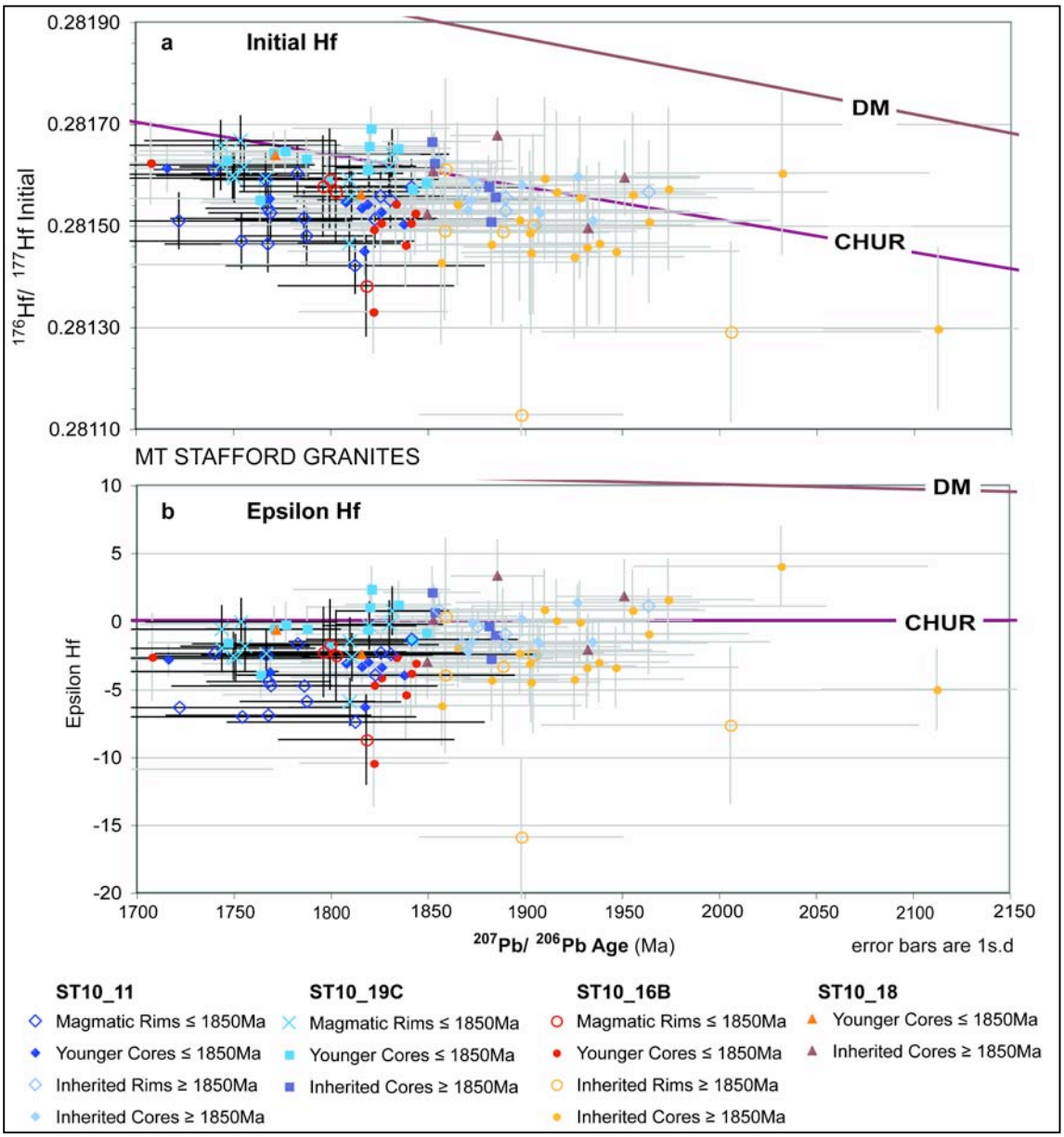

Figure 9.5 Combined Mt Stafford Granites Hf-Isotope Analysis (Hf_i & εHf)
a) Initial Hf (Hf_i) after Blichert-Toft *et al*., 1997. **b**) Epsilon Hf (εHf) after Scherer *et al*., 2001

The GEMOC Classification and Regression Tree (CART) diagram presented in Figure 9.6 indicates zircons are of broadly similar composition (Belosouva *et al*., 2002). From *n* = 104 U-Pb grains, 72 (55.8%) are derived from a granitoid source with 70-75% SiO_2. 24.0% indicate a granitoid source with 65-70% SiO_2. CART rock type results are a summarised in Table 9.1.

Five grains (4.8%) from ST10-19C indicate a doleritic source. However, the discriminating value for this bin on the CART diagram is ≤ 0.58ppm. Given that minimum detection limits report in this study are 2.5ppm, this result is within uncertainty of the technique and is treated accordingly.

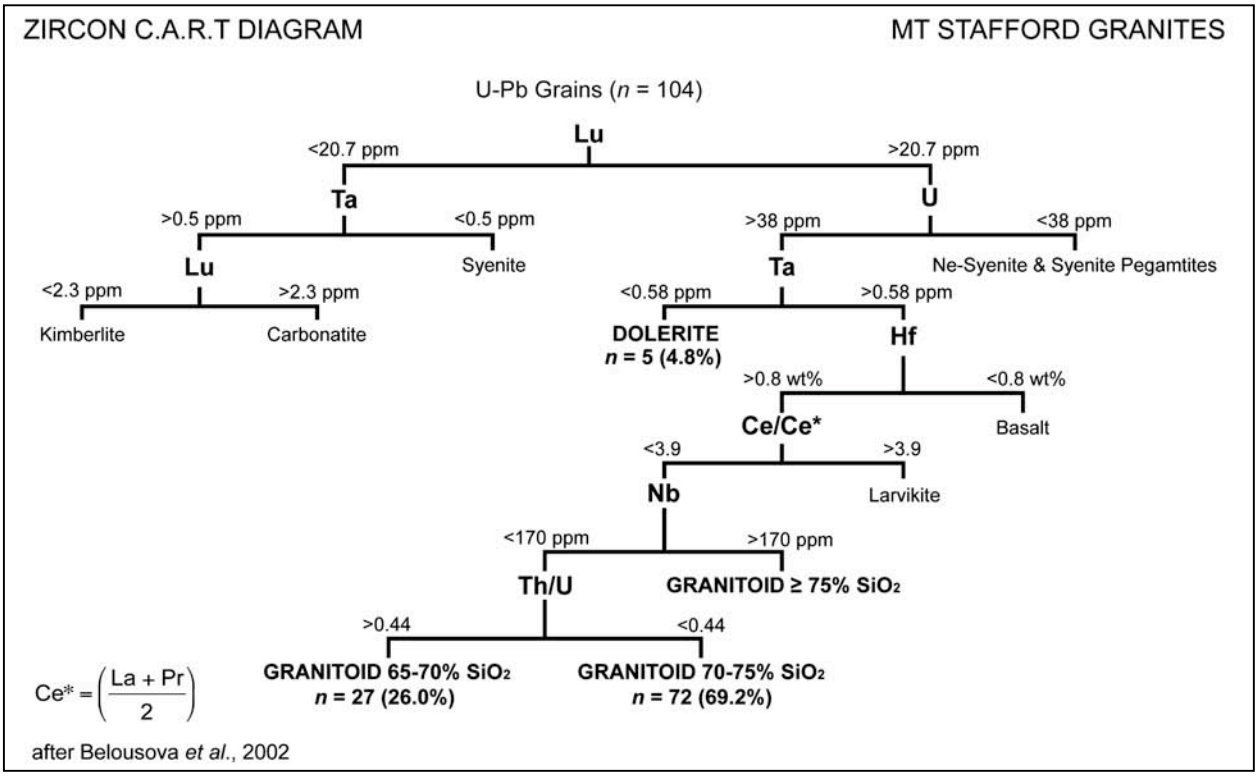

Figure 9.6 Combined Mt Stafford Granites CART Classification Diagram after Belousova *et al*. (2002). Total Population *n* = 104. Using data obtained during EMP, LAM-ICP-MS and LAM-MC-ICP-MS, as summarised in the Zircon Composition Summary, Appendix F-1. Ce* calculated as shown. Lu & U inferred for grains rejected from U-Pb analysis, Appendix F-3.

Table 9.1 CART Rock Type Summary: All Grains, U-Pb Grains & Magmatic Grains ≤1850Ma

CART Diagram Source Rock Type						
	All Grains		**U-Pb Grains**		**Grains ≤ 1850Ma**	
ROCK TYPE	***n***	***n*%**	***n***	***n*%**	***n***	***n*%**
Total No. Grains	210		104		57	
Dolerite	12	5.71	5	4.81	3	5.26
Granitoid 65-70% SiO2	61	29.05	27	25.96	10	17.54
Granitoid 70-75% SiO2	133	63.33	72	69.23	44	77.19
Granitoid ≥ 75% SiO2	4	1.90	0	-	0	-

CART Rock Type after Belousova *et al*., 2002

9.3 Discussion of Hf-Isotope Analysis

Hf-isotope analyses indicate no discernable trends or significant variation in Hf_i and/or εHf with increasing or decreasing age; core and rim analyses cover a similar range of values. While most samples show a minimal increase in $^{177}Hf/^{176}Hf$ ratio with age, ST10_16B from the northern granite has generally consistent $^{177}Hf/^{176}Hf$ ratios with age. All samples define a generally confined population, with few outlying less radiogenic rim analyses (ST10_16B). εHf values increase with increasing age.

Analyses ≥ 1850Ma interpreted as derived from inherited detrital grains, cluster about the CHUR model evolution line. Those grains younger than 1850Ma plotted below the CHUR in all cases. Less radiogenic Hf values toward the CHUR model evolution line indicate zircon compositions with a higher crustal-derived component (Belousova *et al*., 2006b, Shaw & Flood, 2009). The results reflect the contribution of recycled crustal material during granite production at Mt Stafford.

During U-Pb analysis, the spread of individual ages also reflects the contribution of older, inherited grains in the zircon population. In the field, the diffuse and gradational nature of the contact between the metasedimentary rocks, hybrid diatexite and northern granite also suggest a significant contribution of inherited material at this location.

10. DISCUSSION

A range of geochemical and geochronological methods have been presented to characterise two granite plutons and associated hybrid diatexite and quartz-diorite samples from the Mt Stafford area. Bringing the results together shows the eastern and northern granites are related in mineralogy and chemical composition. The data highlights the intimate relationship between the hybrid diatexite (and metasedimentary rocks) with the northern granite.

10.1 MINERAL & GEOCHEMICAL COMPARISON

The results of petrography, EMP mineral chemistry and XRF indicate mineral and chemical similarities between the four granite samples and the hybrid diatexite sample. Petrography shows granite mineral assemblages of K-feldspar (microcline), cordierite and quartz, with plagioclase and biotite in varying amounts. While there are some differences in texture, the irregular and embayed shape of individual mineral grains is consistent across the samples. There is a general absence of euhedral feldspar; most grains show irregular morphology.

Samples associated with the quartz-diorite mingling zone included higher proportions of plagioclase and mafic minerals including epidote, amphibole and titanite. Titanite was also identified in the adjacent samples of the eastern granite, consistent with mechanical mixing of grains between granite and quartz-diorite.

Evidence of sericite alteration is visible in all samples, indicating varying degrees of hydrous alteration. The northern granite is more extensively recrystallised than the eastern granite, hybrid diatexite or mingling zone samples, with significant alteration of biotite and muscovite. Myrmekite intergrowths in several samples from the eastern granite, northern granite and hybrid diatexite (ST10_11, ST10_16B and ST10_19D) reflect high temperature alteration.

XRF data indicates that whole rock chemistry is comparable between the granite samples. The granite samples may be distinguished from the mafic mingling zone and hybrid diatexite samples, but no trends to distinguish the eastern and northern granites themselves. REE compositions obtained by XRF also show that values between the granite samples are comparable, and offer no means by which these granites may be distinguished. High SiO_2 content of the hybrid diatexite sample is consistent with assimilation of silica-rich country rock xenoliths.

Zircon trace element patterns show both cores and rims of grains from the eastern granite at the mingling zone site (ST10_19C) have enriched LREE compositions, along with many analyses from other samples. This reflects processes of alteration of the grains and incorporation of LREE. These grains were shown to contain common-Pb and were rejected from age calculations. In the eastern granite, there was no evidence for lead loss, and the ages were therefore not affected.

10.2 TIMING OF MAGMATIC & METAMORPHIC EVENTS

The similar age of granite emplacement and metamorphism of the Mt Stafford meta-sedimentary rocks reflect the complex relationships between the timing of magmatism and metamorphism (Vernon *et al.*, 1993, White *et al*., 2003). The Stafford event, responsible for widespread bi-modal magmatism and emplacement of the northern and eastern granites, is estimated to have been active ca. 1810 to 1790Ma.

From the samples analysed in this study, there is some disparity in age between the eastern and northern granites. The eastern granite, in all steps of U-Pb dating, provided more concordant ages with more acceptable uncertainty than the northern granite samples. Since grains from the northern granite samples had significantly higher incidence of common-Pb and discordance, the calculation of age on a limited number of grains yielded ages with higher uncertainty.

The results indicate the eastern granite is dated at 1786 ±15Ma, calculated using the rims of grains ≤1850Ma, interpreted as being magmatic. This is just outside 1σ uncertainty of published values of 1805 ±3Ma (Rubatto *et al*, 2006). Older inherited cores produced an age of 1824 ±14Ma, suggesting a source younger than the surrounding Mt Stafford metasedimentary rocks (1866 ±3Ma).

The apparent older age of the northern granite suggests that this study dated inherited grains, producing an age ca. 1843 ±16Ma using the pooled analyses of cores and rims. This age is within uncertainty of core ages of the eastern granite. Therefore, magmatic crystallisation age is not reported for the northern granite. The older age reported by Rubatto *et al*. (2006) must be questioned in the light of this study. It is possible that some near-crystallisation inherited grains may have been pooled.

The difference in calculated age for the eastern and northern granites has more significance when combined with field relationships and published data. The northern granite intruded into partly molten zone 5 migmatites, which implies that magmatism was active during peak metamorphism M_{1a}. The intrusion cuts the D_{1a} metamorphic isograds. This also accounts for higher proportion of inherited detrital zircon within age-uncertainty of the Mt Stafford metasedimentary rocks.

Foliation identified in the eastern granite is co-magmatic, with inclusion of biotite-rich mafic enclaves, interpreted as being entrained xenoliths of Mt Stafford metasedimentary rocks. The granite post-dates the S_{1b} foliation, but is locally foliated by S_{1c} (Vernon *et al*., 1993, this study). Field relationships and textural observations suggest the eastern granite intruded post-D_1 but pre-D_2 deformation, marginally later than the northern granite.

10.3 ZIRCON INHERITANCE

Inherited zircon grains could not be distinguished from magmatic grains on the basis of morphology, trace element composition or Hf-isotopic ratios. Zircon picked from all samples showed similarities in morphology, colour and generally dark CL-response. Grains picked from the northern granites did exhibit more pervasive fractures, and more grain fragments were present.

The calculated age for pooled zircon analyses in the northern granite is 1843 ±16Ma. However, grains are commonly affected by lead loss (sample ST10_18), and field relationships show this age is too old to be the magmatic crystallisation age. This older age likely reflects the inclusion of Mt Stafford member detrital zircons during intrusion into partly-molten zone 5 migmatites during peak D_{1a}-M_{1a} metamorphism (Greenfield *et al*., 1996, White *et al*., 2003). The pooled age likely reflects a mix of xenocrystic near crystallisation age zircon and magmatic zircon.

Using a detrital peak of ≥ 1850Ma as the upper limit for magmatic rims, ages for the eastern granite were constrained to 1786 ±15Ma. This detrital peak was based on reported ages of Mt Stafford metasedimentary rocks of 1866 ±3Ma (Claoué-Long *et al*., 2008), and a lack of individual grains with ages 1850 – 1870Ma. The age produced by analyses of inherited cores suggest an age of 1824 ±24Ma, outside of uncertainty of the accepted age of the meta-sedimentary country rocks.

This suggests the source of inherited material is younger than the surrounding Mt Stafford metasedimentary rocks. The granites intruded at depth in the crust, reflected by the increase in grade during peak metamorphic temperatures of ≥ 750ºC at a pressure of 2.5 ±0.6kbar increased to 3.7 ±0.5kbar (Clarke *et al*., 1990). The accepted tectonic model (Collins & Vernon, 1991, Collins *et al*., 1991, Collins & Williams, 1995,) is an environment of crustal thickening following crustal thinning, where granites are produced from partial melting of the crust and spread laterally as sheets (shown in Figure 10.1). Shorting of the crust is accommodated by deep thrusting and folding (Collins & Vernon, 1991) demonstrating a means by which younger crustal source material may be involved in granite formation at depth below overthrust rocks now represented by the Mt Stafford metasedimentary rocks (Figure 10.1).

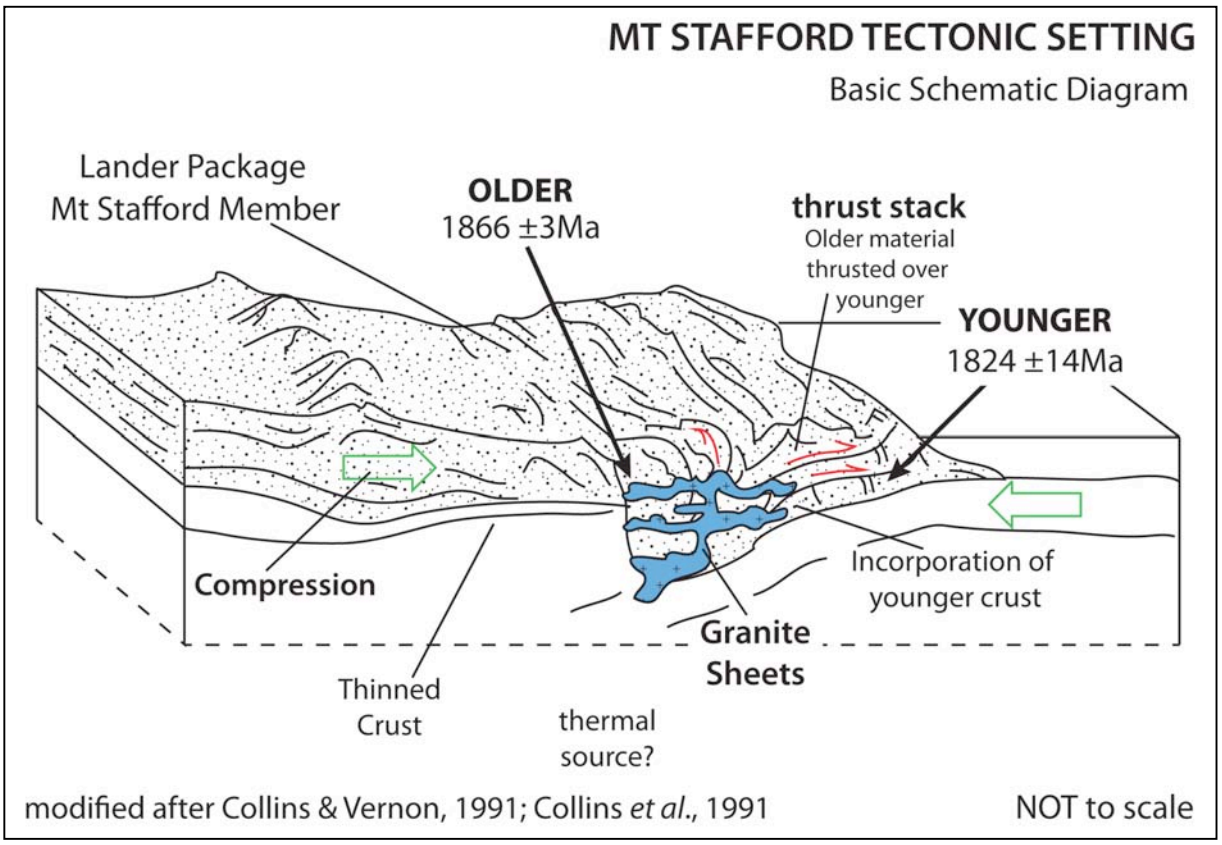

Figure 10.1 Schematic Tectonic Diagram of Granite Formation Mt Stafford

Compression shortly following crustal thinning (thermal source not known with certainty). Older material is thrust over younger material. Younger material at the base of the "thrust stack" is dragged in and incorporated in granite production. Modified after Collins & Vernon, 1991, Collins *et al*., 1991

10.4 Contribution of Juvenile & Recycled Material in Granite Production

Comparison of Hf-isotope composition indicates values are similar for all samples. Inherited cores and magmatic rims, or discordant grains are not distinguished by Hf-isotopic composition. Results show $^{176}Hf/^{177}Hf$ ratios and εHf values generally below the CHUR model line, indicating a significant contribution of recycled crust in local granite production at Mt Stafford.

The Hf-isotope data reflects the high proportion of inherited detrital zircon and the intimate and gradational relationship between the northern granite and zone 5 migmatites. Zircon from the mingling zone do show slightly higher initial $^{176}Hf/^{177}Hf$ ratios, but the variation is minimal.

10.5 Quartz-Diorite – Granite Mingling Zone

Although thorough investigation of the proposed quartz-diorite - granite mingling zone is beyond the scope of this study, the limited data indicates compositional differences between the mafic samples, and minor variation in Hf-isotope ratios when compared with other granite samples. Field occurrence, along with petrographic and XRF analyses, indicate a mixing or mingling relationship between the quartz-diorite samples and quenching of the eastern granite at this location.

Hf-isotope ratios from the mingling zone allude to more radiogenic values, with marginally higher initial $^{176}Hf/^{177}Hf$ ratios. Whilst values do not indicate a mantle-derived source material, the data implies an influence of more juvenile material on granite production at this location. This may be a topic for further study, including detailed analysis of the quartz-diorite samples.

11. CONCLUSIONS

The Mt Stafford granites form part of a variably deformed package of metasedimentary and igneous rocks. The eastern and northern granites are mineralogically, chemically and isotopically similar, forming part of a larger tectonothermal system responsible for the metamorphism at Mt Stafford. Hf-isotope zircon compositions suggest a significant contribution of recycled crustal material in local granite production. This is also reflected by the abundance and variety of inherited zircon in granite plutons, creating a complex geochronological problem.

The timing of magmatism and metamorphism are similar, if not identical. Removing inherited grains ≥ 1850Ma suggest an age of 1786 ±15Ma for granite emplacement, based on magmatic rims of zircon from the eastern granite. There were no apparent affects of alteration on $^{207}Pb/^{206}Pb$ ages. Inherited crustal material is reflected by the age of grain cores, suggesting inheritance from a source dated 1824 ±14Ma, younger than the surrounding metasedimentary rocks dated at 1866 ±3Ma. The zircon population in the northern granite is dominated by inherited grains suggesting a source dated ca. 1843 ±16Ma, or a mix of 1824 ±14Ma source grains and 1866 ±3Ma emplacement level contamination.

This study highlights the complex relationship between the timing of magmatic and metamorphic events at Mt Stafford. Geochronolgical investigation has shown the contribution of inherited zircon at Mt Stafford is significant. This study suggests the relationship between the granites and metasedimentary units is not a simple case of inherited material from country rock, but involves processes of incorporation of younger source material during granite emplacement at varying depth in the crust.

12. LIMITATIONS & FURTHER RESEARCH

12.1 LIMITATIONS OF THIS STUDY

Limitations of this study are typically related to the number of samples analysed in the limited time available. A greater number of granite samples from different locations may characterise these intrusions to a more detailed degree. Given the large number of discordant U-Pb analyses from the northern granite, more time may have permitted the analysis of further grains to achieve a more concordant U-Pb dataset. A greater number of individual grains are required to provide more conclusive information surrounding core-rim relationships.

Initially, a Terranechron® assessment of modern stream sediments was planned to be included with this study. Due to the time constraints and lengthy analysis processes, this part of the study was removed. The subject location also has diffusive and poorly defined catchment areas, so any investigation of the sediment source may have been inconclusive.

12.2 SUGGESTIONS FOR FURTHER RESEARCH

The proposed quartz-diorite – granite mingling zone provides an opportunity for further study. Trace element and Hf-isotope data from this study indicates an influence of source material that may be different from the granites. Thorough trace element and Hf-isotope analysis of all samples from this location may provide insight into relationships in this area. Personal communication with Ron Vernon indicates he observed, but never published on, similar mingling features in the northern granite. The investigation of any granite mingling in the northern granite also presents a complementary objective for further investigation.

Further research on the Mt Stafford metasedimentary rocks is continuing through the PhD research of Eileen Dunkley (Macquarie University) and Wei Wang (Univeristy of Sydney), and the honours research of Kristina Gordon (Macquarie University). It is hoped the granite samples investigated during this study can be incorporated for further research to provide a greater understanding of inheritance, magmatism and metamorphism at Mt Stafford. The role of the mafic sills and dykes throughout the metasedimentary rocks in advection of heat to drive the metamorphism is one poorly understood aspect of the Mt Stafford geology. Further research into the field relationships, timing and history of the mafic sills and dykes is needed.

REFERENCES

Andersen, T., 2002, *Correction of Common Lead in U–Pb Analyses that do not Report 204Pb*, in Chemical Geology, Vol. 192, pp. 59-79

Andersen, T., 2005, *Detrital Zircons as Tracers of Sedimentary Provenance: Limiting Conditions from Statistics & Numerical Simulation, in Chemical Geology*, Vol. 216, pp. 249-270

Bau, M., 1991, *Rare-Earth Element Mobility During Hydrothermal & Metamorphic Fluid-Rock Interaction & the Significance of the Oxidation State of Europium*, in Chemical Geology, Vol. 93, pp. 219–230

Belousova, E. A., Griffin, W. L., O'Reilly, S. Y. & Fisher, N.L., 2002, *Igneous Zircon: Trace Element Composition as an Indicator of Source Rock Type*, in Contributions to Mineral Petrology, Vol. 143, pp. 602-622

Belousova, E. A., Griffin, W. L. & O'Reilly, S. Y., 2006a, *Zircon Crystal Morphology, Trace Element Signatures & Hf Isotope Composition as a Tool for Petrogenetic Modelling: Examples From Eastern Australian Granitoids*, in Journal of Petrology, Vol. 47, pp. 329-353

Belousova, E.A., Reid, A.J., Schwarz, M.P., Griffin, W.L. & Fairclough, M.C., 2006b, *Crustal Evolution of the Gawler Craton, South Australia: Application of the TerraneChron™ Technique to Detrital Zircon from Modern Stream Sediments*, Report Book RB2006/00004

Black, L.P., Kamo, S.L., Williams, I.S., Mundil, R., Davis, D.W., Korsch, R.J. & Foudolis, C., 2003. *The Application of SHRIMP to Phanerozoic Geochronology: a Critical Appraisal of Four Zircon Standards, in Chemical Geology*, Vol. 200, pp. 171-188

Blichert-Toft, J., Chauvel, C. & Albarede, F., 1997, *Separation of Hf & Lu for High Precision Isotope Analysis of Rock Samples by Magnetic Sector Multiple Collector ICP-MS*, in Contributions to Mineral Petrology, Vol. 127, pp. 248-260

Chappell, B. W. & White, A. J. R., 2001, *Two Contrasting Granite Types: 25 Years Later*, in Australian Journal of Earth Sciences, Vol. 48, pp. 489-499

Clarke, G.L., Collins, R.H. & Vernon, R.H., 1990. *Successive Overprinting Granulite Facies Metamorphic Events in the Anmatjira Range, Central Australia*, in Journal of Metamorphic Geology, Vol. 8, pp. 65-88

Claoué-Long, J. & Edgoose, 2008, *The Age & Significance of the Ngadarunga Granite in Proterozoic Central Australia*, in Precambrian Research, Vol. 166, pp. 219-229

Claoué-Long, J. C., & Hoatson, D. M., 2005*; Proterozoic Mafic–Ultramafic Intrusions in the Arunta Region, Central Australia; Part 2: Event Chronology & Regional Correlations*, in Precambrian Research, Vol. 142, pp. 134-158

Claoué-Long, J., Edgoose, C & Worden, K., 2008, *A Correlation of Aileron Province Stratigraphy in Central Australia*, in Precambrian Research, Vol. 166, pp. 230-245

Collins, W.J. & Shaw, R.D., 1995, *Geochronological Constraints on Orogenic Events in the Arunta Inlier: a Review*, in Precambrian Research, Vol. 71, pp. 315-346

Collins, W.J. & Teyssier C., 1989, *Crustal Scale Ductile Fault Systems in the Arunta Inlier, Central Australia*, in Tectonophysics, Vol. 158, pp. 49-66

Collins, W.J. & Vernon, R.H., 1991, *Orogeny Associated with Anticlockwise P-T-t Paths: Evidence from Low-P, High-T Metamorphic Terranes in the Arunta Inlier, Central Australia*, in Geology, Vol. 19, pp. 835-838

Collins, W.J., Vernon, R.H. & Clarke, G.L., 1991, *Discrete Proterozoic Structural Terranes Associated with Low-P High-T Metamorphism, Anmatjira Range, Arunta Inlier, Central Australia: Tectonic Implications*, in Journal of Structural Geology, Vol. 13, No. 10, pp. 1157-1171

Collins, W.J. & Williams, I.S., 1995, *SHRIMP Ionprobe Dating of Short-Lived Proterozoic Tectonic Cycles in the Northern Arunta Inlier, Central Australia*, in Precambrian Research, Vol. 71, pp. 69-89

Compston, D.M., 1995, *Time Constraints on the Evolution of the Tennant Creek Block*, in Precambrian Research, Vol. 71, pp. 107-129

Deer, W. A., Howie, R. A. & Zussman, J., 1992, *An Introduction to the Rock-Forming Minerals*, 2nd Edition, Pearson Education Limited, England

Electron Microscopy Sciences (E.M.S.)., 2011, *SEM/TEM Carbon Coaters: Techniques & Applications*, accessed via http://www.emsdiasum.com/microscopy/technical/datasheet/carbon_coating.aspx, date accessed 02.02.11, date of last update unknown

Geoscience Australia, 2005, *Stratigraphic Names Database: Lander Rock Formation*, access via http://dbforms.ga.gov.au/pls/www/geodx.strat_units.sch_full?wher=stratno=69780, date accessed 29.03.10, date of last update 07.09.09

Geoscience Australia, 2006, *Stratigraphic Names Database: Mt Stafford Member*, access via http://dbforms.ga.gov.au/pls/www/geodx.strat_units.sch_full?wher=stratno=27090, date accessed 29.03.10, date of last update 16.04.09

Geoscience Australia, 2007, *SHRIMP U-Pb Geochronology Interim Data Release July 2007*, accessed via https://www.ga.gov.au/products/servlet/controller?event=FILE_SELECTION&catno=65358, date accessed 19.01.11, date of last update 16.11.09

Greenfield, J.E., Clarke, G.L., Bland, M. & Clark, D.J., 1996, *In-Situ Migmatite & Hybrid Diatexite at Mt Stafford, Central Australia*, in Journal of Metamorphic Geology, Vol. 14, pp. 413-426

Greenfield, J.E., Clarke, G.L. & White, R.W., 1998, *A Sequence of Partial Melting Reactions at Mt Stafford. Central Australia*, in Journal of Metamorphic Geology, Vol. 16, pp. 363-378

Griffin, W.L., Wang, X., Jackson, S.E., Pearson, N.J., O'Reilly, S.Y., Xu, X., Zhou, X., 2002, *Zircon Chemistry & Magma Genesis, SE China: in-situ Analysis of Hf-Isotopes, Pingtan & Tonglu Igneous Complexes, in Lithos*, Vol. 61, pp. 237-269

Griffin, W.L., Belousova, E.A., Shee, S.R., Pearson, N.J. & O'Reilly, S.Y., 2004, *Archaean Crustal Evolution in the Northern Yilgarn Craton: U-Pb & HF Isotope Evidence from Detrital Zircons*, in Precambrian Research, Vol. 131, pp. 231-282

Griffin, W.L., Belousova, E.A. & O'Reilly, S.Y., 2007, *Crustal History & Metallogenic Fertility: Terrane-Scale Assessment with Detrital Zircons*, Proceedings of Exploration 07: 5th Decennial International Conference on Mineral Exploration, Toronto, September 2007, pp. 311-315. (GEMOC pub. 491)

Griffin, W. L., Powell, W. J., Pearson, N. J. & O'Reilly, S. Y., 2008, *GLITTER*: *Data Reduction Software for Laser Ablation ICP-MS*, in Mineralogical Association of Canada Short Course 40, Vancouver, B.C., Appendix A2, pp. 204-207

Hoskin, P.W.O., & Schaltegger, U., 2003, *The Composition of Zircon & Igneous & Metamorphic Petrogenesis*, in Hanchar, J.M. & Hoskin, P.W.O. (eds), *Zircon: Reviews in Mineralogy & Geochemistry*, Vol. 53, pp. 27-62

Jackson, S.E., Pearson, N.J., Griffin, W.L. & Belousova, E.A., 2004, *The Application of Laser Ablation-Inductively Coupled Plasma-Mass Spectrometry to in situ U-Pb Zircon Geochronology*, in Chemical Geology, Vol. 211, pp. 47-69

Jeon, H., Williams, I. S., & Chappell, B. W., 2012, *Magma to Mud to Magma: Rapid Crustal Recrycling by Permian Granite Magmatism near the Eastern Gondwana Margin*, in Earth & Planetary Science Letters, Vol. 319-320, pp. 104-117

Ludwig, K. R., 2003, *Isoplot EX3.0: A Geochronological Toolkit for Microsoft Excel*, Berkley Geochronology Centre, Special Publication No. 4, accessed via http://www.bgc.org/isoplot_etc/software.html, date accessed 01.02.11, date of last update unknown

Meixner, A. J., & Hotason, D. M., 2004, *Geophysical Interpretation of Proterozoic Mafic-Ultramafic Intrusions in the Arunta Region, Central Australia*, Geoscience Australia Record 2003/29

Norman M.D., Pearson N.J., Sharma A. & Griffin W.L, 1996, *Quantitative Analysis of Trace Elements in Geological Materials by Laser Ablation ICPMS: Instrumental Operating Conditions & Calibration Values of NIST Glass*, in Geostand News, Vol. 20, pp. 247-261.

Pupin, J.P., 1980, *Zircon & Granite Petrology*, in Contributions to Mineral Petrology, Vol. 73, pp. 207-220

Ross Naprurrula, T., 2003, *Making Peace with the Past: Remembering the Coniston Massacre 1928-2003*, Central Land Council publication

Rubatto, D., Hermann, J. & Buick, I.S., 2006, *Temperature & Bulk Composition Control on the Growth of Monazite & Zircon During Low-Pressure Anatexis (Mount Stafford, Central Australia)*, in Journal of Petrology, Vol. 47, No. 10, pp. 1973-1996

Scrimgeour, I., 2006. *An Overview of the North Australian Craton*, In: Lyons, P. & Huston, D.L. (Eds.), Evolution & Metallogenesis of the North Australian Craton, Geoscience Australia Record 2006/16, 1–2

Shaw, S. E., & Flood, R. H., 2009, *Zircon Hf Isotopic Evidence for Mixing of Crustal & Silicic Mantle-derived Magmas in a Zoned Granite Pluton, Eastern Australia*, in Journal of Petrology, Vol. 50, pp. 147-168

Shaw, R.D., Stewart, A.J. & Black, L.P., 1984, *The Arunta Inlier: a Complex Ensialic Mobile Belt in Central Australia. Part 1: Stratigraphy, Correlations & Origin*, in Australian Journal of Earth Sciences, Vol. 31, pp. 445-455

Stewart, A.J., Shaw, R.D. & Black, L.P., 1984, *The Arunta Inlier: A Complex Ensialic Mobile Belt in Central Australia. Part 1: Stratigraphy, Correlations & Origin*, in Australian Journal of Earth Sciences, Vol. 31, No. 4, pp. 445-455

Taylor, S. R. & McLennan, S. M., 1985, *The Continental Crust: Its Composition & Evolution*, Blackwell Scientific Publications, Oxford

Thomas, J.B., Bodnar, R.J., Shimizu, N., Chesner, C.A., 2003, *Melt Inclusions in Zircon*, Reviews in Mineralogy & Geochemistry, Vol. 53 (1), pp. 63-87

Vernon, R., 2004, *A Practical Guide to Rock Microstructure*, Cambridge University Press, Cambridge.

Vernon, R.H., Collins, W.J. & Paterson, S.R., 1993, *Pre-Foliation Metamorphism in Low-Pressure High-Temperature Terrains*, in Tectonophysics, Vol. 219, pp. 241-256

Warren, R.G., 1983, *Metamorphic & Tectonic Evolution of Granulites, Arunta Block, Central Australia*, in Letters to Nature, Vol. 305, pp 300-303

Weidenbeck, M., Alle, P., Corfu, F., Griffin, W. L., Meier, M., Oberli, F., Von Quadt, A., Roddick, J. C. & Spiegel, W., 1995, *Three Natural Zircon Standards for U-Th-Pb, Lu-Hf, Trace Element & REE Analyses*, in Geostandards Newsletter, Vol. 19, pp. 1-24

White, R.W., Powell, R. & Clarke, G.L., 2003, *Prograde Metamorphic Assemblage Evolution during Partial Melting of Metasedimentary Rocks at Low Pressures: Migmatites from Mt Stafford, Central Australia*, in Journal of Petrology, Vol. 44, No. 11, pp. 1937-1960

Whitney, D.L. & Evans, B.W., 2010, *Abbreviations for Names of Rock Forming Minerals*, in American Mineralogist, Vol. 95, pp. 185-187

Winter, J. D., 2001, *An Introduction to Igneous and Metamorphic Petrology*, Prentice Hall, New Jersey